UNIVERSITEIT VAN PRETORIA
UNIVERSITY OF PRETORIA
YUNIBESITHI YA PRETORIA
Faculty of Natural and Agricultural Sciences

The Characterizations of Pyrite from the Ventersdorp Contact Reef of the Kloof Gold Mine in the Witwatersrand Basin in South Africa

by

Full Names: Lowanika Victor Tibane

Student No: 04389603 / 24251365

Submitted in partial fulfilment of the requirements for the degree of MSc Geology

In the Faculty of Natural and Agricultural Sciences
University of Pretoria

**Supervisor:**   Prof. RKW. Merkle

April, 2013

STATEMENT OF AUTHORSHIP

I, Lowanika Victor Tibane, student number 24251365/04389603, declare the following:

1.   I understand what plagiarism entails and am aware of the University's policy in this regard.

2.   I declare that this assignment is my own, original work. Where someone else's work was used (whether from a printed source, the Internet or any other source) due acknowledgement was given and reference was made according to departmental requirements.

3.   I did not copy and paste any information directly from an electronic source (e.g., a web page, electronic journal article or CD ROM) into this document.

4.   I did not make use of another student's previous work and submitted it as my own.

5.   I did not allow and will not allow anyone to copy my work with the intention of presenting it as his/her own work.

Student's signature …………………….   Date……………April, 2013……………
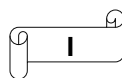
DEDICATION

First and far most, I would like to give my personal gratitude to my mother, Thoko Joyce Ndimande. Mom you are always supportive throughout my academic years; not only financially, but also emotionally. Secondly, I thank you for your constant supporting prayers. Lastly, it is for this reasons that I dedicate this piece of my research work to you.

You are the most well defined, articulate and dedicated mother I ever knew in my life. I thank you mom.
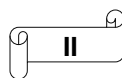
ACKNOWLEDGEMENTS

In the first place, I would like to express my sincere gratitude to all the persons who contributed directly and indirectly to the accomplishment of this project.

I especially give thanks to Prof. Roland Merkle and Prof Wlady Altermann who have dedicated their efforts to review and give comments to the manuscript with good authenticity, absolute composure and their continuous advice as my supervisors. I am equally grateful for their endlessly helpful comments. Mr Eduan Naude and Mr Roger Dixon from the Forensic Laboratory for South African Police Service are thanked for providing assistance with LA-ICP-MS analyses.

I also wish to thank Mr Andre Botha for helping in SEM analyses as well as giving good and faithful assistance. I express my thanks to the late Mr Peter Gräser from Stoneman building for helping with the x-ray facilities at University of Pretoria, and for his contribution to the microprobe analyses. Mr Humbulani Mavhungu and Dr. Chris Franklyn from NECSA are thanked for their help with PIXE work.

Furthermore, my sincere thanks go to many of my relatives and friends who showed love and gave me words of encouragement during the undertaking of this project, which though initially seemed uncomplicated, turned out to be challenging, stimulating and exigent. These people include my beloved Queen Gama, my brother Mr James Tibane, and my mother Miss Joyce Ndimande and not excluding those whose names are not revealed.

I am indebted to the University of Pretoria (UP) Post-graduate Mentorship Bursary Programme for the incredible financial support which enabled the success of this project.

The strengths, success, and quality of this project are due to wise encouragements and contributions given by the above-mentioned people.

ABSTRACT

The approximately 2.9 Ga old Witwatersrand Basin of South Africa hosts different types of pyrite grains. The pyrite grains are hosted in different quartz pebble conglomerate reefs including the Ventersdorp Contact Reef (VCR). The various reefs are accessible from numerous goldfields. Regardless of years of studying the various types of pyrite grains from the VCR, there is still a disagreement as to their origins. Numerous pyrite grains of different types, shapes, and textures have been identified in the VCR of the Kloof Gold Mine. The origin of the different types of pyrite grains have been attributed to various mechanisms. Consequently, different depositional models were suggested for the mineralisation of the pyrite grains. Nevertheless, the style of mineralisation and origin of the different types of pyrite grains require further work especially for the VCR. This study determined whether a single or multiple processes were responsible for the formation of the different pyrite grains.

The different types of pyrite grains including the rounded porous, rounded massive and angular massive grains were identified using a reflected light microscopy, scanning electron microscopy, and Röntec energy-dispersive x-ray spectroscopy. The above techniques were used to describe the shapes, sizes, and textures of the different types of pyrite grains in order to classify and group the pyrite grains for further investigation by chemical analysis. Identification and description of minerals associated with pyrite were conducted to determine the environment and conditions under which pyrite grains were formed. Genetic structures were identified in order to resolve whether the pyrite grains were transported or crystallised in situ. Different types of inclusions hosted in pyrite grains were identified and described to determine the nature of pyrite grains. Rounded zircon grains were identified in rounded massive pyrite grains, and the appearance the rounded zircon grains might suggest that the rounded massive pyrite grains formed later after the deposition of the Witwatersrand basin sediments.

A particle induced x-ray emission, an electron microprobe, and a laser ablation inductively coupled plasma mass spectrometry were used to carry out chemical analysis of the major, minor and trace elements of the different pyrite grains. The chemical analyses were conducted to investigate and determine the chemical signatures and the composition of the different types of the pyrite grains to determine their processes of formation. Compositional zonation patterns and overgrowths of the pyrite grains were identified in order to determine whether the pyrite grains were formed through multiple mechanisms.

The compositional zonation patterns were observed in the rounded porous pyrite grains. The zonations suggest multiple stages of growth processes resulting in most porous parts of the pyrite being enclosed by nearly pure pyrite. The rounded pyrite grains are generally containing high concentrations of Ni and Co as opposed to angular pyrite grains. The Ni/Co ration is low in the angular pyrite grains, but high in the rounded grains. The high Ni/Co ratio in rounded grains may be related to low-temperature sedimentary processes, whereas the low Ni/Co ratio in angular pyrite grains may indicate hydrothermal source. The differences between rounded and angular pyrite grains can be interpreted as a result of different genetic history, and origin from different sources. Thus the different pyrite grains formed under different chemical and atmospheric conditions, and by different depositional mechanisms.

TABLE OF CONTENTS

LIST OF FIGURES

LIST OF TABLES

LIST OF APPENDICES

CHAPTER ONE
BACKGROUND OF THE STUDY

1. Introduction

The approximately 2.9 Ga old Witwatersrand (Wits) Basin of South Africa hosts different types of pyrite grains (Rundle and Snelling, 1977; Robb et al., 1991; Hall, 1994; Reimold et al., 1999 & 2004; Zartman and Frimmel, 1999; England et al., 2002; Zhao et al., 2005). The pyrite grains are hosted in different quartz pebble conglomerate reefs including the Ventersdorp Contact Reef (VCR) (Utter, 1978; Poujol et al., 1999; Kirk et al., 2002). The various reefs are accessible from numerous goldfields (Figure 1.1) (Els, 1998; Poujol et al., 1999). Regardless of years of studying the various types of pyrite grains from the VCR (Schidlowski, 1968; Rundle and Snelling, 1977; Utter, 1978; Barton and Hallbauer, 1996; England, 2002; Hofmann et al., 2009), there is still a disagreement as to their origins. Numerous pyrite grains of different types, shapes, and textures have been identified in the VCR of the Kloof Gold Mine (KGM) (Ramdohr, 1958; Hallbauer, 1996; England, 2002; Hofmann et al., 2009). The origin of the different types of pyrite grains have been attributed to various mechanisms. Consequently, different depositional models were suggested for the mineralisation of the pyrite grains (Schidlowski, 1968; Rundle and Snelling, 1977; Utter, 1978; Barton and Hallbauer, 1996; England, 2002; Hofmann et al., 2009). Nevertheless, the style of mineralisation and origin of the different types of pyrite grains require further work especially for the VCR (Toma and Murphy, 1978; Robb and Meyer, 1995, Minter, 1999; Kirk et al., 2002; Jolley et al., 2004; Grove and Harris, 2010; Koglin et al., 2010). This study aims to examine the chemistry of the pyrite grains, in order to determine whether a single or multiple processes are responsible for the formation of the pyrite grains.

The CVR separates the underlying clastic sediments of the Wits Supergroup from the overlying volcanic Ventersdorp Supergroup (Scott, 1951; Roux, 1967; Utter, 1978; Duane et al., 1997; Zhao et al., 1999; Frimmel and Minter, 2002; Frimmel et al., 2005), see Figure 1.1.

The VCR represents an auriferous and uraniferous conglomerate horizon currently being exploited for gold (Scott, 1951; Burke et al., 1986; Duane et al., 1997; Els, 1998; Eriksson et al., 2001; England et al., 2002; Alexandre et al., 2006; Hofmann et al., 2009).
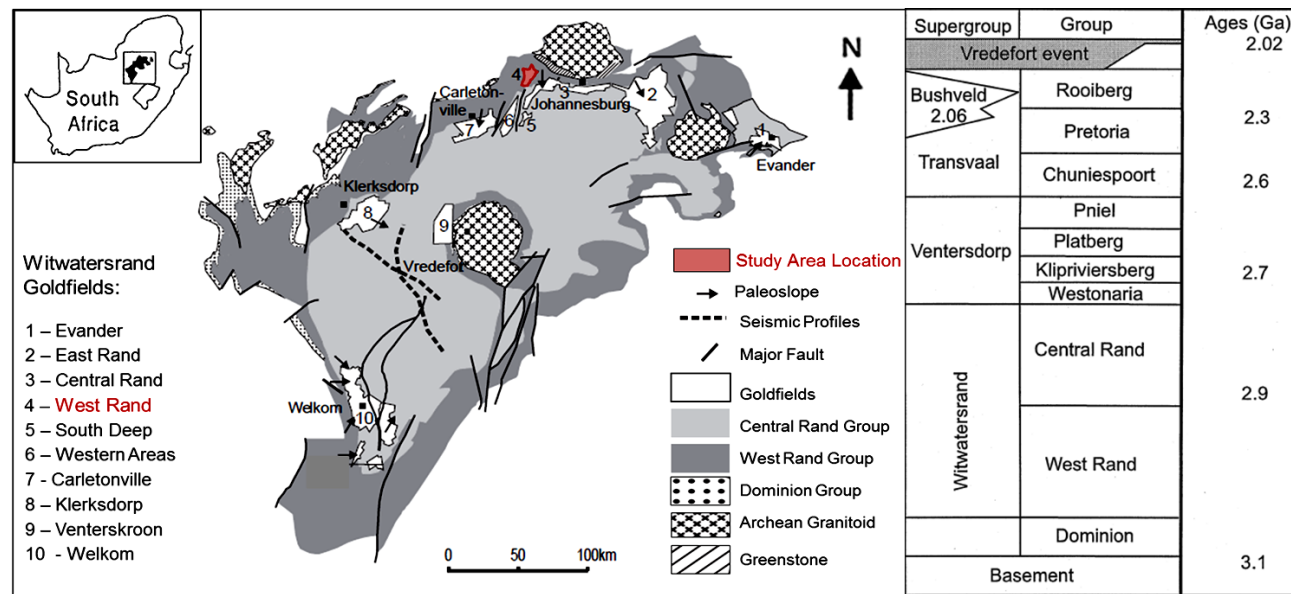
Figure 1.1: *Simplified map showing the outcropping Wits Basin, and the geographical location of the Kloof Gold Mine indicated by a red shaded area, Welkom, Klerksdorp, Carletonville, Evander, West Rand, and Central Rand Goldfields, and stratigraphic column (modified from Frimmel and Minter, 2002; England et al., 2002).*

According to Gold Fields Limited (2009), the KGM is situated in the West Rand Goldfield. The first mine shaft was established in 1934 and the KGM has contributed significantly to the total gold production of South Africa. Presently, KGM includes the former Venterspost, Libanon, Kloof and Leeudoorn gold mines, after amalgamation in April 2000. The active underground mining at present, reaches a depth exceeding 3300 m below surface, over an area of 20087 ha, which extends for more than 28 km in strike and 8 km in dip direction of the reefs. Next to the VCR of the Venterspost Conglomerate Formation, the KGM exploits gold mineralisation within quartz pebble conglomerates of the Kloof Reef of the Kimberley Conglomerate Formation and the Middelvlei Reef of the Main Conglomerate Formation (Gold Fields Limited 2009).

The VCR remains however the most significant contributor, as it continues to supply more than three quarters of the mineral reserve of the mine (Robb et al., 1991; Hall, 1994; Reimold et al., 1999; Zhao et al., 1999; 2005).

Previous studies on the Wits Basin have identified different types of grains of pyrite, including rounded or angular grains originating from the VCR (Ramdohr, 1958; Hallbauer, 1996; England, 2002; Hofmann et al., 2009). The rounded and angular pyrite grains may contain different genetic structures, textures, shapes, and major, minor, and trace element chemistry. The literature suggests that the rounded pyrite grains are detrital origin and were derived from numerous sources such as mantle magma, hydrothermal deposits found in granitoid-greenstones, older sedimentary units or syn-depositional to diagenetic sulphides of primary chemical precipitates, or secondary replacements (England et al., 2002; Hofmann et al., 2009). The rounded pyrite grains could have been eroded from different source rocks, transported, and deposited in a different environment by migrating hydrothermal fluids (Utter, 1978; Hallbauer, 1986; Barton and Hallbauer, 1996; England, 2002; Hofmann et al., 2009).

In contrast, the angular pyrite grains may have formed in situ by hydrothermal processes that occurred after sedimentation of the Wits Basin (Utter, 1978). The angular pyrite grains should be uniform or at least have similar chemical zonation under the assumption that they formed under similar conditions by fluids of similar chemical composition (Hofmann et al., 2009). Thus the angular pyrite grains should be analogous to one another. Furthermore, England et al. (2002); Hofmann et al. (2009) argued that the angular pyrite grains are present as secondary features associated with diagenesis, metamorphism or hydrothermal alteration.

However, the intrusion of the Bushveld Igneous Complex (BIC) around 2.06 Ga ago and a meteorite impact which formed the Vredefort Dome about 2.02 Ga ago may have caused the remobilisation of the Wits deposits (Utter, 1978; Robb et al., 1995; Frimmel et al., 1999; Reimold et al., 1999; Roberts and Schweitzer, 1999; Kositcin and Krapež, 2004; Alexandre et al., 2006).

The BIC and Vredefort meteorite impact would have initiated crystallisation of various angular grains of pyrite. Therefore the angular pyrite grains could have diverse compositions as a result of the different chemical composition of the hydrothermal fluids initiated by separate geological events at different time periods. Nevertheless, the angular pyrite grains should be distinguishable from rounded pyrite grains in terms of genetic structures, shape, texture, and geochemical signatures (England et al., 2002; Hofmann et al., 2009).

Hofmann et al. (2009) carried out sulphur (S) ($\Delta^{34}S$ and $\Delta^{33}S$) isotope analyses of the rounded pyrite grains from Archaean Wits conglomerates. The study tried to identify the origin of the detrital pyrite grains, and also to investigate their provenance should they be detrital. Photolysis of SO_2 under ultraviolet (UV) radiation is responsible for non-mass dependent fractionation (NMDF) of S isotopes (Farquhar et al., 2001; Canfield, 2005; Hofmann et al., 2009; Watanabe et al., 2009). Nonetheless, there is a lack of evidence to support the accountability for the NMDF observed in Archaean sediments (Lyons, Kah and Gellatly, 2004; Hofmann et al., 2009). The deficiency of an ozone shield in the anoxic Archaean atmosphere has been responsible for NMDF of the sulphides in Archaean period (Kasting and Howard, 2006; Anabar et al., 2007; Hofmann et al., 2009). Sulphur isotope values of detrital rounded pyrite grains were reported and distinguished between igneous, hydrothermal, and various sedimentary sources (Kasting and Howard 2006; Anabar et al., 2007; Hofmann et al., 2009).

The findings provided support on the provenance of gold and uranium placer deposits similar to Wits ores. Hofmann et al. (2009) found that the rounded massive also called massive pyrite grains have $\Delta^{34}S$ values ranging from as low as -1.5 to 4.3 ‰, with values of $\Delta^{33}S$ being close to 0.0 ‰, and equivalent to $\Delta^{34}S$ and $\Delta^{33}S$ values of the intergrowths of chalcopyrite. Nevertheless, numerous rounded pyrite grains indicate a negative signal of NMDF with values of $\Delta^{33}S$ being as low as -0.47‰ (Kasting and Howard, 2006; Anabar et al., 2007; Hofmann et al., 2009).

Conversely, values close to 0 ‰ of $\Delta^{34}S$ were reported by England et al., (2002) for angular pyrite grains taken from the VCR. The values revealed a narrower range than that of the rounded pyrite grains; therefore these values support a hydrothermal origin for the angular massive pyrite grains (Shepherd, 1977). Using sulphur isotope analysis, the sulphur that passed through the Archaean atmosphere can be distinguished from sulphur of magmatic origin incorporated into hydrothermal fluids (Anabar et al., 2007; Hofmann et al., 2009). Pyrite nodules of Archaean shales rich in organic matter have mostly negative $\Delta^{33}S$ values. The negative values might reflect a reduction of sulphate of seawater in sediments during diagenesis (Kasting and Howard, 2006; Bekker et al., 2008a; Ono et al., 2009; Hazen et al., 2011).

Sulphide minerals including pyrite are likely to weather very fast in the presence of O_2, consequently the partial pressure of atmospheric O_2 (PO_2) could have been low when pyrite grains were formed (Canfield, 2005; Kasting and Howard, 2006; Anabar et al., 2007), otherwise pyrite crystals would have oxidised completely under high PO_2.

An elevated rate of oxidative pyrite weathering in crustal rocks throughout and subsequent to the period of the Great Oxidation Event (GOE) was responsible for the raise of concentrations of ocean sulphate (Anabar et al., 2007). Furthermore, the effects of reduced remarkable oxygenation at 2.5 Ga may be predictable by the negative shift in sedimentary $\Delta^{34}S$ (Kasting and Howard, 2006). The existence of "chemicofossils" at least 2.5 Ga ago lightened the understanding of the development of actual life (Rutten, 1966; Rasmussen and Buick, 1999). The chemicofossils indicate the existence of vegetable life forms, capable of organic photosynthesis for the production of free oxygen accounting for the oxidation of surface minerals including pyrite grains (Rutten, 1966).

The Earth's temperatures were very low at about 2.5 Ga ago because of hydrogen liberation into space, suggesting reducing conditions during Archaean time (Spangenberg and Frimmel, 2001). The Earth was dominated by NH_3 and water greenhouse gases. A gradual decline in temperatures was produced by reaction and oxidation of the reduced gases. At around 2.0 Ga ago, the planetary atmosphere approached the present day greenhouse conditions (Sagan and Mullen, 1972).

NH_3 is unstable in an excess of O_2 hence the occurrence of NH_3 suggests the absence of contemporary values of O_2 for a major fraction of the history of the Earth. This is consistent with and supports a variety of other evidence including data on banded iron formations (BIF), on the oxidation of uraninite, and on the comparatively small ^{34}S enrichment of barites (Canfield, 2005), and makes the suggestion of an early oxidizing atmosphere on Earth quite implausible (Sagan and Mullen, 1972). Using S and Fe isotope composition of the rounded grains, Hofmann et al. (2009) suggested that the rounded pyrite grains are detrital origin. This idea is supported by the petrography and sulphur isotope studies conducted by England et al. (2002).

1.1. Hypothesis

The different types of pyrite grains in the VCR of the KGM have been investigated for more than a century. Even though years of studying Wits pyrite grains have elapsed, there is still a continuing debate as to their origins. The origins of the texturally different grains of pyrite remain a subject of discussion. Different mechanisms for the origin of the various pyrite grains have been proposed, but the mechanisms are susceptible to scrutiny for the lack of available evidence. Thus, the various pyrite grains require further investigations to unravel the ambiguity between the contesting depositional models.

1.2. Aims of the Study

This study aims to characterise the textural different types of pyrite grains and examine their chemistry, in order to determine whether one or more processes are responsible for their formation.

1.3. Objectives of the Study

1. The study aims at characterising the various pyrite grains by petrographic investigation of polished sections.

→ Description of the shapes and textures of the different types of pyrite grains in order to classify and group the pyrite grains for further investigation by chemical analysis.

→ Identification and description of minerals associated with pyrite to determine the environment and conditions under which pyrite grains were formed.

→ Identification of genetic structures, to resolve whether the pyrite grains were transported or crystallised in situ.

→ Identification and description of inclusions in the pyrite to determine the nature of pyrite grains.

→ Documentation of compositional zonations and overgrowths of the pyrite grains, to determine whether the pyrite grains were formed through multiple mechanisms.

The above objectives are achieved using a Nikon Eclipse E200, 2325 reflected light microscopy (RLM), the JEOL 5800LV scanning electron microscopy (SEM) and Röntec energy-dispersive x-ray spectroscopy (EDS) system. These techniques are available at the University of Pretoria.

2. The study aims to examine the chemistry of the various pyrite grains and the chemistry of the inclusions in pyrite and the minerals associated with pyrite.

→ Carry out chemical analysis of the major, minor and trace elements to investigate the chemical signatures and composition of the different types of the pyrite grains.

The examination of the chemistry of the pyrite grains is achieved using a particle induced x-ray emission (PIXE) method at the Nuclear Energy Corporation of South Africa (NECSA), a Cameca SX100 electron microprobe (EMPA**)** system available at the x-ray facilities at the University of Pretoria, and an Agilent 7500 series laser ablation inductively coupled plasma mass spectrometry (LA-ICP-MS) technique performed at the Forensic Laboratory of the South African Police Service (SAPS).

CHAPTER TWO

TECTONIC SETTING OF THE WITS BASIN

2. Geological Background

2.1. Archaean Basement

The approximately 3.1 Ga old Archaean basement rocks of the Kaapvaal Craton underlie the volcanics of the Dominion Group (Armstrong et al., 1991; Barton and Hallbauer, 1996; Duane et al., 1997; Killick and Scheepers, 2005).

2.2. Dominion Group

The 3.0 Ga old rocks of the Dominion Group are underlying the units of the Wits Supergroup (Rundle and Snelling, 1977; Armstrong et al., 1991; Burke et al., 1986; Els, 1998; Kirk et al, 2002; Eriksson et al., 2001). The predominant rock types found in the Dominion Group include granite, gneiss, and predominantly basaltic lavas and metamorphic rocks (Burke et al., 1986; Barton and Hallbauer, 1996; Els, 1998; Duane et al., 1997; Frimmel, 1997). The Dominion Group occupies an area of 15 000 km^2, and attains a thickness of 2 250 m, summarised in Burke et al. (1986). The Dominion Group is divided into three formations, including the Renosterspruit, Renosterhoek, and Syferfontein (Burke et al., 1986).

The Renosterspruit formation forms the base of the Dominion Group and consists of approximately 60 m of sandstones, quartz-pebble conglomerates and argillaceous materials (Burke et al., 1986). The Renosterhoek formation consists of 1 100 m of basaltic andesites and tuffs, paleosols which can be used as an indicator of atmospheric O_2, and sandstones (Beukes et al., 1990, Canfield, 2005). The Syferfontein formation attains a thickness of 1 500 m and contains rhyolites, silicic tuffs, volcanic breccias, and subordinate andesitic lavas, as summarised in Burke et al. (1986).

2.3. Wits Supergroup

The Wits Supergroup of South Africa is found on the Kaapvaal craton, and is stratigraphically divided into the lower West Rand Group (WRG) and upper Central Rand Group (CRG) (Scott, 1951; Burke et al., 1986; Duane et al., 1997; Els, 1998; Eriksson et al., 2001; England et al., 2002; Alexandre et al., 2006; Hofmann et al., 2009). The lower WRG is underlain by the Dominion Supergroup which forms the basement to the Wits Basin. The CRG overlies the WRG, and is in turn overlain by andesitic lavas of the 2.7 Ga old Ventersdorp Supergroup (Armstrong et al., 1991; Els, 1998; Vollbrecht, 2001; Kositcin and Krapež, 2004). The Ventersdorp Supergroup is overlain by the Transvaal Supergroup (Barton and Hallbauer, 1996; Frimmel et al., 1999); see Figure 1.1.

According to the earlier published literature, the Wits Basin (Figure 1.1) represents sedimentary rocks which accumulated on the Kaapvaal craton (Scott, 1951; Schidlowski, 1968; Burke et al., 1986; Duane et al., 1997; England et al., 2002; Kositcin and Krapež, 2004). The age of this basin was constrained from Pb-Pb (^{207}Pb/^{204}Pb versus ^{206}Pb/^{204}Pb) dating and the basin is known to be between 3.0 and 2.8 Ga old (Rundle and Snelling, 1977; Armstrong et al., 1991; Zartman and Frimmel, 1999; England et al., 2002; Koglin et al., 2010). The age dating work carried by Kirk et al. (2002) produced a rhenium-osmium isochron age of roughly 3.1 Ga for gold and rounded pyrite grains from the Wits conglomerate reefs, and an initial ^{187}Os/^{188}Os ratio of 0.1079 ± 0.0001.

The proposed Wits stratigraphic column (Figure 1.1) contains interbedded argillaceous and arenaceous sediments (Scott, 1951; Schidlowski, 1968; Burke et al., 1986; Frimmel et al., 1999). These sediments were derived by erosion of older granite greenstone belts similar to the Barberton and Murchison Greenstone Belts in the Mpumalanga and Limpopo provinces respectively. The argillaceous and arenaceous sediments are clast-supported oligomictic and loosely packed conglomerates, and pebbly arenites associated with trough cross-bedded quartz arenites laid down in fluvial deltaic settings (Scott, 1951; Schidlowski, 1968; Burke et al., 1986; Frimmel et al., 1999). Black argillaceous sedimentary rocks are observed in addition to quartz pebbles and shales (Frimmel and Minter, 2002).

The tectonic history of the Wits basin is described by Roering et al. (1987). The Wits basin has experienced faulting and intrusion of dykes within the vicinity of the KGM. The faulting and intrusion of dykes significantly influenced the distribution of ore-bodies including the CVR. A detailed discussion of the tectonic evolution of the Wits Basin is beyond the scope of this study. However, Berlenbach, (1995) has discussed north-east thrusting faults at KGM. The Wits basin has experienced a development of a half-graben system and deformation of the crust during the Ventersdorp Supergroup deposition (Burke et al., 1986). Folding and thrusting occurred before and during the deposition of the Transvaal Supergroup (Frimmel and Minter, 2002; Jolley et al., 2004). The folding and thrusting events were superseded by the intrusion of the Bushveld Igneous Complex (BIC) into the upper Transvaal Supergroup, with simultaneous extrusion of the Rooiberg lavas at around 2.06 Ga ago (Robb et al., 1995; Kositcin and Krapež, 2004).

It is argued that the Wits basin has been modified by later eruption of flood basalts at the time of the Ventersdorp Supergroup formation at c. 2.7 Ga ago (Armstrong et al., 1991; Poujol et al., 1999; England et al., 2002). Thereafter, the BIC intrusion and the extrusion of the Rooiberg lavas were accompanied by extension in conjunction with high heat flow (Frimmel, 1997; Reimold et al., 1999; Spangenberg and Frimmel, 2000; Alexandre et al., 2006). In addition, the Wits basin underwent deformation and strike-slip faulting resulting from a meteorite impact which formed the Vredefort Dome at about 2.02 Ga ago (Utter, 1978; Frimmel et al., 1999; Reimold et al., 1999; Roberts and Schweitzer, 1999; Alexandre et al., 2006). The later history of the Wits basin remains open to scrutiny owing to a lack of record in the cover sequences until the Palaeozoic when the basin was metamorphosed (Rubatto and Hermann, 2006). The Mesozoic to recent extension and partial exhumation mechanism were restricted to small areas which permitted the preservation of crustal features, and are not attributed to magmatic events (Gibson and Jones, 2002).

2.4. West Rand Group

The WRG is traditionally subdivided into three subgroups known as Hospital Hill, Government and Jeppestown (Burke et al., 1986; Frimmel and Minter, 2002). Mud-rocks, texturally matured sandstones, and shales are the predominant rock types constituting the WRG (Schidlowski, 1968; Burke et al., 1986; summarized in Eriksson et al., 2009). The Hospital Hill and Jeppestown subgroups consist mainly of shales, separated by basin-wide disconformities (Burke et al., 1986; England et al., 2002; Koglin et al., 2010). In addition to the chlorite-rich shale bed units, the Hospital Hill subgroup also contains quartz-arenite sandstones (Burke et al., 1986; England et al., 2002; Alexandre et al., 2006). The Government subgroup contains auriferous sub-economic reefs such as the Rivas Reef, Coronation Reef, and Government Reef (England et al., 2002; Alexandre et al., 2006).

The WRG reflects a shallow marine depositional environment (Eriksson et al., 2001; England et al., 2002; Koglin et al., 2010). Cycles in the deposition of sediments are an indication of eustatic sea level changes (England et al., 2002). Moreover, the depositional cycles reflect fluctuations between fluvial and marine shelf environments (Burke et al., 1986; England et al., 2002). Cold climatic conditions are suggested during the period of deposition of the WRG, supported by the presence of diamictite which in turn correspond to the glacial period of the Pongola Supergroup (Von Brunn and Gold, 1993; Eriksson et al., 2001). An age of 2.9 Ga was proposed for the WRG based on U-Pb dating obtained from the volcanic sequence of the Crown Formation lava in the Jeppestown subgroup (Armstrong et al., 1991; Burke et al., 1986; Duane et al., 1997; Poujol et al., 1999; Koglin et al., 2010). The WRG is inferred to attain an approximate thickness of 7.5 km and covers an area of 42 000 km^2 (Burke et al., 1986; Frimmel and Minter, 2002; Frimmel et al., 2005). The WRG thins (pinches) out with its thickness decreasing to about 830 m toward the Evander Goldfield area (Burke et al., 1986; Frimmel and Minter, 2002).

2.5. Central Rand Group

The CRG consists of two subgroups, including Johannesburg and Turffontein (Burke et al., 1986). According to Frimmel and Minter (2002), the CRG is underlain by the WRG. In comparison to the WRG, the CRG comprises predominantly of graywackes, conglomerates, sandstones, siltstones, and shales (Burke et al., 1986; Els, 1998; England et al., 2002). The Johannesburg subgroup consists of the Main Reef, Carbon Leader Reef, Leader Reef, and Vaal Reef (Scott, 1951; Rundle and Snelling, 1977; Utter, 1978; Burke et al., 1986; Frimmel and Minter, 2002). In contrast, the Turffontein subgroup encompasses the Kimberley Reef, Denny's Reef, Elsburg Reef, Beatrix Reef, Composite Reef, Kalkoenkrans Reef, and Bastard Reef (Scott, 1951; Rundle and Snelling, 1977; Utter, 1978; Kirk et al., 2002).

The Elsburg reef underlies the VCR (Scott, 1951; Rundle and Snelling, 1977). The Bastard Reef and the upper Elsburg Reef are closely associated with quartz-arenite and related to low-angle unconformities (Frimmel and Minter, 2002). Comparably to WRG, the CRG consists of alternating cycles of deposition reflecting fluvial coarse siliciclastic rocks accumulated above surface of erosion (Frimmel and Minter, 2002). Contrary to Frimmel and Minter (2002), England et al. (2002) suggested that argillaceous rocks are found in the WRG whereas the arenaceous rocks make up the CRG. The coarse grained siliciclastic rocks and shales dominating the CRG represent fluviodeltaic environments (England et al., 2002). The siliciclastic rocks of the CRG (Figure 1.1) are overlain by the Klipriviersberg Group of the Ventersdorp Supergroup (Roux, 1967; Utter, 1978; Frimmel et al., 2005). The CRG covers an area of 10 000 km^2; its thickness is greatest near the centre of the basin at around 2.8 km, but decreases toward the margins (Burke et al., 1986; Kirk et al., 2002; Frimmel et al., 2005). The CRG was deposited around 2.8 Ga ago as reflected by the age of detrital zircons (Armstrong et al., 1991; Poujol et al., 1999; Kirk et al., 2001; Frimmel et al., 2005; Koglin et al., 2010). Conversely, an age of 2.7 Ga old was determined from ^{187}Os/^{188}Os isotopic data derived from dating pyrite sections from Vaal Reef (Kirk et al., 2001; Koglin et al., 2010).

2.6. Ventersdorp Contact Reef

The clastic sediments of the Wits Supergroup are separated from the overlying volcanic Ventersdorp Supergroup by the VCR (Scott, 1951; Roux, 1967; Utter, 1978; Duane et al., 1997; Zhao et al., 1999; Frimmel and Minter, 2002; Frimmel et al., 2005); see Figure 1.1. The VCR represents an auriferous and uraniferous conglomerate horizon which is the economic ore body at the top of the Wits Supergroup (Scott, 1951; Schidlowski, 1968; Rundle and Snelling, 1977; Utter, 1978; Zartman and Frimmel, 1999; Frimmel et al., 2005; Zhao et al., 2005).

The VCR is pervasively metamorphosed to low grade (greenschist metamorphism) and represents a hydrothermally altered conglomerate horizon (Robb et al., 1991; Hall, 1994; Reimold et al., 1999; Zhao et al., 1999; 2005). The VCR is overlain by the Black Reef of the Transvaal Supergroup (Scott, 1951; Rundle and Snelling, 1977)

2.7. Ventersdorp Supergroup

The Ventersdorp Supergroup unconformably overlies the basement rocks of the Wits Supergroup, and the Ventersdorp Supergroup is in turn unconformably overlain by the Transvaal Supergroup (Els, 1998), see Figure 1.1. The U-Pb and zircon dating provided an age of about 2.7 Ga old for the lavas of the Ventersdorp Supergroup (Rundle and Snelling, 1977; Armstrong et al., 1991; Poujol et al., 1999). The Ventersdorp Supergroup covers an area of more than 200 000 km^2 and consists mainly of andesitic lavas, and attains a thickness of 8 km (Duane et al., 1997; Els, 1998).

2.8. Transvaal Supergroup

The Transvaal Supergroup extends for an area of 700 000 km^2 and has a thickness of 12 km (Burke et al., 1986; Barton and Hallbauer, 1996). The age of the sedimentary rocks of the Transvaal Supergroup is between 2.6 and 2.1 Ga old (Rundle and Snelling, 1977; Walraven and Martini, 1997; Altermann and Siegfried, 1997; Altermann and Nelson, 1998).

2.9. Wits Goldfields

The Wits basin is considered the world's most important source of gold and contributes significantly to the economy of South Africa (Utter, 1978; Reimold et al., 1999; Frimmel and Minter, 2002). The conglomerate beds have been, and still are, the most important producer of gold from the Wits basin (Scott, 1951; Utter, 1978; Frimmel and Minter, 2002). According to the annual report by Gold Fields Limited (2009), the Wits Basin remains the most important gold depository in the history of mining of South Africa. This basin consists of the Welkom, Klerksdorp, Carletonville, Evander, West Rand, and Central Rand Goldfields (Frimmel and Minter, 2002). Nevertheless, this thesis will only focus on the VCR, situated in the Carletonville area, in the West Rand Goldfields, south-west of Johannesburg.

The Wits goldfields extend for 80 km from Randfontein to Springs, for 32 km from Springs to Heidelberg, and for 64 km from Randfontein to the Mooi River (Scott, 1951). The goldfields cover an area of 52 000 km^2 with a thickness of 7 km (Poujol et al., 1999; Vollbrecht, 2001; Gibson and Jones, 2002).

2.10. The Kloof Gold Mine

According to Gold Fields Limited (2009), the KGM is situated in the West Rand Goldfield. The first mine shaft was established in 1934 and the KGM has contributed significantly to the total gold production of South Africa. Presently, the KGM includes the former Venterspost, Libanon, Kloof, and Leeudoorn gold mines after amalgamation in April 2000. The active underground mining at present reaches a depth exceeding 3 300 m below surface over an area of 20087 ha which extends for more than 28 km along strike and 8 km in the dip direction of the reefs. Next to the VCR of the Venterspost Conglomerate Formation, the KGM exploits gold mineralisation within quartz pebble conglomerates of the Kloof Reef of the Kimberley Conglomerate Formation and the Middelvlei Reef of the Main Conglomerate Formation (Gold Fields Limited 2009). The VCR remains however the most significant contributor, as it continues to supply more than three quarters of the mineral reserve of the mine (Robb et al., 1991; Hall, 1994; Reimold et al., 1999; Zhao et al., 1999; 2005).

2.11. Mineralisation

According to Koglin et al. (2010), mineralisation in the conglomerate rocks occurs within pebbles and in the conglomerate matrix. Pebbles may include vein quartz, white and banded chert, shales, and schist, whereas the matrix consists predominantly of quartz, pyrite, and different types of white micas and accessory minerals such as zircon, uraninite, brannerite, anatase, rutile, magnetite, ilmenite, chalcopyrite, apatite, and barite.

2.12. Depositional Models

Different depositional models have been suggested for the mineralisation of the Wits Basin (Schidlowski, 1968; Rundle and Snelling, 1977; Utter, 1978; Barton and Hallbauer, 1996; England, 2002; Hofmann et al., 2009).

Nevertheless, these models have been concentrated on the form and style of mineralisation of gold (Toma and Murphy, 1978; Robb and Meyer, 1995, Minter, 1999; Kirk et al., 2002; Jolley et al., 2004; Grove and Harris, 2010; Koglin et al., 2010), and less work has focused on investigating the depositional mechanisms for the different types of pyrite grains originating from the VCR. The different suggested depositional models include (a) a placer model; (b) a hydrothermal model; and (c) a modified placer model.

2.12.1. A Placer Model

A placer model was first proposed by Mellor in 1916 (Rundle and Snelling, 1977; Utter 1978; Frimmel, 1997). The placer model states that gold grains exist in association with pyrite and uraninite grains in conglomerate rocks of the Wits basin and they were derived from different rock sources representing old granite greenstone belts similar to the Barberton Greenstone Belt (Robb and Meyer, 1995; Minter, 1999; Reimold et al., 1999; Kirk et al., 2002; Jolley et al., 2004; Grove and Harris, 2010). Basically, the placer model suggests the source rocks were subjected to a cycle of weathering and erosion, and the grains of gold and pyrite were transported and deposited in a different place (Rutten, 1966; Rundle and Snelling, 1977).

The rounded pyrite grains are anticipated to represent primarily detrital grains (Utter, 1978; Hallbauer, 1986; Barton and Hallbauer, 1996; England, 2002; Hofmann et al., 2009), and should be morphologically distinguishable from the younger secondary pyrite grains. Deep erosion of the tonalite–trondhjemite–granodiorite (TTG) and greenstone belts and transportation of non-oxidised uraninite and pyrite pebbles was possible because of the CO_2 rich and O_2 deficient Archaean atmosphere (Ohmoto et al., 2004). However, the debate on the O_2 content of the Archaean atmosphere is not fully resolved (Farquhar et al., 2001; Ohmoto et al., 2004; Canfield, 2005; Hofmann et al., 2009; Watanabe et al., 2009). The literature has shown that the detrital pyrite grains were formed during an anoxygenic atmosphere in the Archaean time period (Holland, 1984; Rasmussen and Buick, 1999; Lyons, Kah, and Gellatly, 2004; Anabar et al., 2007).

The pyrite grains are reactive in the present oxygenic surface setting and only oxides such as quartz and magnetite can be formed because both quartz and magnetite are resistant to chemical weathering (Rutten, 1966; Rasmussen and Buick, 1999; Canfield, 2005). Any considerable quantity of sulphides indicates either extreme conditions during sedimentation, subsequent to rapid burial and prohibiting interaction with the atmosphere, or tremendous climate prohibitive to chemical weathering (Rutten, 1966). In contrast, a limited chemical weathering occurred under anoxygenic atmosphere, hence sands and conglomerates were formed consisting of oxides such as quartz and sulphides such as pyrite (Rutten, 1966; Canfield, 2005).

2.12.2. A Hydrothermal Model

The placer model was opposed by Graton (1930) who advocated a hydrothermal model in the 1930s, as indicated in the history summarised by Utter (1978). The hydrothermal model proposes hydrothermal fluids originating from outside the Wits Basin. The hydrothermal fluids could have been responsible for the deposition of gold and pyrite grains (Barnicoat et al., 1998; Phillips and Law, 2000; Grove and Harris, 2010).

Supplementary work carried out by researchers of the detrital pyrite has suggested that the detrital rounded massive and angular massive pyrite grains have grown in situ by pyritization of non-sulphide minerals such as oxides through post sedimentary hydrothermal processes (Barnicoat et al., 1997; Phillips and Law, 2000; Hofmann et al., 2009; England et al., 2002).

2.12.3. A Modified Placer Model

The hydrothermal model was criticized ten years after being proposed (Frey et al., 1987; Meyer et al., 1987; Frimmel, 1997; Grove and Harris, 2010), and a modified placer model came into play. In essence, the modified placer model represents a revised version of the placer model. This modified placer model hypothesises that the gold, pyrite, and uraninite grains are detrital in origin and were in part affected by recrystallisation, and remobilisation for a short distance during metamorphism by migrating hydrothermal fluids and re-deposited in a new location (Frey et al., 1987; Meyer et al., 1987; Frimmel, 1997; Grove and Harris, 2010). The mobilization of certain minerals was later on supported by Spangenberg and Frimmel (2001).

Schidlowski (1968) argued that the reconstruction of the distribution pattern undergone by the Wits gold and detrital rounded pyrite grains during the post-depositional history of the conglomerates did not require any major migration processes. He claimed that the bulk of the metals still lie where they collected when the placer was formed. Furthermore, he discussed that the mobilization of certain minerals within the reefs was localised and barely surpassed the distance of a few millimetres. It is therefore arguable that the secondary processes have seriously affected the primary alluvial distribution pattern of the detrital minerals including the rounded pyrite grains.

CHAPTER THREE

SAMPLING AND ANALYTICAL METHODS

3. Methodology

The polished sections used during this investigation were prepared from samples that originated from the VCR of the KGM in the Wits Basin of South Africa. A total of 29 polished sections including section 3719, g52200, g52201, g52203, g52008, g52210, g52213, g52214, g52216, g52224, g52227, g52228, g52229, g52230, g52233, g52236, g52237, g52239, g52258, g52260, g52261; g52263, g52288, g52688, VL226, VL228, VL2203, VL2232, and section 3472 were made available for investigation by Prof RKW Merkle at the Geology Department, University of Pretoria. This study does not by any means provide a full coverage of the Wits Basin, as it only focused on the pyrite grains from the VCR in the West Rand Goldfields.

3.1. Reflected Light Microscopy (RLM)

A Nikon Eclipse E200 reflected light microscope at the UP was used for identification and description of grain morphologies, sizes, and textures. The grain morphologies, sizes, and textures are used to classify and group the various pyrite grains for further chemical investigation. RLM was also used to estimate the abundance of the different minerals, capture reflected light photomicrographs, and measure pyrite grain sizes.

Eighteen polished sections containing large (roughly 1500 μm) pyrite grains were selected from the total of 29. The size of the pyrite grains ranges between 200 μm and 1800 μm. The pyrite grains are therefore big enough to recognise in the polished sections even without the aid of magnifying lenses. Five grains of pyrite were selected from each of the 18 chosen polished sections. Each of the five chosen pyrite grains was circled using a diamond marker, and then investigated further using different techniques. The polished sections were coated with a 25 nm thick carbon layer which allows dispersion of charging during the SEM, PIXE, and EMPA analyses. A silver stripe was used for conduction between carbon coating on the section and the section holder during the analysis.

3.2. Scanning Electron Microscopy (SEM)

A JEOL 5800LV scanning electron microscope (SEM) equipped with a Röntec energy-dispersive x-ray spectroscopy (EDS) system is available at the University of Pretoria. The SEM and EDS methods were used to study the same polished sections previously investigated using RLM. The SEM technique was used for determination of textures, shapes, and diagenetic structures, for classification and grouping of the pyrite grains. The SEM was also used for determination of compositional zonation and inclusions. The EDS was used to chemically analyse major and minor elements to determine whether the pyrite grains consist of similar chemical composition or whether the pyrite grains were formed through a single mechanism, or several mechanisms.

The JEOL 5800LV SEM was operated at an acceleration voltage of 5 keV for capturing of secondary electron photomicrographs at a working distance of 12 mm from the surface of the polished sections. The images and EDS acquisition were accomplished through auto-beam (digital image acquisition), and Windows software, and at varying magnification. The acceleration voltage was changed to 20 keV, and 0.5 to 1 nA beam current for carrying out the chemical analyses. The elemental analysis was accomplished using Isis analytical software. Five spots per mineral grain were selected and analysed for major and minor elements. The spot selection was based purely on obviously visible colour differences that possibly indicate compositional zonation in pyrite grains. The sections were analysed for 100 seconds with full scale counts on an average of 25 000 counts per spot.

3.3. Particle Induced X-ray Emission (PIXE)

PIXE technique was carried out at the South African Nuclear Energy Corporation (NECSA) for spot-analyses of trace elements in pyrite grains. The spot-analyses of trace elements were performed to investigate the chemical signatures of the different types of the pyrite grains which in turn would indicate differences of the processes by which the different types of pyrite grains were formed. The particle induced x-ray emission analytical beam line attached to the 3.75 MeV van der Graaff accelerator at NECSA was used.

The PIXE is considered a quantitative, accurate, and highly sensitive method for multi-elemental analysis of pyrite (Franklyn and Merkle, 1999; Franklyn et al., 2001). The characteristic x-ray lines of the elements used in this study were generated by the PIXE method under vacuum by bombarding pyrite with a 2.45 MeV proton beam. The beam was collimated by apertures to a diameter of 1 mm, and was introduced to a scattering chamber where polished sections were mounted on a manipulator. The polished sections containing the pyrite grains were oriented at 45° to the beam. Beam currents of up to 1 nA were used on the sections. A 100 µm beam spot size was used. The PIXE method has a detection limit between 5 and 50 weight percentage ranges (Wilson et al., 2002).

The X-ray energies were analysed using an ORTEC Si (Li) detector mounted at 135° to the beam direction with full width half maximum (FWHM) resolution of 170 eV at 5.9 keV. The 135° position was chosen because it has the advantage of two fold reduction in electron beam (Franklyn and Merkle, 1999; Franklyn et al., 2001). A 127 µm beryllium window absorber of the detector casing was used between the section and zinc detector (Merkle et al., 2002). The PIXE measurements were carried out using Acquisition and Display Multichannel Analyser (ADMCA) software. The spectra were analysed using the ADMCA which is a Windows software package that provides data acquisition, display, and control signal processors for the Amptek software package. A single zinc standard was used to confirm detection sensitivities.

The non-destructive character of the analysis allows the pyrite sections to be firstly analysed by using the PIXE technique before making use of other analytical techniques (Franklyn and Merkle, 1999; Franklyn et al., 2001). The results obtained using this technique were of less significance for this study, and therefore they are discussed only very shortly in this report for the reasons outlined in section 4.

3.4. Electron Probe Microanalysis (EMPA)

The same polished sections investigated using RLM, SEM, and PIXE, were further chemically investigated using a Cameca SX100 EMPA at UP. The chemical analysis of the major, minor and trace elements was done to investigate the chemical signatures of the different types of pyrite grains. The chemical investigation was achieved by wavelength dispersive EMPA analysis at 20 keV accelerating potential and a beam current of 20 pA. Beam spot sizes were typically 4 μm.

A total of 172 data points were analysed by EMPA for the concentration of Co and Ni at weight percentages (wt %). The 172 data points were obtained from a selection of 14 different pyrite grains chosen from five polished sections taken from a total of 29 sections. The five sections have big pyrite grains of 250 μm diameter on average. The grains of this size are suitable for this study because at least five points with 25 μm spot sizes can be placed on each grain.

The analyses of 30 points were carried out on six rounded pyrite grains of section g52228, g52236, and g52237 (see Table 5.1). Two rounded pyrite grains were selected per section and five points were marked on each pyrite grain. The other 142 points were placed on angular massive pyrite grains of section g52233 and g52239. Again two pyrite grains were chosen from section g52233 and a total of nine points were marked. The first four spots were placed on one grain and the other five spots were placed on the second pyrite grain. The last 133 data points were acquired from nine grains of section g52239 where each pyrite grain has between 12 and 15 data points. The rims and cores of zoned pyrite were carefully selected and analysed for nickel (Ni) and cobalt (Co).

The first five points were placed on the rim and other five spots were positioned at the core of the grain. The Ni and Co were determined in wt %. Cobalt and nickel were chosen because they occur in all types of pyrite. Despite pyrite grains being a stoichiometric FeS_2 phase, significant amounts of As, Ni, Co and Au amounts are found from VCR pyrite grains (Hem and Makovicky, 2004; Reich and Becker, 2006).

The work of Klemm (1965) summarised by Hem and Makovicky (2004) have demonstrated experimentally solid solutions between pyrite (FeS_2), cattierite (CoS_2), and vaesite (NiS_2) at temperatures approximately 500 °C and higher. The EMPA results were needed for pyrite standardisation in LA-ICP-MS analysis. However, standardisation of LA-ICP-MS data using EMPA results was only possible when considering the spots analysed using both techniques. It is not possible to use EMPA data to standardise LA-ICP-MS data for the LA-ICP-MS data points that do not contain EMPA data points. This difficulty arises because of the non-homogeneity of the pyrite grains.

3.5. Laser Ablation Inductively Coupled Plasma Mass Spectrometry (LA-ICP-MS)

An Agilent 7500 series laser ablation inductively coupled plasma mass spectrometry (LA-ICP-MS) technique was used for further investigation of the chemistry of the different grains of pyrite. The chemical analyses obtained using the LA-ICP-MS method were compared to the chemical analyses obtained using the EMPA system, and the results were used to produce scatter plots needed to investigate the discrepancy of the chemical signatures of the different types of the pyrite grains. This LA-ICP-MS method was performed at the Forensic Laboratory of the South African Police Service (SAPS). The spot selection was carried out using a mounted coaxial video camera attached to an Agilent 7500 series ICP-MS machine. The machine was optimised daily, and every time before starting with ablation.

There were more than 10 large pyrite grains (larger than 250 µm) in diameter per section. These grains were of desirable and suitable size requirement for the selected beam size. Five replicates per pyrite grain for five grains per section were performed. The five spots were selected and ablated for 45 seconds by a laser beam at carrier gas flow rate set at 50%, and at 15 seconds delay time. A pulse repetition rate of 10 Hz was used. The penetration depth of the beam into the section was 25 µm for a spot size of 25 µm in diameter.

Three spots were placed at the same position on the same pyrite grain where EMPA analyses were carried out. This was done for section g52228, g52236 and g52237 containing rounded pyrite grains, and section g52233 and g52239 containing angular pyrite grains.

Standards from the National Institute of Standards and Technology (NIST) were used as reference materials for trace elements (Walder et al., 1993). Homogeneous NIST 610 and NIST 612 glass standards were used to check the performance of the machine prior to analysing the pyrite. The NIST glass standards are calibration materials with elemental compositions, and were used for comparison of the pyrite composition. It is important to note that the composition of the NIST 610 and NIST 612 glass standards do not exactly match the matrix of pyrite, which may also include substantial amounts of Ag, Cu, Co, Ni and other elements, in addition to variable Au. Therefore, it is important to indicate that the NIST standards were not used to standardise the concentrations of the trace elements of the pyrite, since the NIST standards cover a broad general range of material composition. The laser ablation of the section and the NIST standards was done to compare the precision of the counts per second (cps) obtained from each ablated spot on the section. Blank spots were ablated on the NIST standards each time before starting with the section analysis. The blanks were used as control points for the corrections between cps of NIST 610 and NIST 612 glass standards, and cps of the ablated pyrite grains. The values in cps of the blanks were subtracted from the values in cps of the analysed spots on pyrite grains. The subtractions of high values from low values produced negative values. The negative values suggest elements below the limit of detection. Therefore all the negative values are removed, and replaced by dashes, and the negative values are omitted during plotting of the graphs.

So, the LA-ICP-MS was used as a semi-quantitative method, because of a number of factors such as daily instrumental drift of the LA-ICP-MS machine. The ablation rates are not constant as the instrument tends to drift from one ablated spot to the next, therefore making it impossible to measure the same number of counts each time the material is analysed.

Furthermore, the glass standards (NIST 610 and NIST 612) do not match the matrix of the analysed material. All these uncertainties were accounted for by calibrating the instrument to a standard every time before starting with the measurements, and by regularly ablating the standards in between the measurements.

Therefore, the LA-ICP-MS data was standardised internally by subtracting the blanks and recalculating the data by normalisation to the analytical counts of each element to total counts. The normalisation was achieved by using the following method:

$$\text{Elemental \%} = \frac{\text{Analytical counts (cps)}}{\text{Total counts (cps)}} \times 100\%$$

Elemental percentage = the percentage of each ablated element
Analytical counts = the counts per second of each ablated element
Total counts = the sum of all the elements ablated at a single spot

The isotopes of certain elements were analysed and the isotope with less interference was then used for the calculation. This calculation enabled the LA-ICP-MS data to be compared to EMPA data.

CHAPTER FOUR

REFLECTED LIGHT MICROSCOPY (RLM) AND SCANNING ELECTRON MICROSCOPY (SEM) DATA

4. Observations

A combination of different microscopic techniques (section 3) was used to investigate the shapes, textures, diagenetic structures, and types of inclusions, compositional zonations, and overgrowths of the different types of pyrite grains. The RLM and SEM have demonstrated that all the investigated polished sections from the VCR consist of different types of pyrite grains, classified either as (1) rounded pyrite grains, or (2) angular pyrite grains (Figure 4.1). The classification was purely based on morphology (Figure 4.3 and Figure 4.7), and textures (Figure 4.3 and Figure 4.5). The rounded pyrite grains have broken and rounded edges, whereas the angular pyrite grains are euhedral and display sharp edges. The various pyrite grains were further texturally classified either as "massive" or "porous". "Massive" implies that the pyrite grains display compact textures, whereas "porous" refers to the pyrite grains with spongy textures.

The diagenetic structures and different inclusions were further used for the discrimination between the different types of pyrite grains. The appearance of certain kinds of inclusions in one type pyrite grains but absent in the other would imply that the various pyrite grains were derived from different rock sources, or the various pyrite grains were formed by multiple or various mechanisms.
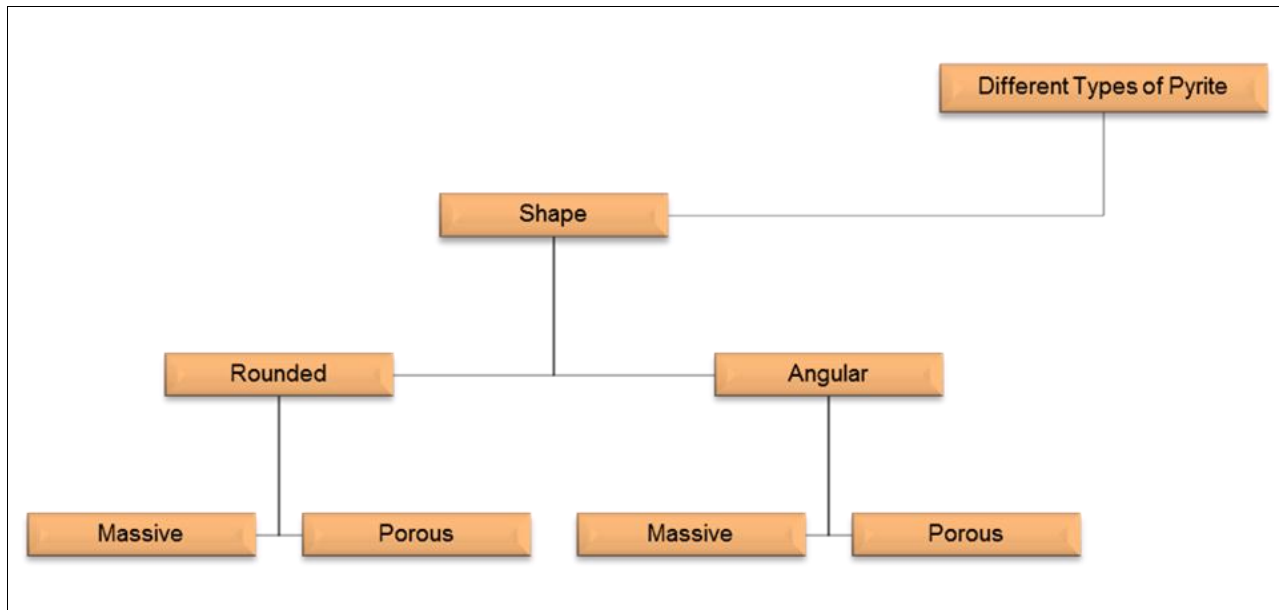
Figure 4.1: *Illustration of a tree diagram providing a classification scheme for the different types of grains of pyrite. The pyrite grains are classified according to their shapes and textures. The pyrite grains are either angular or rounded, and each pyrite type can either be massive or porous.*

4.2. Grain Sizes Distributions of Different Pyrites

The diverse pyrite grains have a wide range of grain sizes, starting from very fined-grained crystals as small as 400 µm to coarse-grained crystals as large as 1800 µm diameters (Figure 4.2). A total of 318 grains of pyrite was randomly selected from 29 polished sections. 140 data points of the selection represent the rounded pyrite grains, whereas 178 data points represent the angular pyrite grains (Figure 4.2).
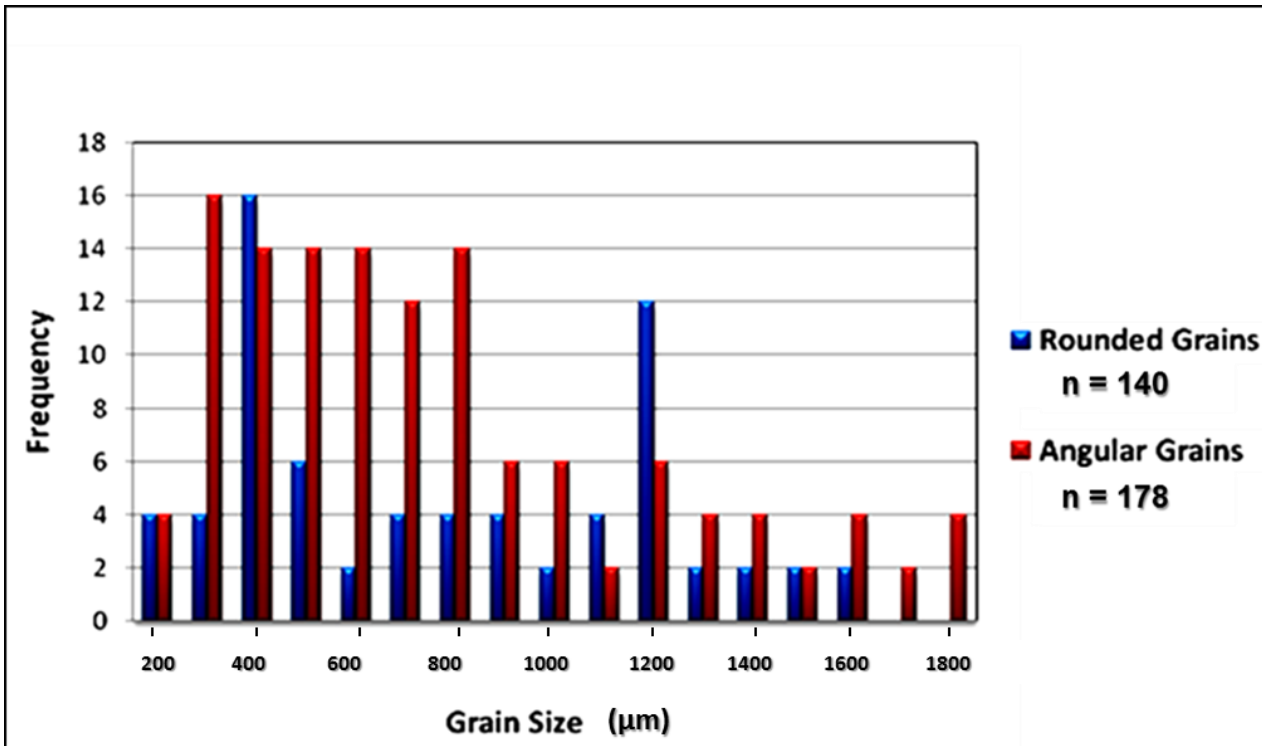
Figure 4.2: *Frequency distribution of grain sizes for pyrite grains. Rounded pyrite grains (n = 140) show two groups, one set with grain sizes ranging 200 μm to 900 μm and a second group with grain sizes between 1000 μm and 1800 μm. The angular massive pyrite grains (n = 178) demonstrate non-normal data distribution with the grain size ranging from 200 μm to 1800 μm.*

4.3. Rounded Pyrite Grains

4.3.1. Rounded Porous Pyrite Grains

The first observed variety of pyrite is the rounded porous pyrite grains with grain sizes of approximately 400 μm and occasionally exceeding 1600 μm (Figure 4.3). These pyrite grains are called rounded because of their round shapes and called porous because of their spongy textures. Generally, the textures of the rounded porous pyrite grains are referred as botryoidal (Utter, 1978). Certain grains consist of circular layers, for example see Figure 4.3 A. The different layers contain sub-parallel individual circular crystals of the rounded porous pyrite. Clear crystals of different orientation are noticed (Figure 4.3 F).

Indentations and cracks radiating outwards in a fan-like form are frequently observed forming skeletal pyrite (Figure 4.3 A). The porous grains with planar laminations, concentric laminations, or radial textures are observed from polished section g52237. Relic pyritized oolitic structures, also called framboidal textures, are visible (Figure 4.3 C). The rounded porous pyrite grains tend to have tiny inclusions of 2 to 5 µm grains of chalcopyrite and galena (Figure 4.4). The chalcopyrite and galena grains are contained within cracks and cavities within the pyrite.
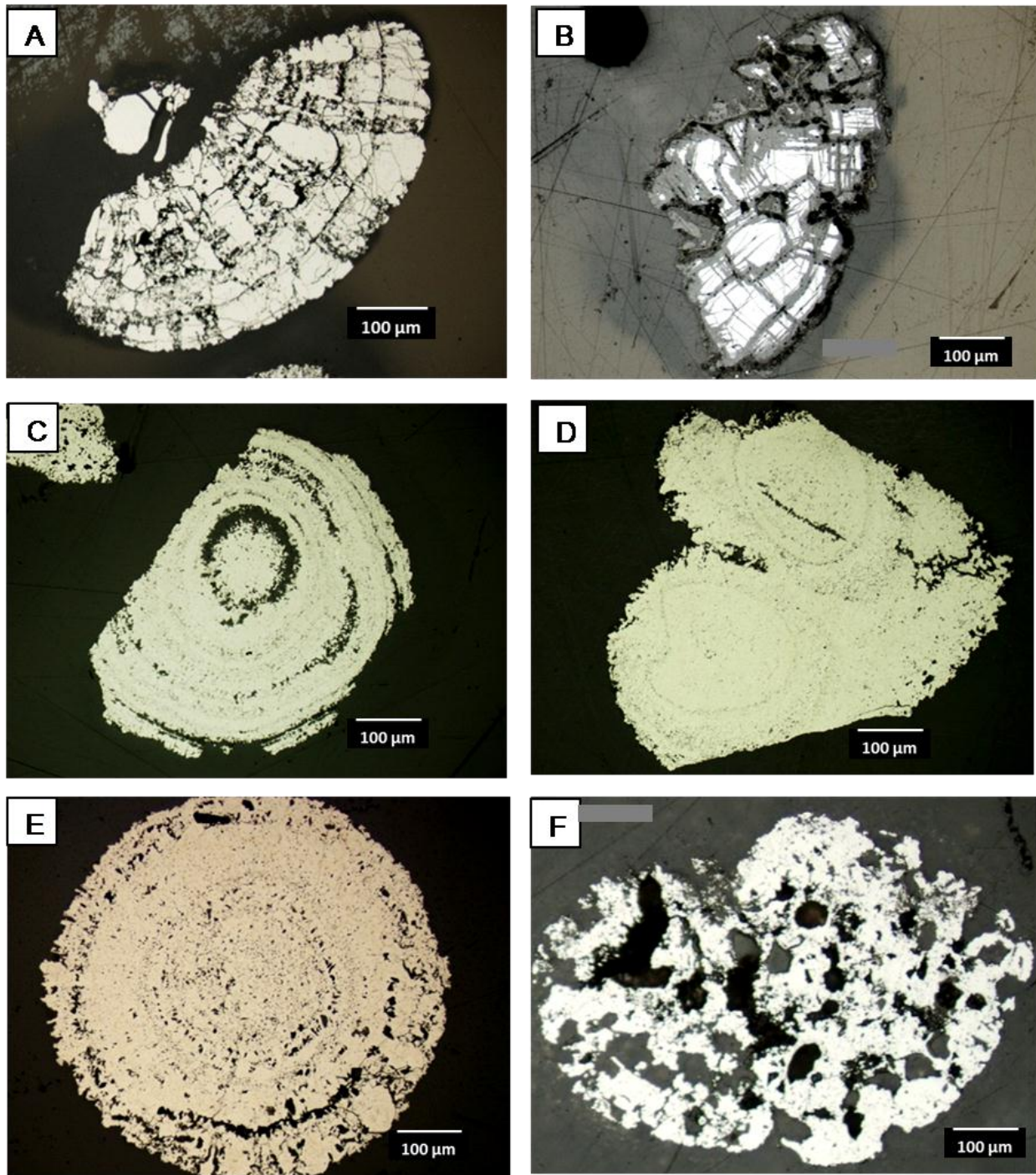
Figure 4.3: *Reflected light photomicrographs of polished sections taken under plane polarised light showing relevant pyrite structures, shapes, and textures. The photomicrographs are aggregated pyrite grains of section g52213; g52224; g52227; and g52237 from the VCR of the KGM. Aggregate of the rounded porous skeletal pyrite (A), zoned pyrite showing fractures (B), relic pyritized oolitic structures also called framboidal (C), overgrown pyrite grain with circular layers (D), rounded pyrite with "spongy textures" in (E) from g52210, and rounded porous pyrite with clear crystals of different orientation (F).*

Two types of inclusions are identified visually in the rounded porous pyrite grains: (1) inclusions of grains of galena and (2) inclusions of grains of chalcopyrite. These inclusions can be extremely fine-grained (200 μm). The inclusions of grains of galena and chalcopyrite can be observed in Figure 4.4.

4.3.2. Inclusions of Grains of Galena in Rounded Porous Pyrite Grains

The inclusions shown in Figure 4.4 A, are grey coloured. The grey grains occur as granular aggregates, and occupy cavities of the rounded porous pyrite grains. Well-developed cleavage is observed. The inclusions show partly irregular and corroded surfaces with sub-angular shapes and occur as specks. The inclusions are isotropic and have a high reflectance, but lower than that of pyrite grains. Based on the description above, these inclusions are grains of galena and this is confirmed by the SEM and EDX results. It is also important to note that the cavities in the rounded porous pyrite grains are only occasionally occupied by minerals such as chalcopyrite (Figure 4.4 B) and gold grains.
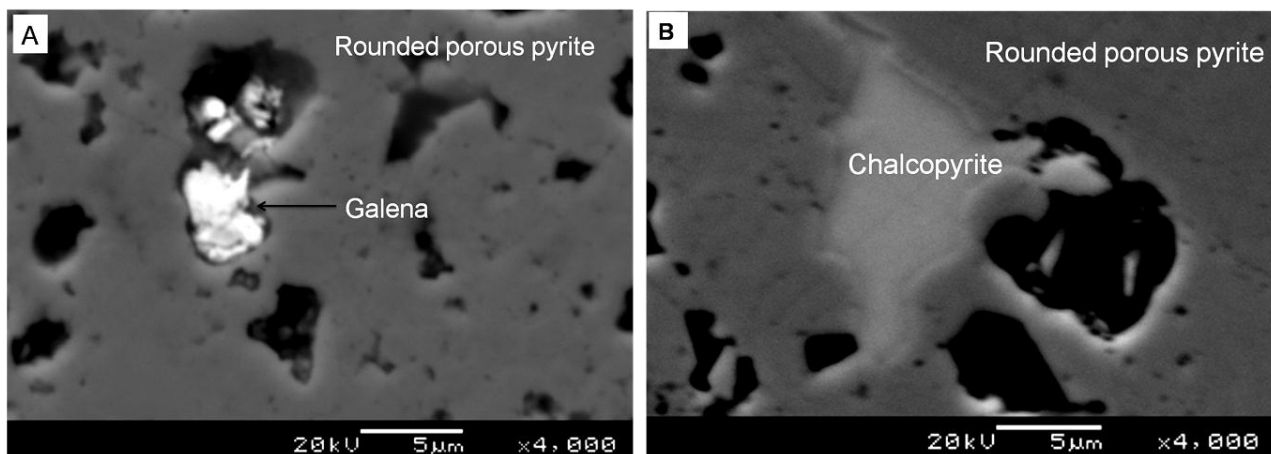
Figure 4.4: *Secondary electron photomicrographs showing inclusions of: (A) grey grains of galena in rounded porous pyrite grains of section VL 2210; and (B) chalcopyrite inclusions in the rounded porous pyrite grains of section g52219.*

4.3.3. Inclusions of Chalcopyrite in Rounded Porous Pyrite Grains

Anisotropic, elongated minerals are identified occurring in rounded porous pyrite grains (Figure 4.4 B). The inclusions show a yellowish colour unlike that of pyrite, and very weak anisotropism; uncrossing the polarizer slightly yields yellowish-brown tints. The inclusions do not show any pleochroism, but have high reflectance similar to that of galena, but lower than the reflectance of pyrite. These inclusions are massive, subhedral in shapes, and average size of 10 μm in diameter when enclosed within the rounded porous pyrite grains, and roughly 140 μm in diameter when along the grain boundaries. It is clear from the descriptions that the inclusions are grains of chalcopyrite. These inclusions of chalcopyrite occur together with pyrrhotite. The grains of chalcopyrite can also occur as inclusions in angular massive pyrite grains (Figure 4.9 D).

4.4. Rounded Massive Pyrite Grains

The second identified type of pyrite consists of rounded massive grains occurring as individual crystals of rounded pyrite (Figure 4.5). The average grain size of the rounded massive pyrite is 500 μm in diameter. The rounded massive pyrite grains have round shapes similar to the previous described group. The rounded massive pyrite grains are subsequently forming overgrowths on the rounded porous type (Figure 4.15 in Appendix I). Replacement of pyrite grains by arsenopyrite occurs in some instances and such replacement is accompanied by chalcopyrite grains. It should be emphasised that the pyrite grains also display several overgrowths of gold. The aureoles of the rounded porous pyrite grains are occasionally coated by younger massive pyrite generations. Chalcopyrite, pyrrhotite, and gold act as interstitial fillings in assemblages of overgrown pyrite crystals (Figure 4.32 in Appendix I). This kind of pyrite grain may have inclusions of pyrrhotite crystals up to 20 μm in size (Figure 4.5 B). Grains of zircon are seen in a few polished sections, such as section VL2232 (Figure 4.6).
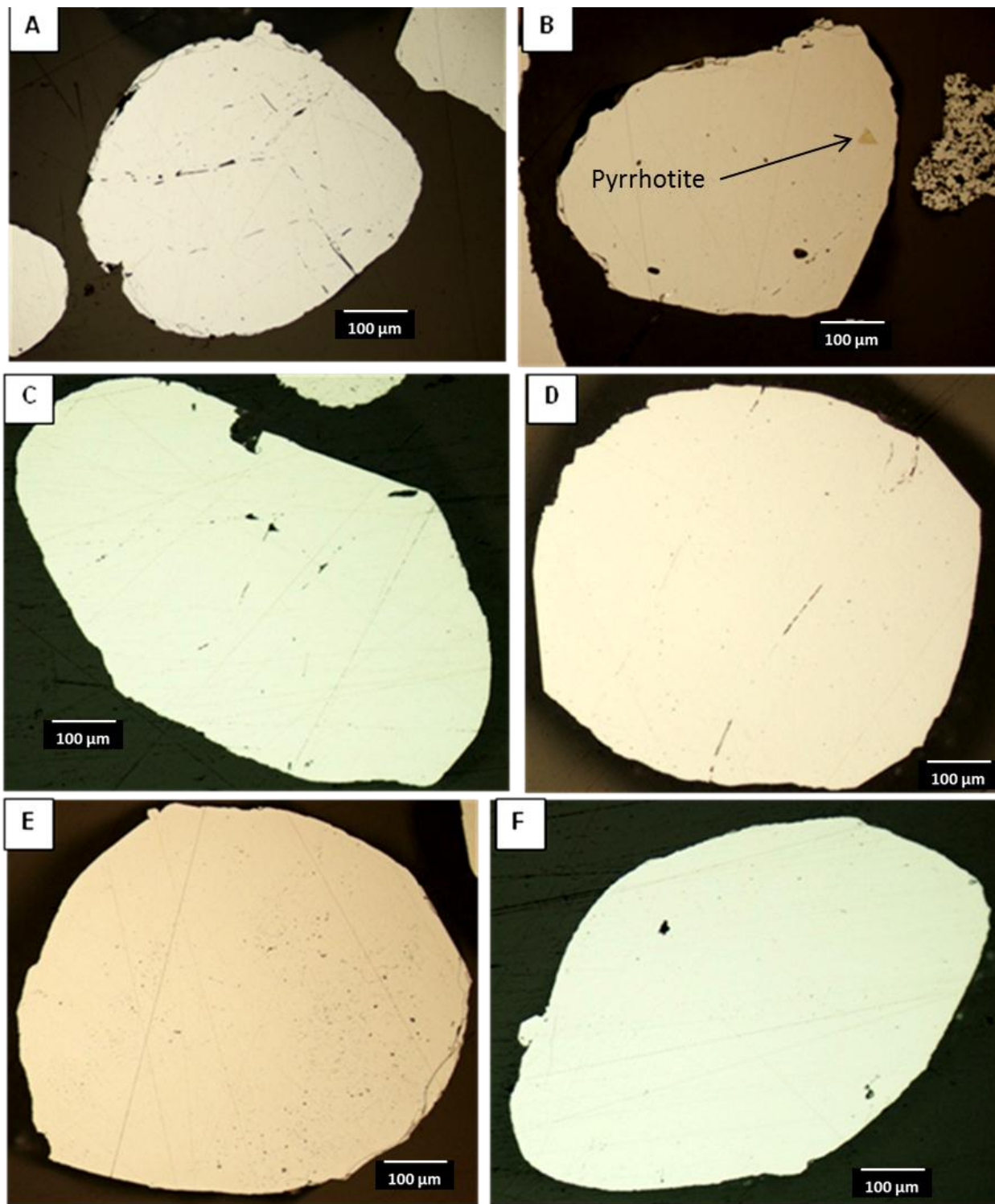
Figure 4.5: *Reflected light photomicrographs of polished sections taken under plane polarised light: (A) shows a massive pyrite grain of sections g52216; (B) a large rounded massive pyrite grain of section g52230 containing inclusions of pyrrhotite grains; (C and D) show rounded massive grains from section g52230; (E and F) show relevant pyrite textures for the rounded massive pyrite grains without inclusions from g52214.*

4.4.1. Inclusions of Sphalerite in Rounded Massive Pyrite Grains

During RLM and SEM investigations, very fine-grained light grey to dark grey minerals of about 2.5 µm are observed enclosed in rounded massive pyrite grains. The inclusions are isotropic and show internal reflection colours of yellowish to reddish-brown, observed along the grain boundaries when viewed under reflected light. The enclosed minerals show low reflectance and were identified as sphalerite; this argument was later on supported by the optical observations using the EDX and SEM. The inclusions of sphalerite were also observed in angular pyrite grains.

4.4.2. Zircon Inclusions in Rounded Massive Pyrite Grains

Grains of grey colour approximately 5 µm in diameter were observed in rounded massive pyrite. The grains showed neither cleavage nor chemical zonation, and have round shapes. Further investigation on the inclusions was carried out using SEM. Two spots (VL2232 (1) _pt1 and VL2232 (1) _pt2) were marked on grain number (1) of section VL2232 and analysed. The analysed areas are roughly 4 µm^2. The results are reported as a spectrum (Figure 4.6). The analysis from point two produced a result that is comparable to that of spot one; therefore only the spectrum from the first spot is indicated in Figure 4.6.
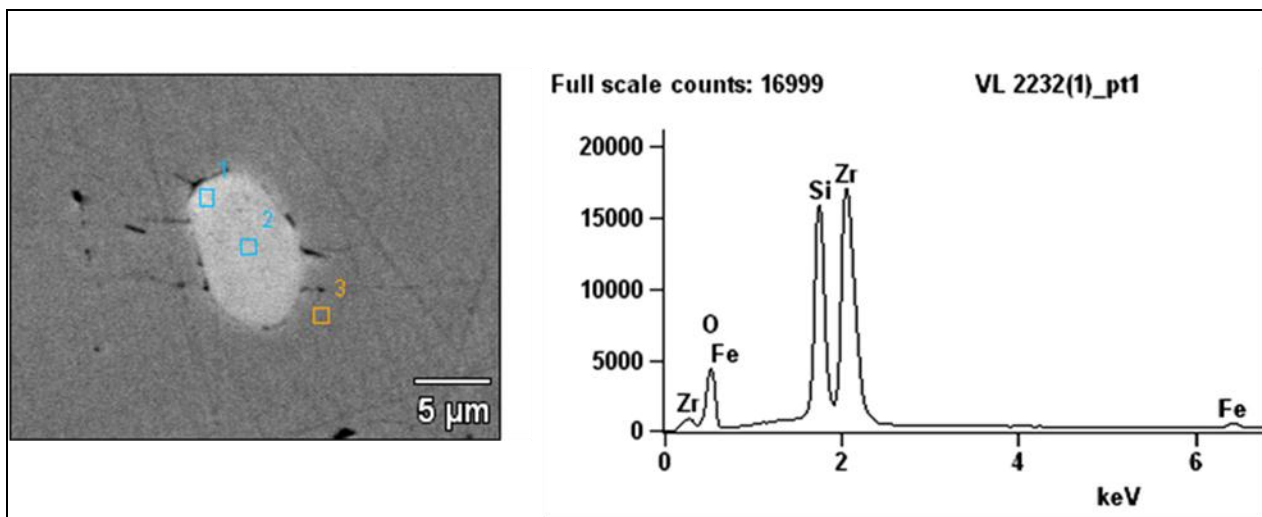
Figure 4.6: *Secondary electron photomicrograph accompanied by a spectrum of a detrital rounded massive pyrite grain of section VL2232 containing an inclusion of zircon grains.*

The SEM analyses provide the chemical compositions of the two areas that were selected from the inclusion and the third spot from the pyrite grain. Spot one and two contain about 39.2 wt % O, 14.3 wt % Si, 1.4 wt % Fe, and 45 wt % Zr (Table 4.1) and this confirms that the inclusions represent zircon grains. In comparison, spot three has chemical composition of 53.4 wt % of S and 46.6 wt % of Fe, and this confirms that spot three represents a pyrite grain. For further details such as atomic %, see Table 4.1.

Table 4.1: *SEM analyses of zircon grains (point one and two) found in the rounded massive pyrite grain (VL 2232(1)_pt3) of section VL 2232. The dashes mean below the limit of detection.*

Section Name	O	Si	S	Fe	Zr	Mineral
K-Ratio						
VL 2232(1)_pt1	0.15	0.20	-	0.03	0.62	Zircon
VL 2232(1)_pt2	0.15	0.21	-	0.02	0.63	Zircon
VL 2232(1)_pt3	-	-	0.52	0.48	-	Pyrite
Weight %						
VL 2232(1)_pt1	39.40	14.30	-	1.70	44.60	Zircon
VL 2232(1)_pt2	39.20	14.40	-	1.30	45.10	Zircon
VL 2232(1)_pt3	-	-	53.40	46.60	-	Pyrite
Weight % Error (+/- 1 Sigma)						
VL 2232(1)_pt1	+/-0.40	+/-0.10	-	+/-0.00	+/-0.20	Zircon
VL 2232(1)_pt2	+/-0.40	+/-0.10	-	+/-0.10	+/-0.20	Zircon
VL 2232(1)_pt3	-	-	+/-0.20	+/-0.20	-	Pyrite
Atom %						
VL 2232(1)_pt1	70.50	14.60	-	0.90	14.00	Zircon
VL 2232(1)_pt2	70.40	14.70	-	0.70	14.20	Zircon
VL 2232(1)_pt3	-	-	66.60	33.40	-	Pyrite
Atom % Error (+/- 1 Sigma)						
VL 2232(1)_pt1	+/-0.70	+/-0.10	-	+/-0.00	+/-0.10	Zircon
VL 2232(1)_pt2	+/-0.70	+/-0.10	-	+/-0.00	+/-0.10	Zircon
VL 2232(1)_pt3	-	-	+/-0.20	+/-0.20	-	Pyrite

4.5. Angular Massive Pyrite Grains

Two types of angular pyrite grains are identified in this study. These are: (a) angular massive pyrite (Figure 4.7), and (b) angular porous pyrite. Photomicrographs of the angular porous pyrite grains are shown in Appendix I. However, the focus here is on angular massive pyrite grains which were dominant, whereas only a few angular porous grains were observed. These grains are called "angular" because of their square or rectangular shapes with sharp edges, and "massive" because of the compact textures, whereas "porous" refers to grains that have spongy textures.

The angular massive pyrite grains form the third group of pyrite described in this study. This group is consisting of large compact idiomorphically developed grains of about 1800 μm (Figure 4.2). The angular massive pyrite grains show rectangular or square outlines (Figure 4.7). Because of limited space during grain growth, the sub-idiomorphic crystals are normally present in between larger grains, and sometimes in cavities.

Irregular (sub-angular) shaped inclusions are prominent under high magnification but barely exceed 200 μm in diameter (Figure 4.19 through Figure 4.32 in Appendix I). Microscopic inclusions of rounded gold of roughly 10 to 50 μm (Figure 4.9 D) are predominant, and sub-rounded to angular chalcopyrite, pyrrhotite, and sometimes carboneous material were observed. The accompanying analytical results for gold inclusions are shown in Figure 4.8. More photomicrographs of angular pyrite grains are shown in Appendix I.
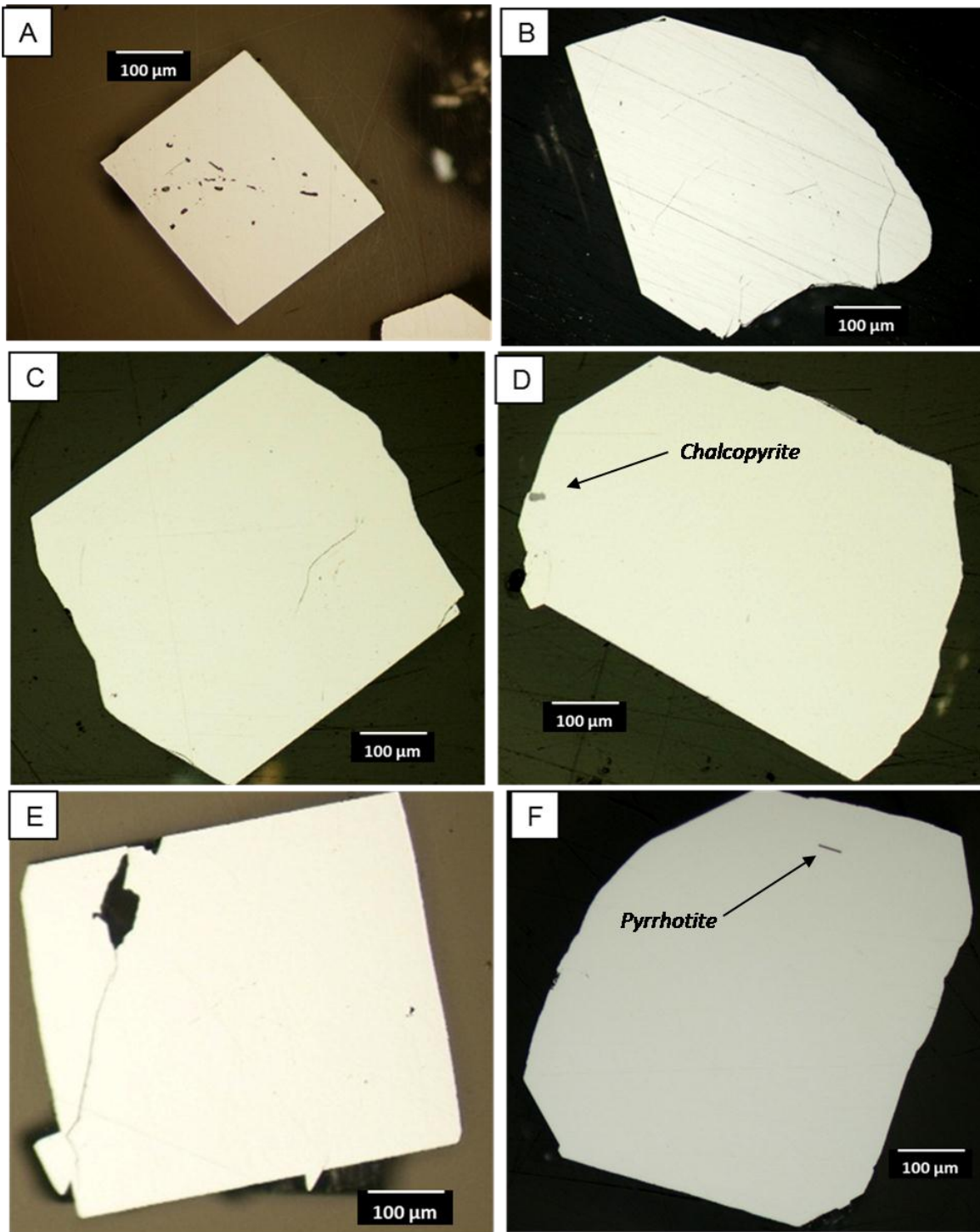
Figure 4.7: *Reflected light photomicrographs of polished sections taken under plane polarised light showing: (A) relevant textures of the angular massive pyrite grain from g52218; (B and F) compact grains from g52233 with (F) occasionally containing inclusions of pyrrhotite; (C) massive angular pyrite grain from section g52263; (D) massive texture with inclusion of chalcopyrite from g52239; and (E) euhedral massive grain from g52239.*

4.5.1. Inclusions of Gold in Angular Massive Pyrite Grains

Inclusions of grains of gold described in section 4.4.3 were also observed in angular massive pyrite grains (Figure 4.8). The gold grains mostly occupy veins, and appear in small sizes between 20 and 50 µm in length. Grains of gold appear within cracks of angular massive pyrite grains, or along the edges (Figure 4.8). Although gold grains often appear as the prominent inclusions in the angular massive pyrite grains. The gold grains rarely occur as primary inclusions in rounded pyrite grains. When the gold grains occur in rounded pyrite grains, they appear in the form of rounded shapes or as elongated grains (Figure 4.8).
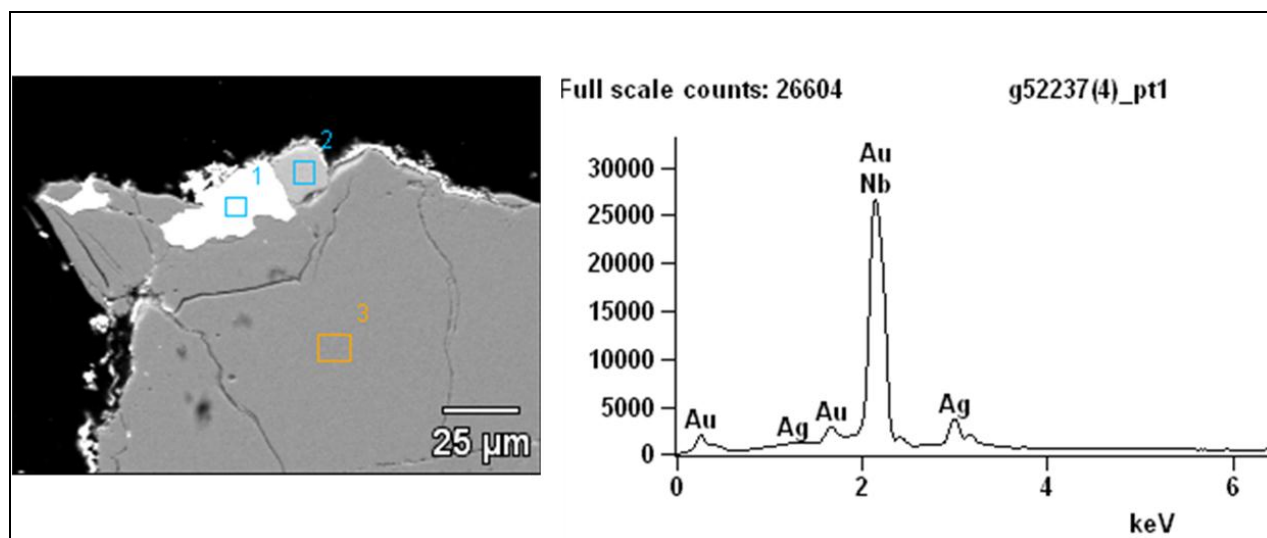
Figure 4.8: *EDX analyses of point one on a gold grain, point two on a sphalerite grain, and point three on angular massive pyrite grain of section g52237.The grain has high counts (25000 cps) for Au and low counts (4000 cps) for Ag.*

These inclusions of gold grains were also investigated using EDX and SEM. The EDX results provided a chemical composition of 82.1 wt % Au and 14.9 wt % Ag (Table 4.2), as seen in the spectrum in Figure 4.8.

Table 4.2: *SEM analyses of section g52237(4)_pt1 contains considerable amounts of Ag with large amounts of Au. g52237(4)_pt2 contains Zn and small amount of Fe. g52237(4)_pt3 contains only S and Fe. The dashes mean below the limit of detection.*

K-Ratio							
Section Name	*S*	*Fe*	*Zn*	*Nb*	*Ag*	*Au*	*Mineral*
g52237(4)_pt1	-	-	-	0.03	0.10	0.86	Gold
g52237(4)_pt2	0.29	0.07	0.64	-	-	-	Sphalerite
g52237(4)_pt3	0.53	0.47	-	-	-	-	Pyrite
Weight %							
Section Name	*S*	*Fe*	*Zn*	*Nb*	*Ag*	*Au*	*Mineral*
g52237(4)_pt1	-	-	-	3.00	14.90	82.10	Gold
g52237(4)_pt2	34.30	6.30	59.50	-	-	-	Sphalerite
g52237(4)_pt3	53.80	46.20		-	-	-	Pyrite
Weight % Error (+/- 1 Sigma)							
Section Name	*S*	*Fe*	*Zn*	*Nb*	*Ag*	*Au*	*Mineral*
g52237(4)_pt1	-	-	-	+/-0.40	+/-0.20	+/-1.10	Gold
g52237(4)_pt2	+/-0.10	+/-0.10	+/-0.40	-	-	-	Sphalerite
g52237(4)_pt3	+/-0.20	+/-0.20	-	-	-	-	Pyrite
Atom %							
Section Name	*S*	*Fe*	*Zn*	*Nb*	*Ag*	*Au*	*Mineral*
g52237(4)_pt1	-	-	-	5.5	23.6	70.9	Gold
g52237(4)_pt2	51.10	5.40	43.50	-	-	-	Sphalerite
g52237(4)_pt3	67.00	33.00	-	-	-	-	Pyrite
Atom % Error (+/- 1 Sigma)							
Section Name	*S*	*Fe*	*Zn*	*Nb*	*Ag*	*Au*	*Mineral*
g52237(4)_pt1	-	-	-	+/-0.80	+/-0.40	+/-0.90	Gold
g52237(4)_pt2	+/-0.20	+/-0.10	+/-0.30	-	-	-	Sphalerite
g52237(4)_pt3	+/-0.20	+/-0.20	-	-	-	-	Pyrite

The results in Table 4.2 show chemical composition in K-ratios, weight percentages, and atomic percentages of the analyses of area 1, 2, and 3 selected from a gold, sphalerite, and pyrite grain (Figure 4.8). The composition in this table corresponds with the illustration of the spectra in Figure 4.8. The analyses of gold show about 3 wt % of Nb which should not be present. About 6.3 wt % Fe is present in the composition of sphalerite, and this is possible because Zn can substitute for Fe in the structures of pyrite.

4.5.2. Inclusions of Pyrrhotite in Angular Massive Pyrite Grains

Fine to medium grained inclusions of between 30 and 200 µm are identified in the angular massive pyrite grains. The inclusions are sub-angular in shape, and show a light brownish colour. The inclusions are predominantly granular aggregates and sometimes display idiomorphic textures. The inclusions have a relatively high reflectance, but lower than the reflectance of chalcopyrite and galena. The grains also show a strong anisotropism of yellowish-brown to brownish grey, and are interlocked with chalcopyrite (Figure 4.9 A, and C). Although the inclusions mostly occur within pyrite grains, they commonly start from cracks, along fissures or grain boundaries. Based on the above descriptions, these inclusions represent grains of pyrrhotite. In turn, the inclusions of pyrrhotite occasionally contain inclusions of chalcopyrite.
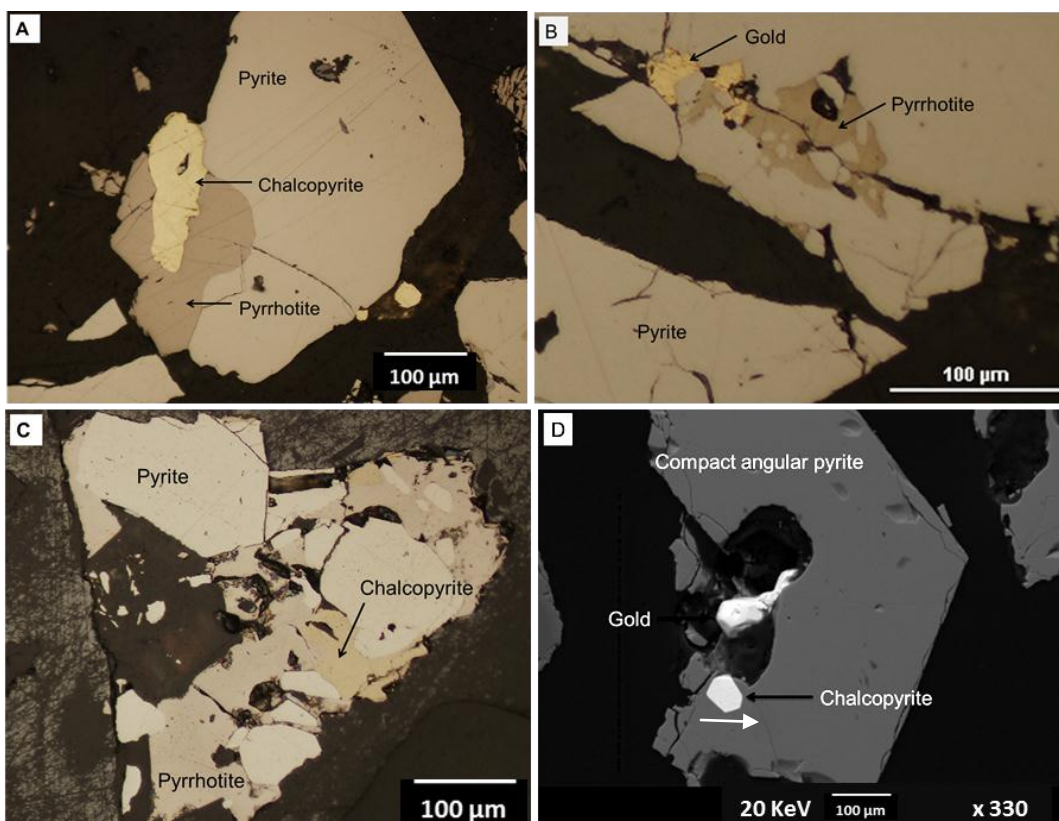
Figure 4.9: *Reflected light photomicrographs of the various pyrite grains. Massive sub-rounded pyrite grain from section VCR Kloof 245 co-existing with chalcopyrite and pyrrhotite (A); (B and C) rounded massive pyrite grains of section g26889 containing inclusions of gold, pyrrhotite, and chalcopyrite. Gold and pyrrhotite grains occur along fractures (B); inclusions of chalcopyrite and pyrrhotite occur in (C); and (D) massive angular grain from section g52234 containing inclusions of chalcopyrite and gold.*

4.5. Chemical Analysis of Angular Pyrite Grains of Section g52237

Spatial distributions, grain sizes, shapes, and chemical compositions were investigated using the SEM and EDX setup. The instrument was operated at 5 keV for the investigation of the shape, the inclusions, the chemical zonations, the intergrowths, and for capturing of the photomicrographs of pyrite. The acceleration voltage was then increased to 20 keV to carry out the chemical analysis (see section 3.2 for more details). Between five and eight points of roughly 20x25 μm sizes were chosen from the angular pyrite grains, and then analysed for major and minor elements (Figure 4.10). The analyses of section g52237 were performed using SEM and the attached energy dispersive x-ray (EDX) detector. The results indicate differences on the chemistry of the analysed spots largely based on the type of inclusions hosted in the pyrite, compositional zonations, and overgrowths.
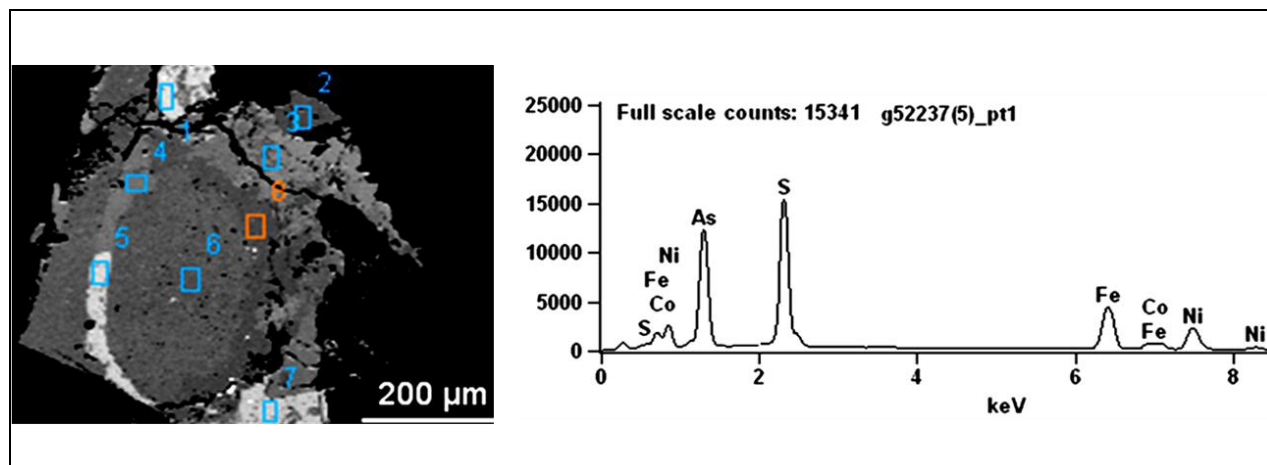
Figure 4.10: *Secondary electron images with the results from seven points selected for chemical analyses on section g52237. The spectrum shows the results from point one.*

Eight points were marked on zoned angular pyrite grains containing inclusions. These pyrite grains were selected primarily based on visible changes in colour which may indicate a change in chemistry (Figure 4.10). Compositional zonations on the grains mark a change from one phase to another, and this was confirmed by the analyses of major and minor elements shown in Table 4.3. The results are displayed on accompanying spectrum (Figure 4.10), while the remaining data is published in Appendix II.

Table 4.3: *SEM data from eight spots of section g52237 analyzed for the chemistry. Spot 1, 5, and 7 contain considerable amounts of Co, Ni, and As. Spot 2, 3, 4, and 6 contain significant amounts of Ni (between 0.6 and 26.6 wt %) but no Co or As. Spot 8 contain Ni and As but no Co. The dashes mean below detection limits.*

Weight %									
Section Name	**Al**	**Si**	**S**	**Fe**	**Co**	**Ni**	**As**	**Mo**	**Mineral**
g52237(5)_pt1	-	0.20	25.00	20.70	3.10	14.90	36.10	-	Arsenopyrite
g52237(5)_pt2	-	-	53.00	46.30	-	0.80	-	-	Pyrite
g52237(5)_pt3	0.10	-	36.80	33.90	-	26.20	-	3.00	Pentlandite
g52237(5)_pt4	-	-	40.20	59.20	-	0.60	-	-	Pentlandite
g52237(5)_pt5	-	-	38.70	35.60	-	7.70	18.10	-	Arsenopyrite
g52237(5)_pt6	-	-	48.20	51.20	-	0.60	-	-	Pyrite
g52237(5)_pt7	-	-	21.40	13.90	2.30	19.90	42.40	-	Arsenopyrite
g52237(5)_pt8	-	-	52.80	46.10	-	0.50	0.60	-	Pyrite

The sizes of the analysed areas in Figure 4.10 were very small and made the analysis difficult. The best analyses were obtained from small areas of about 20x20 μm. The compositions are shown in weight percentages (wt %), see Table 4.1. The analysis of point_1 yielded 22.7 wt % Fe, 36.1 wt % As, and 25 wt % S with traces of 14.9 wt % Ni, 3.1 wt % Co and 0.2 wt % Si (Table 4.3). The chemical composition at point_1 matches the chemistry of an arsenopyrite where arsenic substitutes for sulphur, whereas Co and Ni substitute for iron. Point_5 and 7 represent a similar chemistry as in point_1 but without Si. The chemical analyses of point_7 provided 13.9 wt % Fe, 19.9 wt % Ni, 2.3 wt % Co, 42.4 wt % As, and 21.4 wt % S. These analyses fit the following chemical formula Fe-Co-Ni-As-S. Analysis of point 3 gave good stoichiometry and compositions of approximately 36.8 wt % S, 33.9 wt % Fe, 26.2 wt % Ni, 3 wt % Mo, and 0.1 wt % Al. This composition will be expected for pentlandite; nevertheless the occurrence of both Al and Mo complicates the results. It is difficult to establish whether or not the mineral at point_5 with the following chemical formula Fe-Ni-As-S is similar to point_8. The analyses of point_8 suggest a pyrite with a chemical composition of 52.8 wt % Fe, and 46.1 wt % S and having traces of 0.5 wt % Ni and 0.6 wt % As. It is difficult to differentiate and analysis only confirms its Fe-Ni-As-S composition. Point_2, 4, and 6 suggest a similar phase as in point_3 but without Al and Mo.

4.6. PIXE Results

The PIXE technique was used for the analyses of the chemistry of the pyrite. The PIXE technique uses MeV proton beams to excite the atoms, and detects the characteristic X-ray emitted by the section. It permits the measurement of major, minor, and trace elements. However, the measurements are influenced by the heterogeneity of the surface of the polished sections of the pyrite. PIXE analysis requires the identification of the atomic species present in the target from the energies of the characteristic peaks in the X-ray emission spectrum (Figure 4.11). The amount of a specific element identified in the target is determined from the intensity of its characteristic X-ray emission spectrum.

Sections VL2203, g52203, g52288, LV226, LV228, 3719, g52260, g52201, and the heaves 4372 were analysed for the chemical composition of the major elements such as S and Fe, and minor elements like Cr, Co, Ni, Zn, As, and Cu in the rounded and angular grains of pyrite. For more spectra, see Appendix II. The results of PIXE technique are strongly influenced by the surface heterogeneities of the sections (Guerra, 2004). However, previous published studies have highlighted the effectiveness of combining EPM and PIXE techniques in defining the partitioning of trace elements amongst co-existing Cu–Fe sulphides including chalcopyrite; cubanite ($CuFe_2S_3$); and talnakhite ($Cu_9(Fe, Ni)_8S_{16}$ (Wilson et al., 2002). Nevertheless, in the case of this study, the PIXE results are inconclusive.
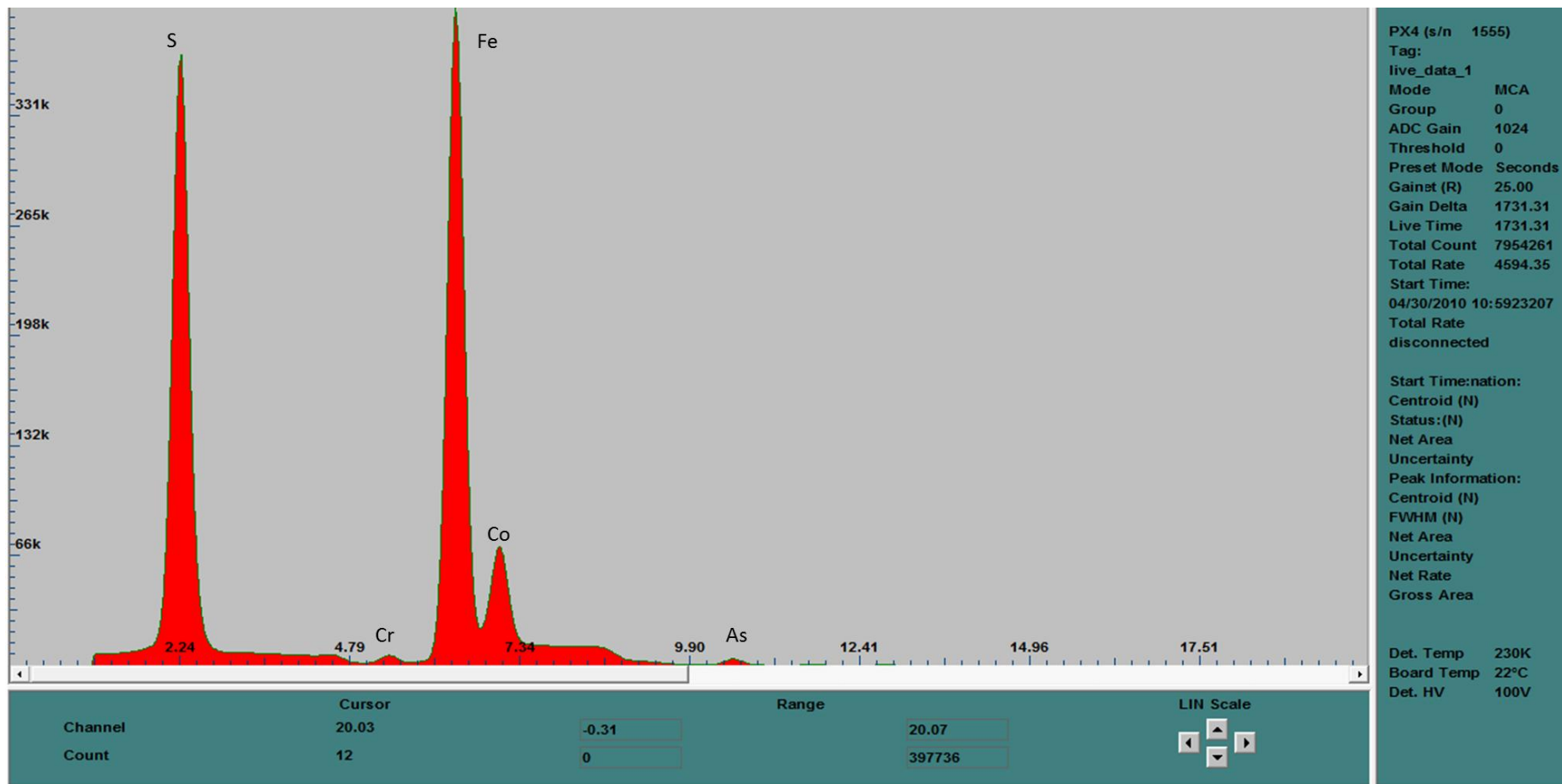
Figure 4.11: *Analyses of section VL2203 show a general chemical composition. The spectrum shows Cr, Co, and As in addition to major elements such as Fe and S with the total counts of 7954162, and live time of 173131 seconds.*

The PIXE spectrum (Figure 4.11) shows a general chemical composition consisting of Fe, Cr, Co, As, and S, with Fe giving the highest peak, then S, followed by Co with a little bit of Cr and As. The chemical composition of Fe-Cr-Co-As-S is similar to the chemical analyses discussed in section 4.7.1 which was Fe-Co-Ni-As-S. Ni was present in the SEM results, but it is missing in the PIXE results, instead, Cr is detected. The Cr replaced Ni in the chemical composition given by the PIXE analyses.

The analyses of section g52203 show an overview of chemical composition with Cr, Fe, Co, Zn, Ge, As, and S being detected at the total counts of 11509543 and live time of 2560.90 seconds (Appendix II). Appendix II shows the analyses of section g52688 which gave the following elemental chemical composition: Ar, Ca, Mn, Fe, Co, Ni, Cu, Zn, As, and Rb, with the total counts of 4665070, and live time of 880.61 seconds.

The PIXE work did not turn out to be useful for this study because the analyses did not provide the required resolution for the different types of pyrite. Instead, the received compositions represented the bulk compositons of the analysed sections. This is because the studied sections are composed of different sulphides such as different types of pyrite, chalcopyrite, sphalerite, arsenopyrite, galena, and gold. Once the sections were inserted into the chamber of the PIXE instrument for analyses, the sections cannot be viewed to choose points on pyrite grains which are intended for analyses. Hence, the results obtained could not be allocated to a specific pyrite grain. Therefore, the PIXE results are in this study only used to provide a general idea about the chemistry of the whole materials rather than giving compositions of the specific grains of the different pyrite types.

CHAPTER FIVE

ELECTRON MICROPROBE (EMPA) AND LASER ABLATION-INDUCTIVELY COUPLED PLASMA-MASS SPECTROMETRY (LA-ICP-MS) ANALYSES

5. Observations

The chemistry of the rounded and angular pyrite grains was further examined using EMPA and LA-ICP-MS techniques. The chemical analysis of the major, minor and trace elements was carried out to investigate the chemical signatures of the different pyrite grains.

5.1. EMPA Data Description

The EMPA analyses were carried out on section g52228, g52236, and g52237 containing rounded pyrite grains, and section g52233 and g52239 containing angular pyrite grains. These polished sections were firstly studied using RLM, EDS, and SEM (section 4) in order to select suitable pyrite grains for EMPA and LA-ICP-MS investigation. The polished sections were placed in the EMPA, and the analytical progress was automatically controlled overnight. The concentration was then calculated (Table 5.1) and the rest of the data are published at Appendix IV.

A total of 172 data points were analysed by EMPA for the concentration of Co and Ni at weight percentages (wt %). The 172 data points are obtained from a selection of 14 different pyrite grains chosen from five polished sections. The five sections contain big pyrite grains of 800 µm diameter on average. The grains of this size are suitable for this study because at least five points of 25 µm spot size can be placed on each grain (Figure 4.3, Figure 4.5, and Figure 4.7). Ni and Co were chosen because they are usually detectable in all concretionary pyrite nodules, especially those from detrital origin. The Ni and Co are useful for the investigation of chemical signatures to differentiate between the rounded and the angular pyrite grains. Furthermore, Ni and Co are useful to differentiate between rounded porous and rounded massive pyrite grains.

Table 5.1(A): Measured concentrations of Ni and Co reported at wt % obtained by EMPA for 172 data points from section g52239 containing angular massive pyrite grains (n = 130). The rest of the table is published in Appendix IV. The dashes mean below detection limits.

Dataset	S (wt %)	Fe (wt %)	Co (wt %)	Ni (wt %)	Total (wt %)	Comment	Pyrite Type
1	52.34	46.70	-	0.2634	99.30	g52239	Angular
2	52.15	46.79	-	0.0433	98.99	g52239	Angular
3	51.83	46.60	-	0.2929	98.73	g52239	Angular
4	52.43	46.74	-	0.1205	99.29	g52239	Angular
5	52.61	47.12	-	0.0047	99.73	g52239	Angular
6	52.36	46.51	-	-	98.87	g52239	Angular
7	52.00	46.93	-	0.2307	99.16	g52239	Angular
8	51.94	46.61	-	0.2558	98.81	g52239	Angular
9	51.12	46.17	0.0055	0.5937	97.89	g52239	Angular
10	51.39	46.43	0.0047	0.4851	98.31	g52239	Angular
11	51.29	46.39	-	0.4139	98.09	g52239	Angular
12	52.35	46.75	-	0.1306	99.23	g52239	Angular
13	51.91	46.66	-	0.1129	98.69	g52239	Angular
14	51.93	46.11	-	0.3133	98.36	g52239	Angular
15	52.44	47.10	-	0.0598	99.60	g52239	Angular
16	52.00	46.64	0.1592	0.2539	99.06	g52239	Angular
17	51.94	46.72	0.0205	0.1032	98.77	g52239	Angular
18	52.29	46.33	0.1834	0.2592	99.07	g52239	Angular
19	52.00	46.64	-	0.1682	98.81	g52239	Angular
20	52.60	46.76	-	0.0525	99.41	g52239	Angular
21	52.09	46.99	-	0.0761	99.16	g52239	Angular
22	51.95	47.08	-	0.0573	99.08	g52239	Angular
23	52.65	46.82	-	0.0615	99.54	g52239	Angular
24	52.20	46.30	-	0.2279	98.72	g52239	Angular
25	51.96	46.52	0.1969	0.1384	98.81	g52239	Angular
26	52.85	46.86	-	-	99.70	g52239	Angular
27	53.06	46.73	-	-	99.79	g52239	Angular
28	52.00	46.86	-	0.0819	98.95	g52239	Angular
29	52.66	47.30	-	-	99.96	g52239	Angular
30	52.49	47.19	-	0.0093	99.68	g52239	Angular
31	52.45	47.35	-	-	99.80	g52239	Angular
32	52.86	46.78	-	-	99.64	g52239	Angular
33	53.07	46.80	-	0.0059	99.87	g52239	Angular
34	52.60	47.03	-	0.0159	99.64	g52239	Angular
35	52.83	46.51	-	0.0222	99.36	g52239	Angular

From the total of 172 data points that were analysed using EMPA, only 29 data points report both Fe and Ni for the angular pyrite grains; see Table 5.1(a). 13 data points report both Fe and Ni for the rounded pyrite grains. The remaining 130 data points report the concentration of Fe but did not contain Ni. A very limited dataset for Co for both angular and rounded pyrite was obtained; see Table 5.1(a). The medians and standard deviations for Co and Ni concentrations for rounded and angular grains of pyrite were calculated (Table 5.2) using Microsoft Office Excel 2010 software.

Table 5.2: *Medians and standard deviations of Co wt % and Ni wt % for the rounded and angular pyrite grains*

Statistic Terms	Element	Rounded Pyrite (wt %)	Angular Pyrite (wt %)
Median	Ni	0.03	0.06
	Co	0.04	0.04
Std dev	Ni	0.17	0.13
	Co	0.02	0.04

The Microsoft Office Excel 2010 software was used to produce graphs for comparisons of the concentrations of Co and Ni in wt % correlating the angular and rounded pyrite populations (Figure 5.1 through Figure 5.3). The median of 0.04 and 0.06 wt % for Co and Ni were calculated respectively in Table 5.2 for both rounded and angular pyrite grains. The rounded pyrite grains have a median of 0.04 wt % for Co and 0.03 wt % for Ni.

The concentrations of Co and Ni in wt % were used to produce scatter plots for 13 data points obtained from the rounded pyrite grains and 29 data points recorded from the angular pyrite grains (Figure 5.1). The scatter plots were produced to investigate chemical similarities or discrepancies between the rounded and angular forms of pyrite grains.
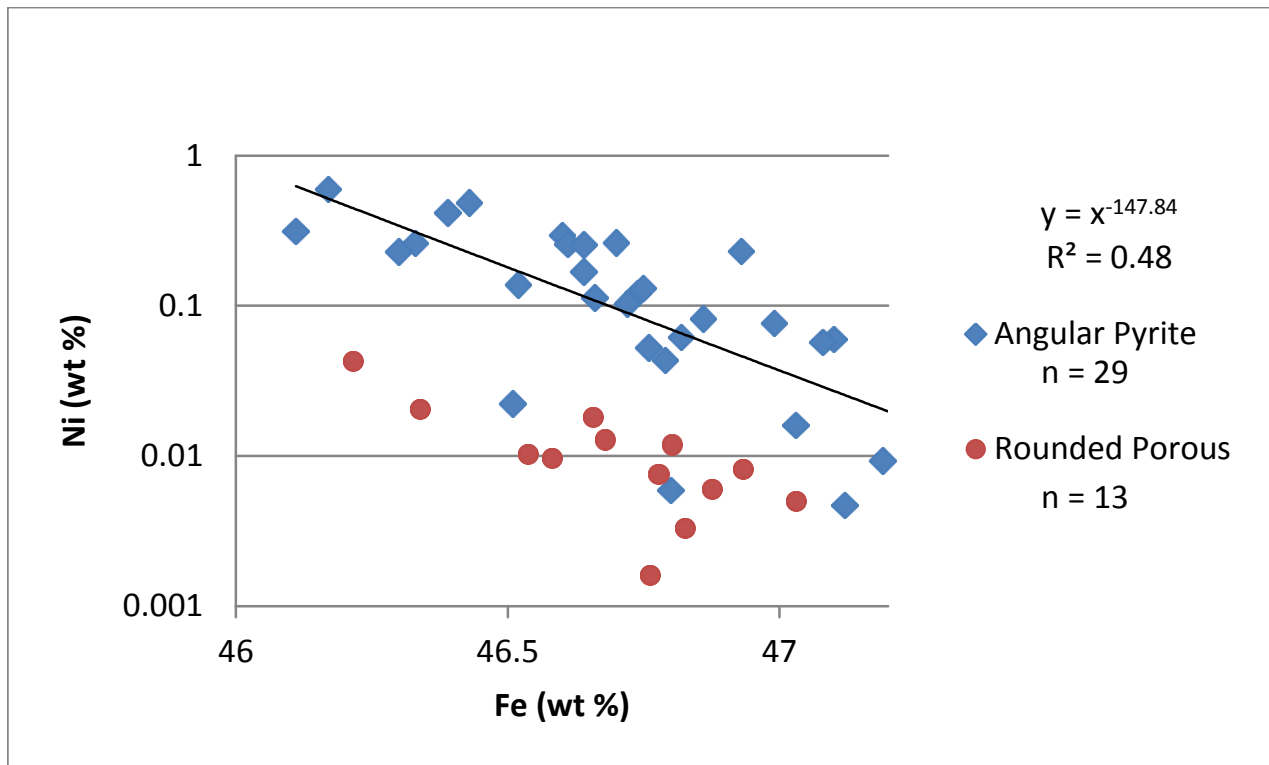
Figure 5.1: Scatter plotfor the concentrations of Fe and Ni of the rounded pyrite grains data
points (n = 13), and the angular pyrite grains (n = 29).

The data points for the concentration of the rounded pyrite grains spread out between 46
and 47.2 wt % Fe and from 0.001 to 0.1 wt % Ni. In comparison, the data points of the
angular pyrite grains spread between 46 and 47.2 wt % for Fe and between 0.06 and 1.0
wt % for Ni. It is clear that Figure 5.1 does not show much difference in terms of Fe
concentration between the rounded and angular pyrite grains. However, it can be seen
that the angular pyrite grains have high Ni concentration than the rounded pyrite grains.
The graphs produced negative trends for the plots of Fe against Ni for both types of
pyrite grains. Similar negative trends were observed for the plots between S and Ni for
the different types of grains of pyrite (Figure 5.25 in Appendix IV).
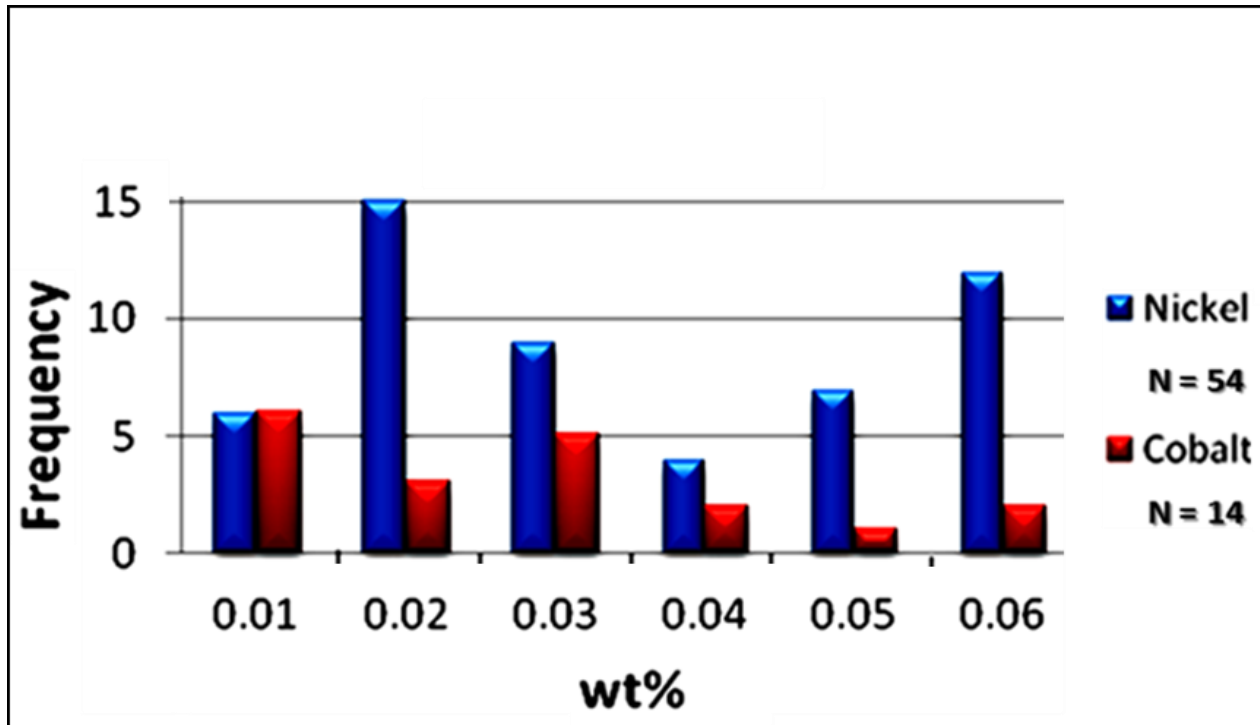
Figure 5.2: *Histograms showing distributions of Co (n = 14) and Ni (n = 54) for the angular pyrite grains from sections g52233 and g52239.*

A total of 68 data points were used to produce the histograms of Ni and Co of the angular pyrite grains. Figure 5.2 illustrates histograms that are showing distributions of Co and Ni for the angular pyrite grains with n = 54 for Ni, and n = 14 for Co. Differences in the concentrations of Ni and Co for the angular pyrite grains are reflected in the deviation between the frequency distributions. The distributions of both Ni and Co are non-normal and the frequency distribution of Ni concentration declines from low concentration values (0.01 wt %) towards high values (0.06 wt %). In comparison, the frequency distribution of Co concentration shows a slight increase from 0.01 wt % to 0.03 wt % and then a decline from 0.03 wt % towards 0.06 wt %.
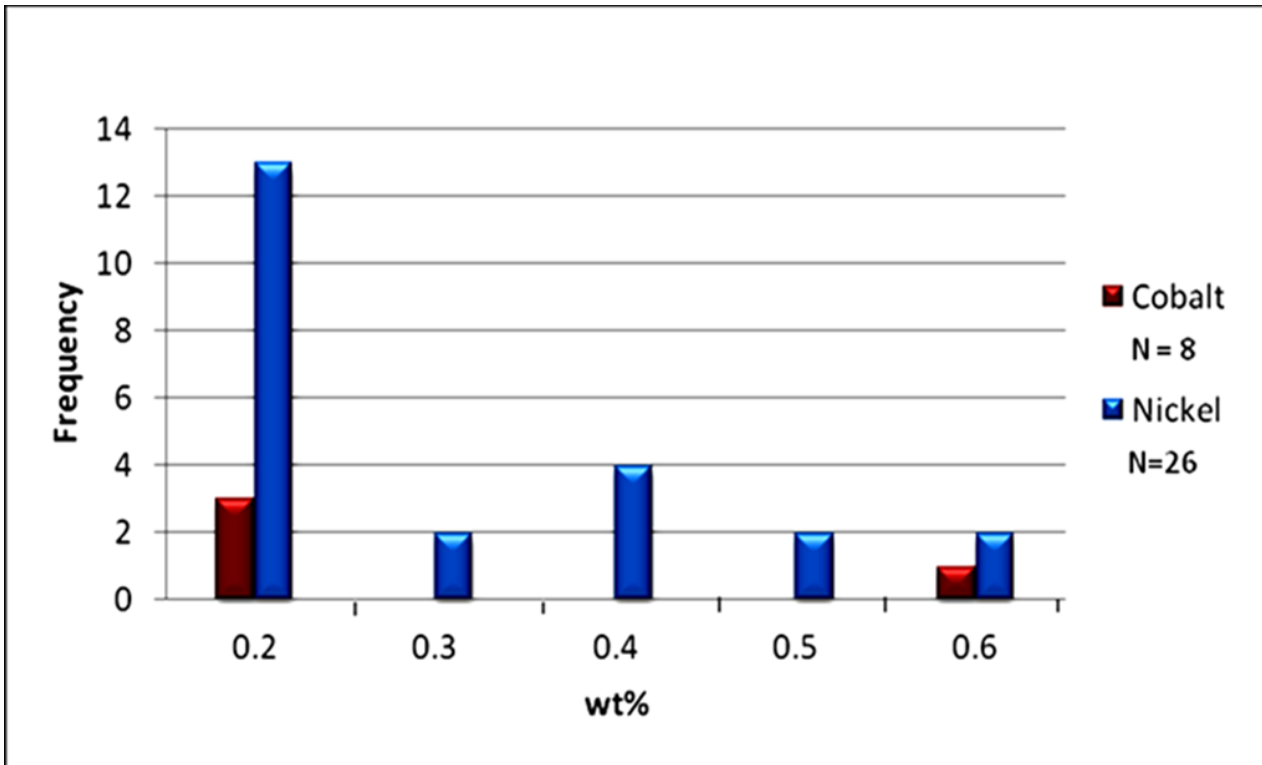
Figure 5.3: *Histograms produced for Co (n = 8) concentration and for Ni (n = 26) concentration for the detrital rounded pyrite grains of sections g52228 and g52237. The graph shows a non-normal concentration distribution for Ni; however there are only five analyses of Co.*

Figure 5.3 illustrates histograms for a non-normal distribution of Ni for the rounded pyrite grains. This kind of distribution is similar to the distribution observed for the concentration of Co and Ni for angular pyrite grains in Figure 5.2. In addition, the histograms for Ni in the rounded pyrite grains show a positive skewness towards high values of Ni concentration (Figure 5.3). The histogram for the rounded pyrite grains for Co is inconclusive because there were few data points.

5.2. LA-ICP-MS Data Description

The LA-ICP-MS technique is capable of providing multi-elemental analyses, and has a very low limit of detection. It also requires minimal preparations of polished sections, since the same concentrates that were firstly used for EMPA method were also examined using the LA-ICP-MS method. However, the destruction of the section caused by the LA-ICP-MS analyses was greater than the damage caused by the EMPA technique; therefore EMPA was conducted before LA-ICP-MS. LA-ICP-MS sensitivity is higher by several orders of magnitude than the sensitivity of the EMPA technique (Outridge et al., 1998; Longerich et al., 1987). Two pyrite grains per section were selected and five data points were analysed on each grain (section 3.5). The reasons for the selection of the sections are discussed in section 5.1.

A total of 207 data points were obtained from 18 polished sections. About 53 of the 207 data points were obtained from five sections that have previously been ablated using EMPA, and hence contain concentrations of Co and Ni reported in both wt % for EMPA and percentage (%) for LA-ICP-MS (Table 5.3). About 24 of the 53 data points were obtained from sections g52233 and g52239, representing angular pyrite grains, whereas the other 21 data points were obtained from sections g52228, g52236 and g52237, representing both rounded porous and rounded massive pyrite grains.

The remaining 154 points of the 207 data points were obtained from 13 polished sections such as g52200; g52227; g52229; g52258 and g52263 containing angular pyrite grains, and sections g52008; g52210; g52213; g52214; g52216; g52224; g52230; and g52261 containing the rounded pyrite grains. These 154 data points represent LA-ICP-MS data points only with no EMPA data. The LA–ICP–MS method offers detection of 75 standard instrumental set-up elements with a spot size of 25 μm diameter. A full scan method was used to obtain a total of 16302 data points. For the purpose of this study only the elements shown in Table 5.3(A) below were used to produce scatter plots and the rest of the datasets are published in Appendix IV. Co and Ni were used for comparisons with EMPA data, whereas the rest of the elements were chosen because they exist in the structure of pyrite and can contribute to the understanding of the chemistry of the different pyrite grains.

Table 5.3(A): *Analyses of 75 isotopes from 18 polished sections. For simplicity, only 11 are shown in table 5.3; the rest of the data is published in Appendix IV. The table shows a section name, grain and spot number, with isotope name indicated by a number after the element name, and the type of the pyrite grains. The concentrations are reported in percentages of total analyzed volume (%). Dashes imply below detection limits. The values of the analyses are rounded off to four decimal places for easier handling of the data without compromising meaningful information.*

Section Name	Sulphur33	Iron57	Cobalt59	Nickel61	Copper65	Zinc68	Arsenic75	Gold197	Lead208	Silver109	Zirconium91	Pyrite Type
G52210-01-01	-	-	10.2677	0.4146	0.4784	-	2.8844	0.0138	1.6143	0.0290	0.0083	Rounded Porous
G52210-01-02	-	-	20.7850	0.4956	0.6842	-	4.0579	0.0092	1.6474	0.0250	0.0038	Rounded Porous
G52210-02-01	-	-	5.3309	0.9108	0.5642	0.0028	2.6999	0.0097	1.8953	0.0373	0.0016	Rounded Porous
G52210-02-02	-	-	7.3725	0.9925	0.5849	0.0077	3.9820	0.0112	3.3636	0.0472	0.0014	Rounded Porous
G52210-03-01	-	-	5.8892	0.2291	0.3953	0.0017	3.5795	0.0059	2.5770	0.0191	0.0040	Rounded Porous
G52210-03-02	-	-	5.4929	0.3487	0.5395	0.0013	5.0845	0.0107	4.3361	0.0309	0.0030	Rounded Porous
G52210-04-01	-	-	7.3129	0.7333	2.0331	0.0731	4.2965	0.0151	3.8390	0.0642	0.0035	Rounded Porous
G52210-04-02	-	-	8.8182	0.7645	0.7879	0.0162	4.5092	0.0229	3.5916	0.0597	0.0018	Rounded Porous
G52210-05-01	-	-	3.8247	0.0850	0.1668	0.0059	2.2164	0.0016	0.6093	0.0107	0.0424	Rounded Porous
G52210-05-02	-	-	3.9334	0.1307	0.3264	0.0040	3.2680	0.0023	0.8374	0.0118	0.0250	Rounded Porous
G52213-01-01	0.1146	2.2889	0.0853	0.0007	0.0012	-	0.0087	0.0001	0.0048	0.0002	-	Rounded Porous
G52213-01-02	0.1123	2.3557	0.0365	0.0003	0.0009	-	0.0041	-	0.0015	0.0001	-	Rounded Porous
G52213-02-01	0.1111	2.1608	0.2152	0.0113	0.0067	0.0018	0.0246	0.0001	3.7048	0.0007	-	Rounded Porous
G52213-02-02	0.1033	2.0354	0.3055	0.0098	0.0250	0.0038	0.0268	0.0001	2.7081	0.0006	0.0002	Rounded Porous
G52213-03-01	0.1108	2.2751	0.3342	0.0055	0.0198	0.0001	0.0289	0.0001	0.0233	0.0005	-	Rounded Porous
G52213-03-02	0.1208	2.3446	0.1737	0.0098	0.0753	0.0005	0.0145	-	0.2667	0.0004	-	Rounded Porous
G52213-04-01	0.1131	2.1457	0.2452	0.0069	0.0059	1.0204	0.0284	0.0001	2.9445	0.0007	-	Rounded Porous
G52213-04-02	0.1088	2.2347	0.2729	0.0197	0.1002	0.0002	0.0225	0.0001	0.8431	0.0006	-	Rounded Porous
G52213-05-01	0.1164	2.3912	0.1784	0.0020	0.0123	0.0001	0.0185	-	0.0337	0.0003	-	Rounded Porous
G52213-05-02	0.1163	2.4054	0.1549	0.0018	0.0131	0.0003	0.0147	0.0001	0.0368	0.0003	0.0001	Rounded Porous
G52214-03-01	-	-	9.2599	0.1695	3.7561	0.0434	2.7663	0.0049	1.0325	0.0117	0.0011	Rounded Porous
G52214-03-02	-	-	5.9235	0.1068	0.0867	0.0183	3.9602	0.0022	0.5397	0.0063	0.0015	Rounded Porous
G52214-05-01	-	-	9.9280	0.1907	0.4432	0.0342	2.7305	0.0025	0.2405	0.0025	0.0025	Rounded Porous
G52214-05-02	-	-	3.2024	0.3335	0.1033	0.0159	0.2420	0.0005	0.2064	0.0020	0.0012	Rounded Porous
G52224-01-01	0.1118	2.2492	0.0545	0.0029	0.0031	0.0001	0.0154	0.0001	0.0209	0.0002	-	Rounded Porous
G52224-01-02	0.1118	2.2791	0.0410	0.0020	0.0026	0.0001	0.0137	0.0001	0.0129	0.0002	-	Rounded Porous
G52224-02-01	0.1101	2.2700	0.0465	0.0065	0.0130	0.0001	0.0323	0.0004	0.0149	0.0006	-	Rounded Porous
G52224-02-02	0.1131	2.2735	0.0299	0.0043	0.0131	-	0.0128	0.0002	0.0670	0.0005	-	Rounded Porous
G52224-03-01	0.1062	2.1668	0.1224	0.0056	0.0043	0.0003	0.1724	0.0002	0.3779	0.0011	0.0002	Rounded Porous
G52224-03-02	0.1082	2.2020	0.1304	0.0024	0.0021	0.0003	0.0790	0.0001	0.3763	0.0008	0.0001	Rounded Porous

It is important to point out that the analyses obtained using the LA-ICP-MS are reported in % of total signal instead of wt % (Table 5.3). The representation of LA-ICP-MS data in % total signal permits a feasible comparison for 53 data points containing Ni and Co concentration in both wt % and % of total signal (Table 5.3).

Among 75 standard instrumental set-up elements; Fe, S, Co, Ni, Ag, As, Cu, Zn, Au, Pb, Bi, and platinum group elements (PGEs) such as Pt, Pd, Rh, Ru, Os, Ir, were detected (Table 5.3). However, this study focused on Ni and Co because they were ablated using both EMPA and LA-ICP-MS techniques and the concentration of both Ni and Co is available in both wt % and % of total signal (Table 5.1 and Table 5.3). In contrast, less attention was given to Ag, As, Cu, Pb, Zn, Au, and PGEs which are only analysed using LA-ICP-MS but not ablated using EMPA, therefore the concentration of these elements is only available in % of total signal. High concentrations of Co, Ni, As, Pd, Pt, and Au were observed in rounded pyrite grains. For example the average concentration of As in angular pyrite grains is 4.1907% of total signal, whereas 8.0472% of total signal is recorded from rounded pyrite grains (Table 5.3 and Appendix IV). Traces of Ag, Co, Ni, As, Cu, Zn, Au, Pb, and Bi are more commonly incorporated into the structure of pyrite.

The concentration of the PGEs (Pt, Pd, Rh, Ru, Os, and Ir) is reported in Table 5.3(B) which is given in Appendix IV. The rest of the elements are omitted in this study for simplicity reasons and because their exclusion does not affect or rather influence the interpretation of the findings of this investigation.

5.2.1. LA-ICP-MS Analyses of Pyrite

The concentration of Co, Ni, As, Ag, Au, Pb, Zn, and Pd was calculated from 202 data points. 70 data points were recorded for the rounded porous pyrite grains, 45 data points were recorded for the rounded massive grains, whereas 87 data points were obtained for the angular pyrite grains. The data points of Co and Ni for the different types of pyrite grains were used to produce scatter plots such as in Figure 5.6. The values of data points were rounded off to four decimal places in the table and six decimal places for the plots.
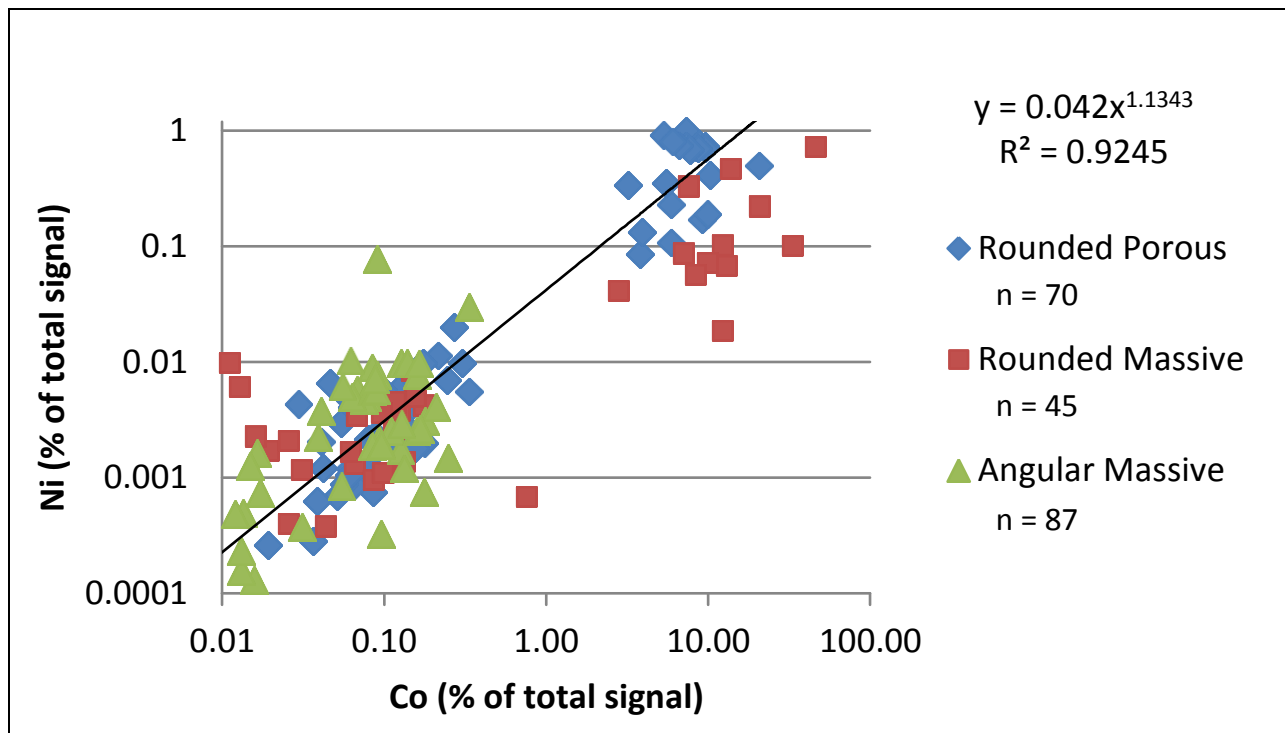
Figure 5.4: *Co plotted against Ni in % of total signal for the different types of pyrite grains showing a positive trend with $R^2 = 0.9272$.*

Figure 5.4 shows that all the three different types of pyrite grains consist of clustered of data points. The rounded pyrite grains, both porous and massive consist of two groups respectively. The first groups of each rounded pyrite type fall below 1% Co and 0.1% of total signal of Ni. The second groups plot between 5% and 80% of total signal of Co, and 0.01% and 1% of total signal of Ni. The angular pyrite grains have concentration of Co ranging from 0.01 to 1% of total signal Co, and 0.0001 to 0.1% of total signal of Ni. It can be seen fron Figure 5.4 that all three types of pyrite produce a positive trend for Co vs Ni plot.
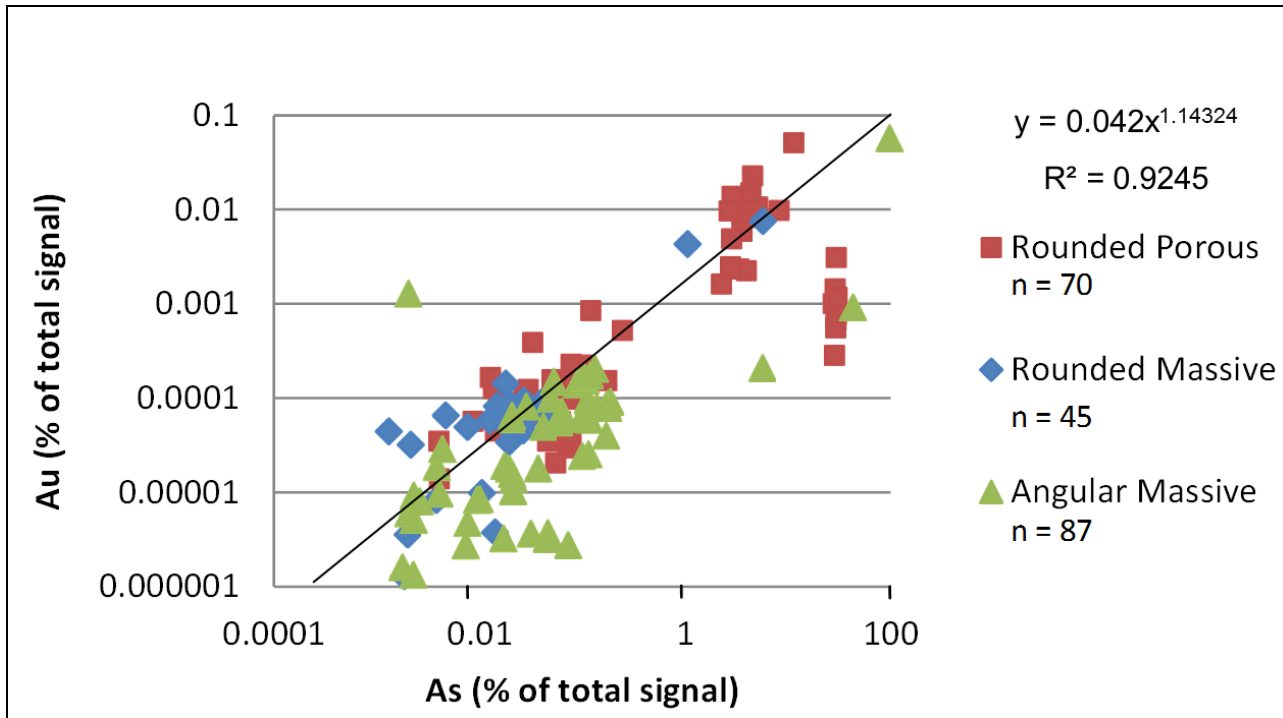
Figure 5.5: *As plotted against Au in % of total signal for the different types of pyrite grains showing a positive trend with $R^2 = 0.9245$.*

Figure 5.5 shows a scatter plot for As against Au for the comparison of the different types of pyrite grains. A linearly spread of the data points is recognisable and produced two groups for the rounded porous pyrite grains accompanied by a positive trend. The first group is below 1% of total signal of As and 0.001 % of total signal of Au, whereas the second group lies between 10 and 80% of total signal of As, and 0.0005 and 0.1% of total signal of Au. It is also clear that the second group of the rounded porous grains with n = 70 overlaps with a few data points of the angular pyrite grains with n = 87 which also overlaps with the rounded massive grains with n = 45. A lot more data points of the rounded massive and the angular massive pyrite grains are clustered together around the same area with the first group of the rounded porous pyrite grains. Similarly, the rounded massive and the angular massive pyrite grains produced positive trends.
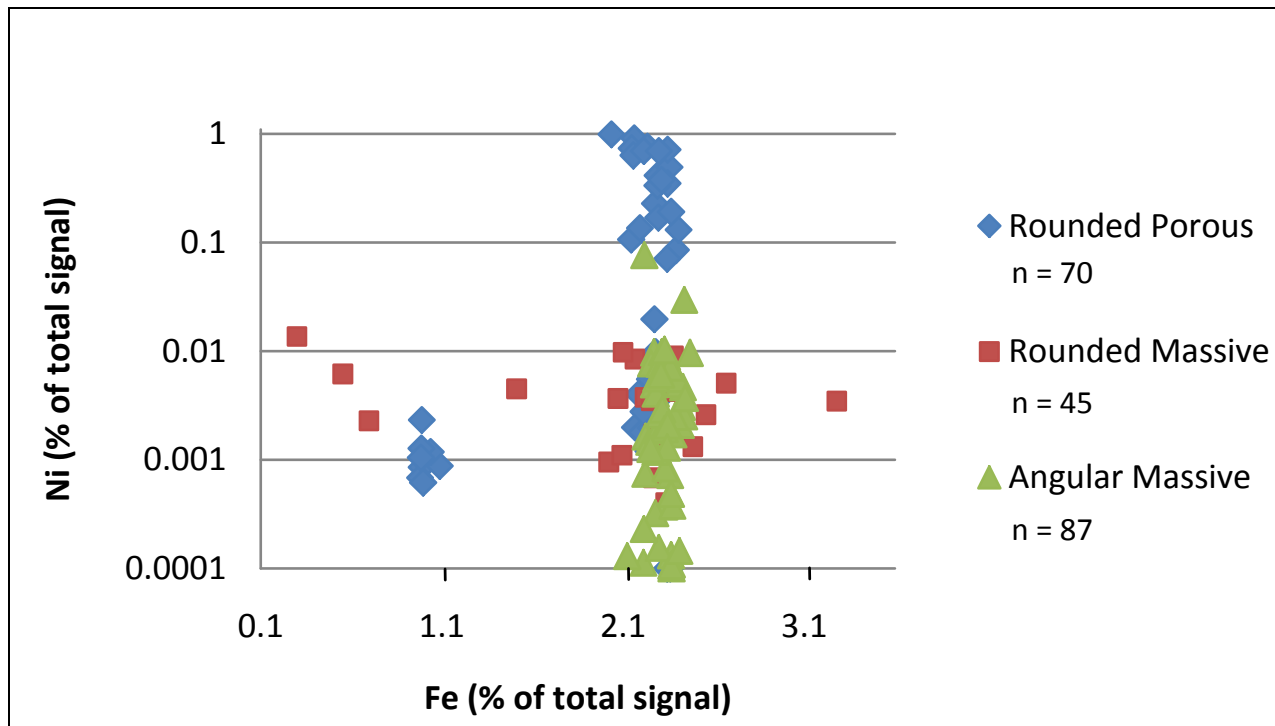
Figure 5.6: *Fe plotted against Ni in % of total signal showing dat distribution for the different types of pyrite grains.*

The relationship between the different types of pyrite grains was also investigated by plotting the concentration of Fe and Ni (Figure 5.6). The rounded porous pyrite grains produced two groups. The first group plots at 1% of total signal of Fe and around 0.001% of total signal of Ni, whereas the data points of second group plot at 2.3% of total signal of Fe and between 0.001 and 1% of total signal of Ni. The rounded massive pyrite grains have a wide spread of data points between 0.2 and 3.2% of total signal of Fe, and 0.001 to 0.01% of total signal of Ni. The plot of the data points of the rounded massive pyrite grains produced a negetive trend. The angular pyrite grains produced a single group with its data points plotting at 2.2% of total signal of Fe, and between 0.0001 and 0.1% of total signal of Ni. The data points of the second group of the rounded porous grains and the data points of the angular pyrite grains plotted at the same area. Nevertheless, the second group of the rounded porous grains has high Ni concentration as compared to the Ni concentration of the angular pyrite grains.

5.3. Statistical Analysis of the Pyrite Grains

The Ni/Co ratio was calculated and used for comparisons to differentiate between the angular and the rounded pyrite grains. The Ni/Co ratio clearly demonstrated a systematic difference between the angular and the rounded pyrite grains. The Ni/Co ratio was calculated as the ratio of the average concentration of Ni divided by the average concentration of Co reported in % of total signal.

The average concentration of Ni was calculated to 0.1901% of total signal for the rounded porous grains, 0.0899% of total signal for the rounded massive grains, and 0.0042% for the angular pyrite grains. The average concentration of Co was calculated to 2.8345% of total signal for the rounded porous grains, 5.0341% of total signal for the rounded massive grains, and 0.0681% of total signal for the angular massive grains. The average Ni concentration of the rounded porous grains is 5% of total signal higher than the average Ni concentration of the rounded massive pyrite grains, also the average Ni concentration of the rounded porous grains is about 1% of total signal more than the average Ni concentration of the angular pyrite grains. The values for the average concentration of Co and Ni, and the Ni/Co ratio of the different types of pyrite grains are provided in (Table 5.4).

Table 5.4: *Co and Ni average concentrations and ratios for the different types of pyrite grains of the VCR for a total of 162 data points.*

Average (% of total signal)	Std dev (% of total signal)	Ni/Co	Data Points	Type of Pyrite
Ni = 0.1901	Ni = 0.3039	0.0671	n = 61	Rounded Porous
Co = 2.8345	Co = 3.4947			
Ni = 0.0899	Ni = 0.0509	0.0179	n = 40	Rounded Massive
Co = 5.0341	Co = 4.4295			
Ni = 0.0042	Ni = 0.0104	0.0615	n = 61	Angular Pyrite
Co = 0.0681	Co = 0.0721			

The standard deviation of Ni was calculated to 0.3039% of total signal for the rounded porous grains, 0.0509% of total signal for the rounded massive grains, and 0.0104% for the angular pyrite grains. The standard deviation of Co was calculated to 3.4947% of total signal for the rounded porous grains, 4.4295% of total signal for the rounded massive grains, and 0.0721% of total signal for the angular massive grains. The standard deviation of Ni of the rounded porous grains is higher than the standard deviation of Ni of the rounded massive pyrite grains which is also higher than the standard deviation of Ni of the angular pyrite grains. In contrast, standard deviation of Co of the rounded porous grains is less than the standard deviation of Co of the rounded massive grains, but higher than the standard deviation of Co of the angular pyrite grains (Table 5.4). Sulphur (S) was plotted against the ratio of Ni/Co such as in Figure 5.7 below. It's acknowledged here that sulphur is probably not being very well recorded by LA-ICP-MS and a lower sulphur signal might have been recorded than real sulphur volume that exists in pyrite materials. Sulphur is light and the sulphur signal may not linearly correlate to the actual sulphur content.
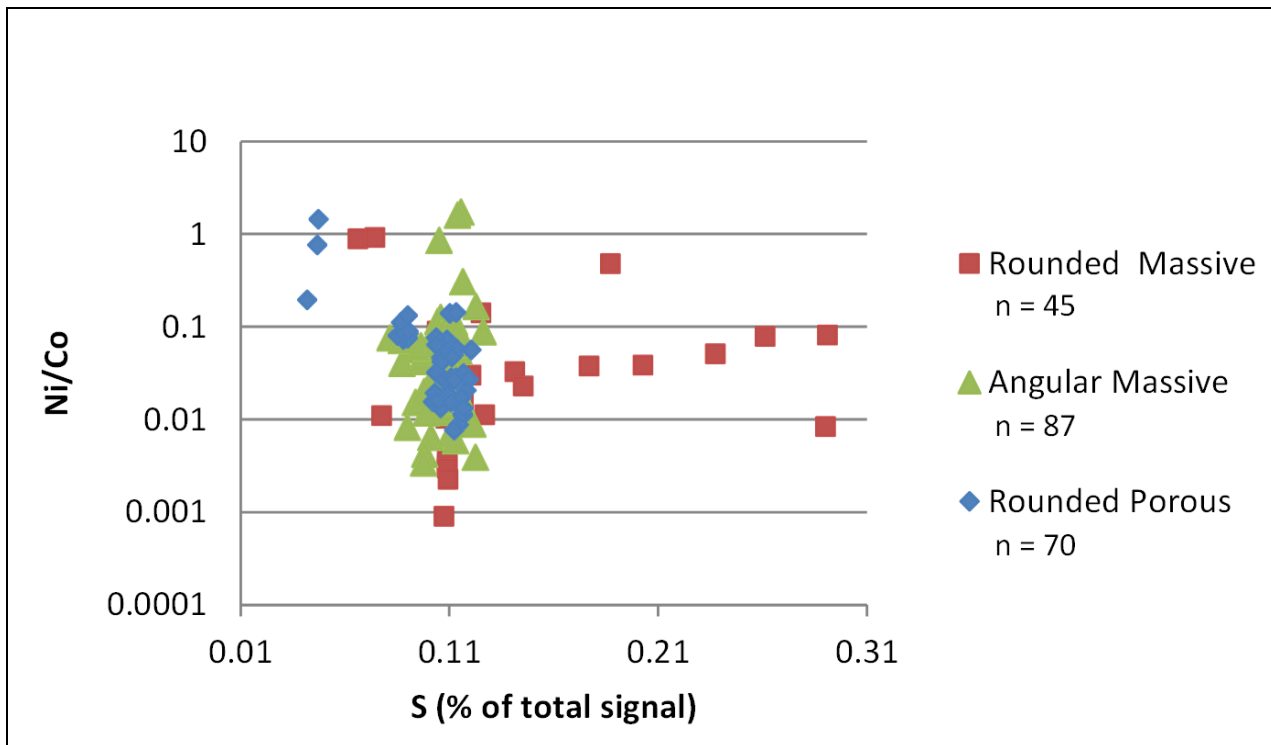
Figure 5.7: *Ni/Co plotted against S for the angular pyrite grains (n = 87), rounded massive grains (n = 45), and rounded porous pyrite grains (n = 70).*

The plot of Ni/Co vs. S produced a clustering around 0.11% of total signal of S, and between 0.001 and 2.0 Ni/Co for the angular grains of pyrite. The data points of the rounded porous grains of pyrite produced a negative trend with data points spreading between 0.07 and 0.11% of total signal of S and from 0.01 to 2.0 Ni/Co. The plot of Ni/Co vs. S has the data points spread between 0.08 and 0.30% of total signal of S, and from 0.001 to 1.0 Ni/Co for rounded massive pyrite grains. The angular grains produced a trend slightly identical to the trend of the rounded porous grains but different to the trend of the rounded massive grains (Figure 5.7). The % of total signal of Fe was plotted against the ratio Ni/Co (Figure 5.8), and produced two groups for the rounded porous pyrite grains. The first group plotted at 1.1% of total signal of Fe, and 0.1 Ni/Co. The data points of the second group plotted at 2.2% of total signal of Fe, and 0.01 and 2 Ni/Co. The rounded massive pyrite grains gave a wide spread of data points for Ni/Co vs. Fe, with the data plotting between 0.5 and 4.1% of total signal of Fe and between 0.01 and 1.0 Ni/Co. The angular pyrite grains produced a single group at 2.2% of total signal of Fe and between 0.1 and 3.0 Ni/Co.
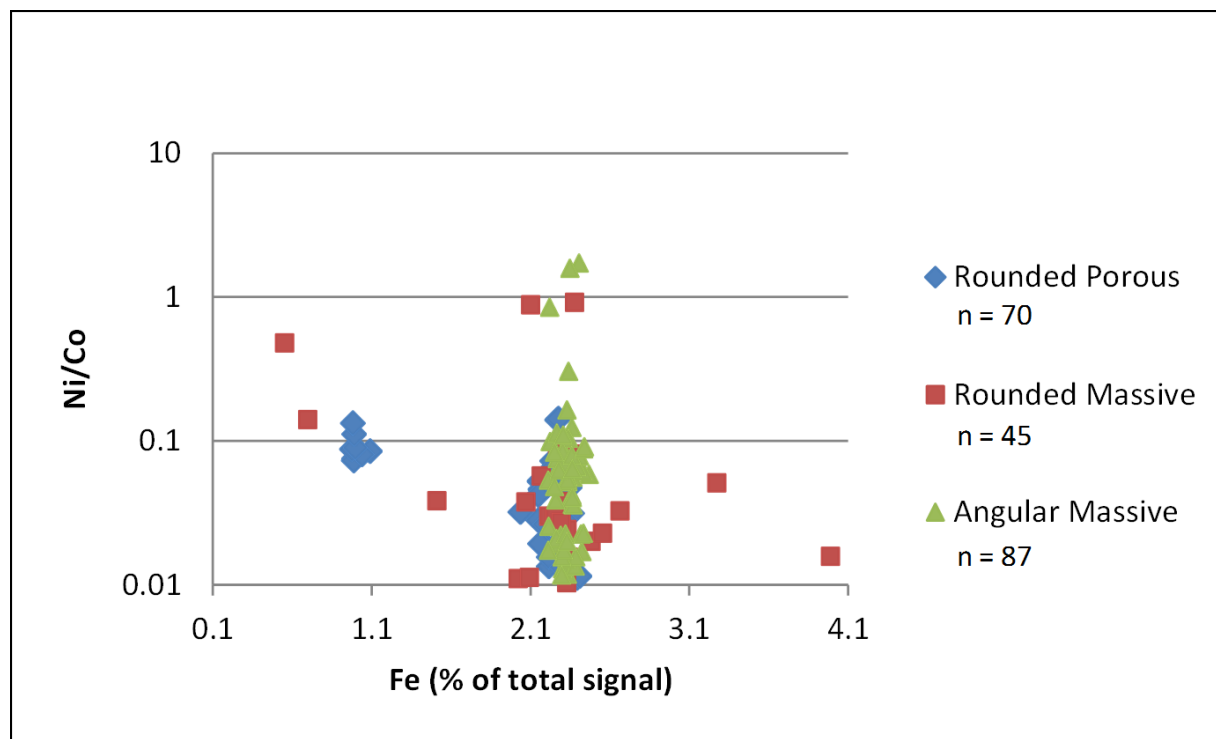
Figure 5.8: *Ni/Co plotted against Fe for the rounded porous pyrite grains (n = 70), rounded massive grains (n = 45), whereas angular pyrite grains (n = 87).*

5.4. Comparison of LA-ICP-MS and EMPA Data

The polished sections were firstly investigated using EMPA method and then studied using LA-ICP-MS technique. The comparison of the data sets obtained by both EMPA and LA-ICP-MS techniques was carried out; see Table 5.5(A). Table 5.5(A) provides the data points used for comparison between the EMPA and LA-ICP-MS data for the angular pyrite grains, whereas the dataset for the rounded grains of pyrite is published in Table 5.5(B) provided in Appendix IV.

Table 5.5(A): *Co and Ni data sets obtained from the same spots analysed using the EMPA and LA-ICP-MS techniques for section g52233 and g52239 containing angular massive pyrite grains. The dashes mean below limits of detection.*

Co (wt %)	Ni (wt %)	Co (% of total signal)	Ni (% of total signal)	Types of Pyrite
0.0055	0.2634	0.0165	0.0016	Angular
0.0047	0.0433	0.0931	0.0021	Angular
0.1592	0.2929	0.0312	0.0004	Angular
0.0205	0.1205	0.0019	0.0001	Angular
0.1834	0.0047	0.0112	0.0007	Angular
0.1969	0.2307	0.1778	0.0003	Angular
0.0052	0.2558	0.0958	0.0001	Angular
0.0241	0.5937	0.0011	0.0017	Angular
0.1102	0.4851	0.1270	0.0007	Angular
0.0255	0.4139	0.0172	0.0005	Angular
0.2032	0.1306	0.0136	0.0049	Angular
0.1043	0.1129	0.0787	0.0057	Angular
0.0176	0.3133	0.0678	0.0001	Angular
0.1654	0.0598	0.0030	0.0001	Angular
0.1027	0.2539	0.0016	0.0004	Angular
0.0264	0.1032	0.0067	0.0005	Angular
0.0009	0.2592	0.0120	0.0008	Angular
0.1101	0.1682	0.0550	0.0001	Angular
0.0596	0.0525	0.0044	0.0012	Angular
0.009	0.0761	0.1334	0.0015	Angular
0.0722	0.0573	0.2485	0.0019	Angular
0.0131	0.0615	0.0848	0.0031	Angular
0.0028	0.2279	0.1800	0.0022	Angular
0.0265	0.1384	0.0390	0.0025	Angular

The concentrations of both Co and Ni were used to produce scatter plots for comparisons between the rounded pyrite grains of section g52233 and g52239, and the angular pyrite grains of section g52228, g52236, and g52237. The concentrations of Co and Ni at % of total signal were plotted against the concentration Co and Ni in wt % (Figure 5.9 and Figure 5.10).
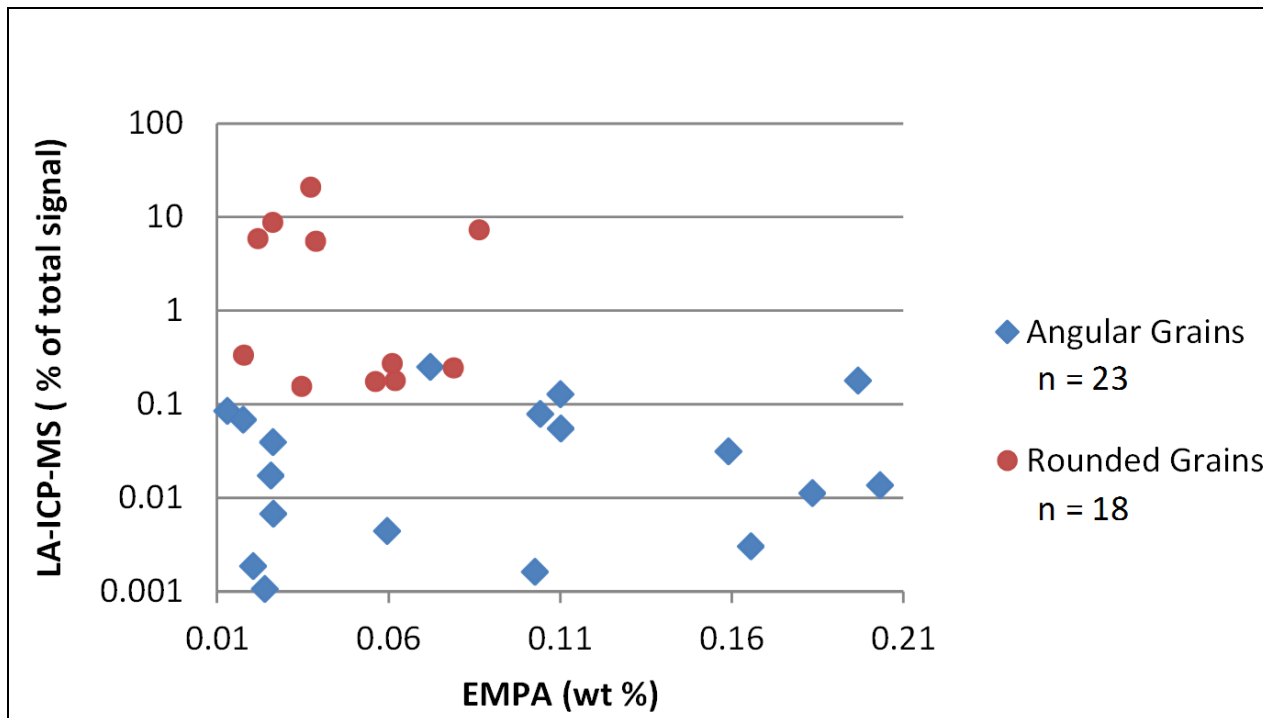
Figure 5.9: *EMPA and LA-ICP-MS plot for Co concentrations for the rounded pyrite grains (n = 18) of section g52228 and g52237, and the angular pyrite grains (n = 23) from section g52233 and g52239.*

The illustration in Figure 5.9 shows a wide spread for the EMPA data points for the angular pyrite grains. The data points spread between 0.01 and 0.21 wt % Co, and from 0.001 to 0.8% of total signal of Co. The rounded pyrite grains show data points between 0.01 and 0.08 wt % Co, and from around 0.5 to 30% of total signal of Co. The Co data sets for both rounded and angular pyrite grains demonstrate no recognisable trends. The angular pyrite grains have higher Co concentration in wt % but low Co concentration in % of total signal, whereas the Co concentration of the rounded pyrite grains is high in % of total signal, but low in wt %.
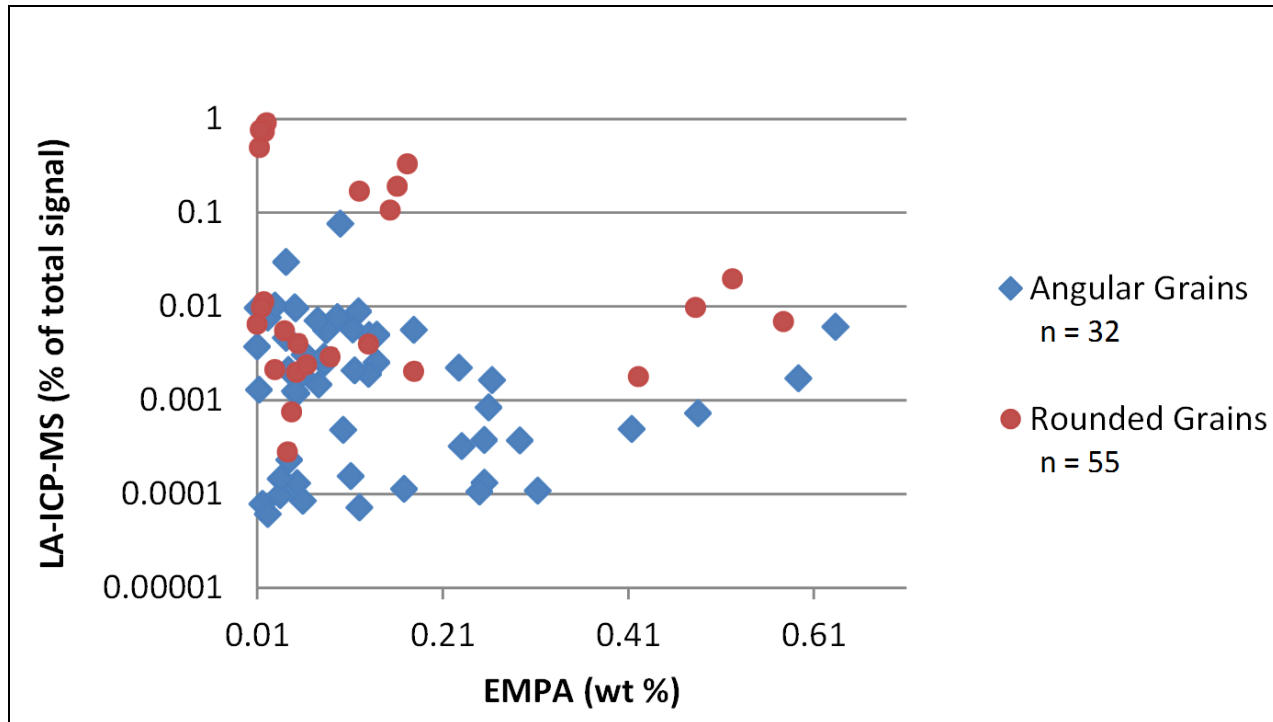
Figure 5.10: *EMPA and LA-ICP-MS plot for Ni concentration for rounded pyrite grains (n = 55) of section g52228 and g52237, and angular pyrite grains (n = 32) from section g52233 and g52239.*

Figure 5.10 shows a spread of the data points for the angular pyrite grains with EMPA data points between 0.01 and 0.62 wt % Ni, and from around 0.0001 to 0.1% of total signal of Ni. The rounded grains of pyrite show data points spreading between 0.01 and 0.6 wt % Ni and from 0.005 to 1% of total signal of Ni. The Ni concentration in % of total signal shows low values for angular pyrite grains, but high for rounded grains. There is no recognisable difference of the concentration of Ni in wt % between the angular pyrite grains and the rounded pyrite grains.

CHAPTER SIX

6. Discussion

Through petrographic investigation (i) rounded porous pyrite grains (Figure 4.3), (ii) rounded massive pyrite grains (Figure 4.5), and (iii) angular massive pyrite grains (Figure 4.7) were identified. The different types of pyrite grains co-exist with arsenopyrite, chalcopyrite, sphalerite, pyrrhotite, zircon, and galena. These observations are in agreement with the findings of Meyer et al. (1987), who indicated a similar mineral association.

6.1. Rounded Porous Pyrite Grains

The rounded porous pyrite grains have been referred as primary (Frimmel, 1997; Kasting and Howard, 2006; Anabar et al., 2007; Hofmann et al., 2009). The following prominent features were observed during investigations:

(a) fragmentation was observed in sections g52213; g52224; g52227; and g52237 (Figure 4.3); these could have being caused during the release of pyrite grains from their parental source rocks; (b) recorded average grain sizes are roughly 400 μm in diameter (Figure 4.2); (c) overgrowths of arsenopyrite and replacements of pyrite with pyrrhotite (Figure 4.3 D and Figure 4.15 in Appendix I); (d) inclusions of chalcopyrite, galena, and gold grains hosted in pyrite grains (Figure 4.4 and Figure 4.9); (e) heterogeneous distribution of very high concentrations of trace elements generally in rounded pyrite grains such as in Figure 5.4 through Figure 5.6, and Figure 5.11 through 5.24 in Appendix IV.

The texture of the rounded porous pyrite grains is referred as botryoidal by Utter (1978). Certain grains consist of circular layers (Figure 4.3 C and D). The different layers contain sub-parallel individual circular crystals of rounded porous pyrite. According to Utter (1978), these types of pyrite grains are called colloform because of their morphology.

The observation of round shapes and porous or spongy textures complement the explanations made by England et al. (2002) that the rounded pyrite grains are of detrital origin. Indentations and cracks radiating outwards in a fan-like form are frequently observed (Figure 4.3 A). According to Utter (1978), the cracks are formed mechanically while the pyrite grains were fragile, meaning the pyrite grains were transported, hence supporting the modified placer model (section 2.12). The porous grains with planar laminations, concentric laminations, or radial texture are observed in section g52237 (Figure 4.3). Nevertheless, based on the above stated features, the rounded porous pyrite grains are tentatively interpreted as being detritally formed and rolled down and abraded during fluvial transportation processes (Frey et al., 1987). This argument is in agreement with the work carried out by Kirk et al. (2002) on rhenium-osmium isochron age dating for Wits conglomerates. The study states that the age of roughly 3.0 Ga for gold grains and rounded pyrite grains is older than the age of the host conglomerates, indicating that the rounded pyrite grains are of detrital origin and are not formed by the later hydrothermal fluids.

The fragmentations and cavities in the rounded porous pyrite grains could have previously being occupied by inclusions which might possibly have dissolved by reacting with migrating fluids (Frimmel, 1997; Kasting and Howard, 2006; Anabar et al., 2007; Hofmann et al., 2009), creating the spaces which are now occupied by hydrothermal minerals such as galena (Figure 4.4). The migrating fluids could have been initiated during the intrusion of the BIC or by normal regional metamorphism, and the Vredefort meteorite impact (Robb et al., 1995; Reimold et al., 1999; Alexandre et al., 2006).

The intrusion of the BIC and the Vredefort meteorite impact consequently may have created the voids which trapped and accommodated the current visible galena grains (Utter, 1978; Frimmel, 1997; Frimmel et al., 1999; Reimold et al., 1999; Spangenberg and Frimmel, 2000). As for the rigid fractured pyrite grains, the cavities are present between crystals and are filled by matrix comprising of quartz cementing the grains (Figure 4.3 B). There is a possibility that the rounded porous and fractured grains were abraded during transportation to the current depositional location (Saager, 1968; Simpson and Bowles, 1977).

6.2. Rounded Massive Pyrite Grains

The second type of the rounded pyrite grains has massive texture. The following features are important: (a) striations are observed on section g52214; g52216; g52228; and g52230 (Figure 4.5), (b) recorded average grain size of roughly 400 μm (Figure 4.2), (c) primary inclusions of chalcopyrite, pyrrhotite (Figure 4.5 B), sphalerite, pentlandite.

Substantial amounts of gold grains are found associated with, and occurring as inclusions, in the rounded massive pyrite grains. Au together with Co, Ni, Ag, Cu, Zn, and Pb must have been mobilised during the overgrowth period during low temperature fluids migration and metamorphism (Frimmel, 1997; Kasting and Howard, 2006; Anabar et al., 2007; Hofmann et al., 2009). Rounded grains of zircon (Figure 4.6) were observed occurring as rounded grains in the rounded massive pyrite grains. The work carried out by Shepherd (l977) on fluid inclusions of the Wits gold-uranium ores demonstrated the significance of the presence or absence of the zircon grains in pyrite grains. The presence of the rounded zircon grains in pyrite grains might suggest that the pyrite grains may have formed later after the deposition of the wits sediments.

Most of the fragmented rounded massive pyrite grains are relatively unaltered, implying that they have survived both the greenschist metamorphism and deformation (Simpson and Bowles, 1977), or that they are rather post metamorphism and deformation, implying that they were formed by hydrothermal fluids during the deposition of the sediments, hence referred as secondary (Frimmel, 1997; Kasting and Howard, 2006; Anabar et al., 2007; Hofmann et al., 2009).

6.3. Angular Massive Pyrite Grains

The third type of the observed pyrite grains is the angular massive grains with the following features: (a) large angular pyrite crystals sometimes greater than 800 μm in diameter (Figure 4.2); (b) micro-fractures occupied with chalcopyrite, pyrrhotite, and gold grains (Figure 4.9B);

The chalcopyrite and gold grains appear in both angular massive and rounded massive pyrite; this is in agreement with the work done by Schidlowski, (1968) which found chalcopyrite, pyrrhotite, and gold grains as inclusions in angular pyrite grains; (c) section g52200, g52229; and g52239 show high concentration of angular pyrite crystals (Figure 4.7); (d) the angular pyrite grains demonstrate low concentrations of Co, Ni, Ag, Cu, Zn, Pb, and Au (Table 5.3) if compared to the rounded porous and rounded massive pyrite grains. Further discussion on Ni and Co content of the angular pyrite grains is given in section 6.5. The massive texture is interpreted as reflecting the origin under temperature and pressure conditions that are different to the conditions when the primary detrital rounded pyrite grains were formed.

The angular grains are tentatively interpreted to have grown in situ and reflect post-sedimentary diagenesis, metamorphism, and hydrothermal fluid movement (England et al., 2002; Hofmann et al., 2009). The angular massive pyrite grains occur as overgrowths on detrital rounded components of the pyrite (Figure 4.15 in Appendix IV). These descriptions are in agreement with the work of Simpson and Bowles (1977), suggesting the angular massive pyrite grains as authigenic in origin. It was also suggested that the angular pyrite grains were formed by mobilisation and re-crystallisation during diagenesis and low grade metamorphism of the Wits sediments (Burke et al., 1986; Utter, 1978; England et al., 2002). Thus, angular massive pyrite grains are considered authigenic constituents of the Wits conglomerates.

6.4. Chemical Compositions of the Pyrite Grains

The chemical investigations using EDX, SEM (section 4), EMPA, and LA-ICP-MS techniques (section 5) demonstrated that the chemistry of the major, minor and trace elements for the rounded pyrite grains are different to the chemical composition of the angular pyrite grains. Histograms, medians, standard deviation, and scatter plots were produced for discriminations between the different types of pyrite grains.

6.4.1. Statistical Analysis

The histogram, medians, averages, and standard deviations of Co and Ni were calculated and used to differentiate between the rounded and angular pyrite grains (Table 5.2 and Table 5.4). It was found that in general, the standard deviation of Ni wt % is higher than standard deviation of Co wt % on both types of pyrite grains. Nevertheless, the standard deviation of % of total signal of Co is higher than standard deviation of % of total signal of Ni on both types of pyrite grains. This discrepancy is caused by the difference in the total data points used for the calculations of the standard deviation.

The histograms presentations have statistical advantages that no postulation regarding the form of distributions is required. The statistics postulate that if multiple pyrite populations are having unrelated frequency distributions either of Co and/or Ni, then the pyrite populations are significantly different. The distribution of Co and Ni of the angular grains in Figure 5.3 showed non-normal distributions with different peaks. The peaks indicate the non-homogeneity of the pyrite grains; each peak represents pyrite grains that come from different source rock. Each type of pyrite grains has more or less non-normally distributed data implying different depositional mechanisms. The histograms illustrate non-normal distributions for Co concentrationsfor the rounded pyrite grains (Figure 5.3). Comparable trends were observed for Ni which also showed non-normal distributions for angular pyrite grains. In this case, the scatter plots such as in Figure 5.6 were produced to add-on to the understanding of the nature of the populations of the different pyrite grains.

6.4.2. Scatter Plots

The comparison graphs in section 5 demonstrated and differentiated between the rounded and angular pyrite grains by comparing the chemical compositions using Co, Ni, Fe, S, and Ni/Co. High concentration of Ni and Co was observed from the rounded pyrite grains (Figure 5.4 through Figure 5.6). The plots of Ni and Co wt % against Fe wt % for both rounded and angular pyrite grains produced negative trends for EMPA dataset, for example see Figure 5.1.

A similar negative trend was observed for the plot of % of total signal of Ni against % of total signal of Fe for the rounded massive pyrite grains (Figure 5.6). The rounded massive pyrite grains produced a wide spread of data points between 0.2 and 3.2% of total signal of Fe, and 0.001 to 0.01% of total signal of Ni with a negative trend. The negetive trend suggest that Ni sibstitutes for Fe in the structure of pyrite to form a NiS_2 phase. The work of Klemm (1965) summarised by Hem and Makovicky (2004) have demonstrated experimentally solid solutions between pyrite (FeS2), cattierite (CoS2), and vaesite (NiS2) at temperatures approximately 500 °C and higher. In contrast, pyrite grains are commonly rich in Co, or Ni, or both (bravoite) when occurring at low-temperatures of about 150 °C.

Nonetheless, this study did not investigate the solid solution but used Co and Ni to indicate the differences between the angular massive, rounded porous, and rounded massive pyrite grains from the VCR. Despite pyrite being a stoichiometric FeS_2 phase, significant amounts of Ag, As, and Au are found in VCR pyrite grains (Hem and Makovicky, 2004; Reich and Becker, 2006). According to Sugawara et al. (2008), arsenic is concentrated in framboidal pyrite when substituting for sulphur because arsenic fits into the structure of pyrite as an arsenopyrite component (Figure 5.15 in Appendix IV). Framboidal pyrite is a typical kind of pyrite which formed mainly in sedimentary rocks (Zachariáš et al., 2008).

The Ag, As, and Au occur in pyrite grains and this complements the work of Chouinard et al. (2005), who proposed that As, Ag, Cu, and Au are used in coupled substitutions for Fe. Appendix IV provides the plots of Ag against Au (Figure 5.24), As against Cu (Figure 5.18), As against Ag (Figure 5.12) produced positive trends for all three types of pyrite grains. Chouinard et al. (2005) showed nearly identical zoning patterns of Ag and As (Figure 4.33) suggesting that Ag enters the structure of pyrite by means of a coupled substitution with As in which one atom of Ag and one atom of As substitute for two Fe atoms, yielding (Ag+0.5As3+0.5)S2. According to Xenophontos et al. (1999), arsenic is typically a mobile element in very low temperature geological processes, and the chemical change is noted along cracks of rounded porous pyrite (Figure 4.3).

The As mobility serves as evidence to support the interpretation of the origin of the rounded porous pyrite grains as being of multiple stages of growth (Sugawara et al., 2008). However, only a few minerals containing As were observed as inclusions in rounded porous pyrite grains (Figure 4.10; Table 4.3).

The PGEs were also used to produce scatter plots for the different types of pyrite grains. The PGEs plots produced widely distributed data points across all the types of pyrite grains. The plots of Pt against Au, and Pd against Ag produced positive trends (Figure 5.21 and Figure 5.22 in Appendix IV). In general, PGEs maybe very mobile and may be dissolved by hydrothermal fluids moving around the Wits basin (Frimmel, 1997; Kasting and Howard, 2006; Anabar et al., 2007; Hofmann et al., 2009). Various platinum group minerals (PGM's) were also observed by Utter, (1978).

The average Pb concentration varied significantly between the rounded and angular types of pyrite grains. Higher average Pb concentrations were recorded for rounded porous pyrite grains than for angular pyrite grains (Figure 5.7). Geochemically, Pb and As behave similar at low temperatures and pressures (Kasting and Howard, 2006; Anabaret al., 2007; Hofmann et al., 2009). However, only few grains of galena inclusions such as in Figure 4.4 were found in rounded porous pyrite of the VCR. The pyrite grains of the Wits basin have experienced a major reworking at 2.04 Ga at varying intensities, thus causing a complete resetting of U: Pb ages to a. 2.04 Ga (Rundle and Snelling, 1977). Radiogenic lead was liberated during the reworking process, and crystallized as galena in veins and along fissures. The veins and fissures cut diagonally through conglomerates (Rundle and Snelling, 1977; Utter, 1978). According to Simpson and Bowles (1977), galena resulted from the migration of radiogenic lead from co-existing uraninite grains. The form and nature of minerals such as galena give a small possibility for galena being of sedimentary origin. The inclusions of galena would smear in between the clasts during remobilisation. Thus the grains of galena must be hydrothermal, perhaps only the nuclei are sedimentary. Nonetheless, these assumptions still remain subject of future investigations.

Cu and Zn were also detected from the different pyrite grains. The scatter plots for Pb against Zn, and Cu against Ni produced positive trends for all types of the analysed pyrite grains (Figure 5.16; Figure 5.19 in Appendix IV). The intergrowths of chalcopyrite (Figure 4.4 B) and sphalerite grains (Table 4.2) may have contributed in introduction of Cu and Zn in the pyrite grains. According to Utter (1978), the solid solution of Cu is uncommon in pyrite in general. The LA-ICP-MS results suggest the highest values for both Cu and Zn for the rounded porous pyrite grains, and lower values for the angular massive pyrite grains (Table 4.3).

The observation of high concentration of Co, Ni, As, Cu, Pb, Zn, and PGEs complements the work carried out by Zachariáš et al. (2008) on the chemistry of trace element of low-temperature pyrite grains as indicators of the past changes in fluid chemistry and fluid migration paths.

6.5. Ni/Co Ratio

Co enrichments were observed in rounded pyrite grains of section g52228 and g52237 but low in the angular pyrite grains of section g52233 and g52239. This observation suggests that the angular grains did not originate from the same source as the rounded grains. The angular grains of pyrite originated from Co-poor hydrothermal fluids percolating through the sediments sometime after deposition of the detrital rounded pyrite grains. Co and Ni concentration and Ni/Co ratio pattern disagree with the findings of the work done by Yamaguchi and Ohmoto (2006) on evidence from sulphur isotope and trace elements in pyrite for multiple post-depositional processes in uranium ores at the Stanleigh Mine, Elliot Lake, Ontario, Canada. The results of the study done by Yamaguchi and Ohmoto (2006) in Evolution of Earth's Early Atmosphere, Hydrosphere, and Biosphere-Constraints from Ore Deposits, showed that Co and As contents were high in young hydrothermal pyrite components.

Metamorphic events such as the intrusion of BIC at around 2.06 Ga ago (Frimmel, 1997; Reimold et al., 1999; Spangenberg and Frimmel, 2000; Alexandre et al., 2006) and the meteorite impact at about 2.02 Ga ago (Utter, 1978; Frimmel et al., 1999; Reimold et al., 1999; Roberts and Schweitzer, 1999; Alexandre et al., 2006) affected the Wits basin. Hydrothermal fluids flow during these events is a probable source for the pyrite overgrowths and recrystallization features observed in reflected light photomicrographs (Figure 4.15 in Appendix I). Yamaguchi and Ohmoto (2006) reported pyrite grains from the 2.45 Ga old Matinenda Formation of the Huronian Supergroup with $\Delta^{34}S$ between -9 ‰ and 5.5 ‰, low Ni/Co (<1), and showed core–rim zonation of As, Ni, and Co. Yamaguchi and Ohmoto (2006) argued that the hydrothermal pyrite grains have low Ni/Co, and the study found that Ni is typically more abundant in rounded pyrite grains, this agrees well with Figure 5.6. The precipitation of Co-rich pyrite, arsenopyrite, and sphalerite as a result of a subsequent introduction of hydrothermal fluids with elevated activities of Au and As complexes, subordinate concentration of Pb, Sb, Ni, and Co was also discussed by Hammond and Tabata (1997).

CHAPTER SEVEN

CONCLUSIONS AND RECOMMENDATIONS

7. Conclusions

This study characterised the different types of pyrite grains and examined their chemistry. Through petrographic investigation using RLM and SEM for determination of grain shapes and textures, the pyrite grains were classified and grouped as rounded massive, rounded porous or angular massive grains.

(1). Rounded Pyrite Grains – the rounded pyrite grains demonstrate fragmentation and abrasion of source rocks which could have occurred during erosion and transportation of sediments. The rounded pyrite grains were subdivided into rounded porous and rounded massive grains.

(a). Rounded Porous Pyrite – the round porous pyrite grains consist of round corners, erosion surfaces, laminations, and fractures, and demonstrate spongy textures. The rounded porous pyrite grains contain inclusions mainly of arsenopyrite, chalcopyrite, and grains of gold. Compositional zonations were observed on rounded porous grains and accompanied by overgrowths of massive grains.

(b). Rounded Massive Pyrite – the rounded massive pyrite grains consist of round corners, minor fractures, and demonstrate massive textures. The rounded massive pyrite grains contain chalcopyrite, galena, pyrrhotite, sphalerite, rounded zircon, and gold grains.

The appearance of detrital rounded grains of zircon in the rounded pyrite grains serve as supporting evidence for detrital sources for the rounded pyrite grains, whereas the relative absence of the zircon grains in the angular massive pyrite grains is an indication of the hydrothermal origin. Multiple processes were responsible for the formation of the rounded massive pyrite grains of the VCR, also supported by the observed overgrowths of massive textures on porous grains.

(2). Angular Pyrite Grains – The angular pyrite grains are euhedral and demonstrate sharp corners mainly with massive textures. These grains contain inclusions of pyrrhotite, sphalerite, chalcopyrite, and grains of gold.

Petrographic investigations showed that the rounded pyrite grains have different shapes, diagenetic structures, textures, types of inclusions, accompanied with overgrowths as opposed to the angular pyrite grains. The findings of this study complement the results of the work carried out by Barton and Hallbauer (1996); Hofmann et al. (2009) which suggested detrital origin for the rounded pyrite grains and angular pyrite grains resulting from hydrothermal processes.

By using EDS, EMPA, and LA-ICP-MS the chemistry of the major, minor and trace elements were investigated and it was observed that the rounded pyrite grains are generally containing high concentrations Ni and Co as opposed to angular pyrite grains. The Ni/Co is low in the angular pyrite grains, whereas the Ni/Co is high for the rounded grains of pyrite. The Ni/Co ratio is about 5% larger for rounded pyrite grains than the Ni/Co ratio for angular pyrite counter parts. The high Ni/Co ratio observed in rounded pyrite grains may be related to low-temperature sedimentary rather than hydrothermal processes, whereas the low Ni/Co ratio in angular pyrite grains may indicates hydrothermal source. The Ni and Co concentrations of the pyrite varieties suggest variations of these elements in the environment, fluids, and source rock from which the pyrite grains have precipitated. Neumann, (1950) studied pseudomorphs of pyrrhotine after pyrite in Ballachulish slates and found that the ratio of Ni/Co is determined by the mobility of Co which is in turn dependent on pressure and temperature conditions.

The compositional zonation patterns in the rounded porous pyrite suggest multiple stages of growth processes resulting in As-rich most porous parts of the grain and enclosed by nearly pure pyrite, whereas the presence of the rounded zircon grains in rounded massive pyrite grains might suggest that the pyrite grains formed later after the deposition of the wits sediments. The differences can be interpreted as a result of different genetic history, origin from different sources. Thus the different pyrite grains formed under different chemical and atmospheric conditions, and by different depositional mechanisms.

7.1. Strengths and Limitations

There is no single analytical technique that can provide all necessary details about the different sorts of pyrite that were investigated during this study. Therefore a combination of different analytical methods was applied to understand the problem. In theory, there are factors related to both instrument, and preparation of the sections which potentially affect the quality of the results. These factors include accuracy of the PIXE, and LA-ICP-MS machines and consistency in the measurements of the elements.

7.2. Recommendations

The hypothesis that the rounded and angular pyrite grains have different genetic history was investigated using the combination of RLM, SEM, EDX, PIXE, EMPA, and LA-ICP-MS techniques as discussed in section 3. The interpretations that the rounded pyrite grains are detrital in origin and angular massive pyrite grains are hydrothermally formed are supported by the determinations of the shape and texture (Figure 4.1), chemical zonations, overgrowths, and inclusions (section 4). These features are substantiated by the differences expressed by the chemistry of the major, minor and trace elements, described in section 5. Therefore, different depositional processes were responsible for formation of the rounded and angular pyrite grains of the VCR.

Future systematic investigations do not only need to focus on different types of pyrite grains from the VCR, but must also include other reefs in the Wits basin. It is also important to compare the pyrite grains from the Wits basin to other places such as Barberton Greenstone Belt, which is proposed to be the parent source of the detrital rounded pyrite. Equally pyrite grains from other possible sources surrounding the Wits basin should be investigated as sedimentation is known to have been responsible for the transportation of pyrite grains from other sources.

CHAPTER EIGHT

8. References

1. Alexandre, P., Marco A.G.A., Antonv J., and Roger, L.G., (2006). ^{40}Ar/^{39}Ar age constraints on low-grade metamorphism and cleavage development in the Transvaal Supergroup (central Kaapvaal Craton, South Africa): implications for the tectonic setting of the Bushveld Igneous Complex. South African Journal of Geology, Vol. 109. pp. 393-410.

2. Altermann, W., and Nelson D.R., (1998). Sedimentation rates, basin analysis and regional correlations of three Neoarchaean and Palaeoproterozoic sub basins of the Kaapvaal Craton inferred from precise U–Pb zircon ages from volcaniclastic sediments, Sediment. Geol. 120. pp. 225–256.

3. Altermann, W., & Siegfried, H.P., (1997). Sedimentology and facies development of an Archean shelf: carbonate platform transition in the Kaapvaal Craton, as deduced from a deep borehole at Kathu, South Africa. J. Afr. Earth Sci.24, pp. 391–410.

4. Anabar. A.D., Duan, Y., Lyons, T.W., Arnold, G.L., Kendall, B., Creaser, R.A. Kaufman, A.J. Gordon, G.W. Scott, C. Garvin, J. Buick. R., (2007). A Whiff of Oxygen before the Great Oxidation Event. Science. Vol. 317. pp. 1903-1906.

5. Armstrong, R.A., Compston, W., Retief, E.A., Williams, I.S., and Welke, H.J., (1991). Zircon ion microprobe studies bearing on the age and evolution of the Witwatersrand Triad. Precambrian Res. Vol. 53; pp. 243-266.

6. Barnicoat, A.C., Henderson, I.H.C., Yardley, B.W.D. & Fox, N.P.C., (1998). Detrital origin of hydrothermal Witwatersrand gold- a review (Frimmel, 1997). Discussion. Terra Nova, 10:347-348.

7. Barnicoat, A.C., Henderson, I.H.C., Knipe, R.J., Yardley, B.W.D., Napier, R.W., Fox, N.P.C., Kenyon, A.K., Muntingh, D.J., Strydom, D., Winkler, K.S., Lawrence, S.R. & Cornford, C., (1997). Hydrothermal gold mineralization in the Witwatersrand basin. Nature, 386:820-824.

8. Barton, E.S. and Hallbauer D.K., (1996). Trace-element and U-Pb isotope compositions of pyrite types in the Proterozoic Black Reef, Transvaal Sequence, South Africa: Implications on genesis and age. Chemical Geology 133, pp. 173-199.

9. Bekker, A., Holmden, C., Beukes, N.J., Kenig, F., Eglinton, B., Patterson, W.P., (2008). Fractionation between inorganic and organic carbon during the Lomagundi (2.22-2.1 Ga) carbon isotope excursion. Earth and Planetary Science. Letters Vol. 271, pp. 278-291.

10. Berlenbach, J.W., (1995). Aspects of bedding-parallel faulting associated with the Ventersdorp Contact Reef on the Kloof Gold Mine. S. Afr. J. Geol., pp. 335–348.

11. Beukes, N.J., & Pather, A., (1998). Regional lithostratigraphic subdivision of the West Rand. SACS Proposals for Witwatersrand Stratigraphy, GSSA, pp. 1-6.

12. Beukes, J.N., (1996). Sole marks and combined-flow storm event beds in the Brixton formation of the siliclastic Archaean Witwatersrand Supergroup, South Africa. Journal of Sedimentary Research, 66:567-576.

13. Beukes, N.J., & Cairncross, B., (1991). A lithostratigraphic-sedimentological reference profile for the late Archaean Mozaan group, Pongola Sequence: application to sequence stratigraphy and correlation with the Witwatersrand Supergroup. South African Journal of Geology, 94(1), pp. 44-69.

14. Beukes, N.J., (1990). Stratigraphy and basin analysis of the Hospital Hill Subgroup of the West Rand Group, Witwatersrand Supergroup. Department of Geology, Rand Afrikaans University, pp. 813-816.

15. Burke, K., Kidd, W.S.F., and Tusky, T.M., (1986). Archaean foreland basin tectonics in the Witwatersrand, South Africa. Tectonics, Vol. 5, no. 3, pp.439-456.

16. Canfield, D.E., (2005). The early history of atmospheric oxygen: Annu. Rev. Earth Planet. Sci. 33:1-36.

17. Chapman[1], J.B., Peter[1], J.M., Layton-Matthews[2], D., and Gemmell[3], J.B., (2009). Geochemistry of Archean sulfidic black shale horizons: combining data at multiple scales for improved targeting in VMS exploration. Proceedings of the 24th IAGS, Fredericton.

18. Chouinard, A., Paquette, J., and Anthony, E., Williams-Jones, (2005). Crystallographic controls on trace-element incorporation in auriferous pyrite from the pascua epithermal high-sulfidation deposit, Chile-Argentina. The Canadian Mineralogist. Vol. 43, pp. 951-963.

19. Czaja, A.D., Johnson, C.M., Yamaguchi, K.E., Beard, B.L., (2012). Comment on "Abiotic Pyrite Formation Produces a Large Fe Isotope Fractionation". Science Vol. 335. pp. 138c.

20. Dankert, B.T., and Hein, K.A.A., (2010). Evaluating the structural character and tectonic history of the Witwatersrand Basin. Precambrian Research 177, pp. 1–22.

21. Dewaele, S., Muchez, P., and Hertogen, J., (2007). Production of a matrix-matched standard for quantitative analysis of iron sulphides by laser ablation inductively coupled plasma-mass spectrometry by welding: a pilot study. Geologica Belgica Vol.10/1-2: pp.109-119.

22. Dimroth, E., Saager, R., and Feather, C. E., (1979). Significance of Diagenesis for the Origin of Witwatersrand-Type Uraniferous Conglomerates. Philosophical Transactions of the Royal Society of London. Series A, Mathematical and Physical Sciences, Vol. 291, No. 1381, Theoretical and Practical Aspects of Uranium Geology, pp. 277-287.

23. Dobrin, M.B., (1960). Introduction to geophysical prospecting. Second edition, McGraw-Hill Book Company, United States of America, pp. 417-419.

24. Dran, J.C., Calligaro, T., Salomon, J., (2000). Particle-induced X-ray emission, in: E. Cilibert, G. Spoto (Eds.), Modern Analytical Methods in Art and Archaeology, Chemical Analysis, 155, Wiley- Interscience, pp. 135-166.

25. Duane, M.J., Pigozzi, G., and Harris, C., (1997). Geochemistry of some deep gold mine waters from the western portion of the Witwatersrand Basin, South Africa. Journal of African Earth Sciences, Vol. 24, No. 1/2, pp. 105-123.

26. Els, B.G., (1998). Unconformity of the Central Rand Group SACS Proposals for Witwatersrand Stratigraphy, GSSA (1998) p 1-3

27. Els, B.G., (1998). The question of alluvial fans in the auriferous Archaean and Proterozoic succession of South Africa. South African Journal of Geology, Vol.101, pp. 17-25.

28. Els, B.G. and Mayer, J.J., (1998). Coarse clastic tidal and fluvial sedimentation during a large late Archaean sea-level rise; the Turffontein Subgroup in the Vredefort Structure, South Africa. In: Alexander, C.R., Davis, R.A. and Henry, V.J., (eds.) Tidalites; Processes and Products. Spec. Publ. Soc. Sed. Geol. 61, pp. 155-165.

29. England, G., Rasmussen, B., Krapez, B., and Groves, D.I., (2002). Palaeoenvironmental significance of rounded pyrite in siliciclastic sequences of the Late Archaean Witwatersrand Basin: oxygen-deficient atmosphere or hydrothermal alteration? Sedimentology 49, pp.1133-1156.

30. Eriksson, P.G., Banerjee, B., Nelson, D.R., Rigby, M.J., Catuneanu, O., Sarkar, S., Roberts, R.J., Ruban, D., Mtimkulu, M.N., and Raju, S. P.V., (2009). A Kaapvaal craton debate: Nucleus of an early small supercontinent or affected by an enhanced accretion event? Gondwana Research 15, pp. 354-372.

31. Eriksson P.G., Martins-Neto N.A., Nelson D.R., Aspler L.B., Chiarenzelli J.R., Catuneanu O., Sarkar S., Altermann W. and Rautenbach C.J. de W., (2001). An introduction to Precambrian basins: their characteristics and genesis.

32. Falconer, D.M., Craw, D., Youngson, J.H., and Faure, K., (2006). Gold and sulphide minerals in Tertiary quartz pebble conglomerate gold placers, Southland, New Zealand. Ore Geology Reviews 28, pp. 525-545.

33. Farquhar, J., Savarino, J., Airieau, S., Thiemens, M.H., (2001). Observation of wavelength sensitive mass-dependent sulfur isotopes effects during SO2 photolysis: implication for the early Earth atmosphere. J. Geophysical. Reserve. 106:29-39.

34. Feather, C., and Koen, G.M., (1975). The mineralogy of the Witwatersrand reefs: Mineral Science and Engineering. Vol.7: pp. 189-224.

35. Fleet, M.E., (1998). Detrital pyrite in Witwatersrand gold reefs: X-ray diffraction evidence and implications for atmospheric evolution. Terra Nova, Vol. 10, pp. 302-306.

36. Fleet, M.E., and Mumin, A.H., (1997). Gold-bearing arsenian pyrite and marcasite and arsenopyrite from Carlin Trend gold deposits and laboratory synthesis. American Mineralogist, Vol. 82, pp 182-193.

37. Foya, S.N., Reimold, W.U., Przybylowicz, W.J., and Gibson R.L., (1999). PIXE microanalysis of gold-pyrite associations from the Kimberley Reefs, Witwatersrand basin, South Africa, Nuclear Instruments and Methods in Physics Research B 158, pp. 588-592.

38. Franklyn, C.B., Ueckermann, H., and Merkle, R.K.W., (2001). Accidental surface contamination – The effect on trace element analysis. Nuclear Instruments and Methods in Physics Research B 181, pp. 145-149.

39. Franklyn, C.B., Merkle, R.K.W., (1999). Milli-PIXE of coexisting cooperite and braggite ± a comparison with electron probe microanalysis. Nuclear Instruments and Methods in Physics Research B 158, pp. 550-555.

40. Frey, M., Saager, R., Buck, S.G., (1987). Heavy mineral distribution and geochemistry related to sedimentary facies variation within the uraniferous intermediate reefs placers, Witwatersrand Supergroup, South Africa. International atomic energy agency, Vienna, pp. 313-334.

41. Frimmel, H.E., (2008). Earth's continental crustal gold endowment. Earth and Planetary Science Letters 267, pp. 45-55.

42. Frimmel, H.E., (2005), The Formation and preservation of the Witwatersrand Goldfields, the World's largest gold province. Economic Geology 100th Anniversary: pp. 769-797.

43. Frimmel, H.E., (2002). Genesis of the World's Largest Gold Deposits. New Series, Vol. 297, No. 5588, pp. 1815-1817.

44. Frimmel, H.E., and Minter, W.E.L., (2002). Recent Developments Concerning the Geological History and Genesis of the Witwatersrand Gold Deposits, South Africa. Society of Economic Geologists, Special Publication. Vol. 9, pp. 17-45.

45. Frimmel. H.E., Hallbauer, D.K., and Gartz, V.H., (1999). Gold Mobilising Fluid in the Witwatersrand Basin: Composition and Possible Sources. Mineralogy and Petrology, Vol. 66, pp. 55-81.

46. Frimmel, H.E., and Zartman, R.E., (1999). Rn-generated 206Pb in hydrothermal sulphide minerals and bitumen from the Ventersdorp Contact Reef, South Africa. Mineral and Petrology, Vol. 66, pp. 171-191.

47. Frimmel. H.E., (1997). Detrital origin of hydrothermal Witwatersrand gold - a review. Terra Nova, Vol. 9, pp. 192-197.

48. Frimmel, H.E., and Gartz, V.H., (1997). Witwatersrand gold particle chemistry matches model of metamorphosed, hydrothermally altered placer deposits. Mineralium Deposita Vol. 32: pp. 523-530.

49. Gibson, R.L., and Jones, M.Q.W., (2002). Late Archaean to Palaeoproterozoic geotherms in the Kaapvaal Craton, South Africa; constraints on the thermal evolution of the Witwatersrand Basin. Basin Research. Vol. 14, pp. 169-181.

50. Gold Fields Limited, Republic of South Africa (2009). Annual report on operating and financial information by mine. F2009 financial highlights. Available on www.goldfields.co.za, Registration number: 1968/004880/06, pp. 1-235.

51. Gold Filed Limited, (2009). A summary of the internally sourced document entitled F2010 Kloof Competent Persons Report. Available online, accessed on 1/8/2011

52. Goldfarb, R.J., Groves, D.I., and Gardoll, S., (2001). Orogenic gold and geologic time: a global synthesis. Ore Geology Reviews 18, pp. 1-75.

53. Govil, I.M., (2001). Proton Induced X-ray Emission - A tool for non-destructive trace element analysis. Current Science, Vol. 80, No. 12. pp. 1542-1549.

54. Grové, D., and Harris, C., (2010). O- and H-Isotope Study of the Carbon Leader Reef at the Tau Tona and Savuka Mines (Western Deep Levels), South Africa: Implications for the Origin and Evolution of Witwatersrand Basin Fluids. South African Journal of Geology, 2010, Vol. 113.1. pp. 1-14.

55. Guerra, M.F., Calligaro, T., Radtke, M., Reiche, I., and Rie Scanning Electron Microscopeeier, H., (2005). Fingerprinting ancient gold by measuring Pt with spatially resolved high energy Sy-XRF Nuclear Instruments and Methods in Physics Research B 240, pp. 505-511

56. Guerra, M.F., (2004). Fingerprinting ancient gold with proton beams of different energies. Nuclear Instruments and Methods in Physics Research. B 226, pp.185-198.

57. Guerra, M.F., Calligaro, T., (2004). Gold traces to trace gold. Journal of Archaeological Science. Vol. 31, pp. 1199-1208.

58. Guerra, M.F., (1998). The analysis of archaeological metals. The place of XRF and PIXE in the determination of technology and provenance. X-Ray Spectrum. Vol. 27, pp.73-80.

59. Hall, R.C.B., (1994). Supporting evidence for the placement of the inter-reef lavas and associated sediments within the Venterspost Conglomerate Formation: Kloof gold mine. South African Journal of Geology 97 (3), 297–307.

60. Hallbauer, D.K., and Barton, E.S., (1994). Crustal evolution in the source region of the Witwatersrand sediments, South Africa - Evidence from quartz pebble and quartzite geochemistry. Extend. Abstr. V.M. Goldschmidt Conf., Edinburgh, Mineral. Mag., 58 A, pp. 364-365.

61. Hallbauer, D.K., (1991). Mineralogical and geochemical "fingerprinting" of hydrothermal pyrite - A possible exploration tool. Proc. Int. Congr. on Applied Mineralogy, ICAM 91, 1.

62. Hallbauer, D.K., (1991). Trace elements contents and isotope geochemistry of Witwatersrand carbonaceous matter. GSSA Western Transvaal Branch in association with the Witwatersrand Interest Group (W.I.N.G), pp. 103-106

63. Hallbauer, D.K., and Barton J.R., J.M., (1987). The fossil gold placers of the Witwatersrand: A review of their mineralogy, geochemistry and genesis Tectonics 5(3), pp. 68-79.

64. Hallbauer, D.K., and Barton, J.M., (1987). The fossil gold placers of the Witwatersrand. Review of Mineralogy, Geochemistry and Genesis. Gold Bull., 20 (3), pp. 68-79.

65. Hallbauer, D.K., (1986). The mineralogy and geochemistry of Witwatersrand pyrite, gold, uranium and carbonaceous matter. In: Anhaeusser, C.R. & Maske, S., (Eds). Mineral Deposits of Southern Africa, Geol. Soc. S. Afr., Johannesburg, 731-752.

66. Hallbauer, D.K. and Els, B.G., (1986). Geochemical identification of provenance-controlled gold distribution patterns in the Ventersdorp Contact Reef Placer of the Carletonville Gold Field. South African Inst of Mining & Metallurgy Symposium Series S8, 1:45-62.

67. Hallbauer, D.K., (1984). Archaean granitic sources for the detrital mineral assemblage in Witwatersrand conglomerates. Ext. Abstr. Geocongress '84, Potchefstroom, pp. 53-56.

68. Hallbauer, D.K., (1983). Geochemistry and fluid inclusions in detrital minerals as guides to their provenance and distribution. Special Publication - Geological Society of South Africa, Vol. 7, pp. 39-57.

69. Hallbauer, D.K., and Von Gehlen, K., (1983). The Witwatersrand pyrite and metamorphism. Mineralogy. Mag., 47:473-479.

70. Hallbauer, D.K., and Kable, E.J.D., (1982). Fluid inclusions and trace element content of quartz and pyrite pebbles from Witwatersrand conglomerates: their significance with respect to the genesis of primary deposits. In: Amstutz et al., (eds) Ore Genesis - the state of the art. Springer-Verlag, Berlin, pp. 742-752.

71. Hallbauer, D.K., and Kable, E.J.D., (1979). Geochemical and fluid inclusion studies of quartz pebbles in the Witwatersrand conglomerates and their relationship to gold mineralization. Geocongress '79, Part 1, pp. 176-186.

72. Hallbauer, D.K., and Utter, T., (1977). Geochemical and morphological characteristics of gold particles from recent river deposits and the fossil placers of the Witwatersrand. Mineral. Deposita, Vol. 12, pp. 293-306.

73. Hallbauer, D.K., and Joughin, N.C., (1973). The size distribution and morphology of gold particles in Witwatersrand reefs and their crushed products. J. S. Afr. Inst. Min. Metall., Vol. 73, pp. 223–233.

74. Hallbauer, D.K., and Joughin, N.C., (1972). An investigation into the distribution, size and shape of gold particles in some Witwatersrand reefs and their effects on sampling procedures. Johannesburg. Chamb. Mines. S. Afr., Res. Rep. no. 43/72.

75. Hammond, N.Q., and Tabata, H., (1997). The characteristics of ore minerals associated with gold at the Prestea mine, Ghana. Mineralogical Magazine, Vol. 61, pp.879-894.

76. Hazen, R.M., Bekker, A., Bish, B.L., Bleeker, W., Downs, R.T., Farquhar, J., Ferry, J.M., Grew, E.S., Knoll, A.H., Papineau, D., Ralph, J.P., Sverjensky, D.A., Valley J.W., (2011). Needs and opportunities in mineral evolution research. American Mineralogist, Volume 96, pp. 953-963.

77. Hem S.R., and Makovicky E., (2004). The System Fe–Co–Ni–As–S. I. Phase Relations in the (Fe, Co, Ni) As0.5S1.5 Section at 650° and 500°C. The Canadian Mineralogist, Vol. 42, pp. 43-62.

78. Hoefs, J., Nielsen, H., and Schidlowski, M., (1968). Sulphur Isotope Abundance in Pyrite from the Witwatersrand Conglomerates. Economic Geology, Vol.63, no.8, pp. 975-977.

79. Hoefs, J., and Schidlowski, M., (1967). Carbon Isotope Composition of Carbonaceous Matter from the Precambrian of the Witwatersrand System. Science, New Series, Vol. 155, No. 3766, pp. 1096-1097.

80. Hofmann, A., Bekker, A., Rouxel, O., Rumble, D., and Master, S., (2009). Multiple sulphur isotope analysis of detrital pyrite as a tool for provenance analysis in Archaean sedimentary rocks. A new tool for provenance analysis. Earth and Planetary Sciences Letters 286, pp.436-445.

81. Hofmann, A., Bekker, A., Rumble, D., and Master, S., (2008). Multiple sulphur isotope analysis of detrital pyrite as a tool for provenance analysis in Archaean sedimentary rocks. Geophysical Research Abstracts, Vol. 10, EGU2008-A-04957.

82. Jolley, S.J., Freeman, S.R., Barnicoat, A.C., Phillips, G.M., Knipe, R.J., Pather, A., Fox, N.P.C., Strydoom D., Birch, M.T.G., Henderson, I.H.C., and Rowland, T.W., (2004). Structural controls on Witwatersrand gold mineralisation. Journal of Structural Geology Vol. 26, pp.1067-1086.

83. Jolley, S.J., Henderson, H.C., Barnicoat, A.C., Fox, N.P.C., (1999). Thrust-fracture network and hydrothermal gold mineralization: Witwatersrand basin, South Africa. In: McCaffrey, K.J.W.,

84. Karpeta, W.P., and Els, B.G., (1999). The auriferous Late Archaean CRG of South Africa: sea-level control of sedimentation? Precambrian Research 97, pp. 191-214.

85. Karpeta, W.P., (1993). Sedimentology and gravel bar morphology in an Archaean braided river sequence: the Witpan Conglomerate Member (Witwatersrand Supergroup) in the Welkom Goldfield, South Africa Geological Society Special Publication No.75, pp. 369-388

86. Karpeta, W.P., and Els, B.G., (1991). Hydrocarbon occurrence in the Vaal Reef and 'A' Reef Placers: Sedimentological controls and economic significance GSSA Western Transvaal Branch in association with the Witwatersrand Interest Group (W.I.N.G), pp. 57-60

87. Kasting, J.F., and Howard, M.T., (2006). Atmospheric composition and climate on the early Earth. Phil. Trans. R. Soc. Vol. 361, pp.1733-1742.

88. Killick, A.M., and Scheepers, R., (2005).Controls to hydrothermal gold mineralisation in the Witwatersberg Goldfield; situated in the floor to the south of the Bushveld Complex, South Africa. Journal of African Earth Sciences, Vol. 41, pp. 235-247.

89. Kingsley, C.S., (1998). The stratigraphic subdivision of the Central Rand Group Sacs Proposals for Witwatersrand Stratigraphy, GSSA, pp. 1-4.

90. Kingsley, C.S., (1992). Placers, sequences and sedimentary tectonics of the Welkom Goldfield Department of Geology Economic Research Unit, University of the Witwatersrand, Johannesburg, Vol. II, pp. 189-193.

91. Kingsley, C.S., (1986). Stratigraphic framework and model of sedimentation of the Eldorado sequence in the Welkom goldfields, Abstracts, GeoCongress '86, pp. 461- 464.

92. Kingsley, C.S., (1983). An alluvial placer to prodelta sequence in the Proterozoic Welkom Goldfield, Witwatersrand, South Africa, Sedimentology of gravels and conglomerates Canadian Society Petroleum Geologists Memoir 10, pp. 321-330.

93. Kirk, J., Ruiz, J., Chesley, J., and Titley, S., (2003). The origin of gold in South Africa: ancient rivers filled with gold, a spectacular upwelling of magmas and a colossal meteor impact combined to make the Witwatersrand basin a very special place. American Scientist 91, i6, pp. 534 (8).

94. Kirk, J., Ruiz, J., Chesley, J., Walshe, J., and England, G., (2002). A major Archaean, gold and crust-forming event in the Kaapvaal Craton, South Africa. Science, 297:1856-1858.

95. Kirk, J., Ruiz, J., Chesley, J., Walshe, J., England, G., (2002). A Major Archaean, Gold and Crust Forming Event in the Kaapvaal Craton, South Africa. Science, New Series, Vol. 297, No. 5588, pp. 1856-1858.

96. Kirk, J. Ruiz, J., Chesley, J., Titley, S., and Walshe, J., (2001). A detrital model for the origin of gold and sulfides in the Witwatersrand basin based on Re-Os isotopes. Geochimicaet Cosmochimica Acta, Vol. 65, No. 13, pp. 2149-2159.

97. Kirk, J., Ruiz, J., Chesley, J., Titley, S., and Walshe, J., (2001). A detrital model for the origin of gold and sulfides in the Witwatersrand basin based on Re-Os isotopes. Geochimicaet Cosmochimica Acta, 65:2149-2159. RE

98. Koeberl, C., Renold, W.U., and Boer, R.H., (1993). Geochemistry and mineralogy of Early Archaean spherule beds, Barberton Mountain Lands, South Africa: Evidence for origin by impact doubtful. Earth and Planetary Science Letters, Vol.119, pp. 441-452.

99. Koglin, N., Frimmel, H.E., Minter, W.E.L., and Brätz. H., (2010). Trace-element characteristics of different pyrite types in Mesoarchaean to Palaeoproterozoic placer deposits. Miner Deposita Vol. 45, pp.259-280

100. Kohn, M.J., Riciputi, L.R., Stakes, D., and orange, D.L., (1998). Sulfur isotope variability in biogenic pyrite: Reflections of heterogeneous bacterial colonization? American Mineralogist, Vol. 83, pp. 1454–1468.

101. Kositcin, N. andnKrapež, B., (2004). Relationship between detrital zircon age-spectra and the tectonic evolution of the Late Archaean Witwatersrand Basin, South Africa. Precambrian Research, Vol. 129, pp.141-168

102. Kuhn, B.K., Karin, B., Lou, Y., and Gunther, D., (2010). Fundamental studies of the ablation behaviour of Pb/U in NIST 610 and zircon 91500 using laser ablation inductively coupled plasma mass spectrometry with respect to geochronology. Journal of Analytical Atomic Spectrometry, Vol. 25. pp. 21-27.

103. Landais, P., (1996). Organic geochemistry of sedimentary uranium ore deposits. Ore geology reviews 11, pp.33-51.

104. Landais, P., Dubessy, J., Robb, L.J., and Nouel, C., (1990). Preliminary chemical analyses and Raman Spectroscopy on selected samples of Witwatersrand kerogen. EGRU, Circular 222.

105. Landais, P., Dubessy, J., Poty, B., and Robb, L.J., (1989). Three examples illustrating the analysis of organic matter associated with uranium ores. Organ. Geochem., 5/6:601-608.

106. Lengke, M.F., and Southam, G., (2007). The Deposition of Elemental Gold from Gold (I)-Thiosulfate Complexes Mediated by Sulfate-Reducing Bacterial Conditions. Economic Geology, Vol. 102, pp. 109-126.

107. Lengke, M.F., and Southam, G., (2005). The effect of thiosulfate-oxidizing bacteria on the stability of the gold-thiosulfate complex. Geochimicaet Cosmochimica Acta, Vol. 69, No. 15, pp. 3759-3772.

108. Longerich, H.P., Fryer, B.J., and Strong D.F., (1987). Determination of lead isotope ratios by laser ablation inductively coupled plasma mass spectrometry (ICP-MS). Spectrochimica Acta, Vol. 42B, No 1/2, pp. 38-48.

109. Lowers, H.A., Breit, G.N., Foster, A.L., Whitney, J., Yount, J., Uddin, Md.N., Muneem, Ad. D., (2007). Arsenic incorporation into authigenic pyrite, Bengal Basin sediment, Bangladesh, Geochimicaet Cosmochimica, Acta 71, pp. 2699–2717.

110. Lyons, T.W. Kah, L.C. and Gellatly. A.M., (2004). The Precambrian sulphur isotope record of evolving atmospheric oxygen. The Precambrian Earth: Tempos and Events. Developments in Precambrian Geology. Vol. 12. pp. 421-440.

111. Matis, K.A., Kydros, K.A., and Gallios, G.P., (1992). Processing a bulk pyrite concentrate by floatation reactants. Minerals Engineering, Vol. 5, Nos. 3-5, pp. 331-342.

112. Merkle, R.K.W., Franklyn, C.B., Przybylowicz, W., Verryn, S.M.C., (2002). Intercomparison of electron probe micro-analyses and particle induced X-ray emission analyses of Pt–Pd–Ni–S matrices. Nuclear Instruments and Methods in Physics Research B 190, pp. 821-825.

113. Meyer, F.M., Mö11er, P and De Bruiyn, D., Przybylowicz, W.J. & Prozesky, V.M., (1994). The gold-pyrite association in Witwatersrand reefs: evidence for electrochemical precipitation of gold. Explor. Min. Geol., 3: 207-218.

114. Meyer, F.M., Möller, P., De Bruiyn, D., Przybylowicz, W.J., and Prozesky, V.M., (1994). The gold-pyrite association in Witwatersrand reefs: evidence for electrochemical precipitation of gold. Explor. Min. Geol., 3: 207-218.

115. Meyer, F.M., Wallmach, T., Henkel, J., and Schweitzer, J.K., (1992). Chlorite compositions and fluid conditions in some Witwatersrand reefs. Geocongress 92, Geol. Soc. S. Afr.: 391-394.

116. Meyer, F.M., (1992). A review of the ore mineralogy and mineral geochemistry of the Witwatersrand reefs with emphasis on the gold-pyrite association. Department of Geology Economic Research Unit, University of the Witwatersrand, Johannesburg, Vol. II pp. 155-167.

117. Meyer, F.M., Drennan, G.R., Robb, L.J., Cathelineau, M., Dubessy, J., and Landais, P., (1991). Conditions of gold mineralization in Witwatersrand reefs. In: Pagel & Leroy (Eds), Source, Transport and Deposition of Metals, pp. 681-684.

118. Meyer, F.M., Oberthür, T., Robb, L.J., Saager, R., and Stupp, H.D., (1990). Cobalt, nickel and gold in pyrite from primary gold deposits and Witwatersrand reefs. S. Afr. J. Geol., 93: pp. 70-82.

119. Meyer, F.M., Saager, R., Koppel, V., (1987). Uranium distribution and redistribution in a suite of fresh and weathered pre-Witwatersrand and Witwatersrand conglomerates from South Africa. International atomic energy agency, Vienna, pp. 255-273.

120. Meyer, M., Robb, L.J., and Anhaeusser, C.R., (1986). Uranium and thorium contents of Archaean granitoids from the Barberton Mountain Land, South Africa. Precambrian Res., 33: 303-321.

121. Meyers, B., (1981). Genesis of Uranium-Gold Pyritic Conglomerates 1944-1945. Geological Survey Professional Paper AA1-AA26

122. Miller, D., Desai, N. and Lee-Thorp, J., (2000). Indigenous Gold Mining in Southern Africa: African Naissance: South African Archaeological Society. Goodwin Series, Vol. 8, pp. 91-99.

123. Minter, W.E.L., (1999). Irrefutable detrital origin of Witwatersrand gold and evidence of Aeolian signatures. Econ. Geol. 94, 665-670.

124. Minter, W.E.L., Goedhart, M., Knight, J. & Frimmel, H.E., (1993). Morphology of Witwatersrand Gold Grains from the Basal Reef: Evidence for Their Detrital Origin. Economic Geology, 88:237-248.

125. Minter, W.E.L., Feather, C.E., and Glatthaar, C.W., (1988). Sedimentological and mineralogical aspects of the newly discovered Witwatersrand placer deposit that reflect Proterozoic weathering, Welkom gold field, South Africa. Economic Geology, 83:481-491.

126. Minter, W.E.L., Buck, S.G., (1985). Placer formation by fluvial degradation of an alluvial fan sequence: the Proterozoic carbon leader placer, Witwatersrand Supergroup, South Africa Journal of the Geological Society London 142, 757-764.

127. Mossman, D.J., Minter, W.E.L., Dutkiewicz, A., Hallbauer, D.K., George, S.C., Hennigh, Q., Reimer, T.O., and Horscroft, F.D., (2008). The indigenous origin of Witwatersrand "carbon", Precambrian Research 164. pp. 173-186.

128. Mossman, D.J., and Dyer, B.D., (1985). The geochemistry of Witwatersrand-type gold deposits and the possible influence of ancient prokaryotic communities on gold distribution and precipitation, Precambrian Research, 30: 303-319

129. Mossman, D.J., and Harron, G. A., (1983). Origin and distribution of gold in Huronian Supergroup, Canada—the case for Witwatersrand paleoplacers. Precambrian Res, 20, 543–84.

130. Neuerberg, G.J., U.S. Geological Survey, Denver, and Colo, (1961). A method of mineral separation using hydrofluoric acid. The American Mineralogist, Vol. 46. pp 1498-1501.

131. Neumann, H., Philos. (0slo), (1950). Pseudomorphs of pyrrhotine after pyrite in Ballachulish slates. Department of Geology, University of Leeds. June 8, 1950. pp. 243-237.

132. Noffke, N., Beukes, N. Gutzmer, J., and Hazen, R., (2006). Spatial and Electron Microprobe oral distribution of microbially induced sedimentary structures: A case study from siliciclastic storm deposits of the 2.9 Ga Witwatersrand Supergroup, South Africa Precambrian Research 146. pp. 35-44.

133. Ohmoto, H., Watanabe, Y., Ikemi, H., Poulson, S.R., and Taylor, B.E., (2006). Sulphur isotope evidence for an oxic Archaean atmosphere. Nature, 442, pp.908-911.

134. Ohmoto, H., Watanabe, Y., and Kumazawa, K., (2004). Archaean atmosphere and climate. Nature 429, pp. 395-399.

135. Ono, S., Beukes, N.J., Rumble, D., 2009. Origin of two distinct multiple-sulfur isotope compositions of pyrite in the 2.5 Ga Klein Naute Formation, Griqualand West Basin, South Africa. Precambrian Research 169, pp. 48–57.

136. Otake, T., Watanabe, Y., Altermann, W., Ohmoto, H., (2004). "Detrital" pyrites in the Archaean Witwatersrand basin (South Africa) are not detrital! Astrobiology, S1, pp. 38-39.

137. Outridge, P.M., Doherty, W., and Gregoire, D.C., (1998). Determination of trace elemental signatures in placer gold by laser ablation–inductively coupled plasma–mass spectrometry as a potential aid for gold exploration. Journal of Geochemical Exploration, Vol. 60. pp. 229-240.

138. Parnel, J., (1999). Petrographic evidence for Electron Microprobe lacement of carbon into Witwatersrand conglomerates under high fluid pressure. Journal of sedimentary research, Vol. 69, no. 1, pp. 164-170.

139. Petterson, D.R., (1951). The Witwatersrand a Unique Gold Mining Community. Economic Geography, Vol. 27, No. 3, pp. 209-221.

140. Phillips G.N., and Law J.D.M., (2000). Witwatersrand gold fields: geology, genesis and exploration. Soc. Econ. Geol. Rev. Ser., 13, 439-500

141. Phillips, G.N., and Dong, G., (1994). Chlorite-rich nodules in the Beatrix Reef, Witwatersrand goldfields. Econ. Geol., 89: 909-918.

142. Phillips, G.N., Law, J.D.M., and Myers, R.E., (1990). The role of fluids in the evolution of the Witwatersrand Basin. South African Journal of Geology, 93:54-69.

143. Phillips, G.N., and Myers, R.E., (1989). Witwatersrand gold fields: Part II: an origin for Witwatersrand gold during metamorphism and associated alteration. In: Keays, R.R., Ramsay, W.R.H. and Groves, D.I. (Eds.), the Geology of Gold Deposits: The Perspective in 1988. Econ. Geol. Monogr., 6, 598-608.

144. Phillips, G.N., Klemd, R., and Robertson, N.S., (1988). Summary of some fluid inclusion data from the Witwatersrand Basin and surrounding granitoids. Memoirs of the Geological Society of India, 11. 59-65.

145. Phillips, G.N., (1987). Metamorphism of the Witwatersrand goldfields: conditions during peak metamorphism. J. Metamor. Geol., 5:307-322.

146. Phillips, G.N., (1987). Anomalous gold in Witwatersrand shales. Economic Geology 82, 2179-2186.

147. Phillips, G.N., Myers, R.E. & Palmer, J.A., (1987). Problems with the placer model for Witwatersrand gold. Geology, 15: 1027-1030.

148. Phillips, G.N., Myers, R.E., Law, J.D.M., Bailey, A.C., Cadle, A.B., Beneke, S.D., and Giusti, L., (n.d). The Witwatersrand goldfields: Part I. Post depositional history, synsedimentary processes, and gold distribution Geology Department, University of the Witwatersrand, pp. 585-597.

149. Phillips, G.N., Myers, R.E., and Palmer, J.A., (n.d). The Witwatersrand goldfields: Part II. An origin for Witwatersrand gold during metamorphism and associated alteration Geology Department, University of the Witwatersrand, pp. 598-608.

150. Poujol, M., Robb, L.J., Anhaeusser, C.R., Gericke, B., (2003). A review of the geochronological constraints on the evolution of the Kaapvaal Craton, South Africa, Precambrian Research, 127, 181-213.

151. Poujol, M., and Anhaeusser, C.R., (2001). The Johannesburg Dome, South Africa: new single zircon U-Pb isotopic evidence for early Archaean granite-greenstone development within the central Kaapvaal Craton. Precambrian Research, 108:139-157

152. Poujol, M., Robb, L.J., and Respaut, J.P., (1999). U–Pb and Pb–Pb isotopic studies relating to the origin of gold mineralisation in the Evander Goldfield, Witwatersrand Basin, South Africa. Precambrian Research 95, pp.167-85.

153. Poujol, M., Robb, L.J., and Respaut, J.P., (1998). U-Pb and Pb-Pb isotopic studies relating to the origin of gold mineralization in the Evander goldfield, Witwatersrand Basin, South Africa. Univ of the Witwatersrand, Econ Geol Res Unit, Inform Circ, 320.

154. Prior, D.J., Boyle, A.P., Brenker, F., Cheadle, M.C., Day, A., Lopez, G., Peruzzo, L., Potts, G.J., Reddy, S., Spiess, R., Timms N.E., Trimby, P., Wheeler, J., and Zetterstrom, L., (1999). The application of the electron backscatter diffraction and orientation contrast imaging in the SEM to textural problems in rocks. American Mineralogist, Vol. 84, pp. 1741-1759.

155. Przybylowicz, W.J., Prozesky, V.M., and Meyer, F.M., (1995). True elemental imaging of pyrites from Witwatersrand reefs. Nuclear Instruments and Methods in Physics Research B 104, pp. 450-455.

156. Ramdohr, P., (1958). New observations on the ores of the Witwatersrand in South Africa and their genetic significance. Transactions of the Geological Society of South Africa, Annexure. 61:1-50.

157. Ramdohr, P., (1955). NeueBeobachtungen an Erzen des Witwatersrandes in Südafrika und ihregenetische Bedeutung. Abh. Dtsch.Akad. Wiss. Berlin, Kl. Math. Allg. Naturw, 5:43.

158. Rasmussen, B.R., and Buick, R., (1999). Redox state of the Archaean atmosphere: Evidence from detrital heavy minerals in ca. 3250 -2750 Ma sandstones from the Pilbara Craton, Australia Geology, Vol. 27, pp.115-118.

159. Reich, M., and Becker, U., (2006): First-principles calculations of the thermodynamic mixing properties of arsenic incorporation into pyrite and marcasite. Chem. Geol. Vol. 225, pp. 278-290.

160. Reimold, W.U., and Gibson, R.L., (2006). The melt rocks of the Vredefort impact structure – Vredefort Granophyre and pseudotachylitic breccias: Implications for impact cratering and the evolution of the Witwatersrand Basin. Chemie der Erde 66, pp. 1-35.

161. Reimold, W.U., Pryzbylowicz, W.J., and Gibson, R.L., (2004). Quantitative major and trace elemental mapping by PIXE of concretionary pyrite from the Witwatersrand Basin, South Africa. X-Ray Spectrom. Vol. 33: pp.189-203.

162. Reimold, W.U., Pryzbylowicz, W.J., and Gibson, R.L., (2002), Quantitative major and trace elemental mapping by PIXE of concretionary pyrite from the Witwatersrand Basin, South Africa: X-Ray Spectrometry 33: pp.189-203.

163. Reimold, W.U., Przybylowicz, W.J., and Koeberl, C., (1999). Micro-PIXE analysis of varied sulphide populations from the Ventersdorp Contact Reef, Witwatersrand basin, South Africa. Nuclear Instruments and Methods in Physics Research B 158, pp. 593-598.

164. Robb, L.J., and Meyer, F.M., (1995). The Witwatersrand Basin, South Africa: Geological framework and mineralisation processes. Ore Geology Reviews 10, pp. 67-94.

165. Robb, L.J., Davis, D.W., Kamo, S.L., and Meyer, F.M., (1992). Ages of altered granites adjoining the Witwatersrand Basin with implications for the origin of gold and uranium. Nature, 357, pp. 677-680.

166. Robb, L.J., Davis, D.W., and Kamo, S.L., (1991). Chronological framework for the Witwatersrand Basin and environs: towards a time constrained depositional model. S. Afr. J. Geol., 94: 86-95.

167. Robb, L.J., Landais, P., Drennan, G.R., (1991). A review of some recent petrographic and chemical/structural studies of Witwatersrand kerogen GSSA Western Transvaal Branch in association with the Witwatersrand Interest Group (W.I.N.G) p 99-101

168. Robb. L.J., Davis, W.D., and Kamo, S.L., (1990). U-Pb ages on single detrital zircon grains from the Witwatersrand Basin, South Africa: Constraints on the Age of Sedimentation and on the Evolution of Granites Adjacent to the Basin. The Journal of Geology, Vol. 98, No. 3, pp. 311-328.

169. Roberts, M.K., and Schweitzer, J.K., (1999). Geotechnical areas associated with the Ventersdorp Contact Reef, Witwatersrand Basin, South Africa, The Journal of The South African Institute of Mining and Metallurgy, pp. 157-166.

170. Roering, C., and Smit, C.A., (1987). Bedding parallel shear, thrusting and quartz vein formation in Witwatersrand quartzites. *J. Struct. Geol.*, 9,. pp. 419–427.

171. Roux, A.T., (1967). The application of geophysics to gold exploration in South Africa. Union Corporation, Johannesburg, South Africa. Reprinted from Mining and Groundwater Geophysics.

172. Rubatto, D., and Hermann, J., (2006). Geochronological constraints on fast exhumation: The example of the Central Alps. Goldschmidt Conference Abstracts.

173. Ruiz, J., Valencia, V.A., Chesley, J.T., Kirk, J., Gehrels, G., and Frimmel, H., (2006). The source of gold for the Witwatersrand from Re–Os and U–Pb detrital zircon geochronology. Goldschmidt Conference Abstracts.

174. Rundle, C.C., and Snelling, N.J., (1977). The geochronology of uraniferous minerals in the Witwatersrand triad; an interpretation of new and existing U-Pb age data on rocks and minerals from the Dominion Reef, Witwatersrand and Ventersdorp Supergroup. Phil. Trans. R. Soc. Lond. A. 286, pp. 567-583.

175. Rutten M.G., (1966). Geologic data on atmospheric history Palaeogeography, Palaeoclimatology, Palaeoecology Elsevier Publishing Company. Vol. 2, pp. 47-57.

176. Saager, R., (1981). Geochemical studies on the origin of the detrital pyrites in the conglomerates of the Witwatersrand goldfields, South Africa. U.S. Geol. Surv., Prof. Pap., ll61-L, pp. 17.

177. Saager, R., (1970). Structures in pyrite from the Basal Reef in the Orange Free State gold field. Trans. Geol. Soc. S. Afr., 73:29-46.

178. Saager, R., (1968). Structures in pyrite from the basal reef in the Orange Free State Goldfield. Economic Geology Research Unit, University of the Witwatersrand, Johannesburg, 45:1-25.

179. Saager, R., and Mihálik, P., (1967). Notes on two varieties of Pyrite from the basal reef of the Free State Guduld Mine, Orange Free State Goldfield Economic Geology Research Unit, University of the Witwatersrand, Johannesburg 37, pp. 1-11.

180. Saager, R., and Mihálik, P., (1967). Two varieties of pyrite from the Basal Reef of the Witwatersrand System. Economic Geology, 62:719-731.

181. Saager, R., Muff, R., and Hirdes, W., (19-). Investigations on pyritic conglomerates and banded iron-formations from Archaean greenstone belts and their bearing on the formation of the Witwatersrand ores, South Africa. Schriften der GDMB

182. Safonov, Y.G., and Prokof'ev, V.Y., (2006). Gold-Bearing Reefs of the Witwatersrand Basin: A Model of Synsedimentation Hydrothermal Formation. Institute of Geology of Ore Deposits, Petrography. Vol. 48, No. 6, pp. 415-447.

183. Sagan, C., Mullen, G., (1972). Earth and Mars: Evolution of Atmospheres and Surface Temperatures. Science, New Series, Vol. 177, No. 4043. pp. 52-56.

184. Schidlowski, M., (1968). The Gold Fraction of the Witwatersrand Conglomerates from the Orange Free State Goldfield (South Africa). I Mineral. Deposita (Berl.) 3, pp. 344-363.

185. Scott, P., (1951). The Witwatersrand Gold Field. Geographical Review, Vol. 41, No. 4, pp. 561-589.

186. Shepherd J.T., (1977). Fluid Inclusion Study of the Witwatersrand Gold-Uranium Ores. Mathematical and Physical Sciences, Vol. 286, No. 1336, pp. 549-565.

187. Simpson, P.R., and Bowles, J.F.W., (1977). Uranium Mineralisation of the Witwatersrand and Dominion Reef Systems. Mathematical and Physical Sciences, Vol. 286, No. 1336, pp. 527-548.

188. Smieja-Król, B., Duber, S., and Rouzaud J., (2009). Multiscale organisation of organic matter associated with gold and uranium minerals in the Witwatersrand basin, South Africa. International Journal of Coal Geology 78, pp. 77-88.

189. Spangenberg J.E., and Frimmel, H.F., (2001). Basin-internal derivation of hydrocarbons in the Witwatersrand Basin, South Africa: evidence from bulk and molecular d^{13}C data. Chemical Geology, Vol. 173, pp. 339-355.

190. Spangenberg, J.E. & Frimmel, H.E., (1999). Tracking the origin of organic matter in the Witwatersrand basin using 13C/12C analysis of individual hydrocarbons. Mineral Deposits: Processes to Processing, SGA-IAGOD Meeting, pp. 271-274.

191. Spangenberg, J.E., and Frimmel, H.E., (1999). Basin-Internal derivation of hydrocarbons in the Witwatersrand basin, South Africa: Evidence from bulk and molecular ÿ^{13}C data. Chemical Geology, 173:339-355.

192. Stanisław Z., Mikulski[1], Bogusław Bagiński[2], Piotr Dzierżanowski[2]., (2005). PolskieTowarzystwo Mineralogiczne – PraceSpecjalne Mineralogical Society of Poland – Special Papers Zeszyt 26, Vol. 26.

193. Sugawara, H., Sakakibara, M., Belton, D., and Suzuki, T., (2008). Quantitative micro-PIXE analysis of heavy metal-rich framboidal Pyrite. Journal of Mineralogical and Petrological Science. Vol. 103, pp 131-134.

194. Sutton, S.J., Ritger, S. D. and Maynard, J.B., (1990). Stratigraphic Control of Chemistry and Mineralogy in Metamorphosed Witwatersrand Quartzites. The Journal of Geology, Vol. 98, No. 3, pp. 329-341.

195. Toma, S.A., and Murphy, S., (1978). Exsolution f gold from detrital platinum. Groupmetalgrainsi n the Witwatersrand auriferous conglomerates. Canadian mineralogist. Vol. 16, pp. 641-650.

196. Ural, Hecht O., Reimold L., Klemd, U. and Reiner, (2008). Electron microprobe and LA-ICP-MS analysis of pyrites from the VCR in the Witwatersrand Basin, South Africa. Museum of Natural History, Humboldt-University Berlin, Department of Research, Invalidenstrasse 43, 10115 Berlin.

197. Utter, T., (1980). Rounding of ore particles from the Witwatersrand gold and uranium deposit (South Africa) as an indicator of their detrital origin. Journal of Sedimentary Petrology, Vol. 50, No. 1, pp. 0071-0076.

198. Utter, T., (1979). The morphology and silver content of gold from the Upper Witwatersrand and Ventersdorp Systems of the Klerksdorp goldfield, South Africa. Econ Geol, 74:27–44.

199. Utter, T., (1978). Morphology and geochemistry of different pyrite types from the Upper Witwatersrand System of the Klerksdorp Goldfield, South Africa. Band 67, Heft 2, 1078, Seite 774-804.

200. Utter, T., (1978). Raster-elektronen mikroskopiscne Untersuchungenan Erzmineralie nausdemoberen Witwatersrand und dem Ventersdorp System des Klerksdorp Goldfeldes, Südafrika. Thesis, PhD, Goethe, Univ. Frankfurt (unpubl).

201. Utter, T., (1977). Morphology and geochemistry of pyrites from the upper Witwatersrand system of the Klerksdorp Chamber of Mines of South Africa, Project no.GT1 3, 1-48

202. Vollbrecht, A., Oberthur, A., Ruedrich. J., and Webber, K., (2001). Microfabric analyses applied to Witwatersrand gold-and uranium-bearing conglomerates: Constraints on the provenance and post-depositional modification of rock and ore components. Mineralium Deposita. Vol. 37, pp.433-451.

203. Von Brunn, V., Gold, D.J.C., (1993). Diamictite in the Archaean Pongola Sequence of southern Africa. Journal of African Earth Sciences 16, pp. 367-374.

204. Walder, A.J., Abell, I.D., and Platzner, I., (1993). Lead isotope ratio measurements of NIST 610 glass by laser ablation inductively coupled plasma mass spectrometry. Spectrochimica Acta, Vol. 42B, No 3, pp. 397-402.

205. Walraven, F., and Martini, J., (1997). Zircon Pb-evaporation age determinations of the Oak Tree Formation, Chunniespoort Group, Transvaal Sequence: implications for Transvaal-Griqualand West basin correlations. South. African Geology. Vol. 98, pp. 58-67.

206. Watanabe, Y., Farquhar, J., and Ohmoto, H., (2009), Anomalous fractionations of sulfur isotopes during thermochemical sulfate reduction: Science, Vol. 324, pp. 370-373.

207. Watanabe, Y., Otake, T., Altermann, W., and Ohmoto, H., (2004). "Detrital" pyrite pebbles from Witwatersrand, South Africa: Evidence for an oxygenated Archaean atmosphere? Goldschmidt Conference, Copenhagen, 5-11th June 2004.

208. Williford, K.H., Van Kranendonk, M.J., Ushikubo, T., Kozdon, R., Valley, W.J., (2011). Constraining atmospheric oxygen and seawater sulfate concentrations during Paleoproterozoic glaciation: In situ sulfur three-isotope microanalysis of pyrite from the Turee Creek Group, Western Australia. Geochimicaet Cosmochimica Acta, Vol. 75, pp. 5686–5705.

209. Wilkin, R.T., Barnes, H.L., and Brantley, S.L., (1996). The size distribution of framboidal pyrite in modern sediments: An indicator of redox conditions. Geochimicaet Cosmochimica Acta, Vol. 60, No 20, pp. 397-3912.

210. Wilkin, R.T., and Barnes, H.L., (1996). Formation process of framboidal pyrite. Geochimicaet Cosmochimica Acta, Vol. 61, No 2, pp. 323-339.

211. Wilson, G.C., Rucklidge, J.C., Campbell, J.L., Nejedly, Z., and Teesdale W.J., (2002). Applications of PIXE to mineral characterization. Nuclear Instruments and Methods in Physics Research B 189, pp. 387-393.

212. Xenophontos, L., Stevens, G., and Przybylowicz, W.J., (1999). Micro-PIXE elemental imaging of pyrites from the Bulawayan-Bubi Greenstone Belt, Zimbabwe. Nuclear Instruments and Methods in Physics Research B, 150 pp. 496-501.

213. Yamaguchi K.E., and Ohmoto H., (2006). Evidence from sulphur isotope and trace elements in pyrites for their multiple post-depositional processes in uranium ores at the Stanleigh Mine, Elliot Lake, Ontario, Canada. In Evolution of Earth's Early Atmosphere, Hydrosphere, and Biosphere-Constraints from Ore Deposits: Geological Society of America Memoir 198 (eds. S. E. Kesler and H. Ohmoto). Geological Society of America, Denver, pp. 143–156.

214. Zachariáš, J., Adamovič, J., and Langrová, A., (2008). Trace element chemistry of low-temperature pyrites – an indicator of past changes in fluid chemistry and fluid migration paths (Eger Graben, Czech Republic). Geologicacarpathica, April, 59, 2, pp. 117-132.

215. Zartman, R.E., and Frimmel, H.E., (1999). Rn-generated [206]Pb in hydrothermal sulphide minerals and bitumen from the Ventersdorp Contact Reef, South Africa. Mineralogy and Petrology, 66: pp. 171-191.

216. Zhao, B., Meyer, F.M., Robb, L.J., Toulkeridis, T., Zwingmann, H., and Clauer, N., (1995). Thermal history of gold mineralization in the Ventersdorp Contact Reef, Witwatersrand Basin, South Africa. Abstr. EUG8, Strasbourg, 292 pp.

217. Zhao, B., Clauer, N., Robb, L.J., Swingmann, H., Toulkiridis T., and Mayer, F.M., (1999). K- Ar dating of white micas from Ventersdorp Contact Reef, of the Witwatersrand Basin, South Africa: timing of post-depositional alteration. Mineralogy and Petrology 66, pp.149-170.

REFLECTED LIGHT AND SECONDARY ELECTRON MICROPHOTOGRAPHS OF THE DIFFERENT TYPES OF PYRITE GRAINS
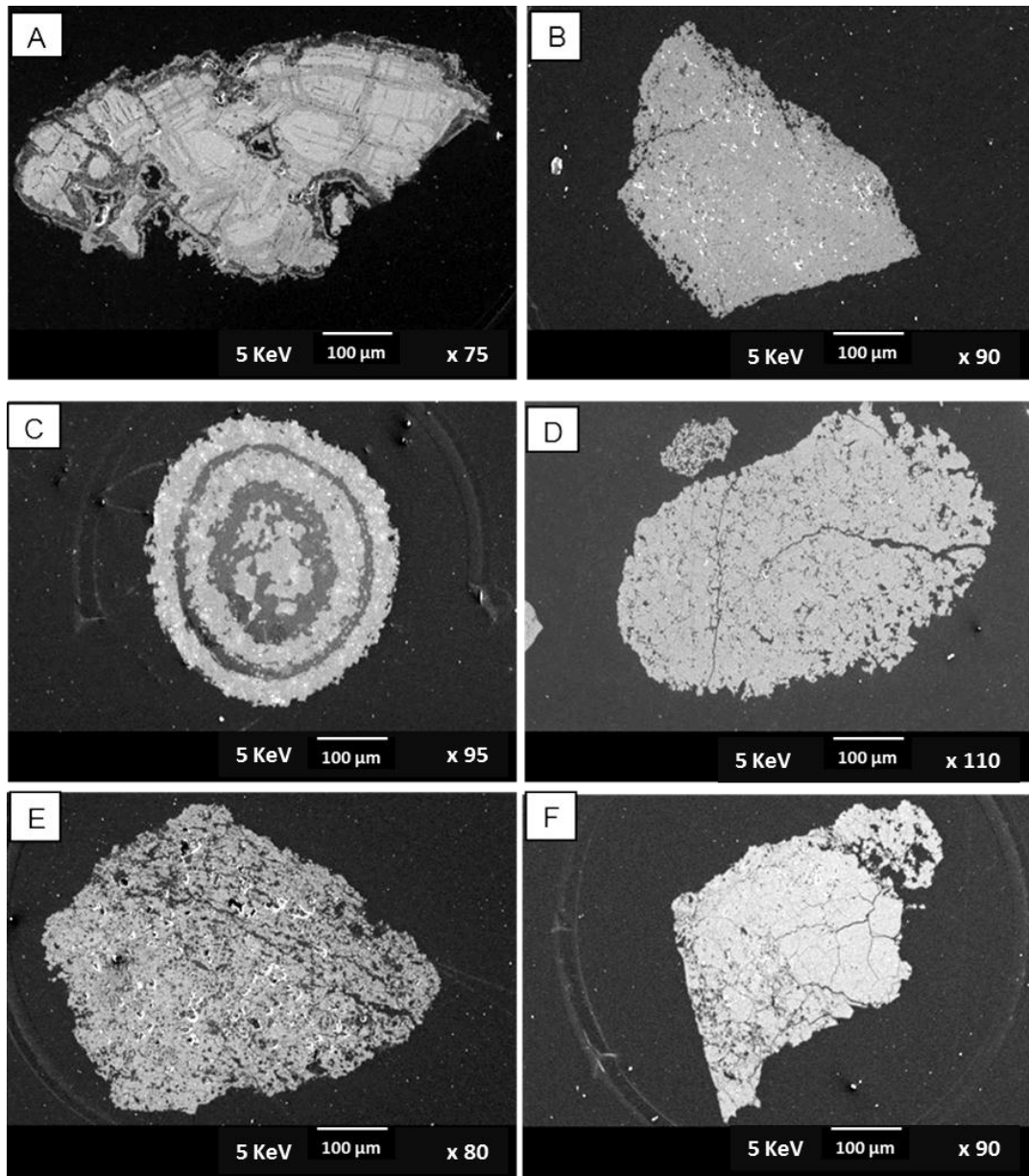
Figure 4.12: *Secondary electron photomicrographs of pyrite grains: (A) angular zoned pyrite of section g52261; (B) rounded porous pyrite grain of section g52224; (C) concretionary pyrite of spherical type composed of alternate circular layers of pyrite of section g52223; (D) concretionary pyrites of section g52230; (E) concretionary pyrites of section g52224; and (F) solid hard mass of angular pyrite crystals of section g52261.*
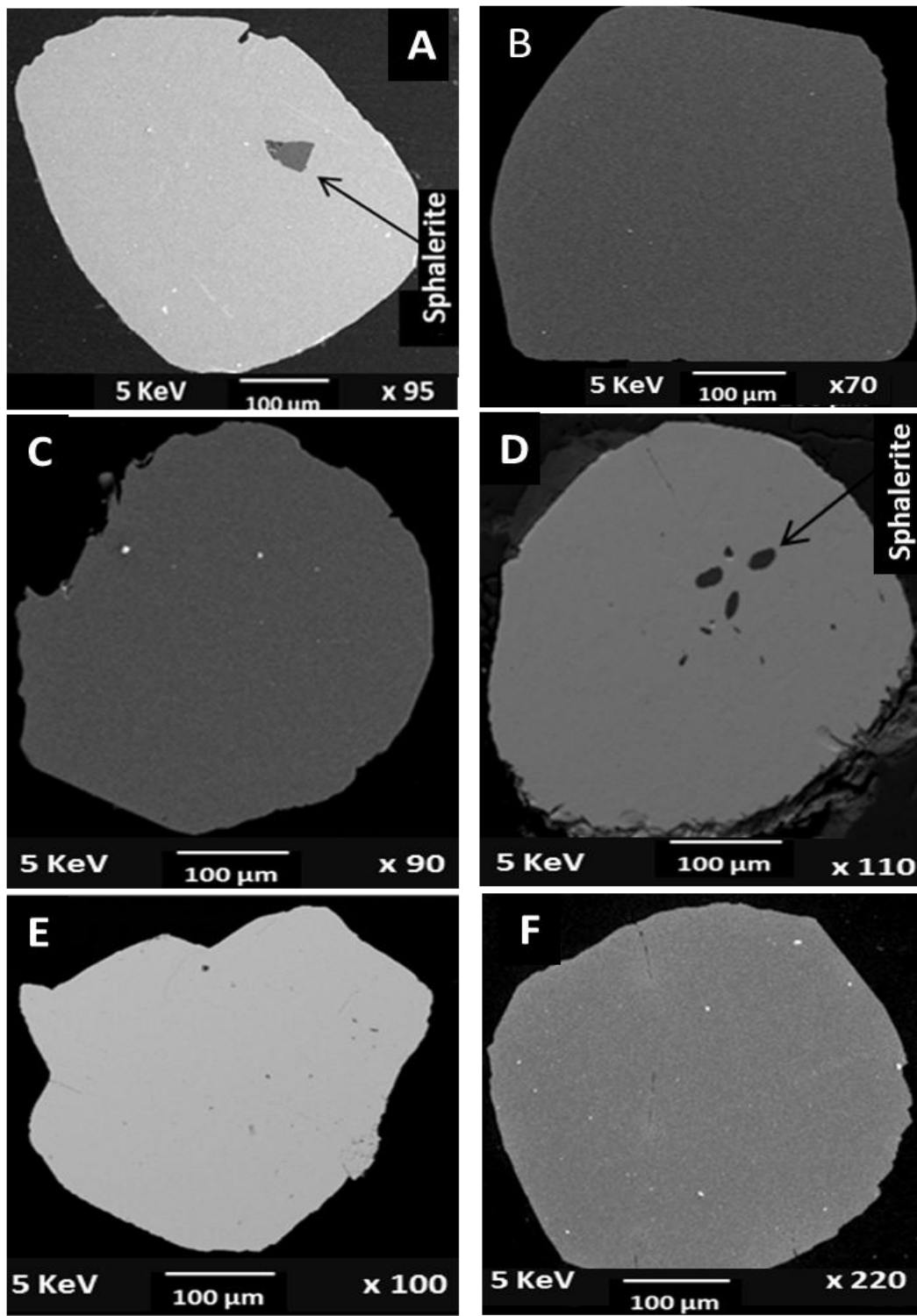
Figure 4.13: *Secondary electron photomicrographs of rounded massive pyrite grains containing inclusions of sphalerite (A) of section g52226; and sub-rounded to rounded pyrite grains without inclusions (B and C) from section g52214; (D) of VL 225; E, and F). The bright white spots represent particles of dust.*
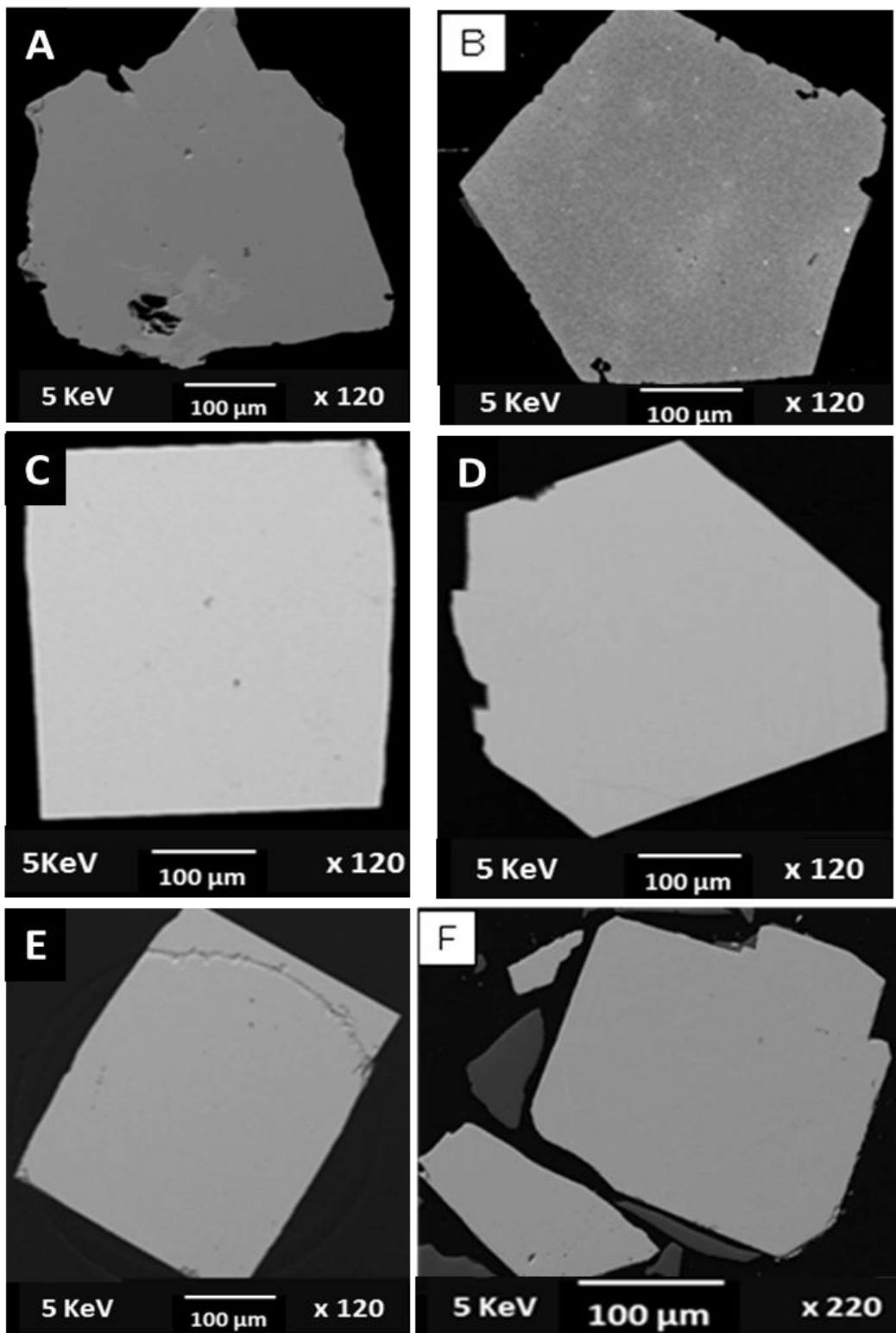
Figure 4.14: *Secondary electron photomicrographs of angular, non-zoned pyrite grains without inclusions (A) of section g52237; angular massive pyrite grains without inclusions or chemical zonations (B, C, and D) of section g52263; (E) from g52239; and (F) of section VL 225.*
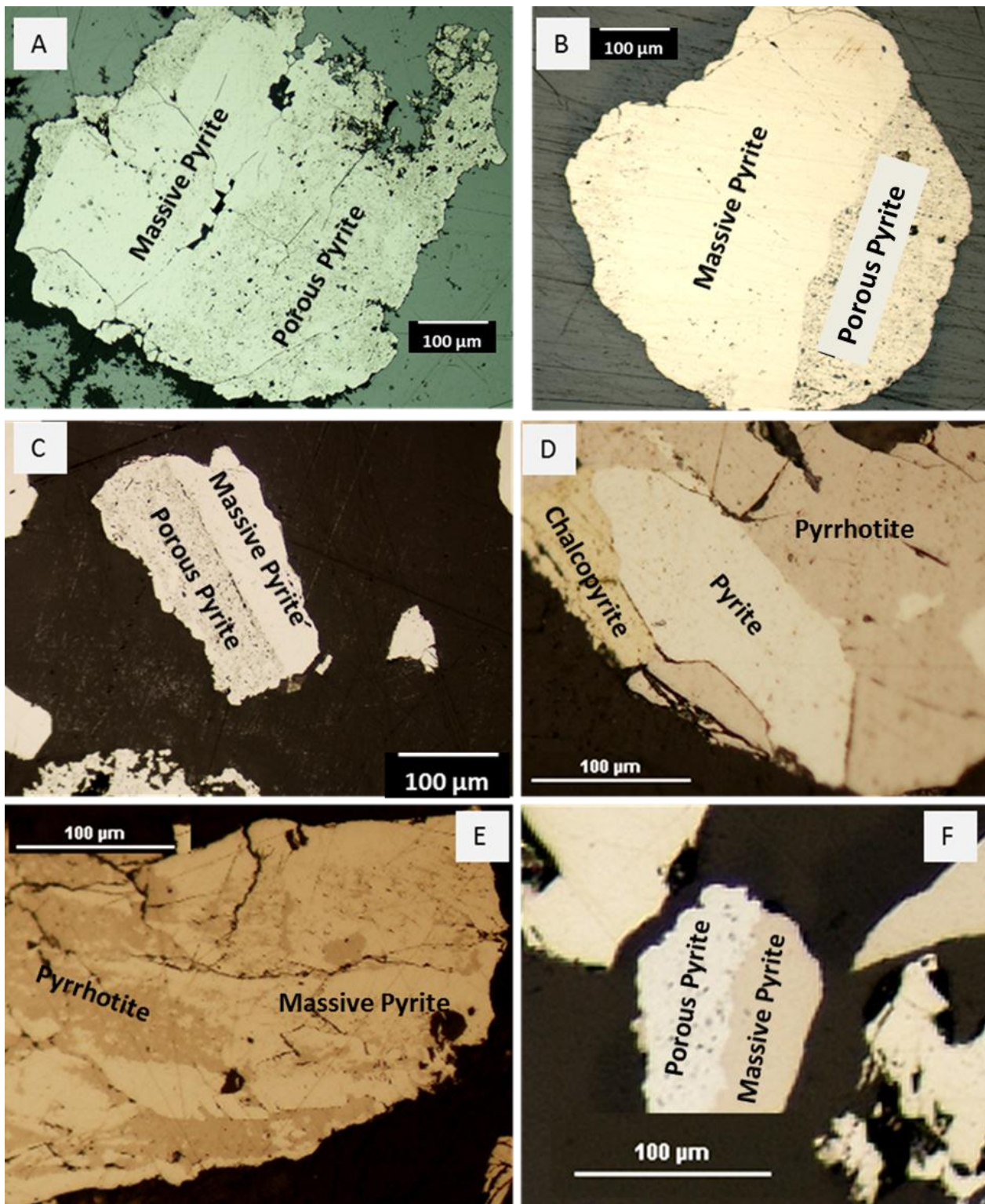
Figure 4.15: *Reflected light photomicrographs of polished sections taken under plane polarised light, showing relevant pyrite textures of the secondary authigenic massive pyrite grains from the primary allogenic pyrites. Grain (A) is from g52210; (B) from g52228; (D and E) from Kloof g52216; and (F) was taken from g52216.*
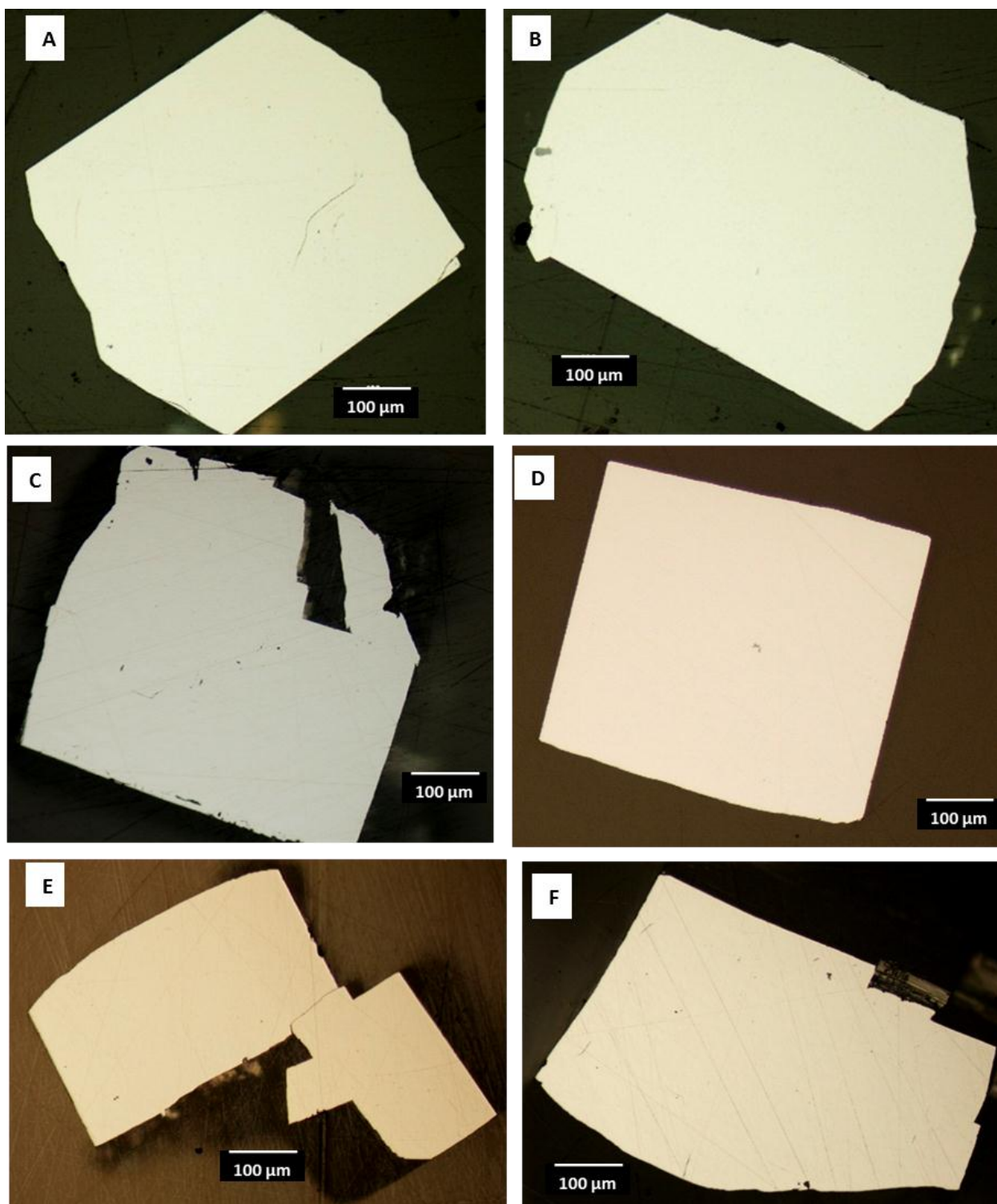
Figure 4.16: *Reflected light photomicrographs of polished sections taken under plane polarised light, showing relevant pyrite textures of angular massive pyrite grains without inclusions or zonation. Grain (A and B) are from g52263; (C) from g52239; (D) from VCR Kloof g52218; and (E and F) were taken from g52239.*
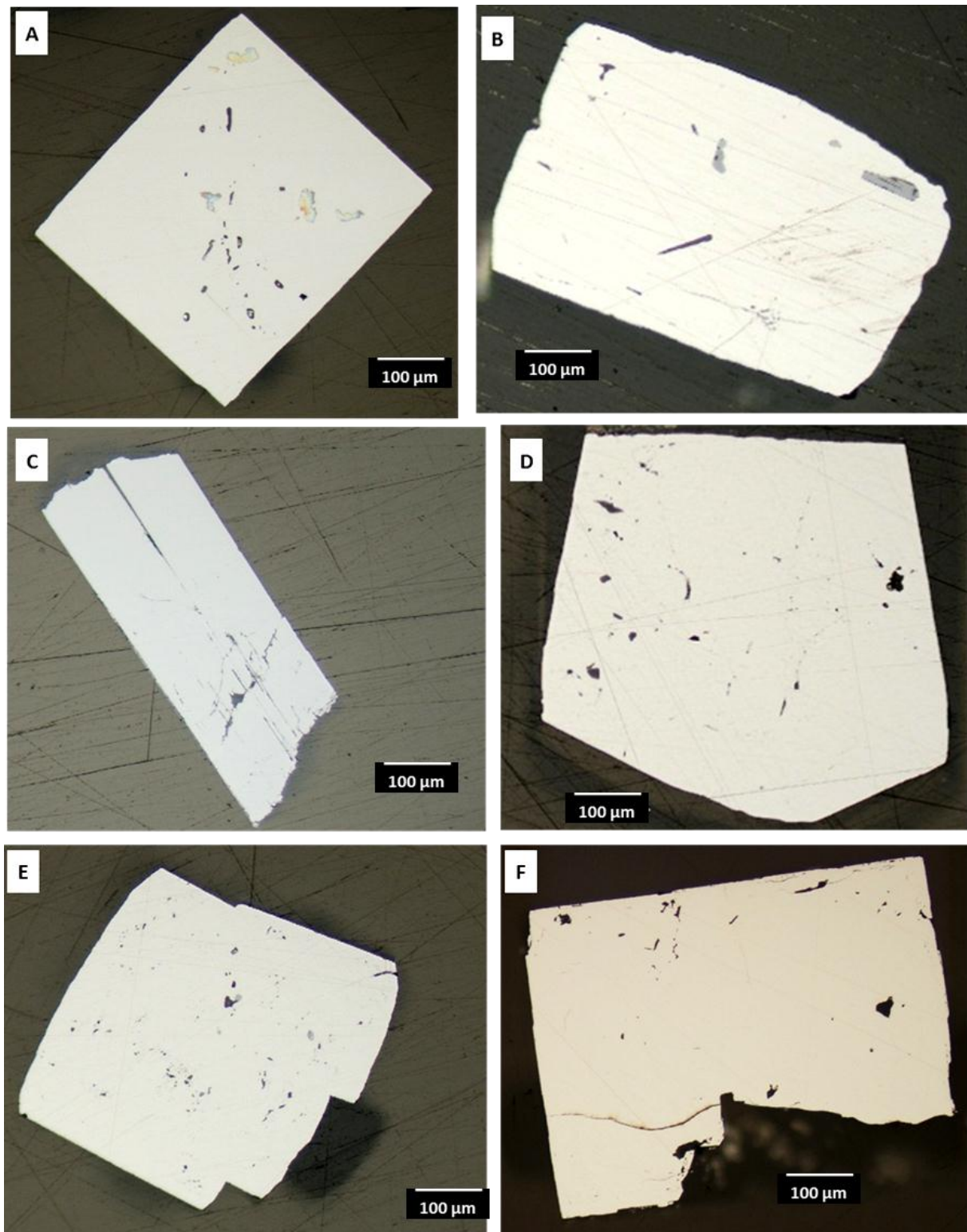
Figure 4.17: *Reflected light photomicrographs of polished sections taken under plane polarised light, showing relevant pyrite textures of angular massive pyrite grains without inclusions and no zonation. (A and E) from g52239; (B) from g52233; (C) from g52255; (D and F) from VCR Kloof g52218.*
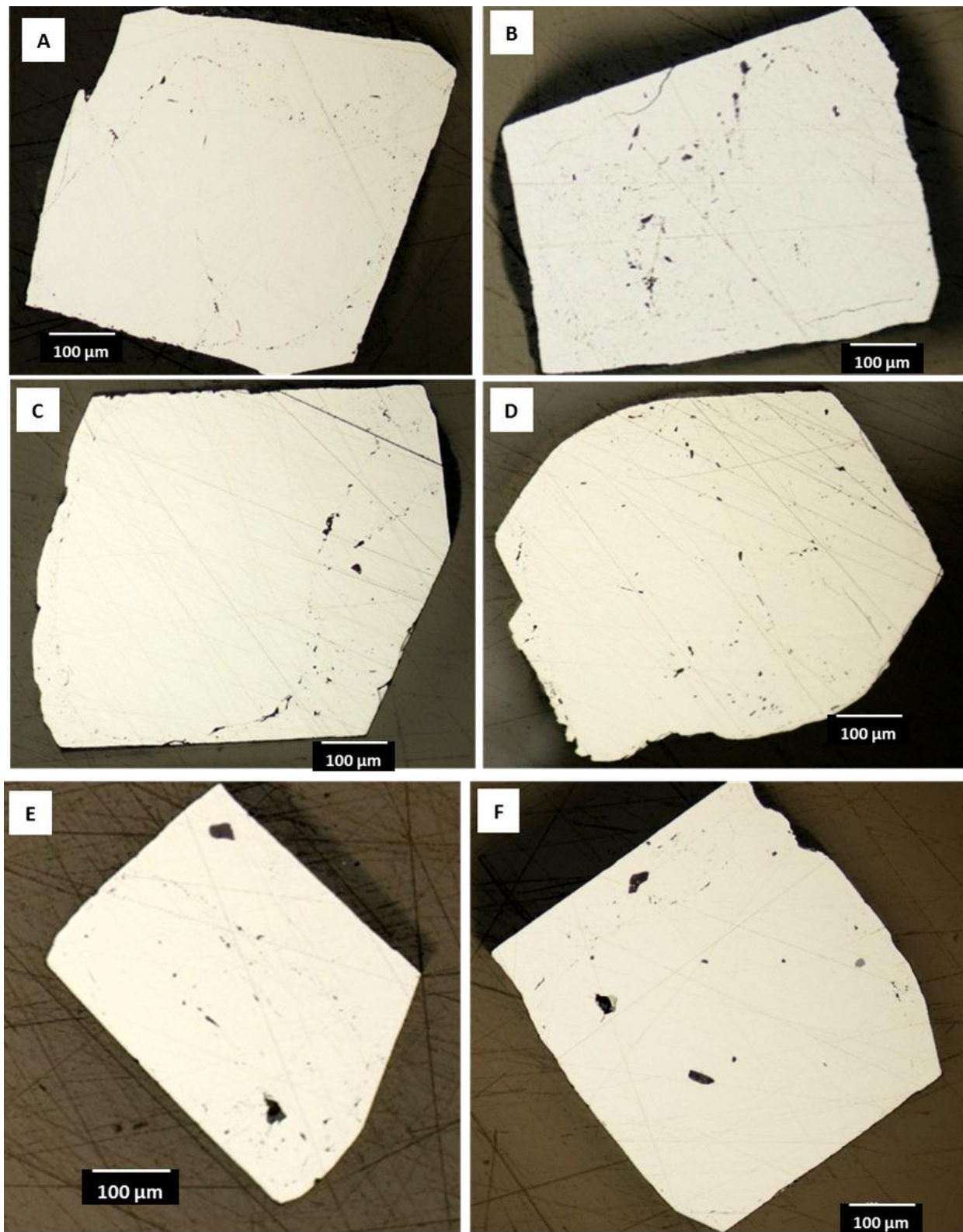
Figure 4.18: *Reflected light photomicrographs of polished sections taken under plane polarised light, showing relevant pyrite textures of angular massive pyrite grains without inclusions and and no zonation. All these grains are from section g52229.*
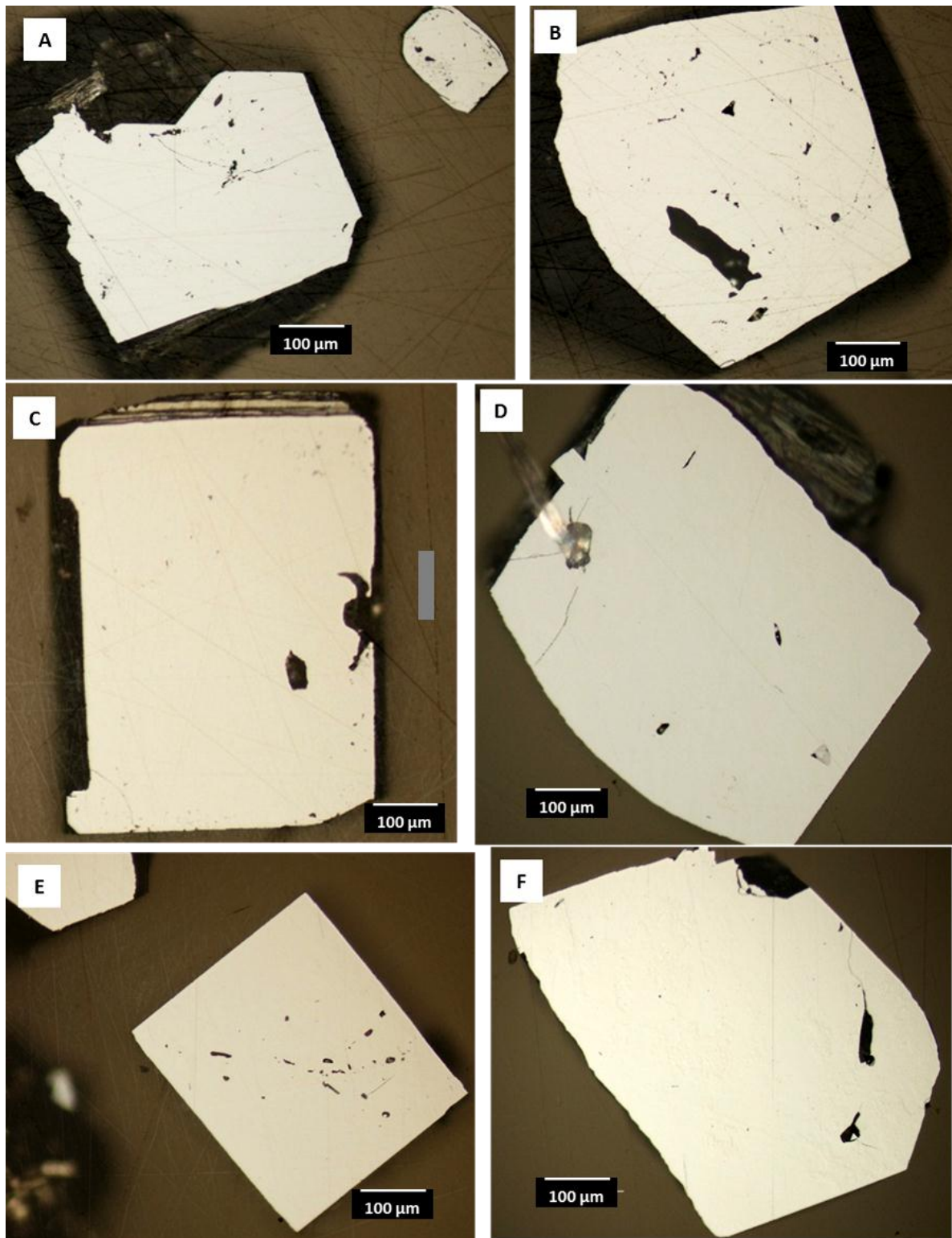
Figure 4.19: *Reflected light photomicrographs of polished sections taken under plane polarised light, showing relevant pyrite textures of angular massive pyrite grains without inclusions and and no zonation. (A, B and E) from g52229; and (C, D and F) from g52239.*
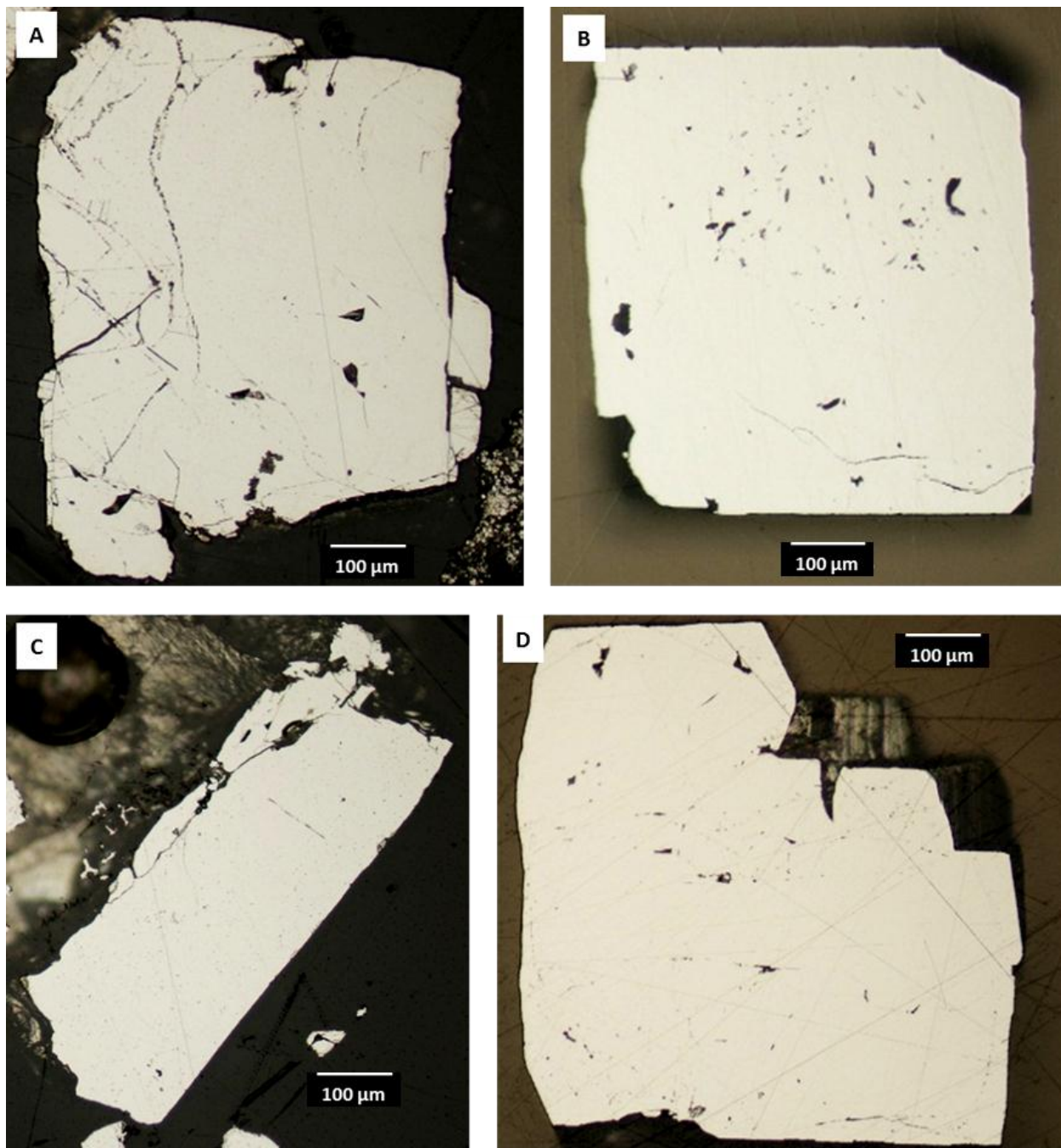
Figure 4.20: *Reflected light photomicrographs of polished sections taken under plane polarised light, showing relevant pyrite textures of angular massive pyrite grains without inclusions and and no zonation. (A and, C) are from section g52200; (B) is from g52239; and (D) is from section g52229.*
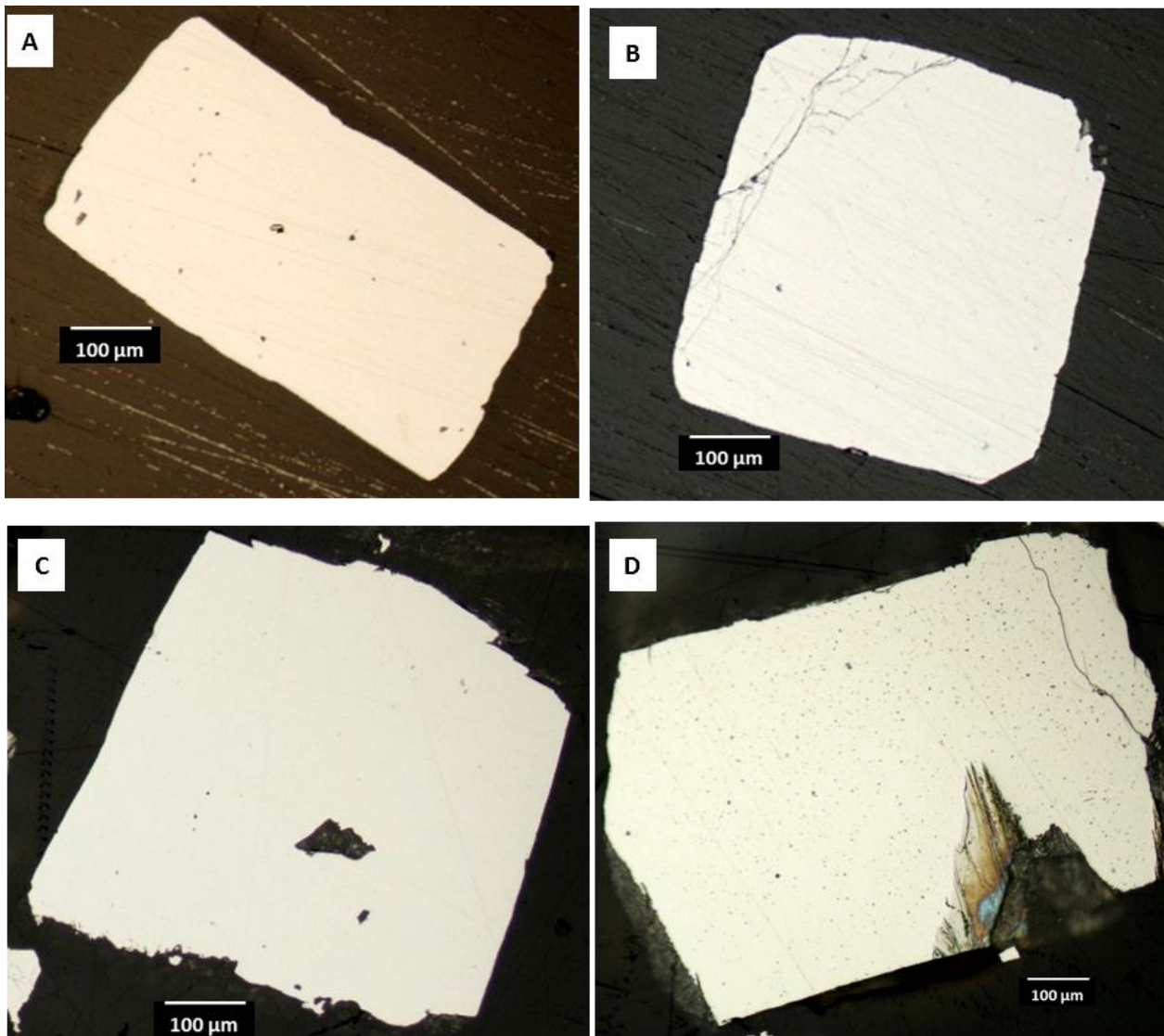
Figure 4.21: *Reflected light photomicrographs of polished sections taken under plane polarised light, showing relevant pyrite textures of angular massive pyrite grains without inclusions and and no zonation. Grain (A) was taken fron section g52233, while (B, C and D) were taken from section g52200.*
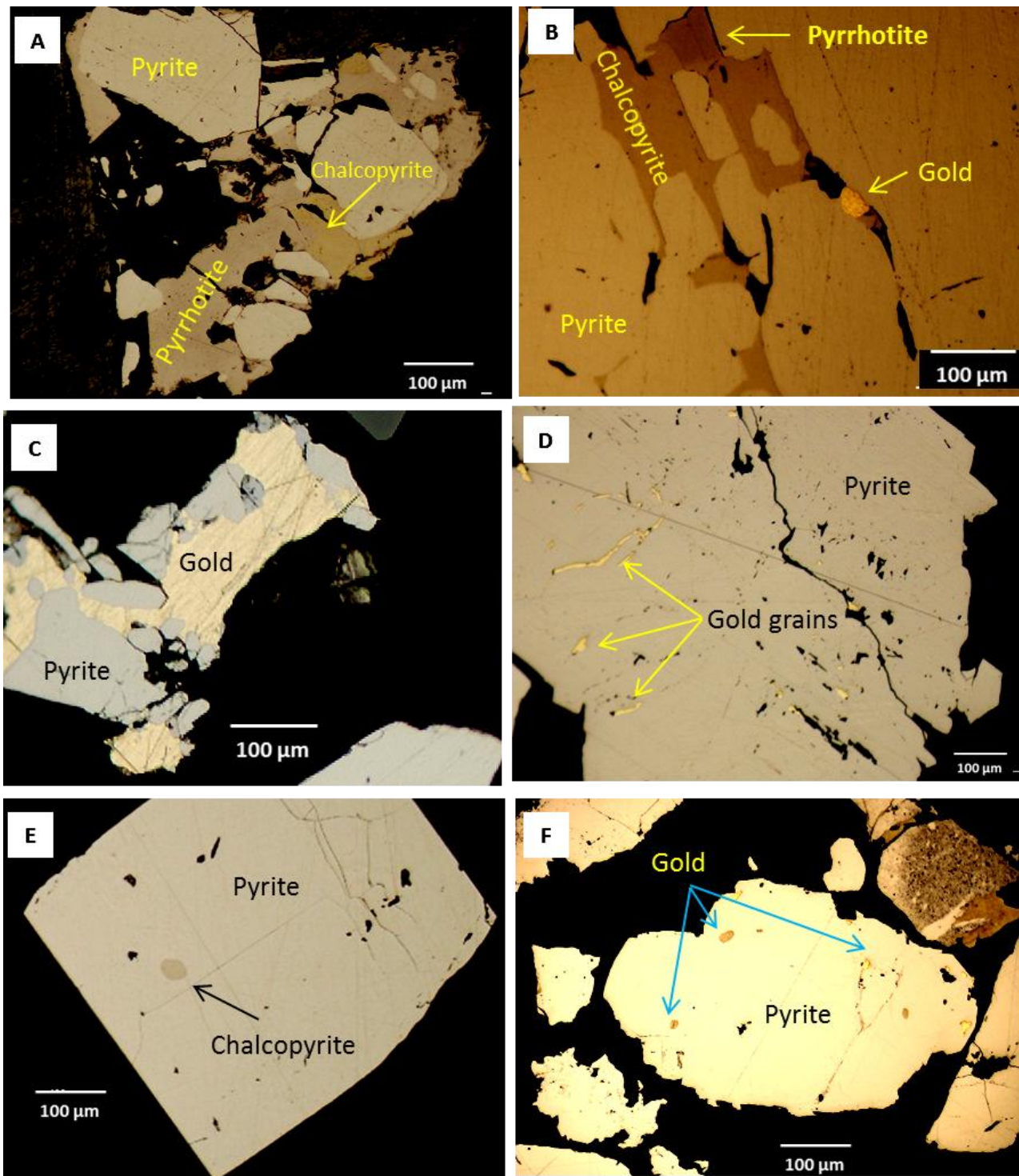
Figure 4.22: *Reflected light photomicrographs of polished sections taken under plane polarised light, showing relevant pyrite textures of angular massive pyrite grains coexisting with chalcopyrite in (A, B, and E), gold grains in (B, C, D, and F), and pyrrhotite in (A and B).*
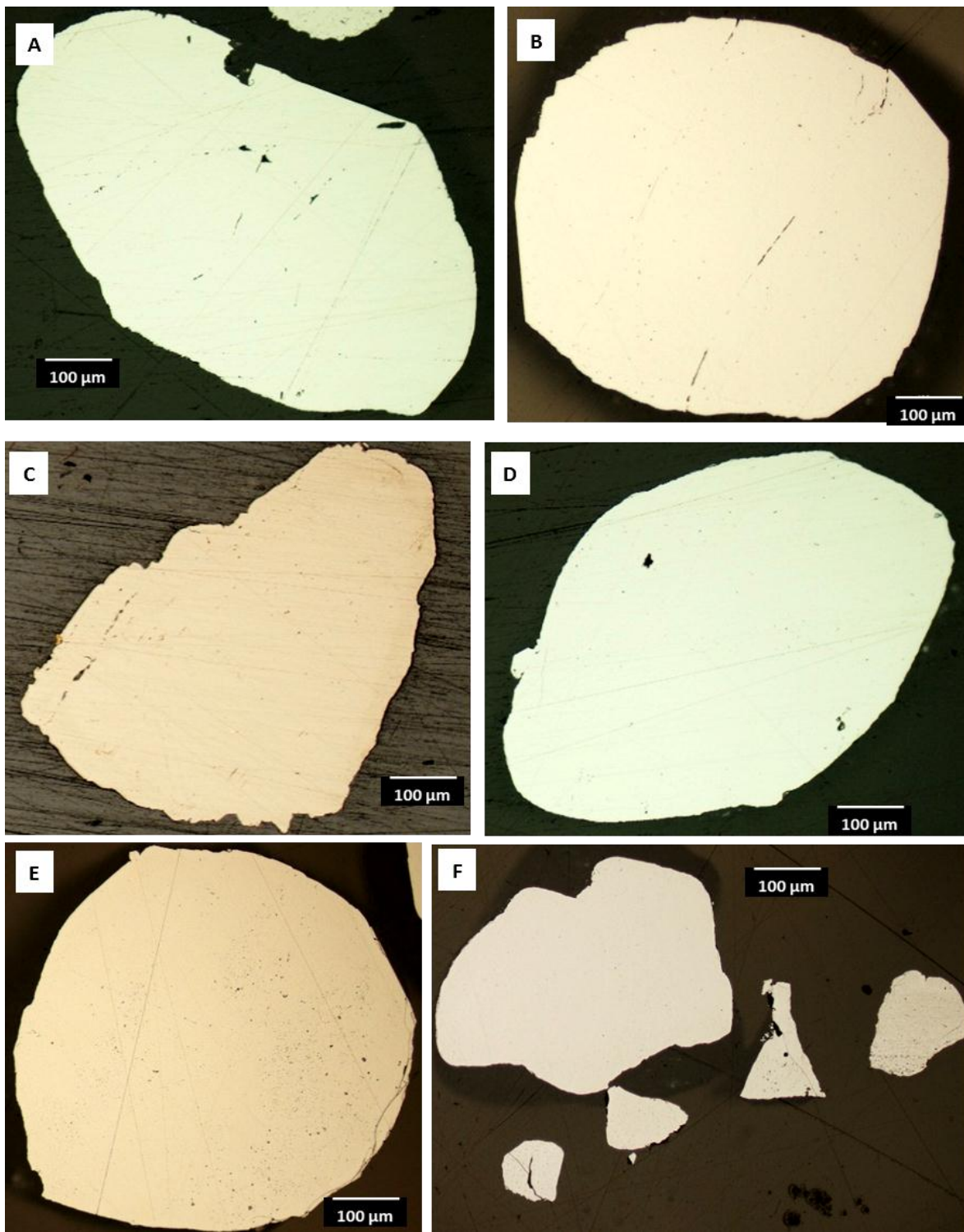
Figure 4.23: *Reflected light photomicrographs of polished sections taken under plane polarised light, showing relevant pyrite textures of rounded massive pyrite grains without inclusions and and no zonation. Grain (A and D) are from g52214; (B) from g52230; (C) from g52228; and (E and F) are from section g52216.*
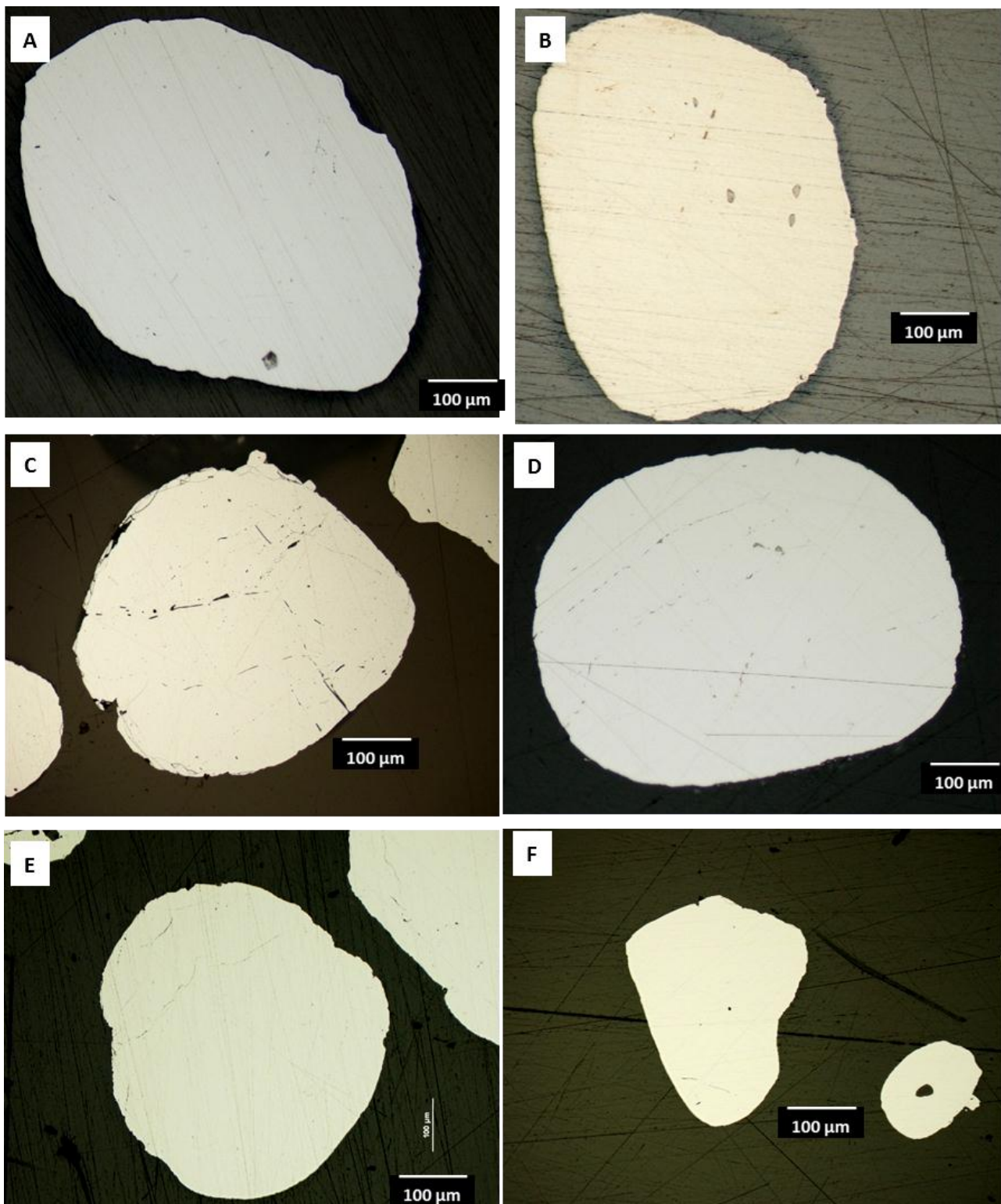
Figure 4.24: *Reflected light photomicrographs of polished sections taken under plane polarised light, showing relevant pyrite textures of rounded massive pyrite grains without inclusions and and no zonation. Grain (A and B) were taken from section g52228; (C) from g52216; (D) from g52233, and (E and F) are from section g52214.*
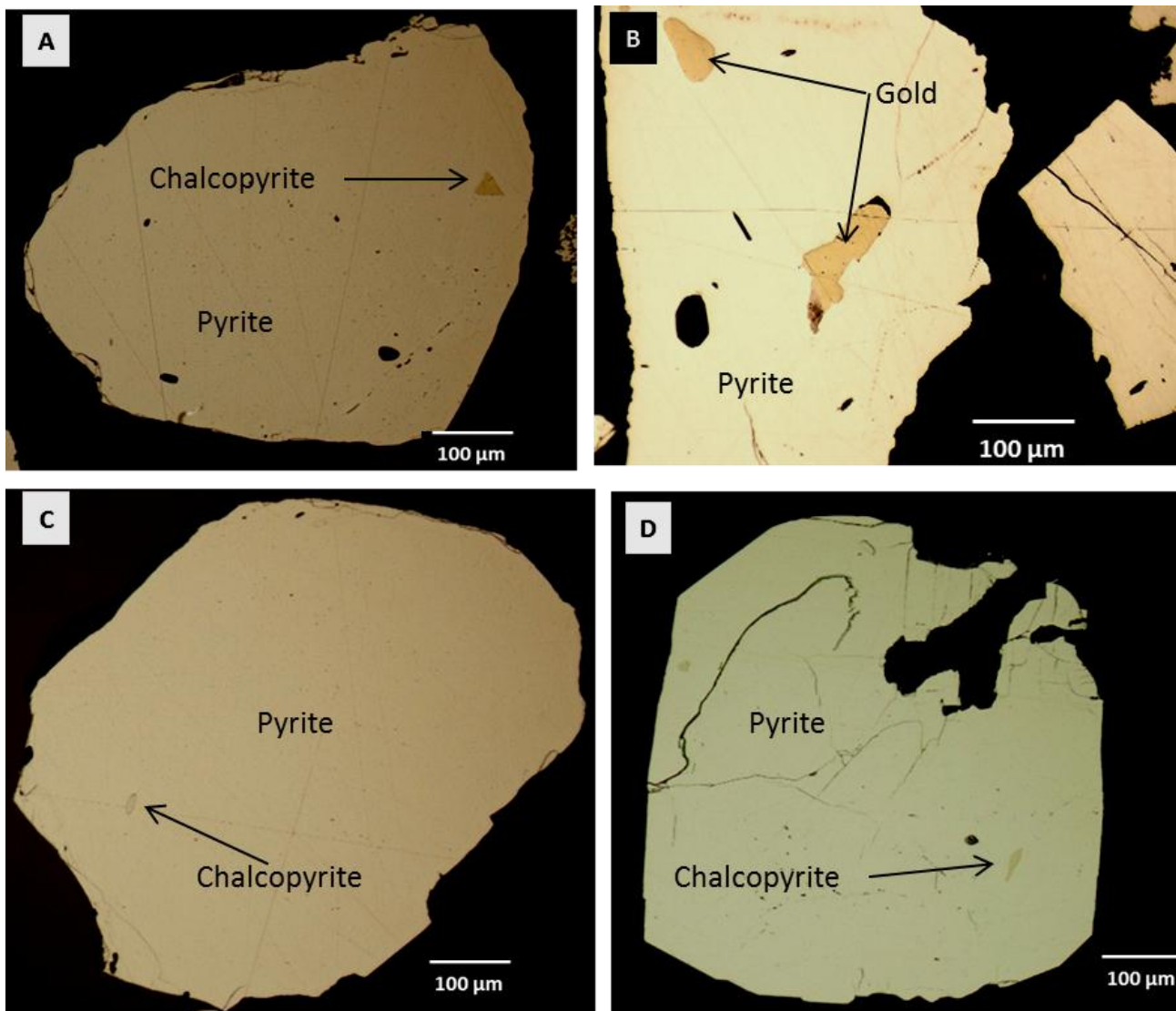
Figure 4.25: *Reflected light photomicrographs of polished sections taken under plane polarised light, showing relevant pyrite textures of rounded massive pyrite grains containing small inclusions of chalcopyrite and gold grains in image (A) from section g52216; a grain of gold in (B). Grain (C and D) contain inclusions of chalcopyrite grains.*
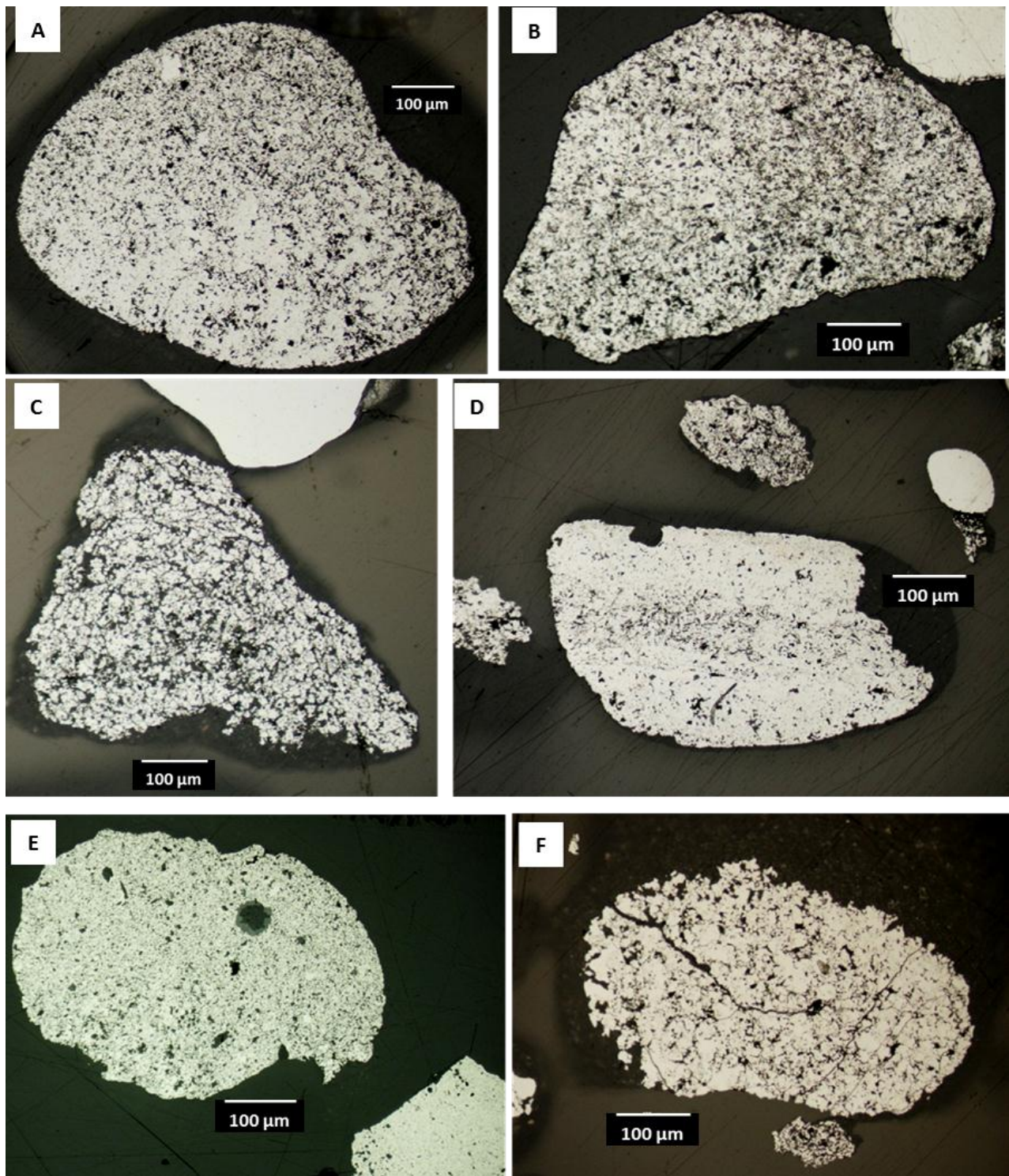
Figure 4.26: *Reflected light photomicrographs of polished sections taken under plane polarised light, showing relevant pyrite textures of aggregated porous pyrite showing internal variation in crystal size and fragmented clast resembling fine growth textures along the edges and coarse within the centre. Grain (A through D) are from section g52236; (E) from g52213; and (F) from section g52230.*
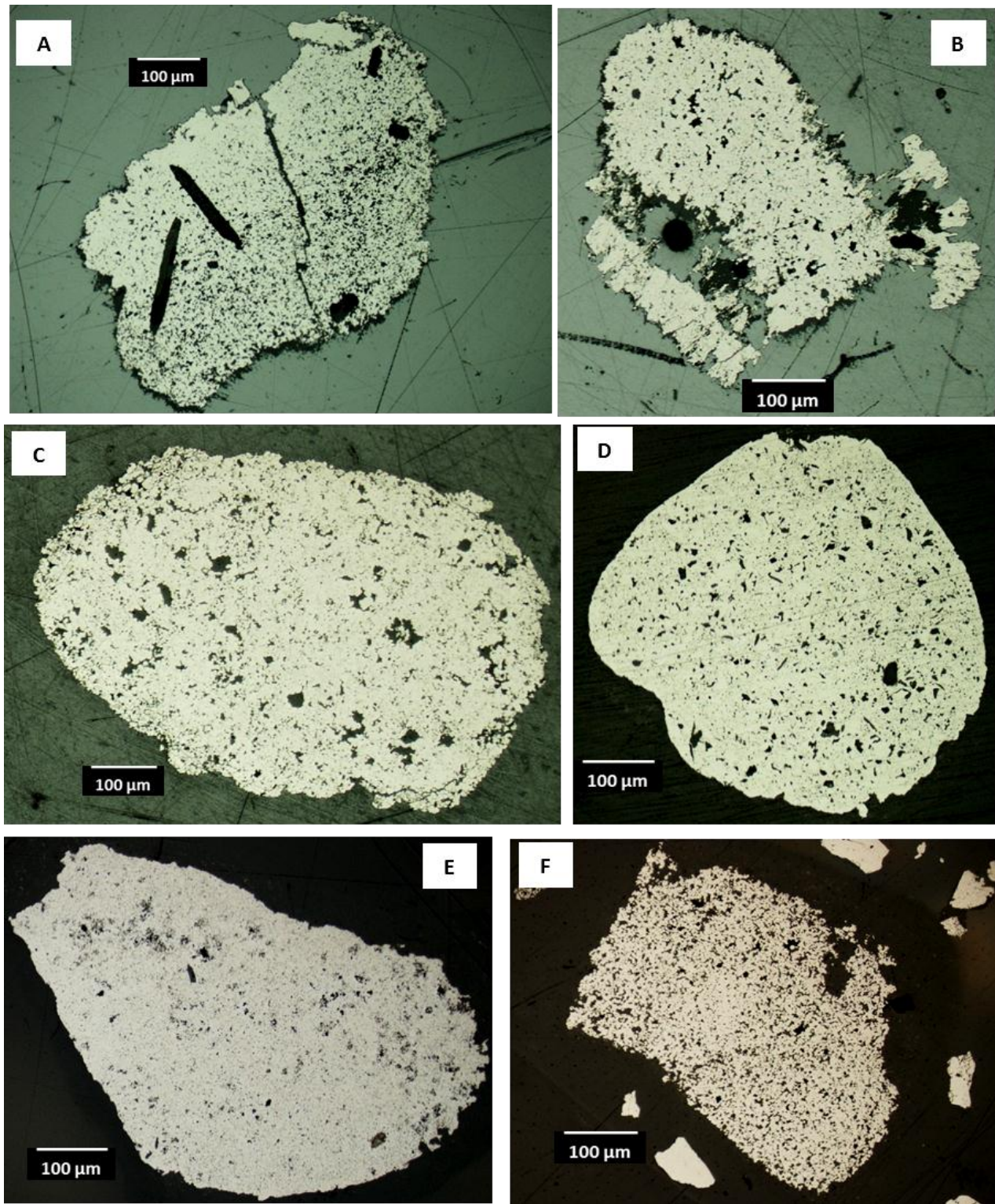
Figure 4.27: *Reflected light photomicrographs of polished sections taken under plane polarised light, showing relevant pyrite textures of porous pyrite grains with an internal texture that resembles randomly orientated crystals.Grain (A and B) were taken from section g52210; (C) from g52213; (D) from g52214; and (E and F) are from section g52227.*
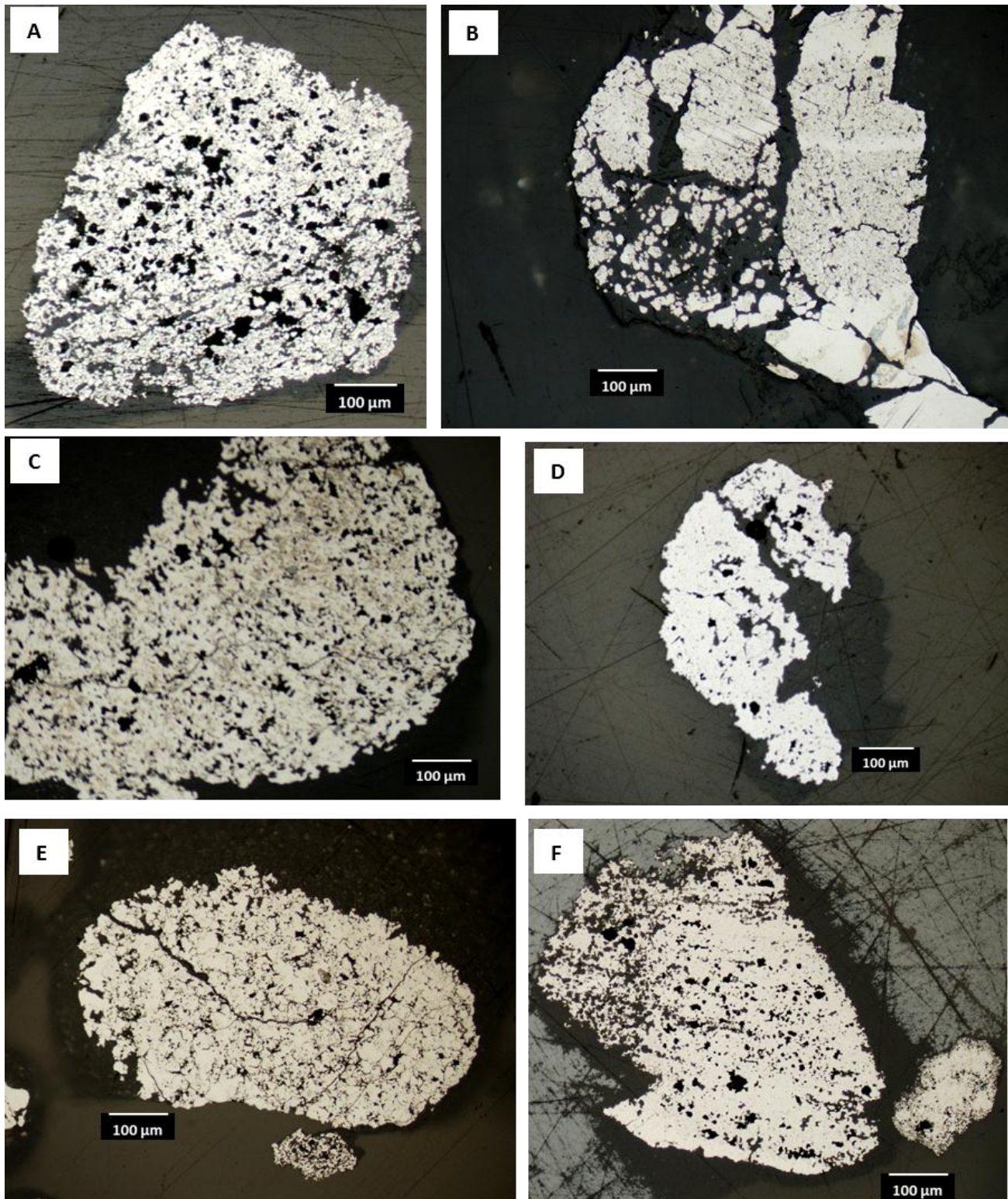
Figure 4.28: *Reflected light photomicrographs of polished sections taken under plane polarised light, showing relevant pyrite textures of rounded pyrite showing sheath-like internal textures in (A, B, and C) from section g52224; (D and E) from g52258; and (F) was taken from section g52237.*
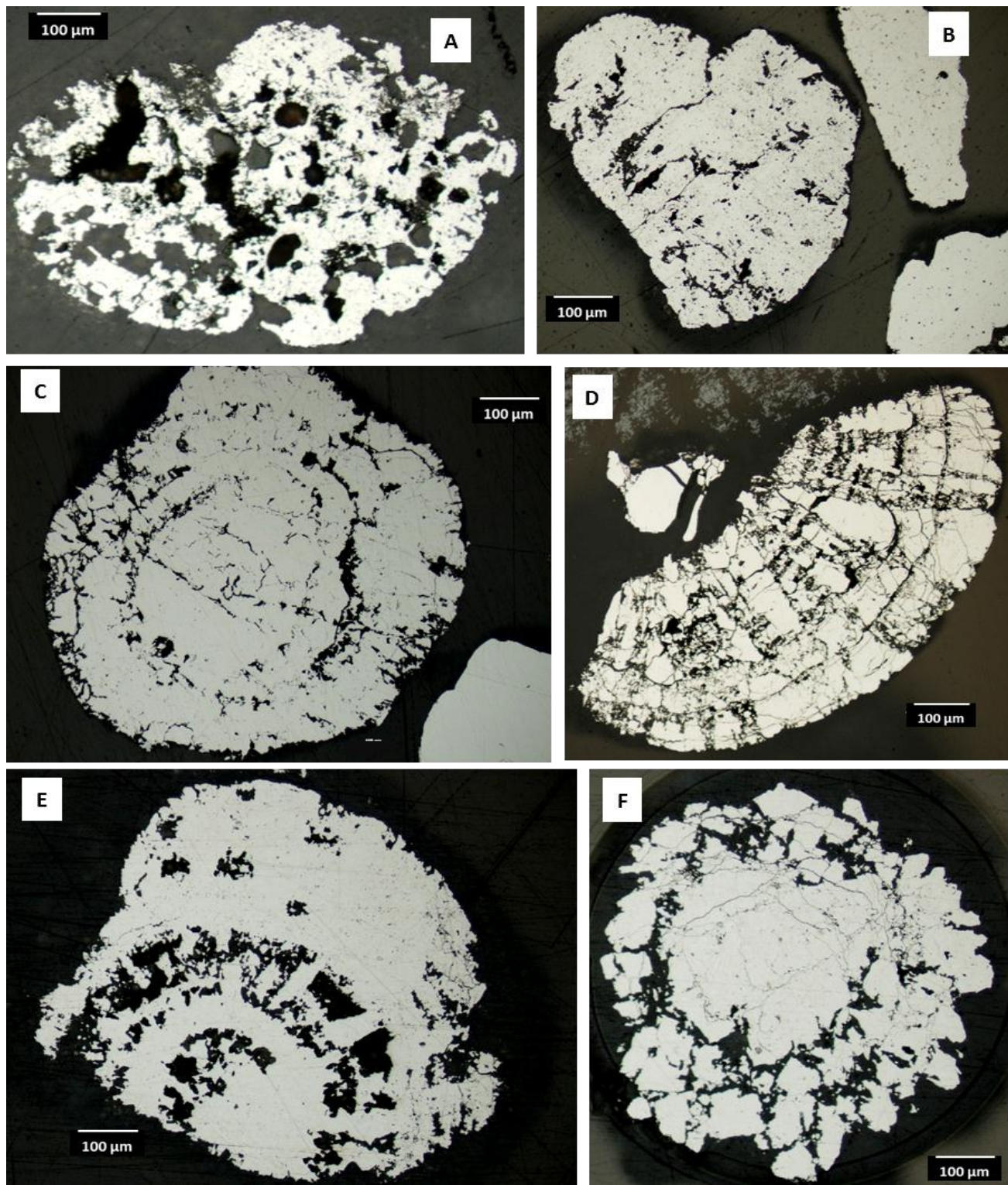
Figure 4.29: *Reflected light photomicrographs of polished sections taken under plane polarised light, showing relevant pyrite textures of pounded porous pyrite grains with an internal texture, and concentric layers. Grain (A and C) are from g52236; (D) from g52237; and (E and F) are from section g52224.*
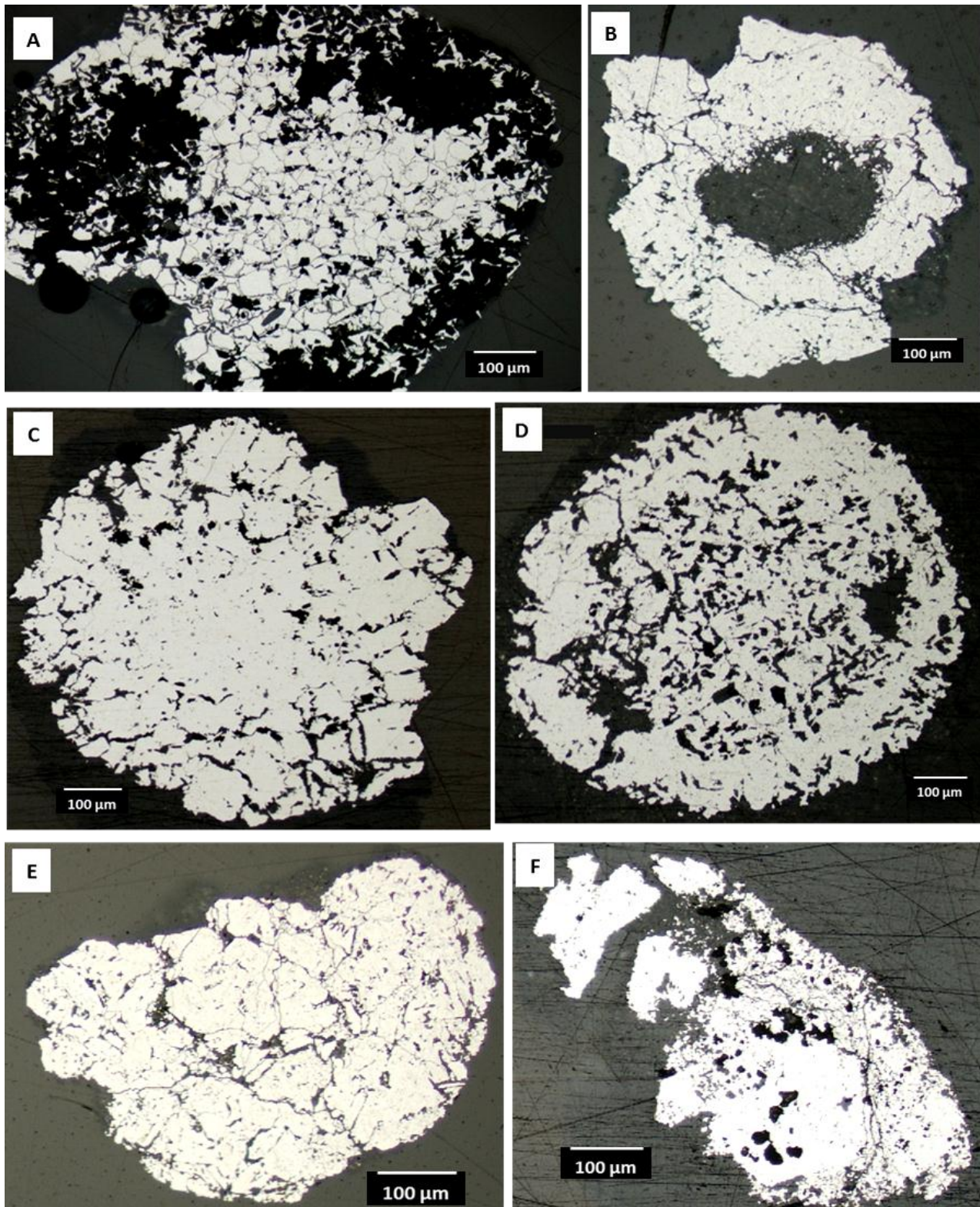
Figure 4.30: *Reflected light photomicrograph of rounded grain (A) from g52226; (B) from g52227; (C and D) from g52224; a grain with an internal texture (E); rounded porous pyrite with distinctly different growth bands (F).*
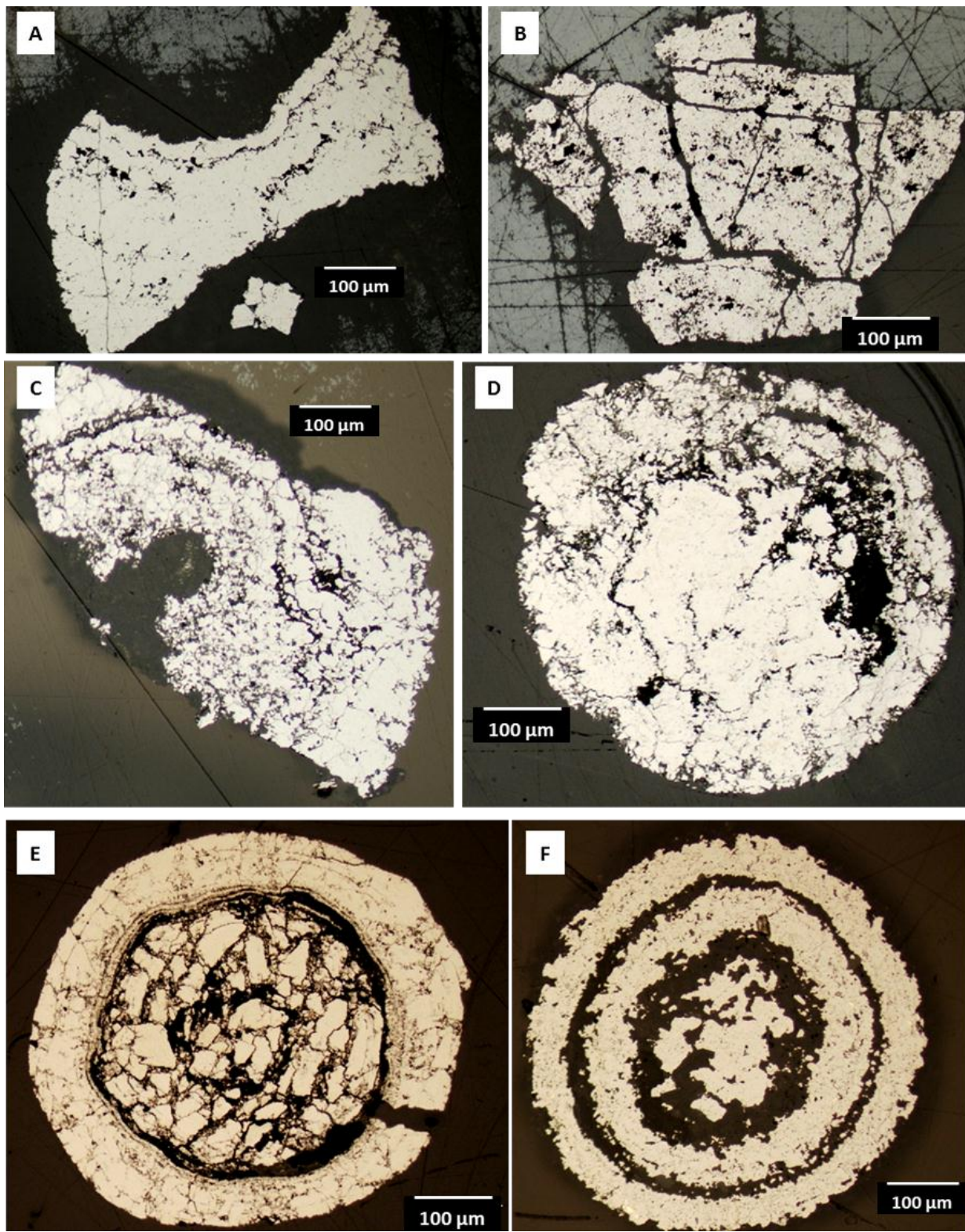
Figure 4.31: *Reflected light photomicrographs of pyrite grains that resembles an original ooid texture. Grain (A through D) are taken from section g52237; (E) from g52219; and (F) from section g52223.*
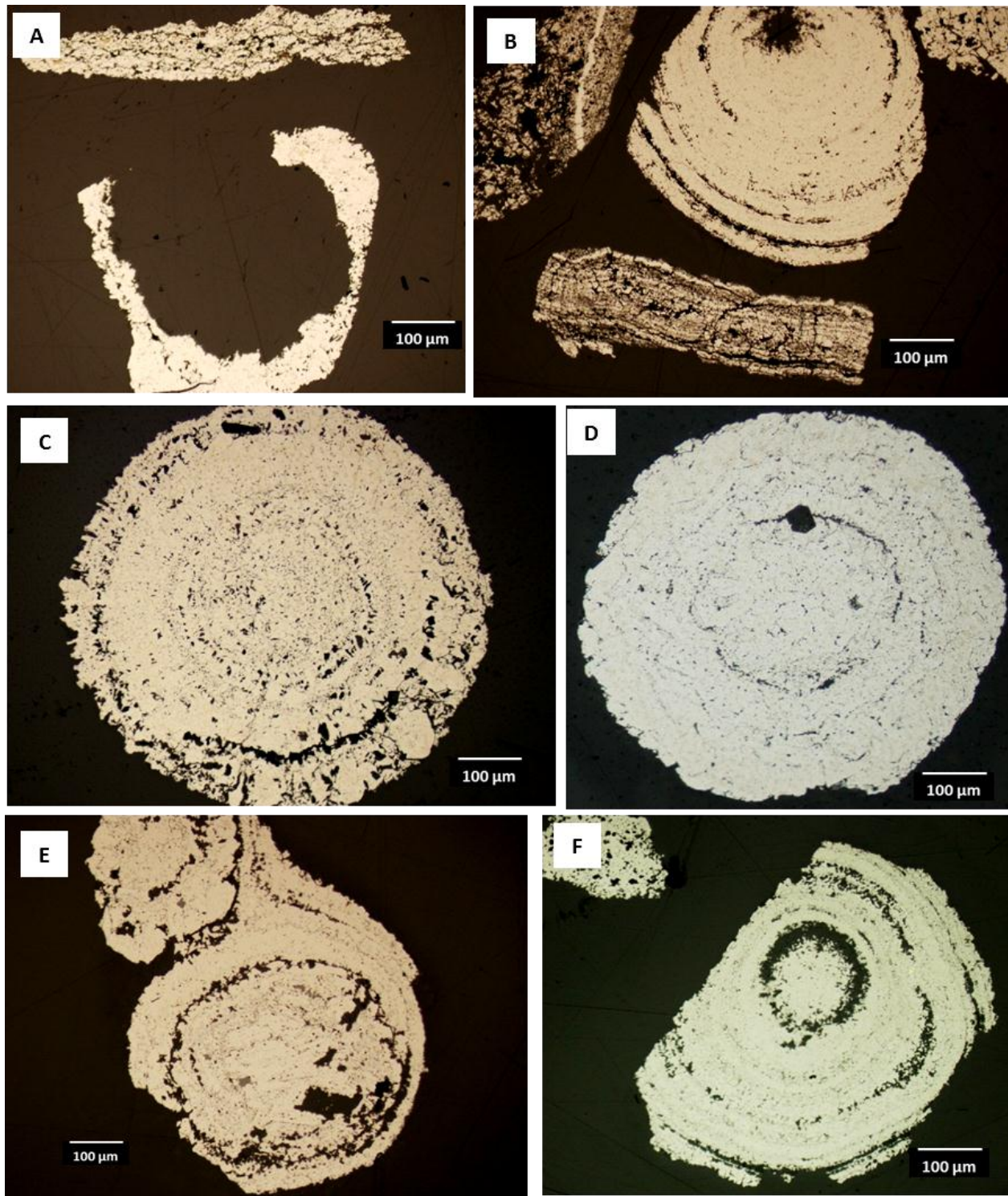
Figure 4.32: *Reflected light photomicrographs of polished sections taken under plane polarised light. (A) is from g52202; (B and C) are from VCR Kloof g52219 show relevant pyrite textures of a detrital fragment of pyrite grains that resemble original ooid texture. (D) from g52227; a pyrite grain showing a truncated colloform (curling) texture (E) from g52223; a pyrite grain that resembles an original ooid texture (F) from g52213.*
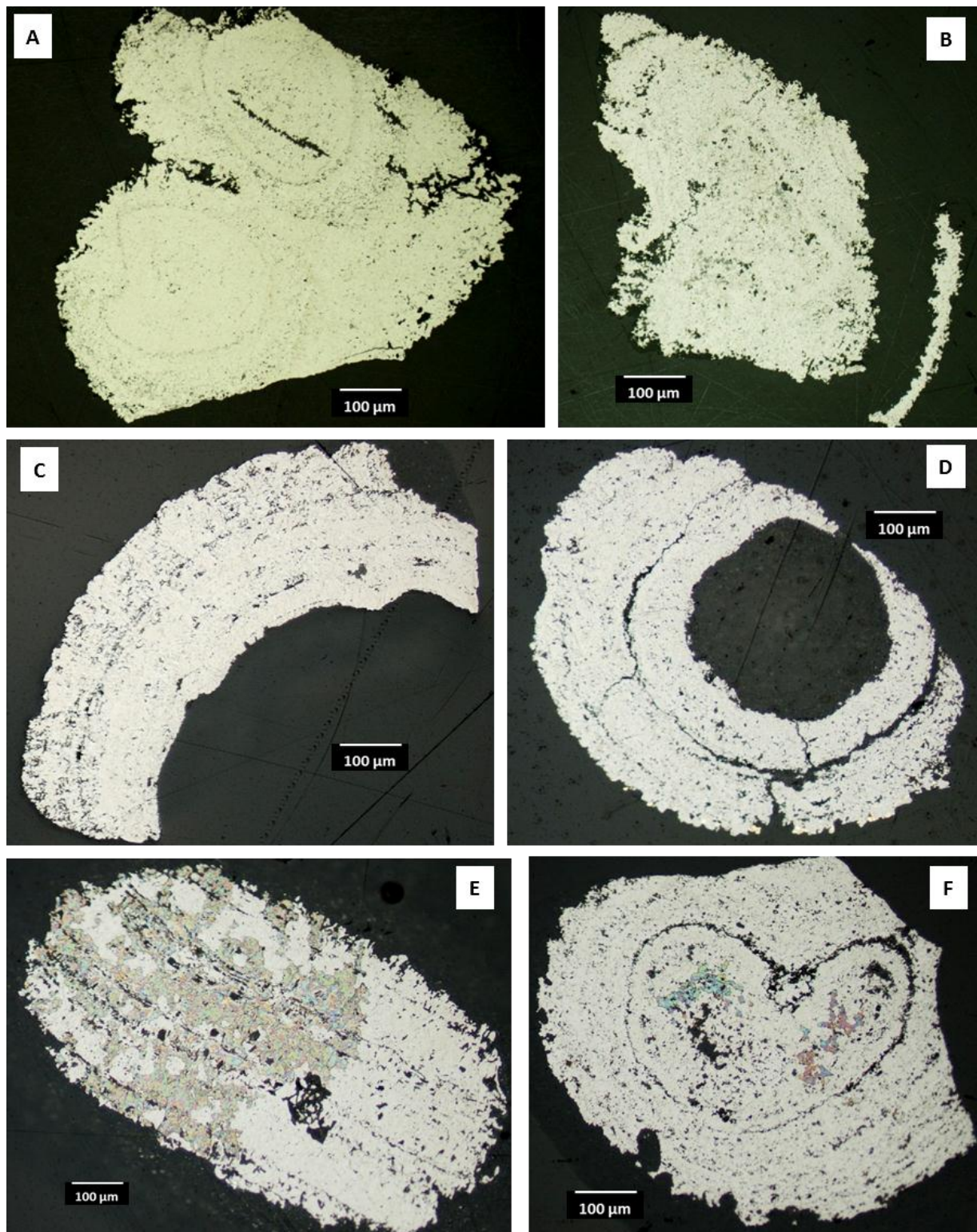
Figure 4.33: *Reflected light photomicrographs of polished sections taken under plane polarised light, showing relevant pyrite textures of pyrite grains showing a truncated colloform (curling) texture (A and B) from g52213; and (C through F) from g52227 show photomicrographs of chevron-textured pyrite clasts.*
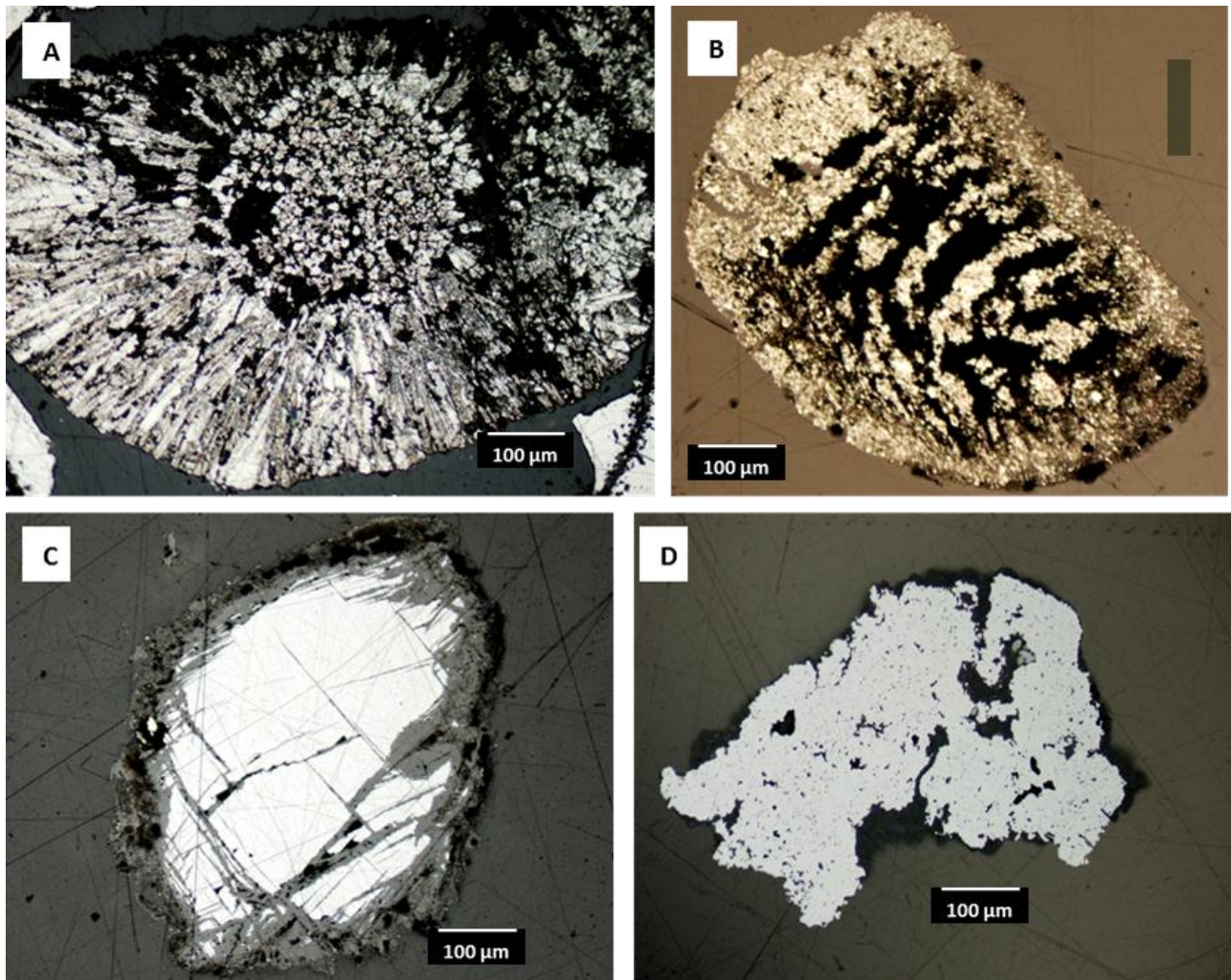
Figure 4.34: *Reflected light photomicrographs of polished sections taken under plane polarised light, showing relevant pyrite textures of pyritic nodule showing internal ooid texture (sunflower) and an outer shell of finely textured radiating pyrite (A) from g52236. (B) Leaf-like texture from VCR Kloof g52219; (C) from g52261; Rounded massive pyrite with fracture-fills of secondary pyrite growth that are connecting with an initial phase of the overgrowth pyrite (D) from section g52258.*
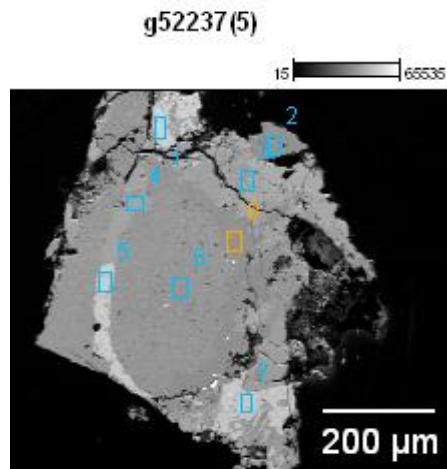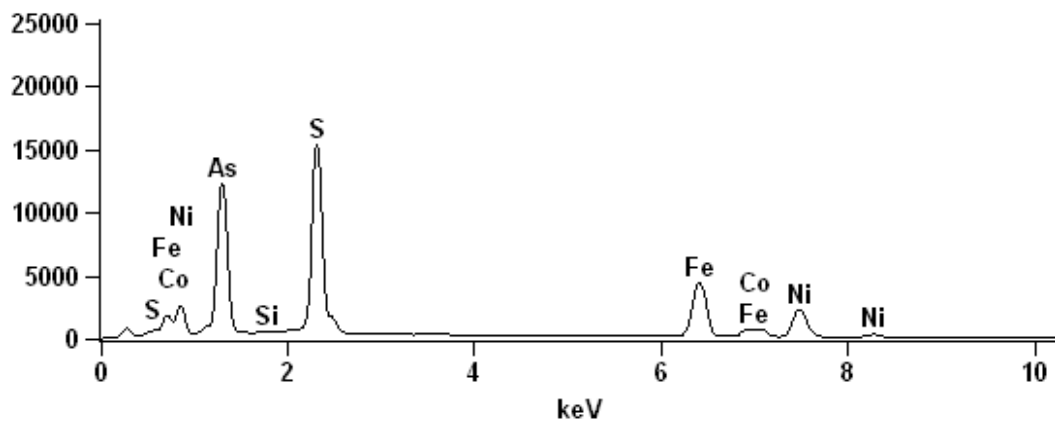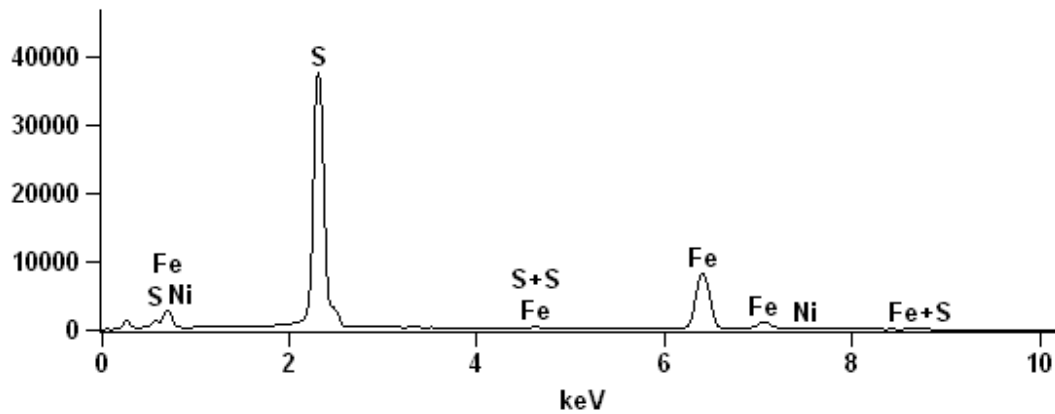
Figure 4.35 (A): Illustration of the results of SEM analyses of point one through eight on arsenopyrite, pyrite, and pentlandite grains of section g52237.
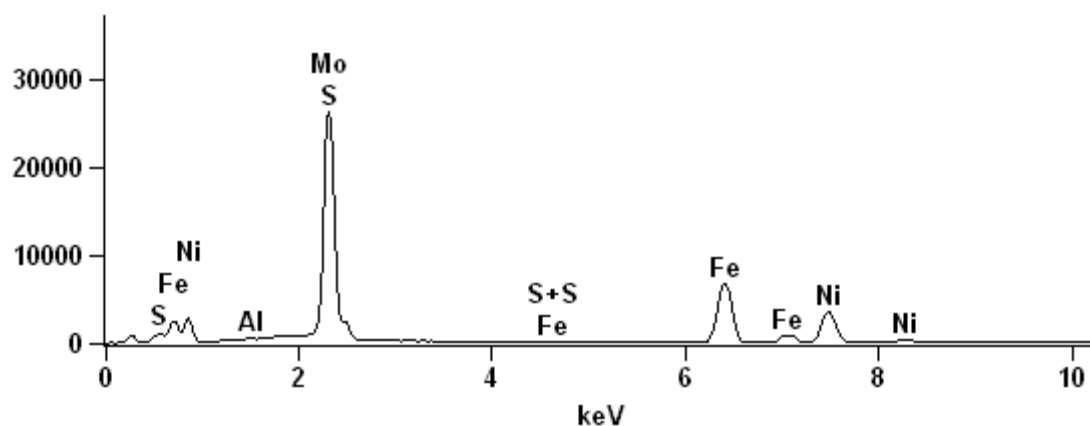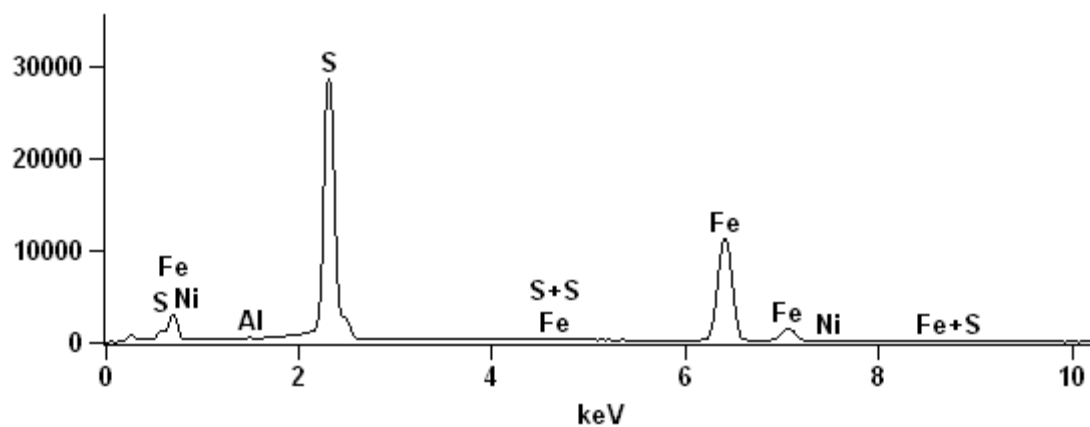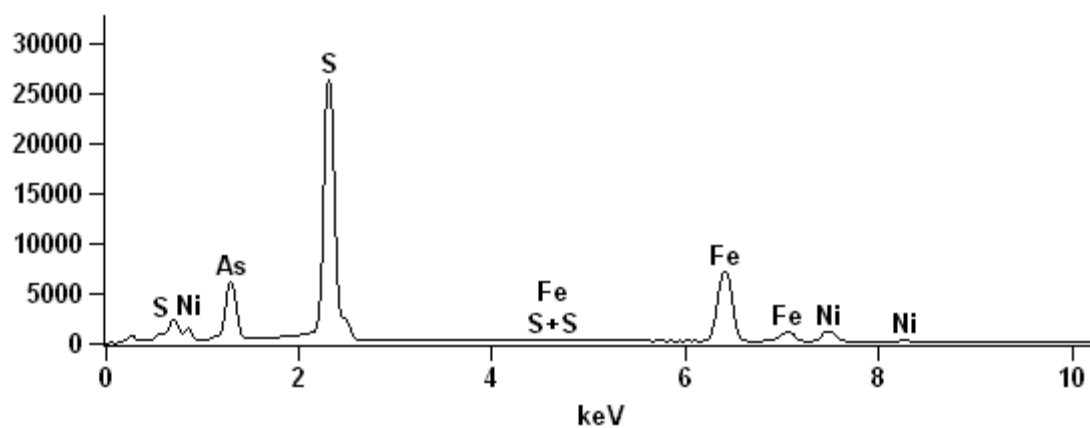
Figure 4.35 (B): *Illustration of the results of SEM analyses of point one through eight on arsenopyrite, pyrite, and pentlandite grains of section g52237.*
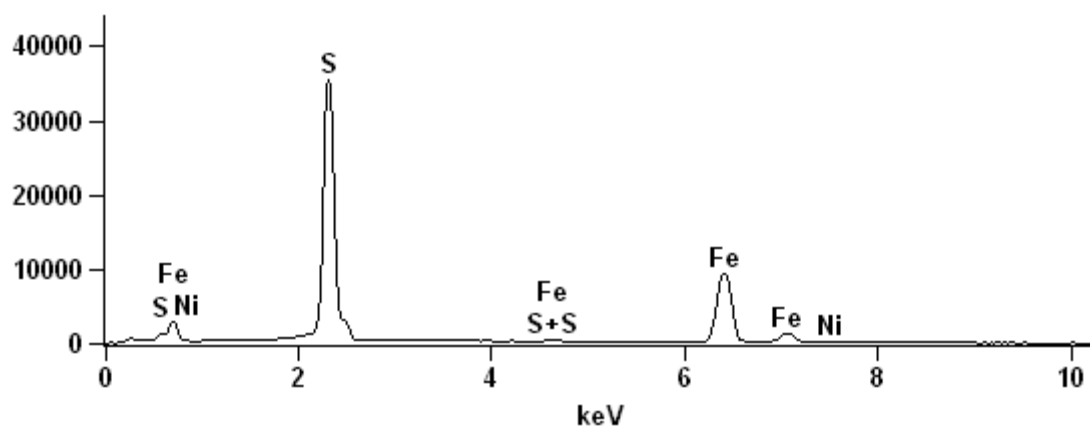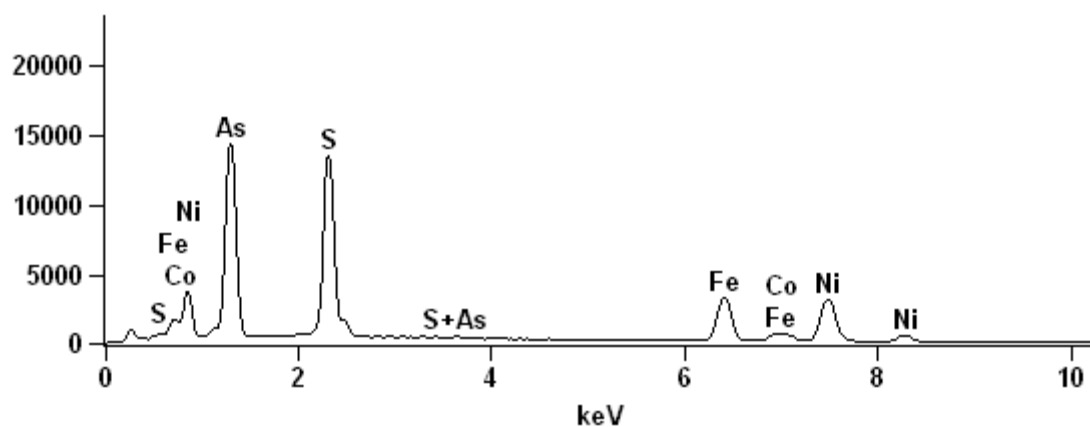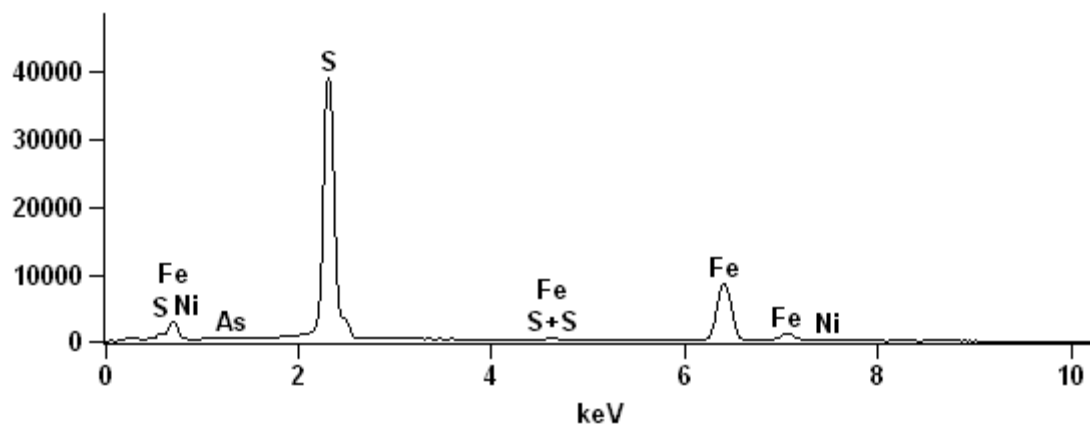
Figure 4.35 (C): *Illustration of the results of SEM analyses of point one through eight on arsenopyrite, pyrite, and pentlandite grains of section g52237.*

Table 4.4(A): *Illustration of the compositions of SEM analyses of point one through eight on arsenopyrite, pyrite, and pentlandite grains of section g52237. The dashes means below detection limits.*

K-Ratio									
Section Name	**Al**	**Si**	**S**	**Fe**	**Co**	**Ni**	**As**	**Mo**	**Mineral**
g52237(5)_pt1	-	0.00	0.20	0.24	0.03	0.17	0.36	-	Arsenopyrite
g52237(5)_pt2	-	-	0.52	0.47	-	0.01	-	-	Pyrite
g52237(5)_pt3	0.00	-	0.33	0.37	-	0.27	-	0.03	Pentlandite
g52237(5)_pt4	0.00	-	0.38	0.62	-	0.01	-	-	Pyrite
g52237(5)_pt5	-	-	0.35	0.39	-	0.08	0.18	-	Arsenopyrite
g52237(5)_pt6	-	-	0.46	0.53	-	0.01	-	-	Pyrite
g52237(5)_pt7	-	-	0.16	0.16	0.03	0.23	0.43	-	Arsenopyrite
g52237(5)_pt8	-	-	0.52	0.47	-	0.00	0.01	-	Pyrite

Weight %									
Section Name	**Al**	**Si**	**S**	**Fe**	**Co**	**Ni**	**As**	**Mo**	**Mineral**
g52237(5)_pt1	-	0.2	25.0	20.7	3.1	14.9	36.1	-	Arsenopyrite
g52237(5)_pt2	-	-	53.0	46.3	-	0.8	-	-	Pyrite
g52237(5)_pt3	0.1	-	36.8	33.9	-	26.2	-	3.0	Pentlandite
g52237(5)_pt4	0.0	-	40.2	59.2	-	0.6	-	-	Pyrite
g52237(5)_pt5	-	-	38.7	35.6	-	7.7	18.1	-	Arsenopyrite
g52237(5)_pt6	-	-	48.2	51.2	-	0.6	-	-	Pyrite
g52237(5)_pt7	-	-	21.4	13.9	2.3	19.9	42.4	-	Arsenopyrite
g52237(5)_pt8	-	-	52.8	46.1	-	0.5	0.6	-	Pyrite

Weight % Error (+/- 1 Sigma)									
Section Name	**Al**	**Si**	**S**	**Fe**	**Co**	**Ni**	**As**	**Mo**	**Mineral**
g52237(5)_pt1	-	+/-0.0	+/-0.1	+/-0.2	+/-0.2	+/-0.2	+/-0.6	-	Arsenopyrite
g52237(5)_pt2	-	-	+/-0.2	+/-0.2	-	+/-0.1	-	-	Pyrite
g52237(5)_pt3	+/-0.0	-	+/-0.3	+/-0.2	-	+/-0.2	-	+/-0.5	Pentlandite
g52237(5)_pt4	+/-0.0	-	+/-0.2	+/-0.2	-	+/-0.1	-	-	Pyrite
g52237(5)_pt5	-	-	+/-0.2	+/-0.2	-	+/-0.2	+/-0.5	-	Arsenopyrite
g52237(5)_pt6	-	-	+/-0.2	+/-0.2	-	+/-0.1	-	-	Pyrite
g52237(5)_pt7	-	-	+/-0.1	+/-0.1	+/-0.1	+/-0.2	+/-0.6	-	Arsenopyrite
g52237(5)_pt8	-	-	+/-0.2	+/-0.2	-	+/-0.1	+/-0.2	-	Pyrite

Table 4.4(B): *Illustration of the compositions of SEM analyses of point one through eight on arsenopyrite, pyrite, and pentlandite grains of section g52237. The dashes means below detection limits.*

Atom %									
Section Name	*Al*	*Si*	*S*	*Fe*	*Co*	*Ni*	*As*	*Mo*	*Mineral*
g52237(5)_pt1	-	0.4	40.1	19.0	2.7	13.0	24.8	-	Arsenopyrite
g52237(5)_pt2	-	-	66.2	33.2	-	0.5	-	-	Pyrite
g52237(5)_pt3	0.1	-	51.3	27.2	-	20.0	-	1.4	Pentlandite
g52237(5)_pt4	0.1	-	53.9	45.6	-	0.4	-	-	Pyrite
g52237(5)_pt5	-	-	54.4	28.8	-	5.9	10.9	-	Arsenopyrite
g52237(5)_pt6	-	-	61.9	37.7	-	0.4	-	-	Pyrite
g52237(5)_pt7	-	-	35.9	13.4	2.1	18.2	30.4	-	Arsenopyrite
g52237(5)_pt8	-	-	66.1	33.2	-	0.3	0.3	-	Pyrite

Atom % Error (+/- 1 Sigma)									
Section Name	*Al*	*Si*	*S*	*Fe*	*Co*	*Ni*	*As*	*Mo*	*Mineral*
g52237(5)_pt1	-	+/-0.1	+/-0.2	+/-0.2	+/-0.1	+/-0.2	+/-0.4	-	Arsenopyrite
g52237(5)_pt2	-	-	+/-0.3	+/-0.2	-	+/-0.0	-	-	Pyrite
g52237(5)_pt3	+/-0.0	-	+/-0.4	+/-0.2	-	+/-0.2	-	+/-0.2	Pentlandite
g52237(5)_pt4	+/-0.0	-	+/-0.2	+/-0.2	-	+/-0.0	-	-	Pyrite
g52237(5)_pt5	-	-	+/-0.2	+/-0.2	-	+/-0.1	+/-0.3	-	Arsenopyrite
g52237(5)_pt6	-	-	+/-0.2	+/-0.2	-	+/-0.0	-	-	Pyrite
g52237(5)_pt7	-	-	+/-0.2	+/-0.1	+/-0.1	+/-0.2	+/-0.4	-	Arsenopyrite
g52237(5)_pt8	-	-	+/-0.2	+/-0.2	-	+/-0.0	+/-0.1	-	Pyrite

g52237(6)

Image Name: g52237-(6)

Accelerating Voltage: 20.0 kV

Magnification: 150

Detector: Nano Trace
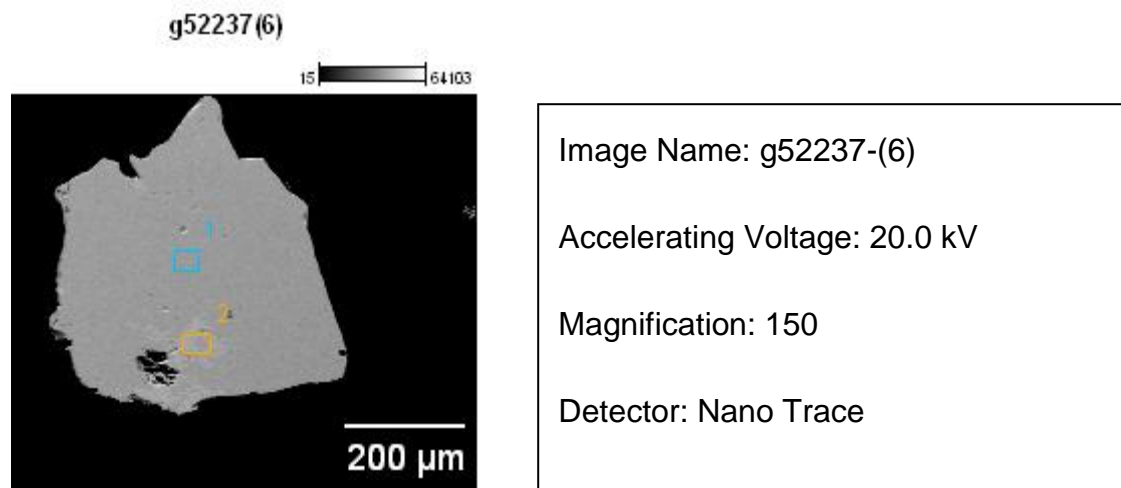
Full scale counts: 28241   g52237(6)_pt1
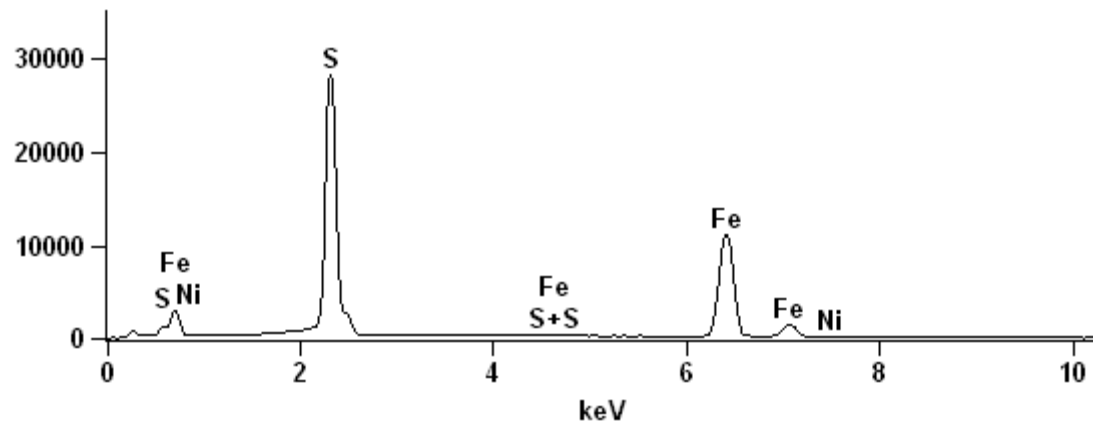
Full scale counts: 25057   g52237(6)_pt2
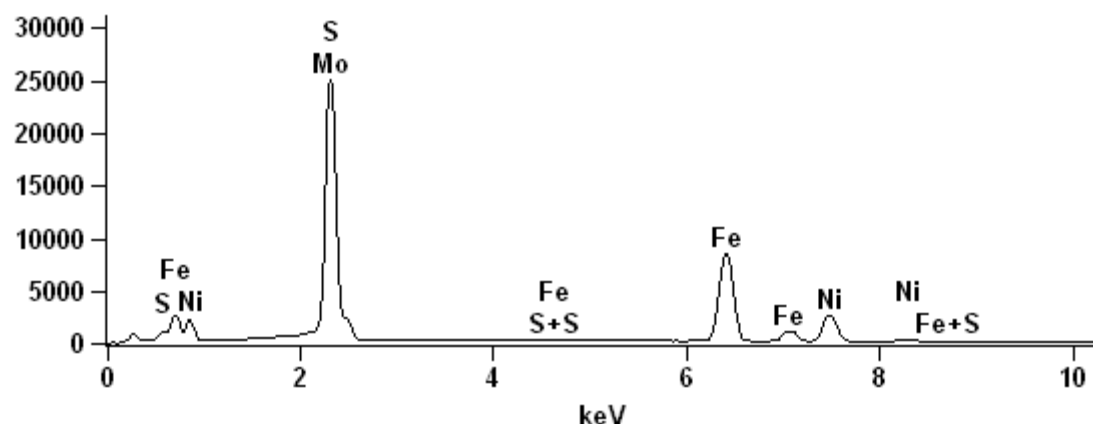
Figure 4.36: *Illustration of the results of SEM analyses point one and two on grain six of pyrite of section g52237.*

Table 4.5: *Illustration of the compositions of SEM analyses of point one and two on grain six of pyrite from section g52237. The dashes means below detection limits.*

K-Ratio					
Section Name	*S*	*Fe*	*Ni*	*Mo*	*Mineral*
g52237(6)_pt1	0.37	0.62	0.00	-	Pyrite
g52237(6)_pt2	0.31	0.46	0.20	0.03	Pyrite

Weight %					
Section Name	*S*	*Fe*	*Ni*	*Mo*	*Mineral*
g52237(6)_pt1	39.9	59.7	0.4	-	Pyrite
g52237(6)_pt2	34.5	42.7	19.6	3.2	Pyrite

Weight % Error (+/- 1 Sigma)					
Section Name	*S*	*Fe*	*Ni*	*Mo*	*Mineral*
g52237(6)_pt1	+/-0.2	+/-0.2	+/-0.1	-	Pyrite
g52237(6)_pt2	+/-0.3	+/-0.2	+/-0.2	+/-0.5	Pyrite

Atom %					
Section Name	*S*	*Fe*	*Ni*	*Mo*	*Mineral*
g52237(6)_pt1	53.6	46.1	0.3	-	Pyrite
g52237(6)_pt2	48.7	34.6	15.1	1.5	Pyrite

Atom % Error (+/- 1 Sigma)					
Section Name	*S*	*Fe*	*Ni*	*Mo*	*Mineral*
g52237(6)_pt1	+/-0.2	+/-0.2	+/-0.0	-	Pyrite
g52237(6)_pt2	+/-0.4	+/-0.2	+/-0.2	+/-0.2	Pyrite
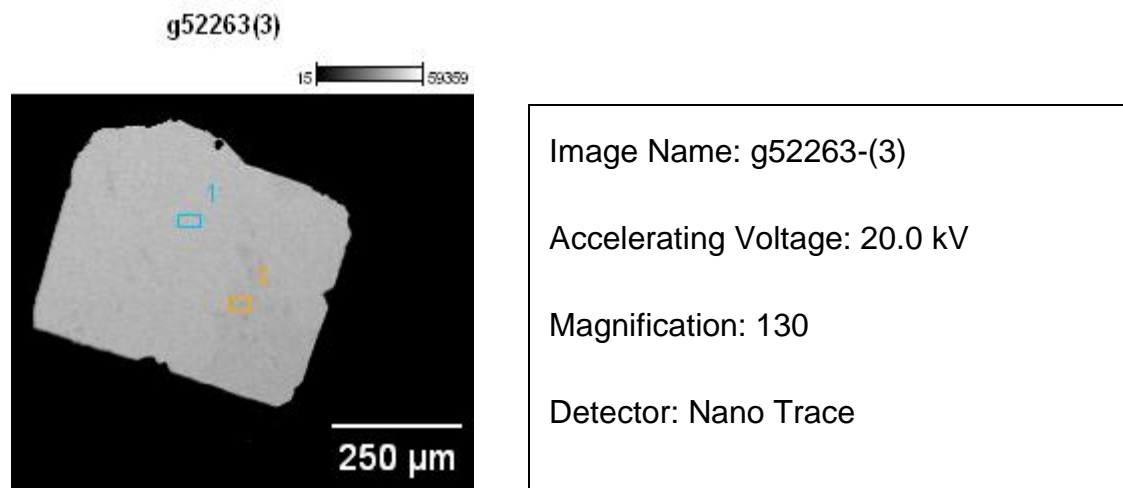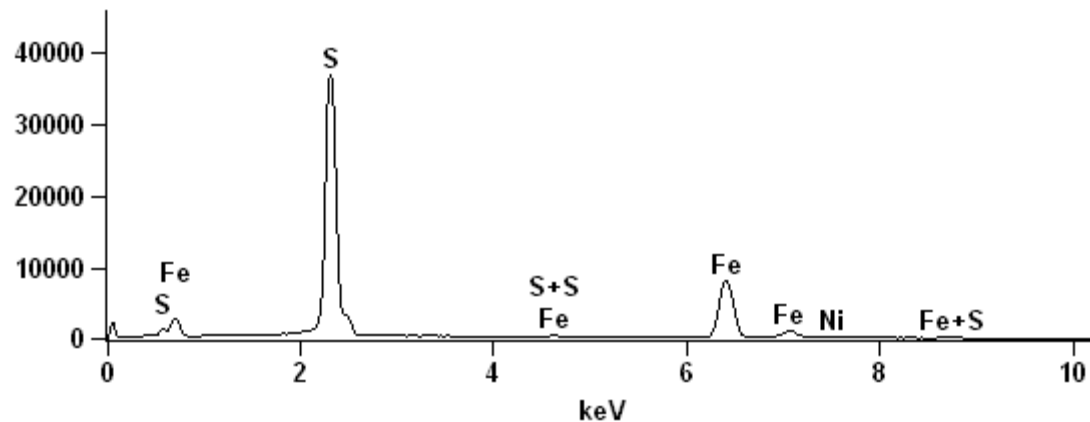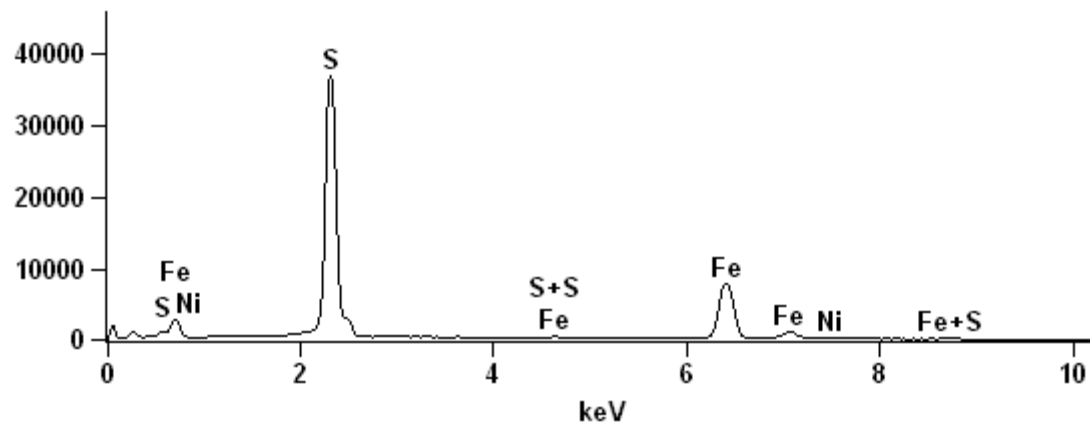
Figure 4.37: *Illustration of the results of SEM analyses at point one and two of grain three of the pyrite from section g52263.*

Table 4.6: *Illustration of the compositions of SEM analyses at point one and two on grain three pyrite from sections g52263. The dashes means below detection limits.*

K-Ratio				
Section Name	**S**	**Fe**	**Ni**	**Mineral**
g52263(3)_pt1	0.53	0.47	-	Pyrite
g52263(3)_pt2	0.53	0.47	-	Pyrite

Weight %				
Section Name	**S**	**Fe**	**Ni**	**Mineral**
g52263(3)_pt1	54.1	45.6	0.3	Pyrite
g52263(3)_pt2	54.2	45.4	0.4	Pyrite

Weight % Error (+/- 1 Sigma)				
Section Name	**S**	**Fe**	**Ni**	**Mineral**
g52263(3)_pt1	+/-0.2	+/-0.2	+/-0.1	Pyrite
g52263(3)_pt2	+/-0.2	+/-0.2	+/-0.1	Pyrite

Atom %				
Section Name	**S**	**Fe**	**Ni**	**Mineral**
g52263(3)_pt1	67.3	32.5	0.2	Pyrite
g52263(3)_pt2	67.3	32.4	0.3	Pyrite

Atom % Error (+/- 1 Sigma)				
Section Name	**S**	**Fe**	**Ni**	**Mineral**
g52263(3)_pt1	+/-0.3	+/-0.2	+/-0.0	Pyrite
g52263(3)_pt2	+/-0.3	+/-0.2	+/-0.0	Pyrite

GS2239(2)
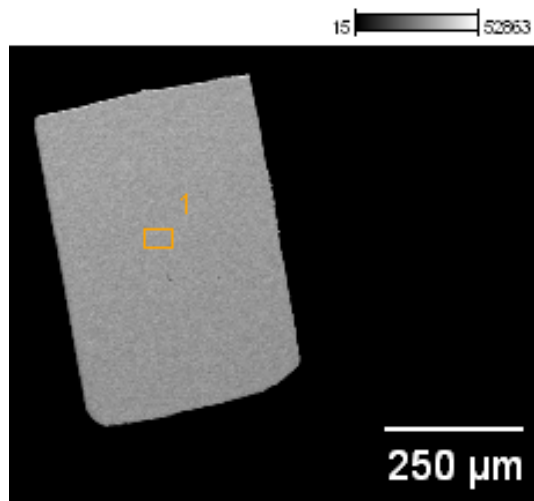
Image Name: GS2239-(2)

Accelerating Voltage: 20.0 kV

Magnification: 120

Detector: Nano Trace

Full scale counts: 17396   GS2239(2)_pt1
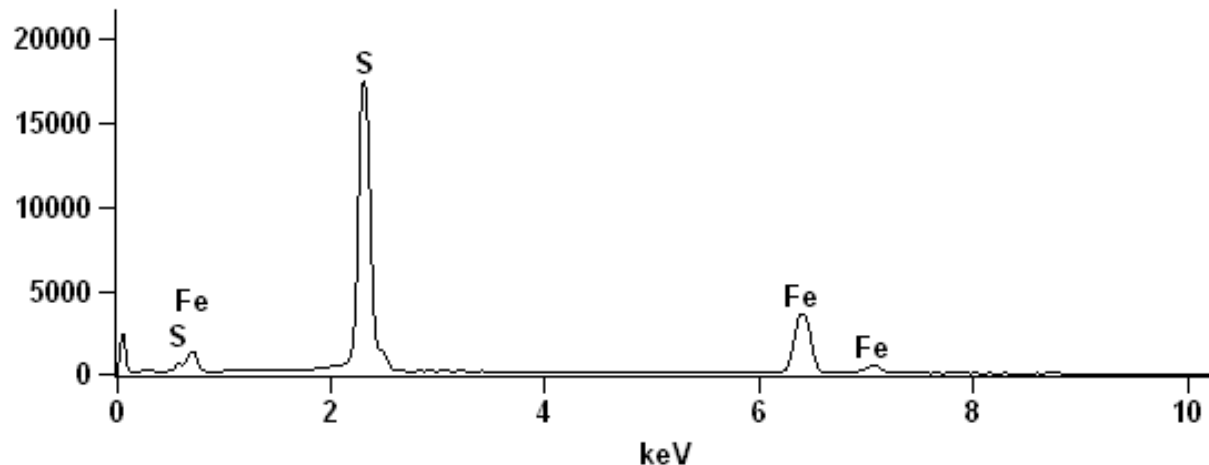
Figure 4.38: *Illustration of the results of SEM analyses of point one of grain two of pyrite from section g52239.*

Table 4.7: *Illustration of the compositions of SEM analyses for a single point on grain two of pyrite from section g52239. The dashes means below detection limits.*

K-Ratio			
Section Name	*S*	*Fe*	*Mineral*
GS2239(2)_pt1	0.54	0.46	Pyrite

Weight %			
Section Name	*S*	*Fe*	*Mineral*
GS2239(2)_pt1	55.0	45.0	Pyrite

Weight % Error (+/- 1 Sigma)			
Section Name	*S*	*Fe*	*Mineral*
GS2239(2)_pt1	+/-0.2	+/-0.3	Pyrite

Atom %			
Section Name	*S*	*Fe*	*Mineral*
GS2239(2)_pt1	68.0	32.0	Pyrite

Atom % Error (+/- 1 Sigma)			
Section Name	*S*	*Fe*	*Mineral*
GS2239(2)_pt1	+/-0.3	+/-0.2	Pyrite
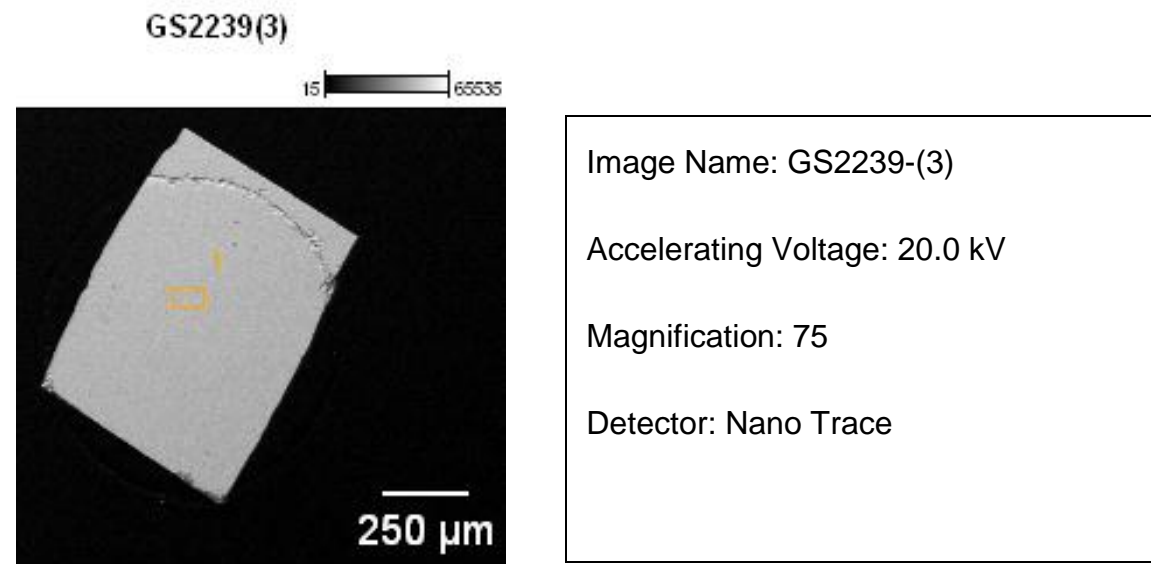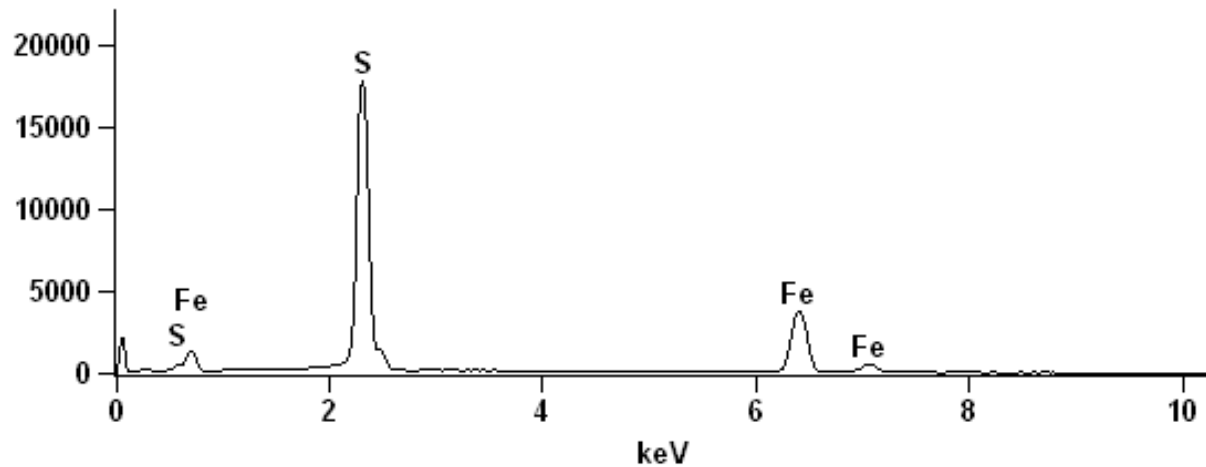
Figure 4.39: *Illustration of the results of SEM analyses for a single point on grain three of pyrite from section g52239.*

Table 4.8: *Illustration of the compositions of SEM analyses for a single pyrite grain two of section g52239.*

K-Ratio			
Section Name	*S*	*Fe*	*Mineral*
GS2239(3)_pt1	0.54	0.46	Pyrite
Weight %			
Section Name	*S*	*Fe*	*Mineral*
GS2239(3)_pt1	55.0	45.0	Pyrite
Weight % Error (+/- 1 Sigma)			
Section Name	*S*	*Fe*	*Mineral*
GS2239(3)_pt1	+/-0.2	+/-0.3	Pyrite
Atom %			
Section Name	*S*	*Fe*	*Mineral*
GS2239(3)_pt1	68.1	31.9	Pyrite
Atom % Error (+/- 1 Sigma)			
Section Name	*S*	*Fe*	*Mineral*
GS2239(3)_pt1	+/-0.3	+/-0.2	Pyrite

VL 225(7)
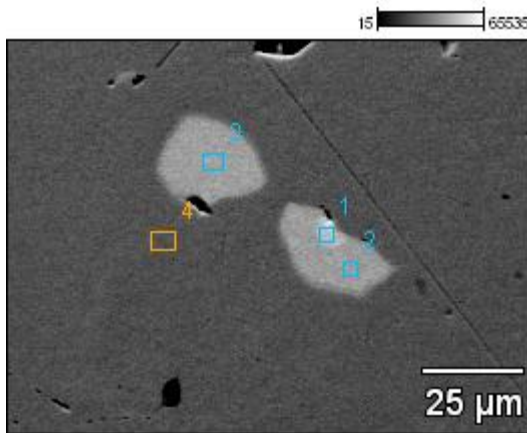
Image **Name:** VL 225(7)

Accelerating Voltage: 20.0 kV

Magnification: 1000

Detector: Nano Trace

Full scale counts: 20856   VL 225(7)_pt1
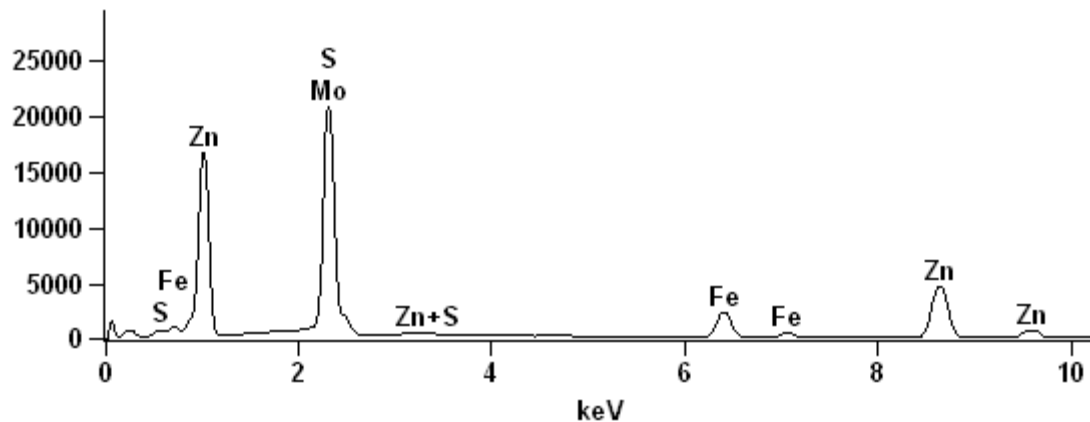
Full scale counts: 22989   VL 225(7)_pt2
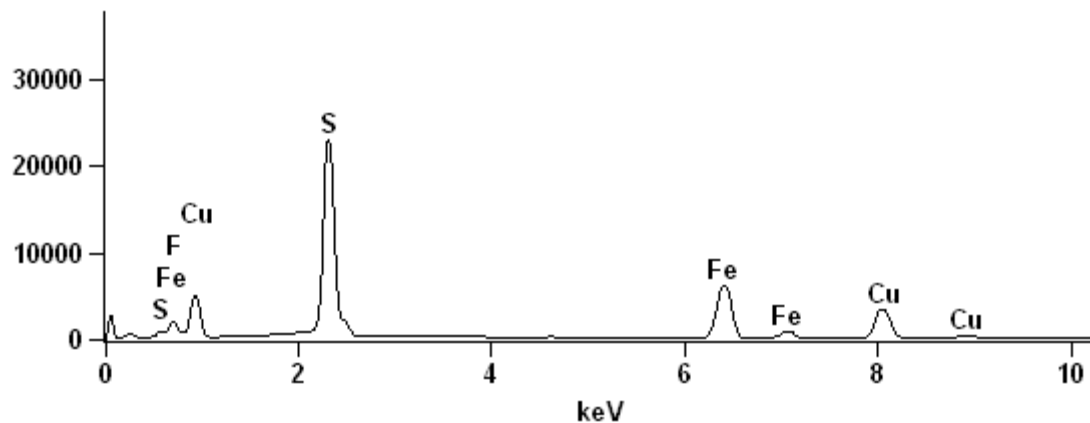
Figure 4.40 (A): *Illustration of the results of SEM analyses at point one through four on grain seven of a pyrite from section VL225.*
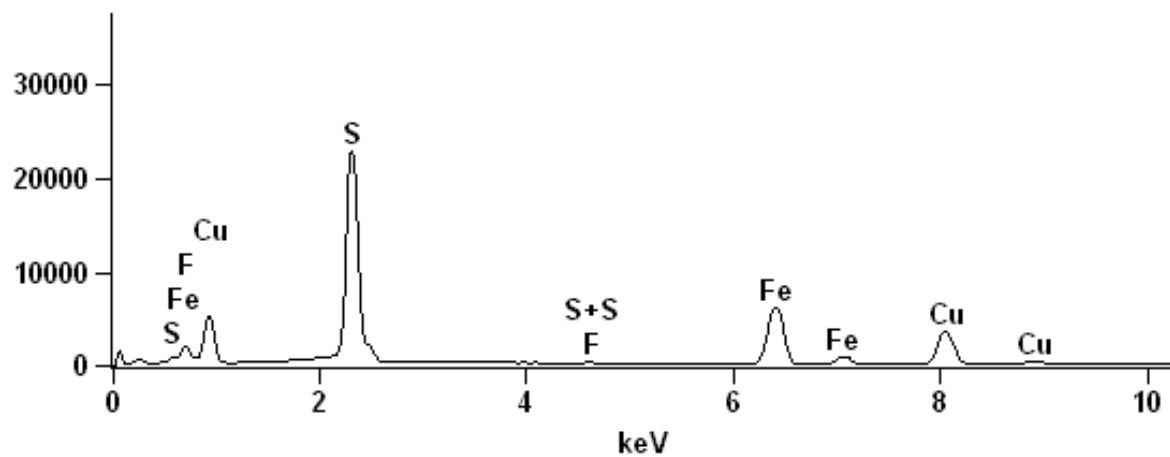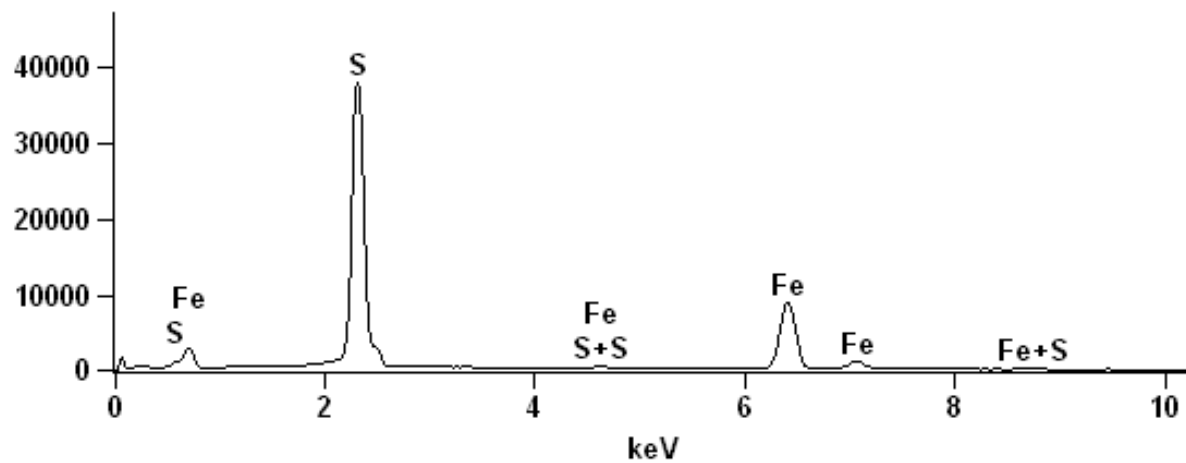
Figure 4.40 (B): Illustration of the results of SEM analyses at point one through four on grain seven of a pyrite from section VL225.

Table 4.9: *Ilustration of the results of SEM analyses at point one through four on grain seven of a pyrite from section VL225. The dashes means below detection limits.*

K-Ratio							
Section Name	**F**	**S**	**Fe**	**Cu**	**Zn**	**Mo**	**Mineral**
VL 225(7)_pt1	-	0.27	0.13		0.58	0.02	Sphalerite
VL 225(7)_pt2	0.00	0.31	0.35	0.34	-	-	Chalcopyrite
VL 225(7)_pt3	0.00	0.31	0.35	0.35	-	-	Chalcopyrite
VL 225(7)_pt4	-	0.52	0.48		-	-	Pyrite
Weight %							
Section Name	**F**	**S**	**Fe**	**Cu**	**Zn**	**Mo**	**Mineral**
VL 225(7)_pt1	-	32.2	11.0		54.1	2.8	Sphalerite
VL 225(7)_pt2	0.0	34.9	31.4	33.7	-	-	Chalcopyrite
VL 225(7)_pt3	0.0	34.9	31.1	33.9	-	-	Chalcopyrite
VL 225(7)_pt4	-	53.3	46.7		-	-	Pyrite
Weight % Error (+/- 1 Sigma)							
Section Name	**F**	**S**	**Fe**	**Cu**	**Zn**	**Mo**	**Mineral**
VL 225(7)_pt1	-	+/-0.3	+/-0.1		+/-0.4	+/-0.5	Sphalerite
VL 225(7)_pt2	+/-0.0	+/-0.1	+/-0.2	+/-0.3	-	-	Chalcopyrite
VL 225(7)_pt3	+/-0.0	+/-0.1	+/-0.2	+/-0.3	-	-	Chalcopyrite
VL 225(7)_pt4	-	+/-0.2	+/-0.2		-	-	Pyrite
Atom %							
Section Name	**F**	**S**	**Fe**	**Cu**	**Zn**	**Mo**	**Mineral**
VL 225(7)_pt1	-	48.8	9.5		40.3	1.4	Sphalerite
VL 225(7)_pt2	0.0	49.9	25.8	24.4	-	-	Chalcopyrite
VL 225(7)_pt3	0.0	50.0	25.6	24.5	-	-	Chalcopyrite
VL 225(7)_pt4	-	66.5	33.5		-	-	Pyrite
Atom % Error (+/- 1 Sigma)							
Section Name	**F**	**S**	**Fe**	**Cu**	**Zn**	**Mo**	**Mineral**
VL 225(7)_pt1	-	+/-0.4	+/-0.1		+/-0.3	+/-0.2	Sphalerite
VL 225(7)_pt2	+/-0.0	+/-0.2	+/-0.2	+/-0.2	-	-	Chalcopyrite
VL 225(7)_pt3	+/-0.0	+/-0.2	+/-0.2	+/-0.2	-	-	Chalcopyrite
VL 225(7)_pt4	-	+/-0.2	+/-0.2		-	-	Pyrite

THE PARTICLE INDUCED X-RAY EMISSION SPECTRA
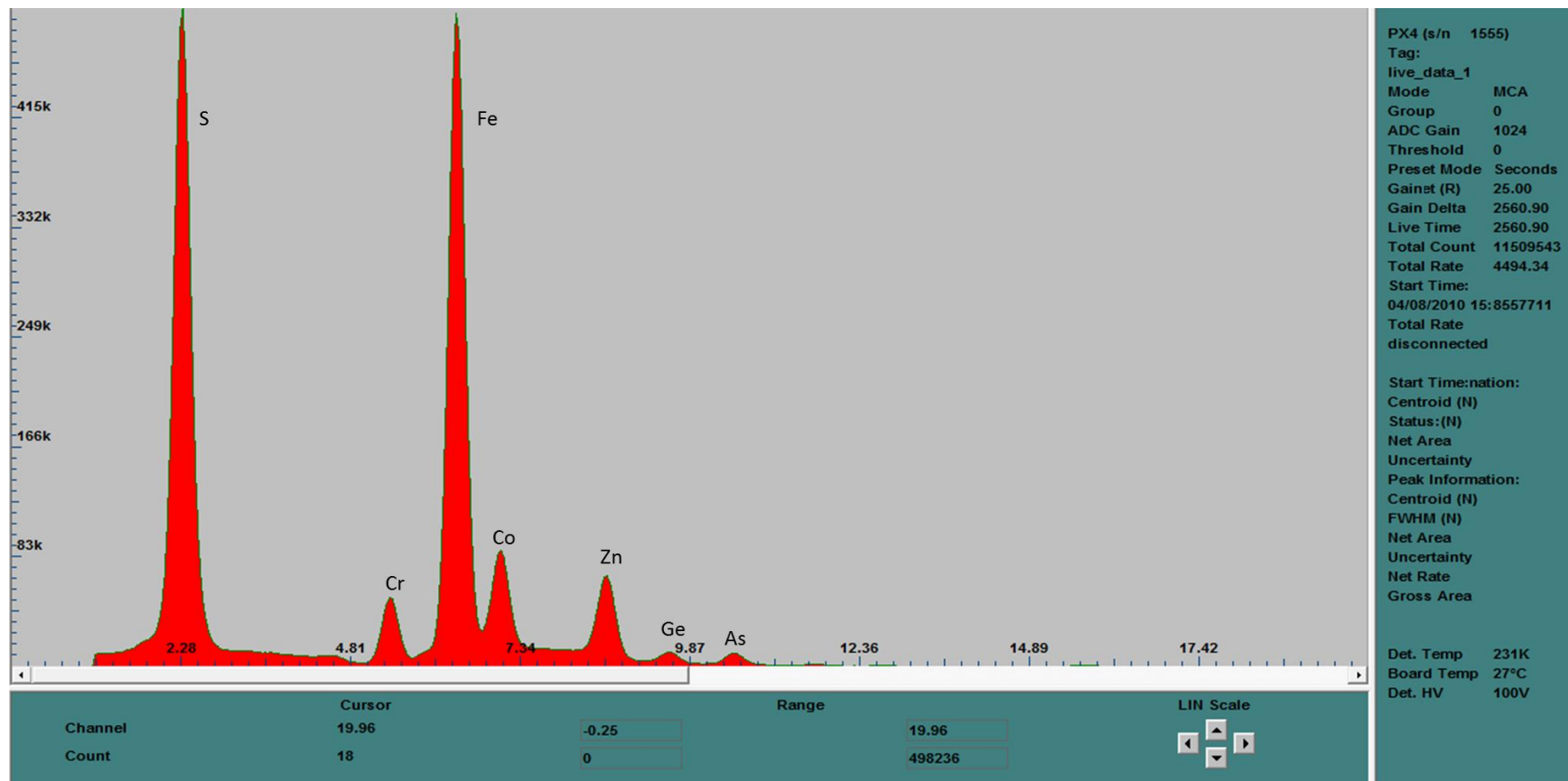
Figure 4.41: *Analyses of section g52203 show a general chemical composition. The spectrum shows S, Cr, Fe, Co, Zn, Ge, and As with the total counts of 11509543, and live time of 2560.90 seconds.*
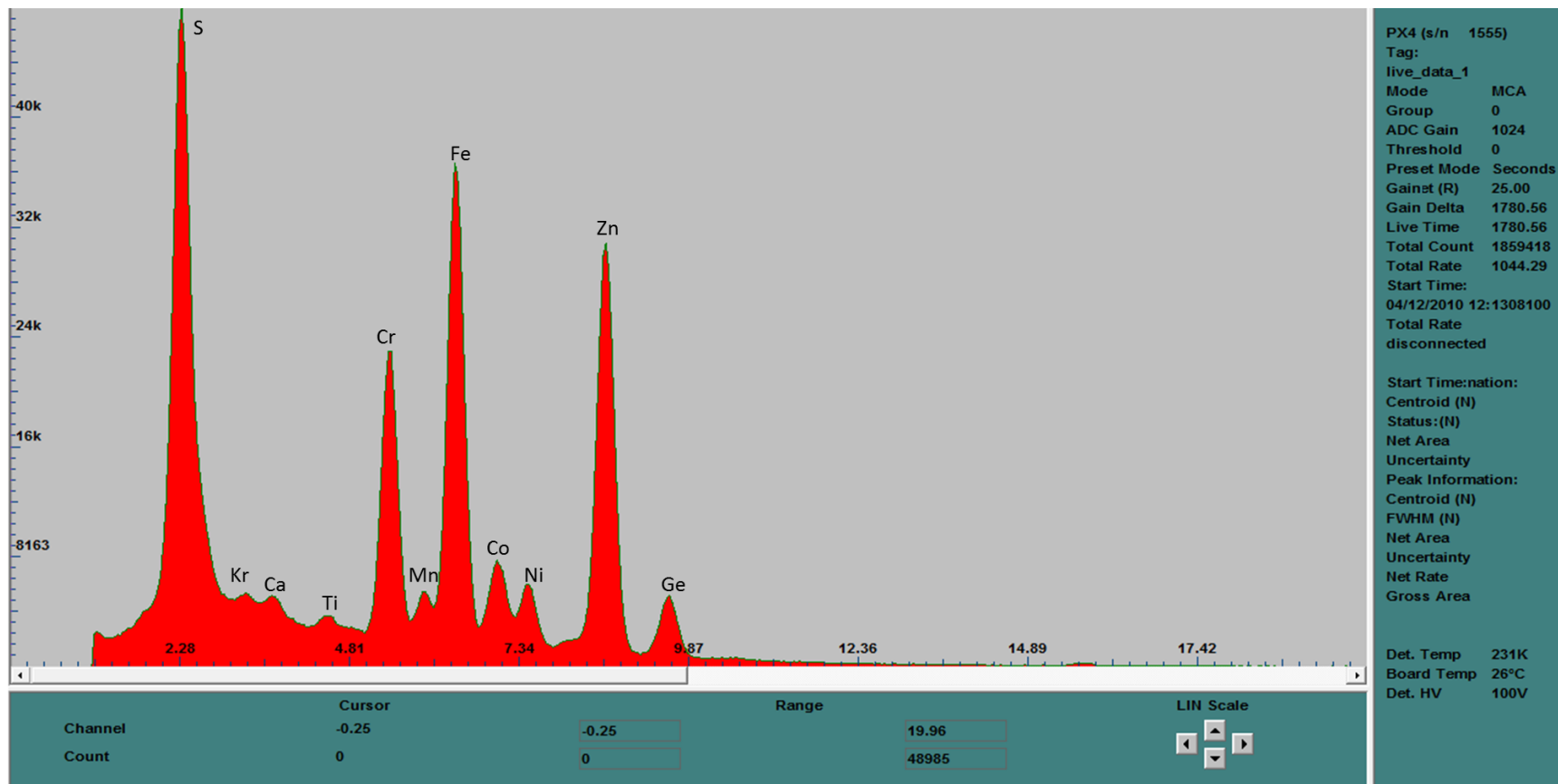
Figure 4.42: *Analyses of section g52288 show a general chemical composition. The spectrum shows S, K, Ca, Ti, Cr, Mn, Fe, Co, Ni, Zn and Ge with total counts of 1859418, and live time of 1780.56 seconds.*
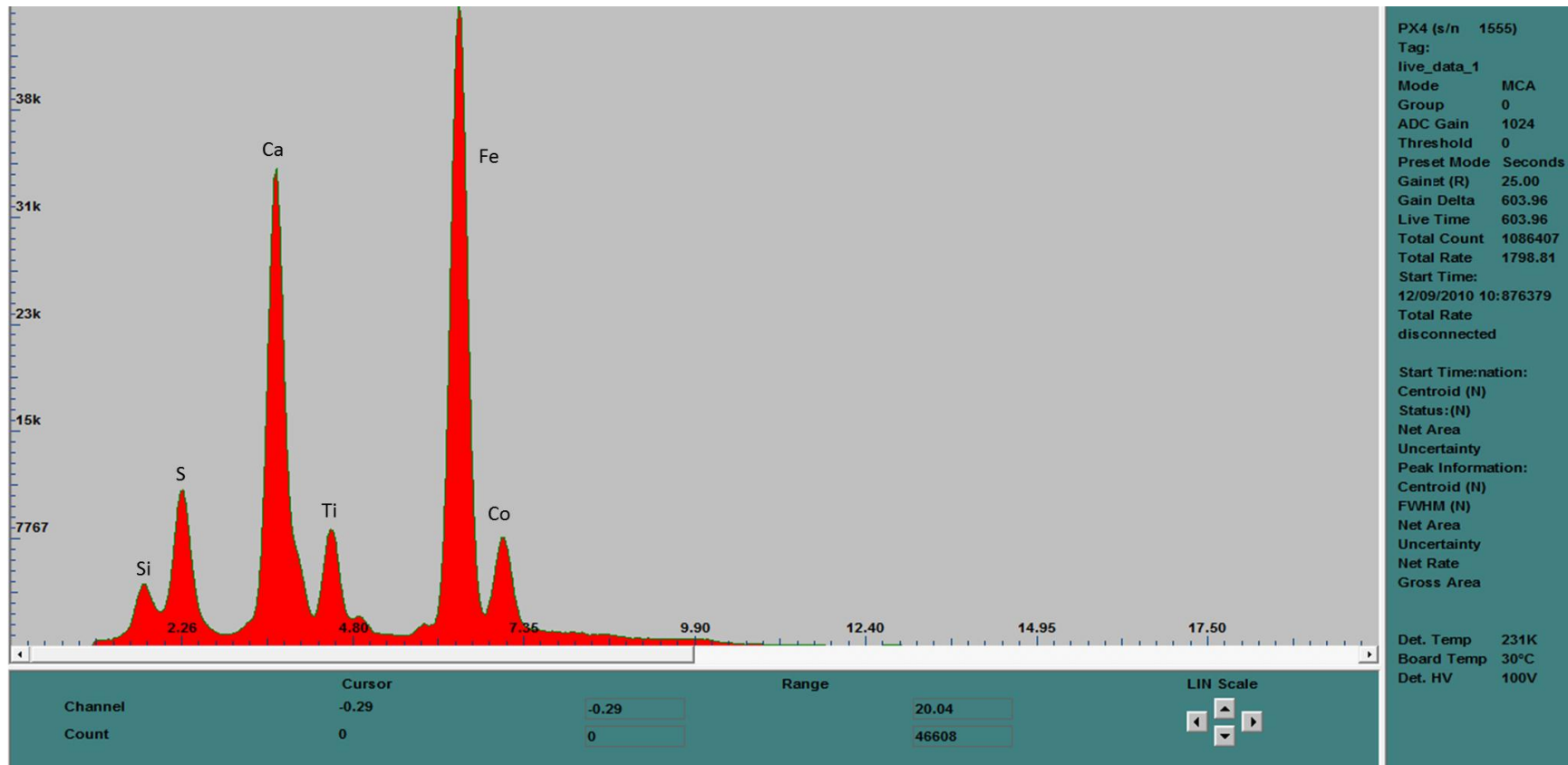
Figure 4.43: *Analyses of section Heaves 3472 show a general chemical composition. The spectrum shows Si, S, Ca, Ti, Fe, and Co with total counts of 1086407, and live time of 603.96 seconds.*
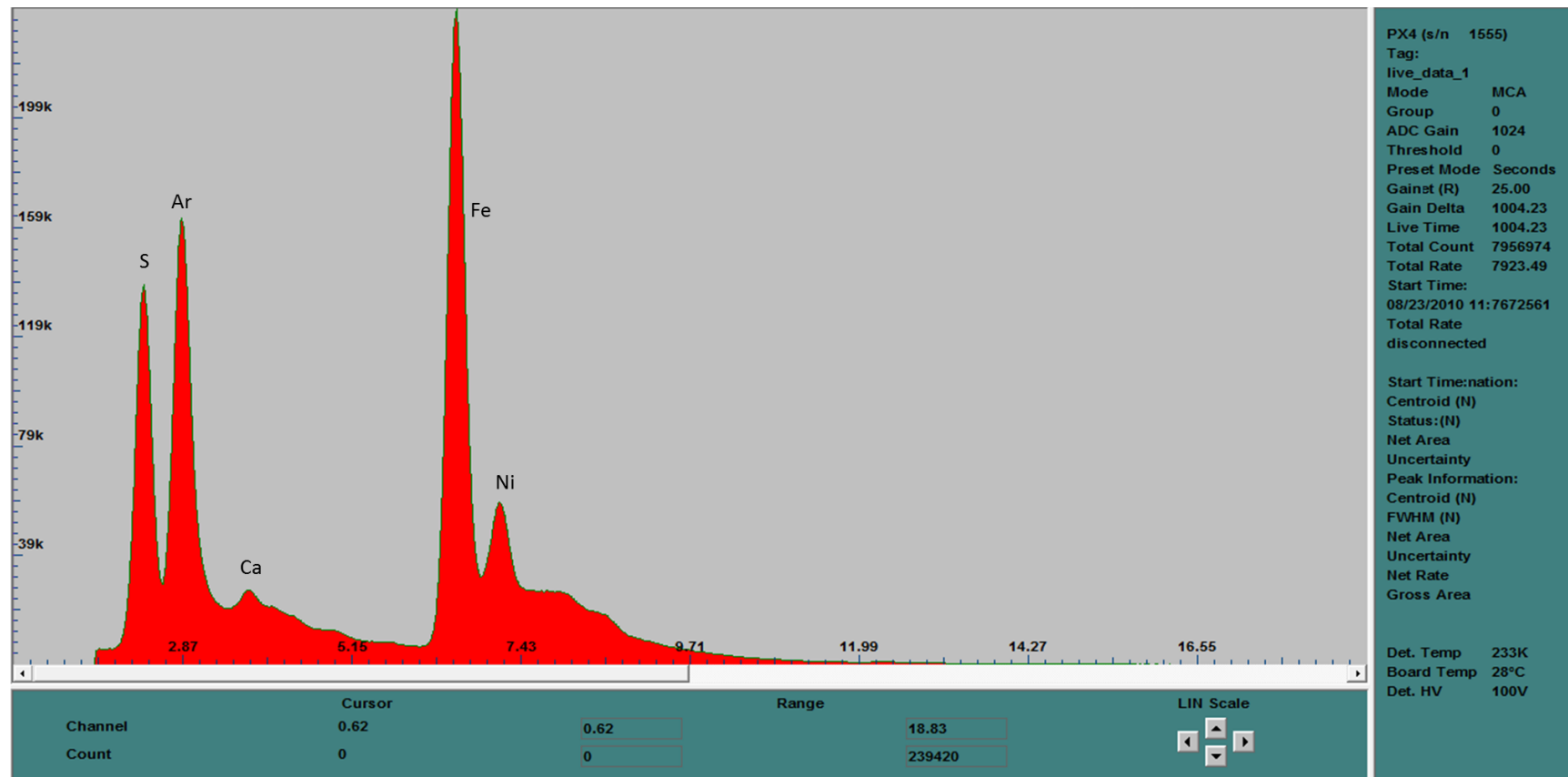
Figure 4.44: *Analyses of section VL228 show a general chemical composition. The spectrum shows S, Ar, Ca, Fe, and Ni with the total counts of 7956974, and live time of 1004.23 seconds.*
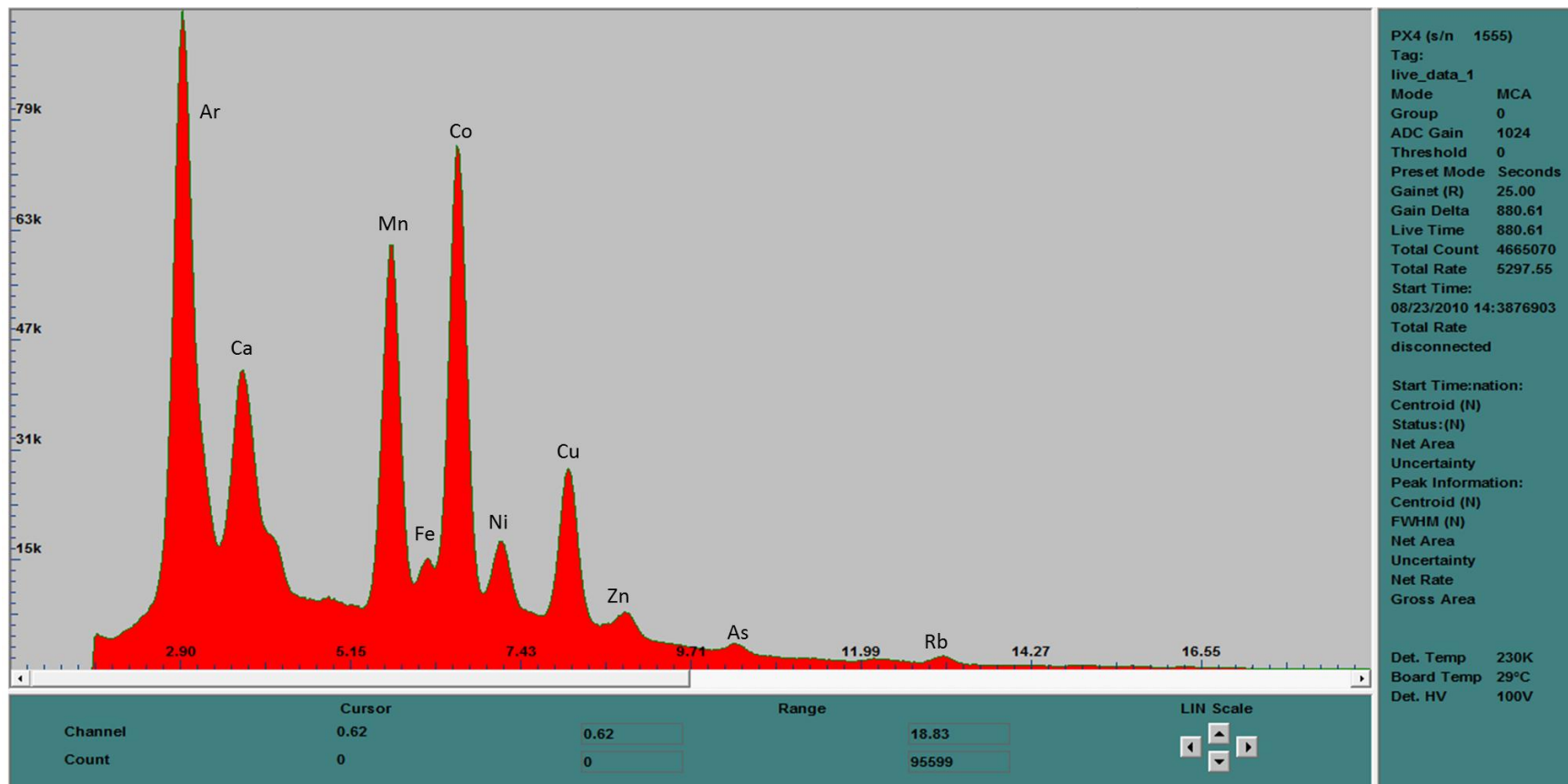
Figure 4.45: *Analyses of section g52688 show a general chemical composition. The spectrum shows Ar, Ca, Mn, Fe, Co, Ni, Cu, Zn, As, and Rb with the total counts of 4665070, and live time of 880.61 seconds.*
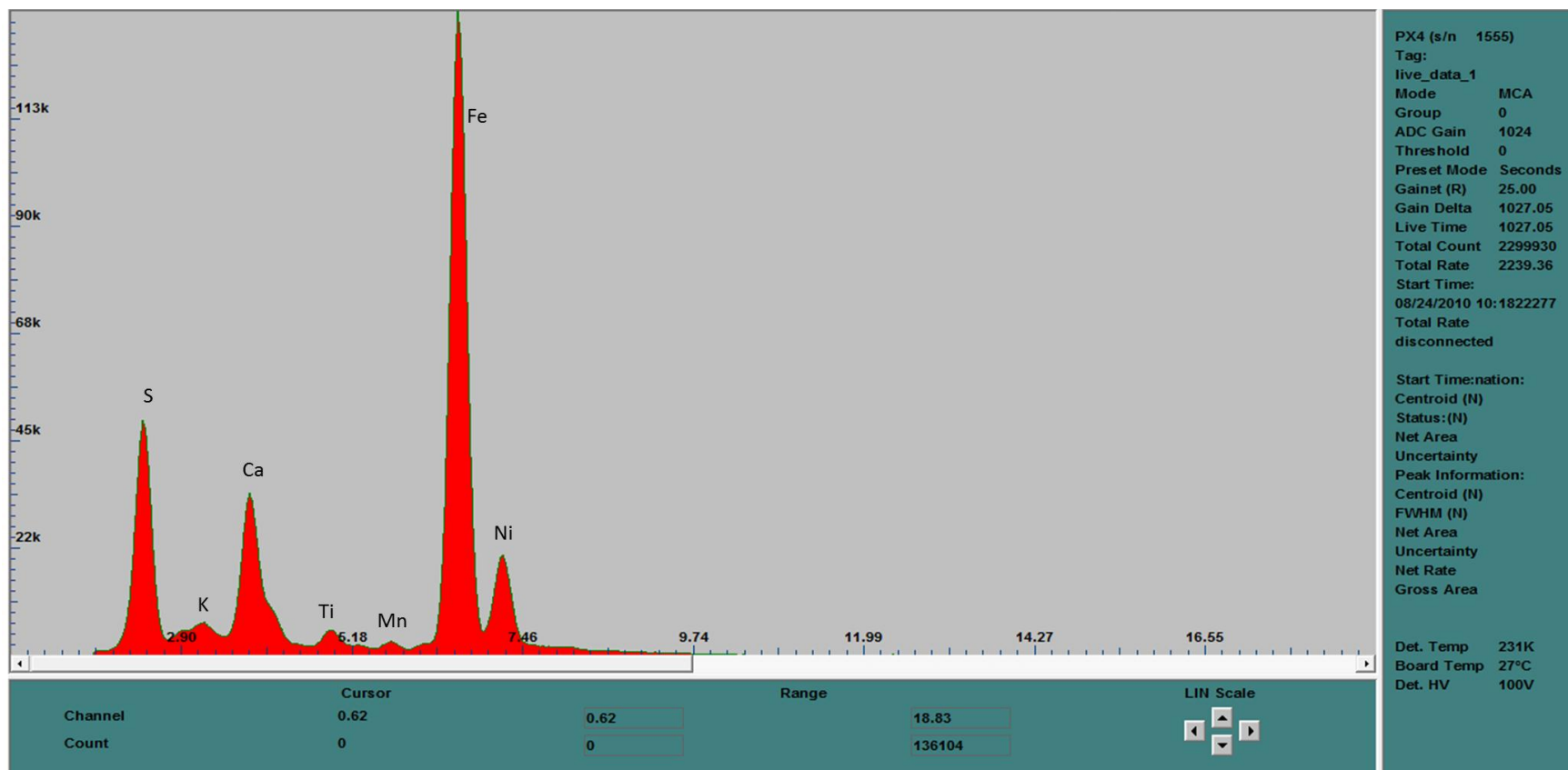
Figure 4.46: *Analyses of section 3719 show a general chemical composition. The spectrum shows S, K, Ca, Ti, Mn, Fe, and Ni and with the total counts of 2299930, and live time of 1027.06 seconds.*
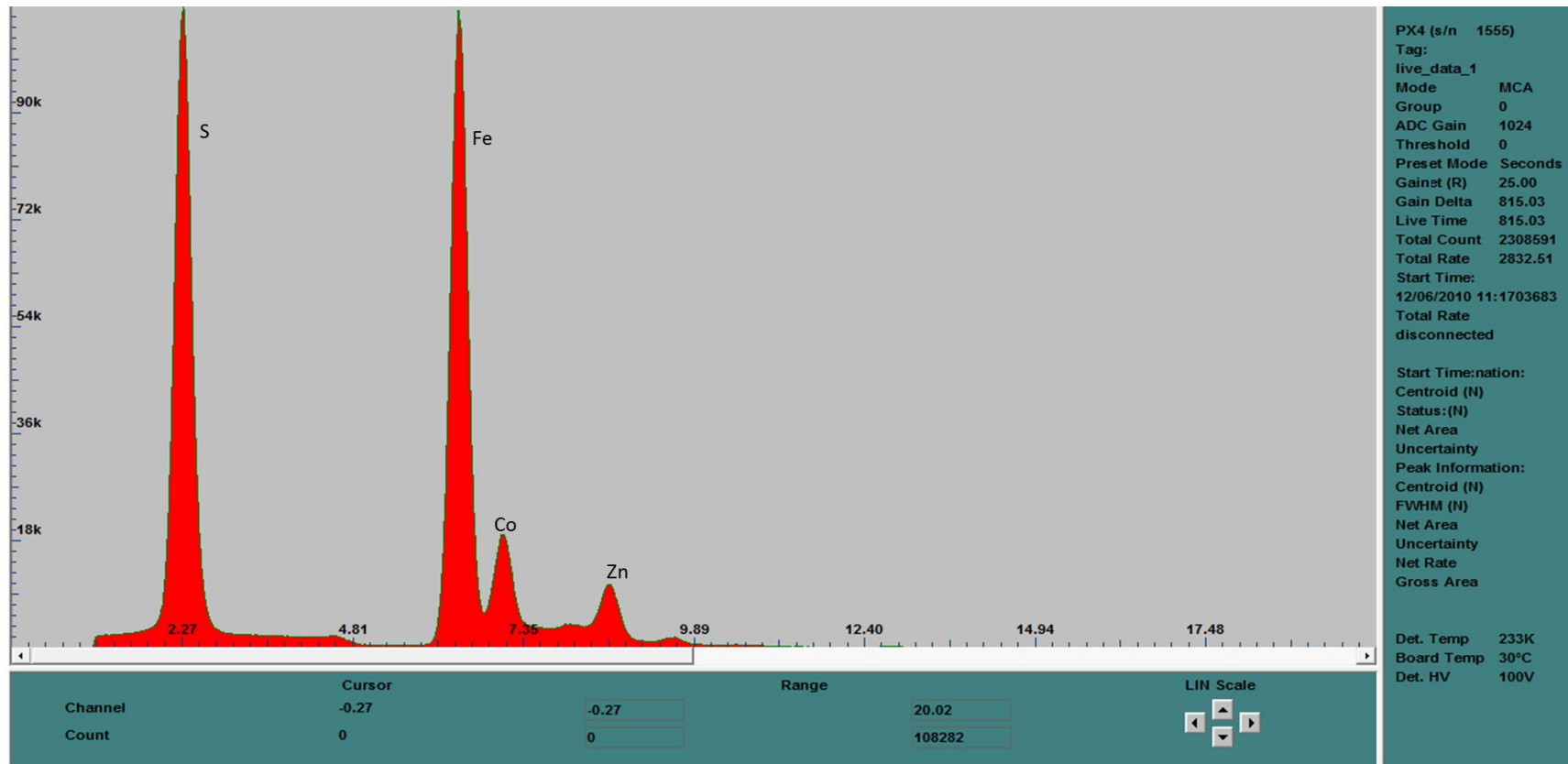
Figure 4.47: *Analyses of section g52260 show a general chemical composition. The spectrum shows S, Fe, Co, and Zn with the total counts of 2308591, and live time of 815.03 seconds.*
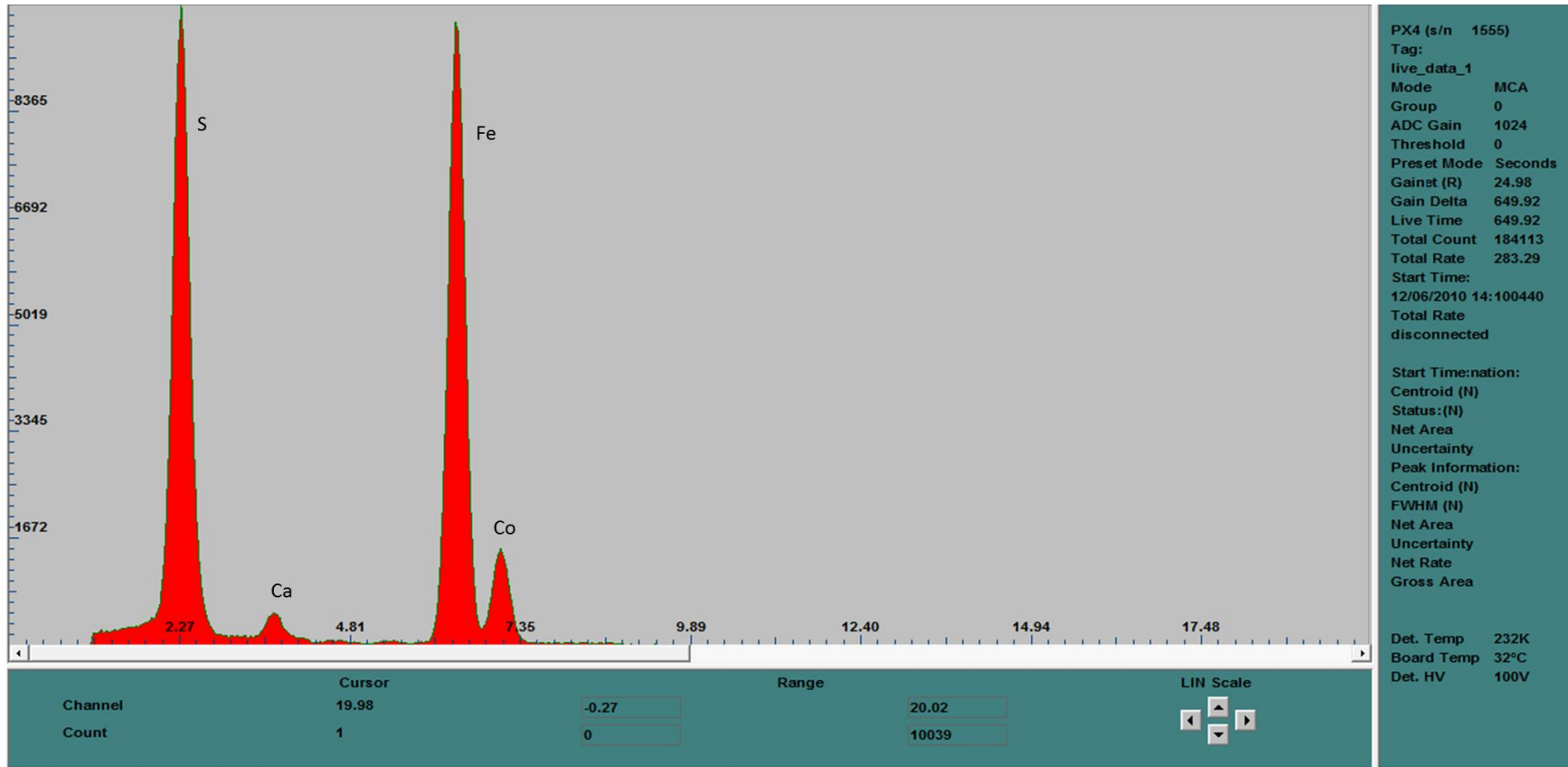
Figure 4.48: Analyses of section g52201 show a general chemical composition. The spectrum shows S, Ca, Fe, and Co with the total counts of 184113 and live time of 649.92 seconds.

TABLES FOR EMPA AND LA-ICP-MS DATA, AND SCATTER PLOTS OF LA-ICP-MS DATA

Table 5.1(B): *Measured concentrations of Ni and Co reported in wt % obtained by EMPA for 172 data points from section g52228, g52236, g52237 containing rounded pyrite grains with n = 30. The dashes mean below detection limits.*

Dataset	S (wt %)	Fe (wt %)	Co (wt %)	Ni (wt %)	Total (wt %)	Comment	Pyrite Type
36	53.29	47.03	-	0.01	100.32	g52228	Rounded
37	53.45	46.80	-	0.01	100.27	g52228	Rounded
38	52.61	46.34	-	0.02	98.97	g52228	Rounded
39	53.56	46.88	-	0.01	100.44	g52228	Rounded
40	53.29	46.78	-	0.01	100.07	g52228	Rounded
41	53.00	46.83	-	0.00	99.83	g52228	Rounded
42	53.21	46.66	-	0.02	99.88	g52228	Rounded
43	53.11	46.68	0.04	0.01	99.84	g52228	Rounded
44	53.55	46.58	-	0.01	100.14	g52228	Rounded
45	53.34	46.93	-	0.01	100.28	g52228	Rounded
46	50.18	44.34	0.00	0.05	94.57	g52237	Rounded
47	52.73	46.22	-	0.04	98.99	g52237	Rounded
48	52.73	45.90	0.00	0.02	98.65	g52237	Rounded
49	52.90	45.94	-	0.01	98.85	g52237	Rounded
50	51.74	45.62	-	0.04	97.41	g52237	Rounded
51	43.26	55.22	0.02	0.48	98.99	g52237	Rounded
52	46.17	52.84	0.04	0.58	99.62	g52237	Rounded
53	51.94	46.17	0.09	0.52	98.72	g52237	Rounded
54	51.76	45.78	-	0.05	97.60	g52237	Rounded
55	49.81	49.39	0.03	0.42	99.65	g52237	Rounded
56	52.88	46.54	-	0.01	99.43	g52236	Rounded
57	52.86	46.76	-	0.00	99.62	g52236	Rounded

Tables 5.3(B): *16302 data points obtained from a total of 75 elements from the analyses of 18 polished sections containing representative grains of rounded and angular pyrite. For simplicity, only 11 from a total of 75 elements are shown in the table. The table shows a section name accompanied by a grain number and spot number, the number after the element name indicates that the element is an isotope, and the type of the pyrite grains. The concentrations are reported in percentages (%). Dashes imply below detection limits*

Sample Name	Sulphur 33	Iron 57	Cobalt 59	Nickel 61	Copper 65	Zinc 68	Arsenic 75	Gold 197	Lead 208	Silver 109	Zirconium 91	Pyrite Type
G52210-01-01	-	-	10.2677	0.4146	0.4784	-	2.8844	0.0138	1.6143	0.0290	0.0083	Rounded Porous
G52210-01-02	-	-	20.7850	0.4956	0.6842	-	4.0579	0.0092	1.6474	0.0250	0.0038	Rounded Porous
G52210-02-01	-	-	5.3309	0.9108	0.5642	0.0028	2.6999	0.0097	1.8953	0.0373	0.0016	Rounded Porous
G52210-02-02	-	-	7.3725	0.9925	0.5849	0.0077	3.9820	0.0112	3.3636	0.0472	0.0014	Rounded Porous
G52210-03-01	-	-	5.8892	0.2291	0.3953	0.0017	3.5795	0.0059	2.5770	0.0191	0.0040	Rounded Porous
G52210-03-02	-	-	5.4929	0.3487	0.5395	0.0013	5.0845	0.0107	4.3361	0.0309	0.0030	Rounded Porous
G52210-04-01	-	-	7.3129	0.7333	2.0331	0.0731	4.2965	0.0151	3.8390	0.0642	0.0035	Rounded Porous
G52210-04-02	-	-	8.8182	0.7645	0.7879	0.0162	4.5092	0.0229	3.5916	0.0597	0.0018	Rounded Porous
G52210-05-01	-	-	3.8247	0.0850	0.1668	0.0059	2.2164	0.0016	0.6093	0.0107	0.0424	Rounded Porous
G52210-05-02	-	-	3.9334	0.1307	0.3264	0.0040	3.2680	0.0023	0.8374	0.0118	0.0250	Rounded Porous
G52213-01-01	0.1146	2.2889	0.0853	0.0007	0.0012	-	0.0087	0.0001	0.0048	0.0002	-	Rounded Porous
G52213-01-02	0.1123	2.3557	0.0365	0.0003	0.0009	-	0.0041	-	0.0015	0.0001	-	Rounded Porous
G52213-02-01	0.1111	2.1608	0.2152	0.0113	0.0067	0.0018	0.0246	0.0001	3.7048	0.0007	-	Rounded Porous
G52213-02-02	0.1033	2.0354	0.3055	0.0098	0.0250	0.0038	0.0268	0.0001	2.7081	0.0006	0.0002	Rounded Porous
G52213-03-01	0.1108	2.2751	0.3342	0.0055	0.0198	0.0001	0.0289	0.0001	0.0233	0.0005	-	Rounded Porous
G52213-03-02	0.1208	2.3446	0.1737	0.0098	0.0753	0.0005	0.0145	-	0.2667	0.0004	-	Rounded Porous
G52213-04-01	0.1131	2.1457	0.2452	0.0069	0.0059	1.0204	0.0284	0.0001	2.9445	0.0007	-	Rounded Porous
G52213-04-02	0.1088	2.2347	0.2729	0.0197	0.1002	0.0002	0.0225	0.0001	0.8431	0.0006	-	Rounded Porous
G52213-05-01	0.1164	2.3912	0.1784	0.0020	0.0123	0.0001	0.0185	-	0.0337	0.0003	-	Rounded Porous
G52213-05-02	0.1163	2.4054	0.1549	0.0018	0.0131	0.0003	0.0147	0.0001	0.0368	0.0003	0.0001	Rounded Porous
G52214-03-01	-	-	9.2599	0.1695	3.7561	0.0434	2.7663	0.0049	1.0325	0.0117	0.0011	Rounded Porous
G52214-03-02	-	-	5.9235	0.1068	0.0867	0.0183	3.9602	0.0022	0.5397	0.0063	0.0015	Rounded Porous
G52214-05-01	-	-	9.9280	0.1907	0.4432	0.0342	2.7305	0.0025	0.2405	0.0025	0.0025	Rounded Porous
G52214-05-02	-	-	3.2024	0.3335	0.1033	0.0159	0.2420	0.0005	0.2064	0.0020	0.0012	Rounded Porous
G52224-01-01	0.1118	2.2492	0.0545	0.0029	0.0031	0.0001	0.0154	0.0001	0.0209	0.0002	-	Rounded Porous
G52224-01-02	0.1118	2.2791	0.0410	0.0020	0.0026	0.0001	0.0137	0.0001	0.0129	0.0002	-	Rounded Porous
G52224-02-01	0.1101	2.2700	0.0465	0.0065	0.0130	0.0001	0.0323	0.0004	0.0149	0.0006	-	Rounded Porous
G52224-02-02	0.1131	2.2735	0.0299	0.0043	0.0131	-	0.0128	0.0002	0.0670	0.0005	-	Rounded Porous
G52224-03-01	0.1062	2.1668	0.1224	0.0056	0.0043	0.0003	0.1724	0.0002	0.3779	0.0011	0.0002	Rounded Porous
G52224-03-02	0.1082	2.2020	0.1304	0.0024	0.0021	0.0003	0.0790	0.0001	0.3763	0.0008	0.0001	Rounded Porous

Section Name	Bismuth209	Ruthenium101	Rhodium103	Palladium 05	Osmium 189	Iridium193	Platinum195	Rubidium85	Niobium93	Molybdenum97	Uranium235	Pyrite Type
G52210-01-01	1.4618	0.0008	0.0011	0.0006	-	-	-	0.0007	-	0.0013	-	Rounded Porous
G52210-01-02	1.4849	0.0006	-	0.0008	0.0006	-	0.0011	0.0068	-	-	0.0001	Rounded Porous
G52210-02-01	2.1166	0.0003	0.0006	0.0008	-	-	-	0.0751	-	0.0066	-	Rounded Porous
G52210-02-02	3.0329	0.0002	0.0008	0.0001	0.0002	-	-	0.0254	0.0001	0.0075	-	Rounded Porous
G52210-03-01	1.9541	-	0.0003	0.0007	0.0001	-	0.0002	0.0494	0.0027	0.0005	0.0002	Rounded Porous
G52210-03-02	3.5891	0.0002	-	0.0010	0.0002	-	-	0.0538	0.0003	0.0003	0.0001	Rounded Porous
G52210-04-01	3.9891	-	0.0007	0.0007	0.0007	-	-	0.0219	0.0010	0.0096	0.0001	Rounded Porous
G52210-04-02	3.7461	-	0.0005	0.0007	0.0002	-	0.0002	0.0278	0.0001	0.0113	-	Rounded Porous
G52210-05-01	0.3926	0.0001	0.0001	0.0002	0.0002	-	-	0.0255	0.0009	0.0025	0.0002	Rounded Porous
G52210-05-02	0.5163	-	0.0002	0.0004	0.0002	-	-	0.0292	0.0035	-	0.0031	Rounded Porous
G52213-01-01	0.0042	-	-	-	-	-	-	-	-	-	-	Rounded Porous
G52213-01-02	0.0017	-	-	-	-	-	-	-	-	-	-	Rounded Porous
G52213-02-01	0.0252	-	0.0007	-	-	-	-	0.0001	-	0.0002	-	Rounded Porous
G52213-02-02	0.0171	-	0.0005	-	-	-	-	-	-	0.0001	0.0004	Rounded Porous
G52213-03-01	0.0163	-	-	-	-	-	-	0.0001	-	-	-	Rounded Porous
G52213-03-02	0.0071	-	-	-	-	-	-	-	-	-	-	Rounded Porous
G52213-04-01	0.0313	-	0.0005	-	-	-	-	0.0001	-	0.0001	-	Rounded Porous
G52213-04-02	0.0140	-	0.0002	-	-	-	-	0.0001	-	0.0002	-	Rounded Porous
G52213-05-01	0.0064	-	-	-	-	-	-	-	-	-	-	Rounded Porous
G52213-05-02	0.0061	-	-	-	-	-	-	-	-	-	-	Rounded Porous
G52214-03-01	1.3290	-	0.0002	0.0001	-	-	-	0.0127	0.0007	0.0003	-	Rounded Porous
G52214-03-02	0.7276	0.0002	0.0001	0.0001	0.0001	-	-	0.0078	0.0009	0.0006	-	Rounded Porous
G52214-05-01	0.2933	0.0001	-	-	0.0002	-	0.0002	0.0056	0.0004	0.0003	0.0001	Rounded Porous
G52214-05-02	0.2203	0.0001	-	0.0002	0.0001	-	0.0002	0.0029	0.0001	-	0.0002	Rounded Porous
G52224-01-01	0.0083	-	-	-	-	-	-	-	-	-	-	Rounded Porous
G52224-01-02	0.0101	-	-	-	-	-	-	-	-	-	-	Rounded Porous
G52224-02-01	0.0023	-	-	-	-	-	-	0.0001	-	0.0001	-	Rounded Porous
G52224-02-02	0.0015	-	-	-	-	-	-	-	-	-	-	Rounded Porous
G52224-03-01	0.0344	-	0.0001	-	-	-	-	0.0001	-	-	0.0001	Rounded Porous
G52224-03-02	0.0282	-	-	-	-	-	-	0.0004	-	-	-	Rounded Porous
G52224-04-01	0.0148	-	0.0001	-	-	-	-	-	-	-	-	Rounded Porous

Section Name	Sulphur 33	Iron 57	Cobalt 59	Nickel 61	Copper 65	Zinc 68	Arsenic 75	Gold 197	Lead 208	Silver 109	Zirconium 91	Pyrite Type
G52224-04-02	0.1061	2.1454	0.0944	0.0040	0.0069	-	0.1000	0.0002	0.5884	0.0009	-	Rounded Porous
G52224-05-01	0.1166	2.3658	0.1284	0.0040	0.0055	0.0020	0.0300	0.0001	0.1500	0.0003	-	Rounded Porous
G52224-05-02	0.1195	2.2902	0.1331	0.0036	0.0095	0.0033	0.0273	0.0001	0.0810	0.0003	-	Rounded Porous
G52230-01-01	-	-	-	-	7.6901	0.0265	-	0.0151	2.5233	0.0505	0.0018	Rounded Porous
G52230-01-02	-	-	-	0.0707	1.5032	0.0210	-	0.0188	38.3198	0.0821	0.0000	Rounded Porous
G52230-02-01	-	-	-	0.3769	4.0441	0.0110	8.2481	0.0098	2.4706	0.0307	0.0158	Rounded Porous
G52230-02-02	-	-	-	0.1363	7.0578	2.5529	4.9977	0.0082	13.8132	0.0226	0.0760	Rounded Porous
G52230-04-01	-	-	-	-	1.1939	0.0864	-	0.0488	17.7718	0.1032	0.0345	Rounded Porous
G52230-04-02	-	-	-	-	1.0842	0.0541	-	0.0687	18.7525	0.1390	0.0224	Rounded Porous
G52230-05-01	-	-	-	0.6311	1.4410	0.1021	11.2431	0.0514	7.4214	0.1677	0.0046	Rounded Porous
G52230-05-02	-	-	-	0.6946	0.6308	0.1193	0.0000	0.0426	5.3318	0.1105	0.0077	Rounded Porous
G52236-01-01	0.1094	2.1853	0.1047	0.0020	0.0024	0.0094	0.0704	-	0.0214	0.0002	0.0003	Rounded Porous
G52236-01-02	0.1180	2.2952	0.1352	0.0028	0.0010	0.0025	0.0822	0.0001	0.2555	0.0028	0.0002	Rounded Porous
G52236-02-01	0.1090	2.3428	0.0881	0.0049	0.0230	0.0002	0.0963	0.0001	0.0483	0.0005	-	Rounded Porous
G52236-02-02	0.1131	2.3424	0.0991	0.0057	0.0097	0.0002	0.0783	0.0002	0.1426	0.0006	0.0001	Rounded Porous
G52236-03-01	0.1110	2.3112	0.0424	0.0012	0.0021	0.0001	0.0350	0.0001	0.0081	0.0003	0.0001	Rounded Porous
G52236-03-02	0.1124	2.1920	0.0883	0.0023	0.0024	0.0003	0.0696	0.0001	0.0211	0.0006	0.0002	Rounded Porous
G52236-04-01	0.1160	2.3423	0.0659	0.0009	0.0015	0.0004	0.0537	-	0.0133	0.0001	0.0001	Rounded Porous
G52236-04-02	0.1023	2.3593	0.0565	0.0009	0.0073	0.0003	0.0502	0.0002	0.0282	0.0002	0.0002	Rounded Porous
G52236-08-01	0.1031	2.1562	0.0616	0.0012	0.0135	0.0015	0.0623	0.0001	0.1554	0.0007	0.0001	Rounded Porous
G52236-08-02	0.1056	2.2135	0.0511	0.0007	0.0030	0.0002	0.0556	-	0.0125	0.0002	0.0002	Rounded Porous
G52236-08-03	0.1051	2.2528	0.0388	0.0006	0.0037	0.0004	0.0459	-	0.0148	0.0001	0.0001	Rounded Porous
G52236-08-04	0.1104	2.2111	0.0815	0.0013	0.0040	0.0005	0.0779	-	0.0370	0.0004	0.0001	Rounded Porous
G52236-08-05	0.1158	2.3194	0.0606	0.0010	0.0063	0.0021	0.0551	0.0001	0.1307	0.0009	0.0002	Rounded Porous
G52237-01-01	0.1033	2.3474	0.0614	0.0047	0.0051	0.0002	0.0819	0.0002	0.0235	0.0006	-	Rounded Porous
G52237-01-02	0.1033	2.2378	0.0634	0.0041	0.0096	0.0002	0.0777	0.0002	0.0315	0.0008	-	Rounded Porous
G52258-01-01	0.0898	0.9877	9.6215	0.7251	0.0014	0.0005	29.4658	0.0031	0.0057	0.0009	0.0068	Rounded Porous
G52258-01-02	0.0884	0.9891	9.5684	0.6964	0.0012	0.0004	28.8805	0.0014	0.0061	0.0005	0.0074	Rounded Porous
G52258-02-01	0.0904	1.0871	8.4338	0.7144	0.0006	0.0003	28.0026	0.0003	0.0112	0.0002	0.0074	Rounded Porous
G52258-02-02	0.0851	1.0378	8.6525	0.6967	0.0007	0.0002	29.6968	0.0007	0.0044	0.0003	0.0072	Rounded Porous
G52258-03-01	0.0871	0.9785	7.7639	0.6773	0.0006	0.0003	29.1346	0.0006	0.0035	0.0002	0.0069	Rounded Porous

Section Name	Bismuth 209	Ruthenium 101	Rhodium 103	Palladium 105	Osmium 189	Iridium 193	Platinum 195	Rubidium 85	Niobium 93	Molybdenum 97	Uranium 235	Pyrite Type
G52224-04-02	0.0142	-	-	-	-	-	-	-	-	-	-	Rounded Porous
G52224-05-01	0.0189	-	-	-	-	-	-	-	-	-	-	Rounded Porous
G52224-05-02	0.0165	-	-	-	-	-	-	-	-	-	-	Rounded Porous
G52230-01-01	3.6046	-	0.0002	0.0005	0.0004	-	-	0.0592	-	0.0089	-	Rounded Porous
G52230-01-02	5.5029	0.0001	0.0026	0.0002	0.0002	-	0.0002	0.0223	-	0.0140	0.0007	Rounded Porous
G52230-02-01	0.8970	0.0003	0.0002	0.0007	-	-	-	0.0101	0.0283	0.0269	0.0002	Rounded Porous
G52230-02-02	0.8697	-	0.0031	0.0001	-	0.0001	0.0002	0.0244	0.0020	0.0016	0.0007	Rounded Porous
G52230-04-01	5.1047	-	0.0056	0.0018	0.0018	0.0015	-	0.0096	0.0088	0.0003	0.0012	Rounded Porous
G52230-04-02	4.8442	-	0.0046	0.0027	-	-	-	0.0039	0.0004	0.0008	0.0081	Rounded Porous
G52230-05-01	6.0636	-	-	0.0022	0.0022	-	-	0.0486	0.0034	0.0572	-	Rounded Porous
G52230-05-02	4.2981	-	0.0008	0.0012	-	0.0004	-	0.0633	0.0252	0.0536	0.0015	Rounded Porous
G52236-01-01	0.0035	-	-	-	-	-	-	0.0094	0.0007	-	-	Rounded Porous
G52236-01-02	0.0105	-	-	-	-	-	-	0.0043	0.0189	-	0.0001	Rounded Porous
G52236-02-01	0.0157	-	-	-	-	-	-	0.0001	-	-	-	Rounded Porous
G52236-02-02	0.0100	-	-	-	-	-	-	0.0006	-	0.0001	-	Rounded Porous
G52236-03-01	0.0034	-	-	-	-	-	-	0.0006	0.0002	-	0.0001	Rounded Porous
G52236-03-02	0.0067	-	-	-	-	-	-	0.0023	0.0002	-	0.0004	Rounded Porous
G52236-04-01	0.0038	-	-	-	-	-	-	0.0004	0.0004	-	-	Rounded Porous
G52236-04-02	0.0055	-	-	-	-	-	-	0.0005	0.0006	-	0.0002	Rounded Porous
G52236-08-01	0.0112	-	-	-	-	-	-	0.0013	0.0003	-	0.0005	Rounded Porous
G52236-08-02	0.0021	-	-	-	-	-	-	0.0014	0.0003	-	0.0001	Rounded Porous
G52236-08-03	0.0024	-	-	-	-	-	-	0.0009	0.0002	-	-	Rounded Porous
G52236-08-04	0.0056	-	-	-	-	-	-	0.0013	0.0006	-	0.0002	Rounded Porous
G52236-08-05	0.0090	-	-	-	-	-	-	0.0012	0.0007	-	0.0003	Rounded Porous
G52237-01-01	0.0125	-	-	-	-	-	-	0.0001	-	0.0001	-	Rounded Porous
G52237-01-02	0.0119	-	-	-	-	-	-	0.0001	-	0.0001	-	Rounded Porous
G52258-01-01	0.0406	-	-	-	-	-	-	0.0001	-	0.0005	-	Rounded Porous
G52258-01-02	0.0428	-	-	-	-	-	-	0.0017	0.0025	0.0007	-	Rounded Porous
G52258-02-01	0.0374	-	-	-	-	-	-	0.0001	0.0035	0.0008	-	Rounded Porous
G52258-02-02	0.0247	-	-	-	-	-	-	0.0001	0.0012	0.0012	-	Rounded Porous
G52258-03-01	0.0431	-	-	-	-	-	-	0.0005	0.0010	0.0004	-	Rounded Porous

Section Name	Sulphur 33	Iron 57	Cobalt 59	Nickel 61	Copper 65	Zinc 68	Arsenic 75	Gold 197	Lead 208	Silver 109	Zirconium 91	Pyrite Type
G52258-03-02	0.0906	0.9968	7.6902	0.6912	0.0011	0.0007	27.3896	0.0010	0.0036	0.0004	0.0071	Rounded Porous
G52258-04-01	0.0868	0.9865	6.6358	0.7405	0.0004	0.0003	29.3982	0.0008	0.0063	0.0003	0.0069	Rounded Porous
G52258-04-02	0.0897	0.9847	6.0520	0.8015	0.0021	0.0003	30.3952	0.0012	0.0052	0.0005	0.0075	Rounded Porous
G52261-01-01	0.0415	-	-	-	-	-	0.0012	-	99.3887	0.0230	-	Rounded Porous
G52261-01-02	0.0477	-	-	-	0.0007	0.0001	0.0026	-	99.2860	0.0220	-	Rounded Porous
G52261-04-01	0.0463	0.0002	-	-	-	-	0.0019	-	99.3098	0.0393	-	Rounded Porous
G52261-04-02	0.0475	-	-	-	-	-	0.0025	-	99.2168	0.0319	-	Rounded Porous
G52261-05-01	0.1109	2.3445	0.0015	0.0001	0.0001	0.0001	0.0014	-	0.0077	-	-	Rounded Porous
G52261-05-02	0.1167	2.2958	0.0194	0.0003	0.0014	0.0001	0.0040	-	0.0022	0.0001	-	Rounded Porous
G52214-01-01	-	-	33.2155	0.1001	-	-	-	-	0.0008	-	-	Rounded Massive
G52214-01-02	-	-	12.2869	0.0186	-	-	-	-	0.0002	0.0000	-	Rounded Massive
G52214-02-01	-	-	7.5515	0.3311	0.3571	-	1.0673	0.0043	1.1079	0.0212	0.0014	Rounded Massive
G52214-02-02	-	-	13.7792	0.4661	0.2270	-	5.7895	0.0075	1.7070	0.0265	0.0023	Rounded Massive
G52214-04-01	-	-	7.0717	0.0873	0.0429	-	0.4091	-	-	-	0.0017	Rounded Massive
G52214-04-02	-	-	20.8386	0.2235	0.0620	-	0.2722	-	0.0019	-	0.0024	Rounded Massive
G52216-01-01	0.1042	2.2701	0.0193	0.0017	0.0010	0.0001	0.0420	0.0001	0.0005	-	-	Rounded Massive
G52216-01-02	0.1121	2.2981	0.0312	0.0012	0.0004	-	0.0408	0.0001	0.0008	-	-	Rounded Massive
G52216-02-01	0.1090	2.3117	0.0066	-	-	-	0.0038	-	-	-	-	Rounded Massive
G52216-02-02	0.1092	2.3136	0.0144	0.0001	-	-	0.0074	-	-	-	-	Rounded Massive
G52216-03-01	0.1093	2.3890	0.0080	-	-	-	0.0195	0.0001	0.0000	-	-	Rounded Massive
G52216-03-02	0.1095	2.3946	0.0156	-	-	-	0.0142	-	0.0006	-	-	Rounded Massive
G52216-04-01	0.1071	2.2685	0.7585	0.0007	-	-	0.0018	-	0.0006	0.0001	-	Rounded Massive
G52216-04-02	0.1083	2.3257	0.1333	0.0014	-	-	0.0023	-	0.0001	-	-	Rounded Massive
G52216-05-01	0.1128	2.3349	0.1747	0.0042	0.0003	0.0007	0.0037	-	0.0015	0.0001	-	Rounded Massive
G52216-05-02	0.1111	2.4826	0.0657	0.0013	0.0002	0.0011	0.0020	-	0.0020	0.0001	-	Rounded Massive
G52227-01-01	0.1044	2.1629	0.1477	0.0084	0.0024	-	0.0149	0.0001	0.0083	0.0001	0.0001	Rounded Massive
G52227-01-02	0.1204	2.2187	0.1257	0.0038	0.0021	-	0.0177	0.0001	0.0106	0.0001	-	Rounded Massive
G52227-02-01	0.1167	2.3365	0.0257	0.0004	0.0010	-	0.0266	0.0001	0.0014	0.0001	-	Rounded Massive
G52227-02-02	0.1153	2.3485	0.0434	0.0004	0.0026	-	0.0269	0.0001	0.0017	0.0001	-	Rounded Massive
G52227-03-01	0.0774	2.0215	0.0866	0.0010	0.0047	0.0001	0.0197	-	0.0028	0.0001	-	Rounded Massive
G52227-03-02	0.1271	2.0936	0.0985	0.0011	0.0064	0.0002	0.0178	0.0001	0.0041	0.0001	-	Rounded Massive

Section Name	Bismuth 209	Ruthenium 101	Rhodium 103	Palladium 105	Osmium 189	Iridium 193	Platinum 195	Rubidium 85	Niobium 93	Molybdenum 97	Uranium 235	Pyrite Type
G52258-03-02	0.0397	-	-	-	-	-	-	0.0020	0.0015	0.0007	-	Rounded Porous
G52258-04-01	0.0322	-	-	-	-	-	-	0.0001	0.0026	0.0004	-	Rounded Porous
G52258-04-02	0.0236	-	-	-	-	-	-	0.0001	0.0001	0.0001	-	Rounded Porous
G52261-01-01	0.0914	-	0.0058	-	-	-	-	-	-	-	-	Rounded Porous
G52261-01-02	0.0861	-	0.0057	-	-	-	-	-	-	-	-	Rounded Porous
G52261-04-01	0.0982	-	0.0060	-	-	-	-	-	-	-	-	Rounded Porous
G52261-04-02	0.0971	-	0.0058	-	-	-	-	-	-	-	-	Rounded Porous
G52261-05-01	0.0001	-	-	-	-	-	-	-	-	0.0002	-	Rounded Porous
G52261-05-02	0.0021	-	-	-	-	-	-	-	-	0.0001	-	Rounded Porous
G52214-01-01	-	-	0.0016	0.0005	0.0003	-	0.0009	0.0009	0.0005	-	-	Rounded Massive
G52214-01-02	0.0124	-	-	0.0013	-	-	-	0.0006	-	0.0036	-	Rounded Massive
G52214-02-01	1.9130	0.0002	0.0019	0.0015	0.0003	-	-	0.0002	-	0.0014	-	Rounded Massive
G52214-02-02	3.0999	-	0.0001	0.0009	0.0009	-	-	0.0017	-	-	-	Rounded Massive
G52214-04-01	-	-	0.0039	0.0026	-	-	-	0.0013	-	0.0002	-	Rounded Massive
G52214-04-02	-	0.0003	0.0002	0.0012	0.0007	-	0.0002	0.0005	-	-	0.0012	Rounded Massive
G52216-01-01	0.0008	-	-	-	-	-	-	-	-	-	-	Rounded Massive
G52216-01-02	0.0022	-	-	-	-	-	-	-	-	-	-	Rounded Massive
G52216-03-02	0.0003	-	-	-	-	-	-	-	-	-	-	Rounded Massive
G52216-04-01	0.0017	-	-	-	-	-	-	-	-	-	-	Rounded Massive
G52216-04-02	0.0003	-	-	-	-	-	-	-	-	-	-	Rounded Massive
G52216-05-01	0.0084	-	-	-	-	-	-	0.0009	0.0001	-	-	Rounded Massive
G52216-05-02	0.0081	-	-	-	-	-	-	0.0005	0.0002	-	-	Rounded Massive
G52227-01-01	0.0042	-	-	-	-	-	-	0.0001	0.0001	-	-	Rounded Massive
G52227-01-02	0.0055	-	-	-	-	-	-	0.0001	0.0001	-	-	Rounded Massive
G52227-02-01	0.0004	-	-	-	-	-	-	-	-	-	-	Rounded Massive
G52227-02-02	0.0005	-	-	-	-	-	-	-	-	-	-	Rounded Massive
G52227-03-01	0.0021	-	-	-	-	-	-	0.0001	-	0.0002	-	Rounded Massive
G52227-03-02	0.0030	-	-	-	-	-	-	0.0002	-	0.0002	-	Rounded Massive

Section Name	Sulphur 33	Iron 57	Cobalt 59	Nickel 61	Copper 65	Zinc 68	Arsenic 75	Gold 197	Lead 208	Silver 109	Zirconium 91	Pyrite Type
G52227-04-01	0.1156	2.2554	0.1172	0.0035	0.0062	0.0001	0.0261	-	0.0102	0.0002	-	Rounded Massive
G52227-04-02	0.1417	2.6671	0.1549	0.0051	0.0127	0.0002	0.0263	0.0001	0.0079	0.0002	-	Rounded Massive
G52227-05-01	0.1455	2.5554	0.1139	0.0026	0.0041	0.0006	0.0200	0.0001	0.0191	0.0002	-	Rounded Massive
G52227-05-02	0.1132	2.2946	0.0619	0.0017	0.0044	0.0002	0.0127	0.0001	0.0168	0.0001	-	Rounded Massive
G52228-01-01	-	-	-	-	-	-	-	-	0.0258	-	-	Rounded Massive
G52228-01-02	0.3710	5.5394	-	-	-	0.0002	0.0038	-	0.0001	0.0001	0.0001	Rounded Massive
G52228-04-01	0.3540	0.2974	-	0.0137	0.0133	-	-	-	0.0002	-	-	Rounded Massive
G52228-04-02	0.1870	0.5529	0.0128	0.0061	0.0021	-	0.0155	-	-	-	-	Rounded Massive
G52228-05-01	0.2908	2.3805	0.0256	0.0021	0.0113	0.0003	-	0.0002	0.0001	0.0004	-	Rounded Massive
G52228-05-02	0.2375	3.2771	0.0678	0.0035	0.0192	0.0005	0.0021	-	0.0052	0.0005	0.0001	Rounded Massive
G52228-05-03	0.2031	1.5122	0.1167	0.0045	0.0091	0.0003	0.0048	0.0001	0.0086	0.0005	-	Rounded Massive
G52228-05-04	0.1770	2.0722	0.0967	0.0036	0.0123	0.0003	0.0077	-	0.0068	0.0005	-	Rounded Massive
G52228-05-05	0.1254	0.6945	0.0162	0.0023	0.0196	0.0006	0.0013	-	0.0011	0.0004	-	Rounded Massive
G52228-06-01	-	-	2.7896	0.0417	0.0829	-	0.0300	-	0.0021	0.0007	0.0017	Rounded Massive
G52228-06-02	0.2899	-	12.2528	0.1027	0.2112	-	-	-	0.5586	0.2198	0.0012	Rounded Massive
G52228-06-03	1.8171	-	13.0516	0.0679	0.0645	-	-	-	0.0594	0.0040	0.0011	Rounded Massive
G52228-06-04	-	-	9.8657	0.0724	0.0537	-	-	-	0.0332	0.0042	-	Rounded Massive
G52228-06-05	-	-	8.4007	0.0571	0.0822	-	-	-	0.0031	0.0017	0.0024	Rounded Massive
G52228-07-01	0.2611	-	16.6421	1.3103	0.0489	-	-	-	0.0001	0.0003	0.0001	Rounded Massive
G52228-07-02	-	3.9913	46.0928	0.7263	0.0479	-	-	-	0.0008	0.0009	0.0004	Rounded Massive
G52230-03-01	-	-	-	0.0329	0.0488	0.0045	-	0.0004	0.2087	0.0068	0.0010	Rounded Massive
G52230-03-02	-	-	-	-	0.1550	0.0103	-	0.0061	6.0019	0.0107	0.0002	Rounded Massive
G52258-05-01	0.0660	2.0972	0.0111	0.0098	0.0001	-	0.0116	-	0.0001	-	-	Rounded Massive
G52258-05-02	0.0745	2.3763	0.0098	0.0090	0.0001	-	0.0105	-	0.0001	-	-	Rounded Massive
G52200-01-01	-	-	-	1.9627	-	-	26.8263	-	-	-	-	Angular Massive
G52200-01-02	-	-	-	-	-	-	-	-	-	-	-	Angular Massive
G52200-02-01	-	-	-	-	0.0459	-	-	0.0230	-	-	-	Angular Massive
G52200-02-02	-	-	-	-	-	0.0091	-	0.0008	-	-	-	Angular Massive
G52200-03-01	-	-	-	-	0.1711	-	-	0.0097	0.5778	-	-	Angular Massive

Section Name	Bismuth 209	Ruthenium 101	Rhodium 103	Palladium 105	Osmium 189	Iridium 193	Platinum 195	Rubidium 85	Niobium 93	Molybdenum 97	Uranium 235	Pyrite Type
G52227-04-01	0.0043	-	-	-	-	-	-	0.0001	-	0.0002	-	Rounded Massive
G52227-04-02	0.0038	-	-	-	-	-	-	0.0001	-	0.0003	-	Rounded Massive
G52227-05-01	0.0088	-	-	-	-	-	-	0.0001	-	0.0002	-	Rounded Massive
G52227-05-02	0.0054	-	-	-	-	-	-	0.0001	-	0.0001	-	Rounded Massive
G52228-01-01	-	-	0.0115	0.0172	0.0115	-	0.0172	0.0172	-	-	-	Rounded Massive
G52228-01-02	-	-	0.0001	0.0001	0.0001	-	-	-	-	-	-	Rounded Massive
G52228-04-01	0.0003	-	-	0.0001	0.0001	-	0.0001	0.0001	-	-	-	Rounded Massive
G52228-05-01	0.0001	-	-	-	-	-	-	0.0002	-	0.0026	-	Rounded Massive
G52228-05-02	0.0034	-	-	-	-	-	-	0.0004	-	0.0032	-	Rounded Massive
G52228-05-03	0.0056	-	-	-	-	-	-	0.0005	-	0.0023	-	Rounded Massive
G52228-05-04	0.0037	-	-	-	-	-	-	0.0003	-	0.0015	-	Rounded Massive
G52228-05-05	0.0005	-	-	-	-	-	-	0.0003	-	0.0010	-	Rounded Massive
G52228-06-01	0.0152	0.0009	0.0024	0.0003	0.0002	-	-	0.0009	-	-	-	Rounded Massive
G52228-06-02	0.4647	-	0.0020	0.0013	-	-	0.0010	0.0009	-	-	0.0010	Rounded Massive
G52228-06-03	0.0246	0.0015	0.0009	0.0008	-	-	0.0011	-	0.0002	-	0.0011	Rounded Massive
G52228-06-04	0.0209	0.0013	-	0.0016	-	-	0.0005	0.0005	-	-	0.0005	Rounded Massive
G52228-06-05	0.0321	-	0.0003	0.0003	0.0009	-	0.0002	0.0009	-	-	-	Rounded Massive
G52228-07-01	-	0.0009	-	0.0011	0.0006	-	-	0.0005	-	-	-	Rounded Massive
G52228-07-02	-	0.0001	0.0003	-	-	-	0.0002	-	-	-	0.0001	Rounded Massive
G52230-03-01	0.0122	0.0001	0.0002	0.0001	-	0.0001	-	0.0363	0.0004	0.0001	-	Rounded Massive
G52230-03-02	0.9189	0.0009	0.0012	0.0013	0.0001	-	-	0.0294	0.0008	-	-	Rounded Massive
G52200-01-01	-	-	0.0056	0.0127	-	-	-	0.0008	0.0024	0.0071	0.0024	Angular Massive
G52200-01-02	-	0.0241	0.0048	0.0241	-	-	-	0.0578	0.0145	-	-	Angular Massive
G52200-02-01	-	0.0046	0.0092	0.0138	-	-	-	0.0046	-	0.0046	0.0092	Angular Massive
G52200-02-02	-	0.0004	0.0015	0.0023	-	0.0008	0.0004	0.0053	-	0.0004	-	Angular Massive
G52200-03-01	0.6908	-	0.0032	0.0290	-	0.0097	0.0097	0.0097	0.0097	0.0194	0.0064	Angular Massive
G52200-03-02	0.0564	-	0.0265	0.0066	-	-	-	-	-	-	0.0033	Angular Massive

Section Name	Sulphur 33	Iron 57	Cobalt 59	Nickel 61	Copper 65	Zinc 68	Arsenic 75	Gold 197	Lead 208	Silver 109	Zirconium 91	Pyrite Type
G52200-04-01	-	-	-	-	0.3332	0.0063	-	0.0388	1.7267	0.1753	0.0000	Angular Massive
G52229-01-01	0.1081	2.2251	0.0165	0.0016	0.0007	0.0001	0.0540	0.0001	0.0176	0.0001	-	Angular Massive
G52229-01-02	0.1054	2.4188	0.0931	0.0021	0.0020	0.0001	0.0490	0.0001	0.0044	0.0001	-	Angular Massive
G52229-02-01	0.1063	2.3279	0.0312	0.0004	-	-	0.0210	-	0.0001	-	-	Angular Massive
G52229-02-02	0.1018	2.3005	0.0019	-	0.0002	-	0.1140	0.0001	0.0004	-	-	Angular Massive
G52229-03-01	0.1008	2.4059	0.0112	0.0001	-	-	0.0010	-	-	-	-	Angular Massive
G52229-03-02	0.0985	2.2211	0.1778	0.0007	0.0002	-	0.0076	-	0.0013	-	-	Angular Massive
G52229-04-01	0.1048	2.3679	-	-	0.0001	-	0.0197	-	0.0006	-	-	Angular Massive
G52229-04-02	0.0973	2.2771	0.0958	0.0003	-	-	0.0010	-	0.0000	-	-	Angular Massive
G52229-05-01	0.1058	2.3653	0.0011	0.0001	0.0016	-	0.0599	0.0001	0.0148	0.0002	-	Angular Massive
G52229-05-02	0.1056	2.3774	0.1270	0.0017	0.0038	-	0.0618	0.0001	0.0076	0.0001	-	Angular Massive
G52208-01-01	0.0963	2.3597	0.0172	0.0007	0.0051	0.0001	0.0979	-	0.0229	0.0002	-	Angular Massive
G52208-01-02	0.1060	2.3617	0.0136	0.0005	0.0048	-	0.1167	-	0.0267	0.0002	-	Angular Massive
G52229-02-01	0.0939	2.2712	0.0787	0.0049	0.0037	0.0001	0.0204	0.0001	0.0062	0.0002	-	Angular Massive
G52229-02-02	0.1071	2.3124	0.0678	0.0057	0.0039	0.0001	0.0211	0.0001	0.0084	0.0003	-	Angular Massive
G52229-03-01	0.1044	2.3687	0.0030	0.0001	0.0002	-	0.0041	-	0.0006	-	-	Angular Massive
G52229-03-02	0.1062	2.3346	0.0016	0.0001	0.0003	-	0.0313	-	0.0002	-	-	Angular Massive
G52229-04-01	0.0962	2.3717	0.0067	0.0004	0.0060	0.0001	0.0211	-	0.0053	0.0003	-	Angular Massive
G52229-04-02	0.0875	2.3642	0.0120	0.0005	0.0045	0.0001	0.0368	-	0.0077	0.0002	-	Angular Massive
G52229-05-01	0.0938	2.3324	0.0550	0.0008	0.0009	-	0.0289	0.0001	0.0047	0.0003	-	Angular Massive
G52229-05-02	0.1029	2.2111	0.0044	0.0001	0.0003	-	0.0101	-	0.0008	0.0001	-	Angular Massive
G52233-05-01	0.1211	2.2779	0.1334	0.0012	0.0025	-	0.0023	-	-	-	-	Angular Massive
G52233-05-02	0.1127	2.2432	0.2485	0.0015	0.0000	0.0001	0.0025	-	-	-	-	Angular Massive
G52233-06-01	0.1136	2.2927	0.0848	0.0019	0.2053	0.0006	0.0225	-	0.0005	0.0006	0.0002	Angular Massive
G52233-06-02	0.1091	2.4244	0.1800	0.0031	0.0011	-	0.0172	-	0.0047	0.0001	0.0004	Angular Massive
G52233-09-01	0.1127	2.3355	0.0390	0.0022	-	-	0.0470	-	-	-	-	Angular Massive
G52233-09-02	0.1139	2.4365	0.1104	0.0025	0.0001	-	0.0742	-	-	-	-	Angular Massive
G52233-09-03	0.1159	2.3866	0.1592	0.0025	0.0001	-	0.0018	-	0.0001	-	-	Angular Massive

Section Name	Bismuth 209	Ruthenium 101	Rhodium 103	Palladium 105	Osmium 189	Iridium 193	Platinum 195	Rubidium 85	Niobium 93	Molybdenum 97	Uranium 235	Pyrite Type
G52200-04-01	0.7741	0.0038	-	0.0125	-	-	-	0.0038	-	0.0038	-	Angular Massive
G52200-04-02	-	-	0.0063	0.0271	0.0042	-	-	0.0021	-	-	0.0083	Angular Massive
G52200-05-01	-	-	-	-	-	-	0.0193	-	0.0039	-	-	Angular Massive
G52200-05-02	-	-	-	-	-	-	-	0.0088	-	-	-	Angular Massive
G52229-01-02	0.0020	-	-	-	-	-	-	-	-	-	-	Angular Massive
G52229-02-01	0.0001	-	-	-	-	-	-	0.0001	-	-	-	Angular Massive
G52229-02-02	0.0001	-	-	-	-	-	-	-	-	-	-	Angular Massive
G52229-03-02	0.0002	-	-	-	-	-	-	-	-	-	-	Angular Massive
G52229-04-02	0.0006	-	-	-	-	-	-	0.0003	-	-	-	Angular Massive
G52229-05-01	0.0019	-	-	-	-	-	-	-	0.0001	-	-	Angular Massive
G52229-05-02	0.0015	-	-	-	-	-	-	-	-	-	-	Angular Massive
G52208-01-01	0.0030	-	-	-	-	-	-	0.0001	0.0001	-	0.0001	Angular Massive
G52208-01-02	0.0023	-	-	-	-	-	-	-	-	-	-	Angular Massive
G52229-02-01	0.0110	-	-	-	-	-	-	0.0026	-	0.0001	-	Angular Massive
G52229-02-02	0.0112	-	-	-	-	-	-	0.0018	-	0.0007	-	Angular Massive
G52229-03-01	0.0006	-	-	-	-	-	-	-	-	0.0008	-	Angular Massive
G52229-03-02	0.0004	-	-	-	-	-	-	-	-	0.0006	-	Angular Massive
G52229-04-01	0.0003	-	-	-	-	-	-	0.0021	-	-	-	Angular Massive
G52229-04-02	0.0019	-	-	-	-	-	-	0.0022	-	-	-	Angular Massive
G52229-05-01	0.0094	-	-	-	-	-	-	0.0001	-	0.0129	-	Angular Massive
G52229-05-02	0.0005	-	-	-	-	-	-	-	-	0.0046	-	Angular Massive
G52233-05-01	0.0004	-	-	-	-	-	-	-	-	-	-	Angular Massive
G52233-06-01	0.0005	-	-	-	-	-	-	0.0001	0.0004	-	-	Angular Massive
G52233-06-02	0.0014	-	-	-	-	-	-	0.0001	-	-	-	Angular Massive

| Section Name	Sulphur 33	Iron 57	Cobalt 59	Nickel 61	Copper 65	Zinc 68	Arsenic 75	Gold 197	Lead 208	Silver 109	Zirconium 91	Pyrite Type
G52233-09-04	0.1146	2.2810	0.2102	0.0041	0.0002	0.0001	0.1146	0.0001	0.0006	-	0.0001	Rounded Porous
G52233-09-05	0.1129	2.3000	0.1666	0.0026	0.0005	-	0.0275	-	0.0006	-	-	Rounded Porous
G52233-10-01	0.1106	2.3138	0.0015	-	0.0002	0.0001	0.0023	-	-	-	-	Rounded Porous
G52233-10-02	0.1095	2.2645	0.0013	-	0.0004	0.0001	0.0019	-	0.0002	-	-	Rounded Porous
G52233-11-01	0.1045	2.2652	-	-	0.0003	-	0.0020	-	-	-	-	Rounded Porous
G52233-11-02	0.1146	2.3384	0.0003	-	0.0003	0.0001	0.0023	-	-	-	-	Rounded Porous
G52233-11-03	0.1129	2.2550	0.0002	-	0.0003	0.0001	0.0020	0.0013	0.0001	-	-	Rounded Porous
G52233-11-04	0.1138	2.3075	0.0045	0.0001	0.0006	0.0001	0.0048	-	0.0004	-	-	Rounded Porous
G52233-11-05	0.1081	2.2157	0.0011	0.0001	0.0007	0.0001	0.0026	-	0.0005	-	-	Rounded Porous
G52237-02-01	0.0820	2.2699	0.1281	0.0097	0.0007	0.0001	0.1351	0.0001	0.0430	0.0005	-	Rounded Porous
G52237-02-02	0.0982	2.2536	0.1598	0.0077	0.0020	-	0.1877	0.0001	0.1057	0.0005	-	Rounded Porous
G52237-02-03	0.0869	2.3138	0.1391	0.0098	0.0009	0.0001	0.1757	0.0001	0.0371	0.0006	-	Rounded Porous
G52237-02-04	0.0994	2.4684	0.1638	0.0096	0.0014	0.0001	0.1805	0.0001	0.0682	0.0005	-	Rounded Porous
G52237-02-05	0.1049	2.2177	0.0901	0.0764	0.0006	0.0002	0.1712	-	1.7035	0.0005	-	Rounded Porous
G52237-03-01	0.0961	2.4304	0.0751	0.0046	0.0173	0.0003	0.0896	0.0001	0.0706	0.0006	-	Rounded Porous
G52237-03-02	0.1041	2.4056	0.0636	0.0050	0.0120	0.0003	0.0880	0.0001	0.0598	0.0005	0.0001	Rounded Porous
G52237-07-01	0.1069	2.3163	0.1288	0.0029	0.0019	0.0008	0.0961	0.0001	0.0150	0.0002	0.0008	Rounded Porous
G52237-07-02	0.0979	2.3293	0.0957	0.0019	0.0023	0.0003	0.0410	-	0.0112	0.0001	0.0006	Rounded Porous
G52237-08-01	0.1097	2.3993	0.0841	0.0056	0.0048	0.0003	0.0981	0.0002	0.0983	0.0003	-	Rounded Porous
G52237-08-02	0.1069	2.3424	0.0850	0.0089	0.0051	-	0.1091	0.0002	0.0302	0.0003	-	Rounded Porous
G52237-08-03	0.1063	2.3023	0.0908	0.0076	0.0035	-	0.1330	0.0002	0.0254	0.0003	-	Rounded Porous
G52237-08-04	0.1064	2.2824	0.0894	0.0056	0.0041	0.0035	0.1061	0.0002	0.0256	0.0003	-	Rounded Porous
G52237-08-05	0.1084	2.3607	0.0888	0.0071	0.0040	0.0017	0.1184	0.0002	0.0443	0.0003	-	Rounded Porous

| Section Name	Bismuth 209	Ruthenium 101	Rhodium 103	Palladium 105	Osmium 189	Iridium 193	Platinum 195	Rubidium 85	Niobium 93	Molybdenum 97	Uranium 235	Pyrite Type
G52261-02-01	0.0018	-	-	-	-	-	-	-	-	-	-	Angular Massive
G52261-02-02	0.0016	-	-	-	-	-	-	-	-	-	-	Angular Massive
G52263-03-01	0.1154	2.4100	0.0001	0.0001	-	-	0.0070	-	-	-	-	Angular Massive
G52263-03-02	0.1140	2.3462	0.0013	0.0021	-	-	0.0055	-	-	-	-	Angular Massive
G52263-04-01	0.1162	2.3425	0.0042	0.0013	-	-	0.0231	-	0.0001	-	-	Angular Massive
G52263-04-02	0.1134	2.4424	0.0409	0.0037	-	-	0.0094	-	0.0003	-	-	Angular Massive
G52263-05-01	0.1132	2.2521	0.0150	0.0013	-	-	0.0054	-	0.0001	-	-	Angular Massive
G52239-01-01	0.1208	4.4751	-	0.1070	0.0019	0.0008	5.5741	0.0002	0.0135	0.0002	-	Angular Massive
G52239-01-02	-	0.0069	7.9136	-	0.0049	0.0005	-	-	0.0192	0.0001	-	Angular Massive
G52239-01-03	58.2055	-	-	-	0.0833	0.1137	-	-	-	-	-	Angular Massive
G52239-01-05	1.6992	-	-	1.0286	0.0266	0.0284	43.0459	0.0009	0.2535	0.0055	0.1007	Angular Massive
G52261-02-01	0.0902	2.1234	0.0158	0.0001	0.0012	0.0001	0.0039	-	0.0065	-	-	Angular Massive
G52261-02-02	0.0988	2.2960	0.0132	0.0002	0.0008	0.0001	0.0043	-	0.0393	-	-	Angular Massive
G52261-03-01	0.1139	2.3638	0.0016	0.0001	0.0003	-	0.0216	-	0.0003	-	-	Angular Massive
G52261-03-02	0.1074	2.2157	0.0132	0.0002	0.0018	-	0.0214	-	0.0004	0.0001	-	Angular Massive
G52263-01-01	0.1225	2.3423	0.0250	0.0001	-	-	0.0091	-	0.0001	-	-	Angular Massive
G52263-01-02	0.1124	2.3096	0.0555	0.0061	0.0004	-	0.0072	-	0.0014	-	-	Angular Massive
G52263-02-01	0.1232	2.3290	0.0624	0.0102	0.0007	-	0.0170	-	0.0017	-	-	Angular Massive
G52263-02-02	0.1262	2.4373	0.3365	0.0296	0.0004	-	0.0459	-	0.0003	-	-	Angular Massive
G52239-02-01	-	-	-	-	0.1783	0.2312	-	0.0396	5.4099	0.2641	6.3412	Angular Massive
G52239-02-02	-	-	-	1.0351	2.8832	0.5906	-	-	-	0.0417	-	Angular Massive
G52239-02-03	-	-	-	-	-	0.2607	-	-	-	-	-	Angular Massive
G52239-02-04	-	-	-	-	-	0.0084	-	-	-	-	-	Angular Massive
G52239-02-05	-	-	-	-	0.0155	-	97.8631	0.0570	-	-	0.0040	Angular Massive
G52239-03-01	-	-	-	-	0.0000	-	-	0.1131	-	-	-	Angular Massive
G52239-03-02	-	-	-	0.8063	0.1986	0.0105	50.1200	-	0.1749	0.0059	0.0033	Angular Massive
G52239-04-01	-	-	-	1.0542	0.0066	0.0027	55.7010	-	-	0.0004	0.0033	Angular Massive
G52239-04-02	-	-	-	0.0000	0.0000	0.0059	90.8225	-	-	-	0.0071	Angular Massive
G52239-05-01	-	-	-	-	1.1589	0.2321	-	0.0053	-	0.2848	-	Angular Massive
G52239-05-02	-	-	-	-	-	0.0286	-	-	-	-	-	Angular Massive
G52239-01-01	0.0083	-	-	0.0001	-	-	-	-	-	-	-	Angular Massive

Section Name	Bismuth 209	Ruthenium 101	Rhodium 103	Palladium 105	Osmium 189	Iridium 193	Platinum 195	Rubidium 85	Niobium 93	Molybdenum 97	Uranium 235	Pyrite Type
G52239-01-02	0.0047	0.0003	0.0001	0.0003	-	0.0001	0.0001	-	-	0.0002	0.0001	Angular Massive
G52239-01-03	-	0.0455	0.0606	0.1061	-	-	-	-	0.0076	0.0303	-	Angular Massive
G52239-01-04	-	0.3520	0.1600	0.3200	-	-	-	0.2560	0.0639	-	0.1280	Angular Massive
G52239-01-05	0.1346	0.0009	-	0.0039	-	-	-	0.0135	0.4032	0.0005	-	Angular Massive
G52239-02-01	2.5294	0.0132	0.0132	0.0198	0.0132	-	-	-	-	-	0.0066	Angular Massive
G52239-02-02	0.6604	0.0625	-	0.0278	0.0069	-	-	0.0208	0.0347	-	0.0417	Angular Massive
G52239-02-03	-	-	0.1738	0.1955	-	-	0.0434	0.1520	-	-	0.1086	Angular Massive
G52239-02-04	-	0.0501	0.0000	0.0752	-	-	-	0.1086	-	0.0501	0.0083	Angular Massive
G52239-02-05	-	0.0090	0.0010	0.0030	-	-	0.0025	-	0.0035	-	-	Angular Massive
G52239-03-01	-	-	0.1131	0.0943	-	-	-	0.0377	0.1037	-	0.0283	Angular Massive
G52239-03-02	0.1277	-	0.0011	0.0016	-	-	-	0.0127	0.0353	-	0.0011	Angular Massive
G52239-04-01	-	-	-	0.0005	-	-	-	0.0005	-	-	-	Angular Massive
G52239-04-02	-	0.0036	0.0142	0.0047	-	-	-	-	0.0024	0.0024	-	Angular Massive
G52239-05-01	13.7876	0.0316	0.0528	0.0158	0.0105	-	-	0.0211	-	0.2954	-	Angular Massive
G52239-05-02	-	0.0036	-	0.0179	-	0.0155	-	-	0.0012	-	-	Angular Massive

Table 5.5 (B): *Co and Ni data sets obtained from the same spots analysed using the EMPA and LA-ICP-MS techniques for section g52228 and g52237 containing detrital rounded pyrite grains. The dashes mean below limits of detection.*

Co (wt %)	Ni (wt %)	Co (% of total signal)	Ni (% of total signal)	Types of Pyrite
0.0373	0.005	-	0.4146	Rounded
0.0015	0.0119	-	0.4956	Rounded
0.0039	0.0203	-	0.9108	Rounded
0.0219	0.006	-	0.9925	Rounded
0.0388	0.0076	-	0.2291	Rounded
0.0864	0.0033	-	0.3487	Rounded
0.0262	0.0181	-	0.7333	Rounded
0.0024	0.0128	-	0.7645	Rounded
0.0064	0.0097	-	0.0850	Rounded
0.0061	0.0082	0.0853	0.1307	Rounded
0.0036	0.0464	0.0365	0.0007	Rounded
0.0064	0.0428	0.2152	0.0003	Rounded
0.0028	0.0168	0.3055	0.0113	Rounded
0.0176	0.0144	0.3342	0.0098	Rounded
0.0562	0.0401	0.1737	0.0055	Rounded
0.079	0.4819	0.2452	0.0098	Rounded
0.0609	0.5772	0.2729	0.0069	Rounded
0.0622	0.5216	0.1784	0.0197	Rounded
0.0349	0.0527	0.1549	0.0020	Rounded
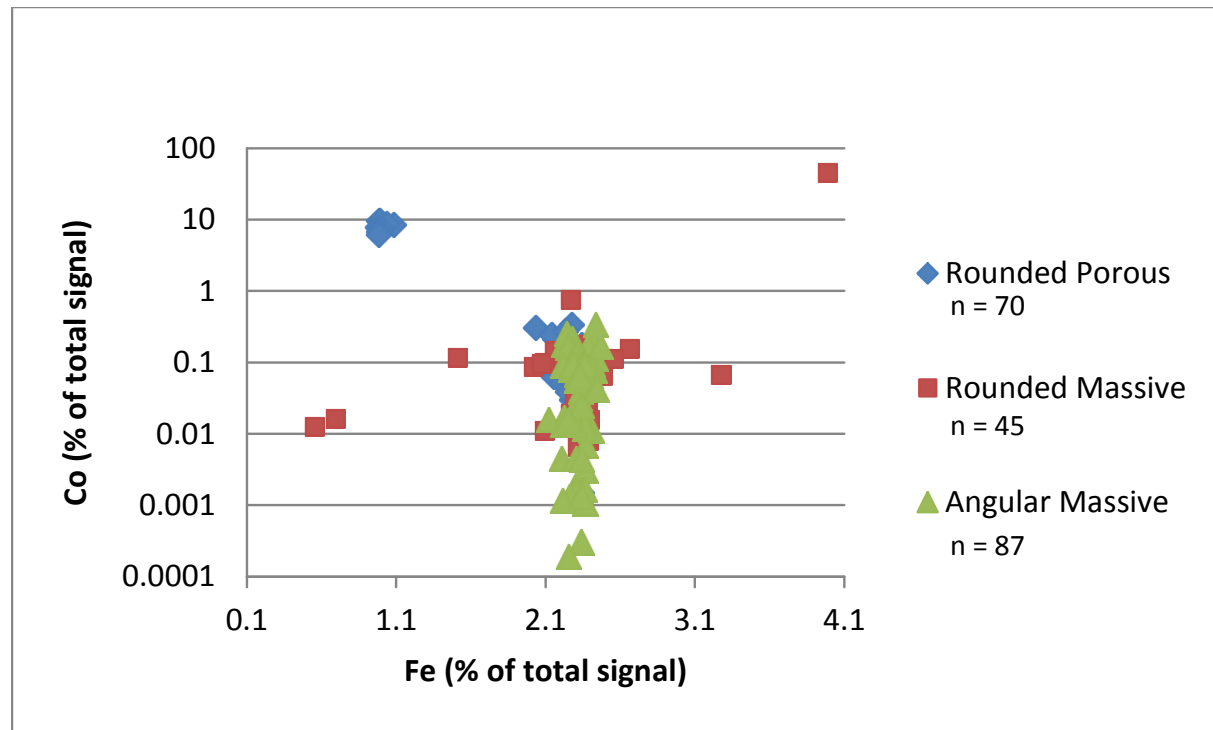
Figure 5.11: *Illustration Fe plotted against Co for the different types of rounded and angular pyrite grains.*
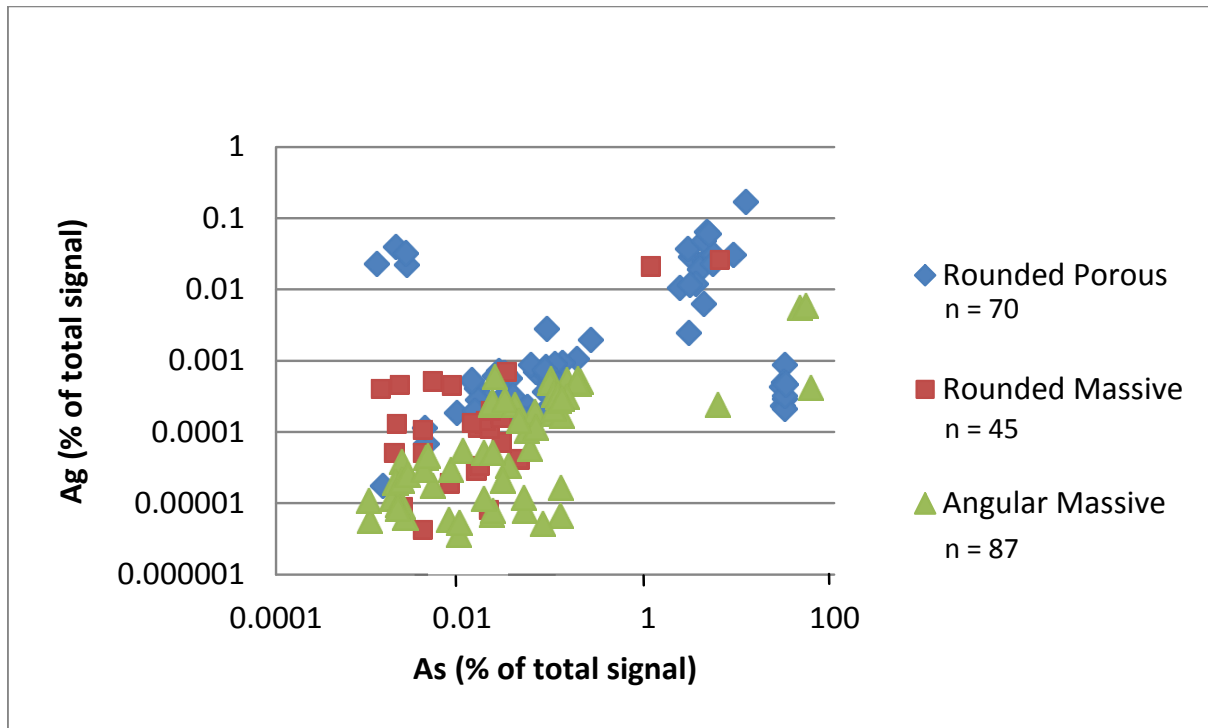
Figure 5.12: *Illustration As plotted against Ag for the different types of rounded and angular pyrite grains.*
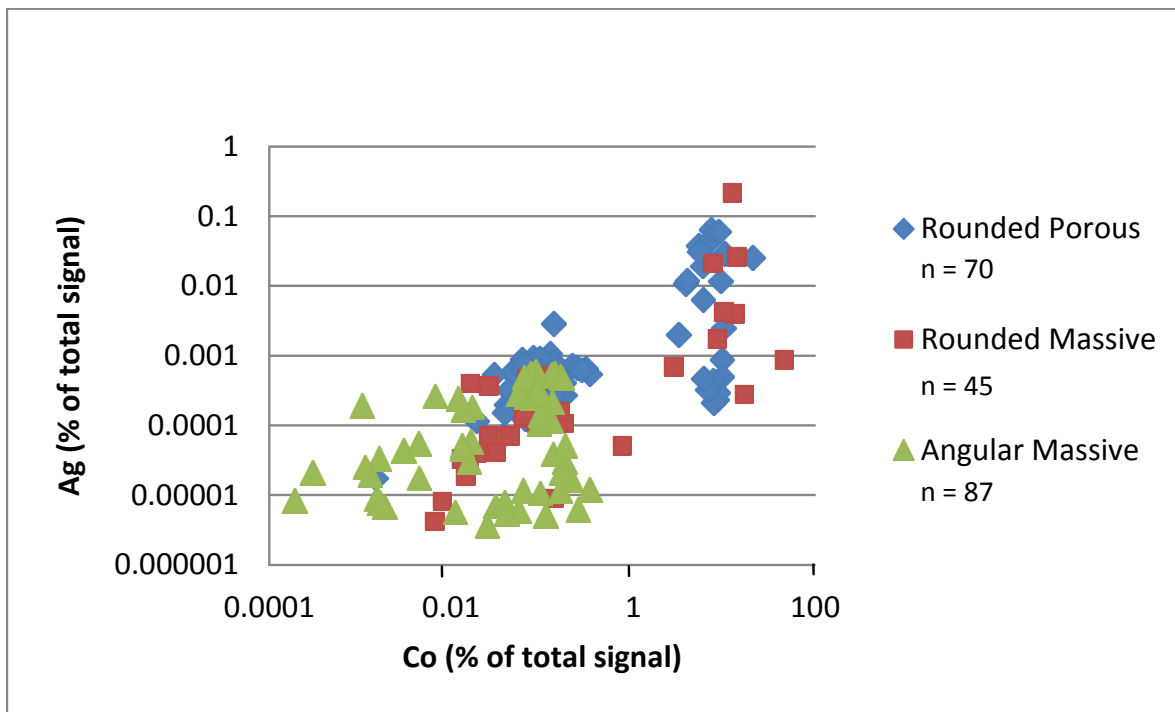
Figure 5.13: *Illustration Co plotted against Ag for the different types of rounded and angular pyrite grains.*
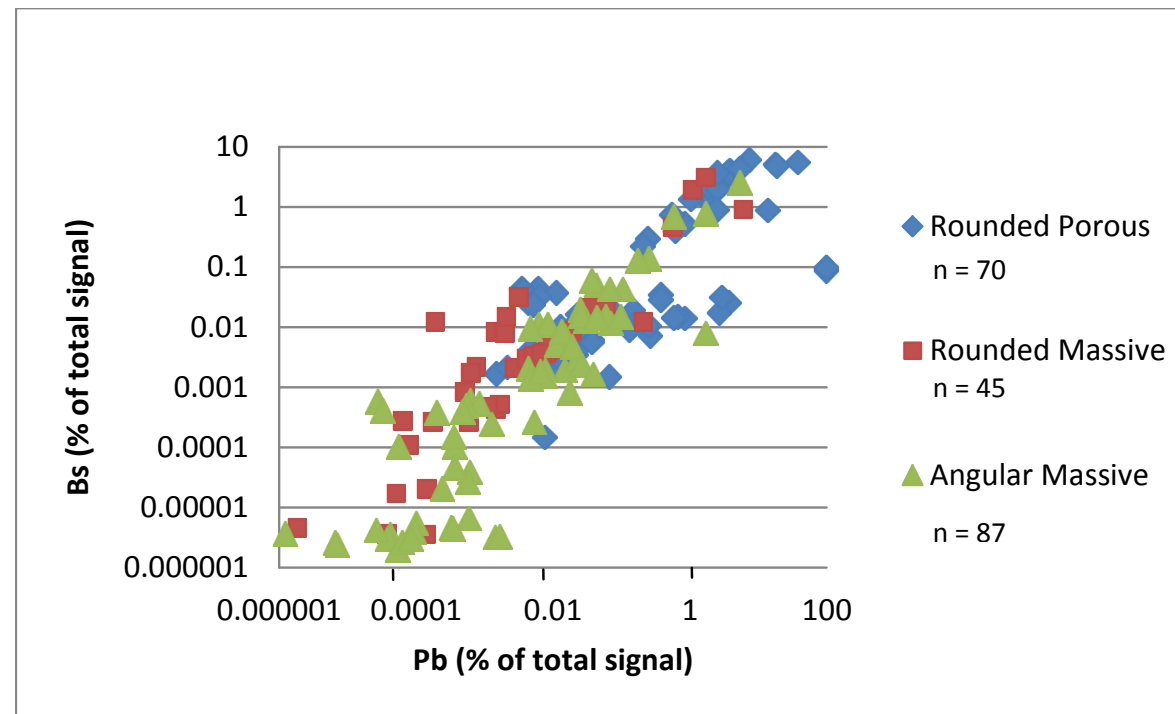

Figure 5.14: *Illustration Pb plotted against Bs for the different types of rounded and angular pyrite grains.*
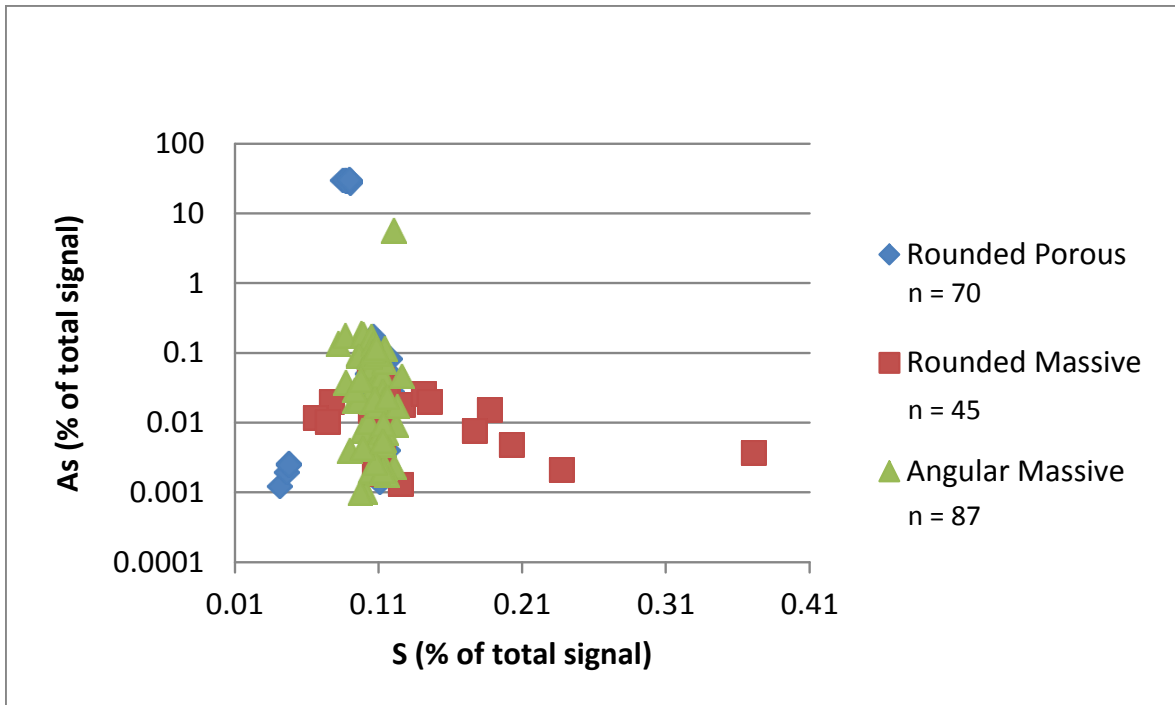
***Figure 5.15:*** *Illustration S plotted against As for the different types of rounded and angular pyrite grains.*
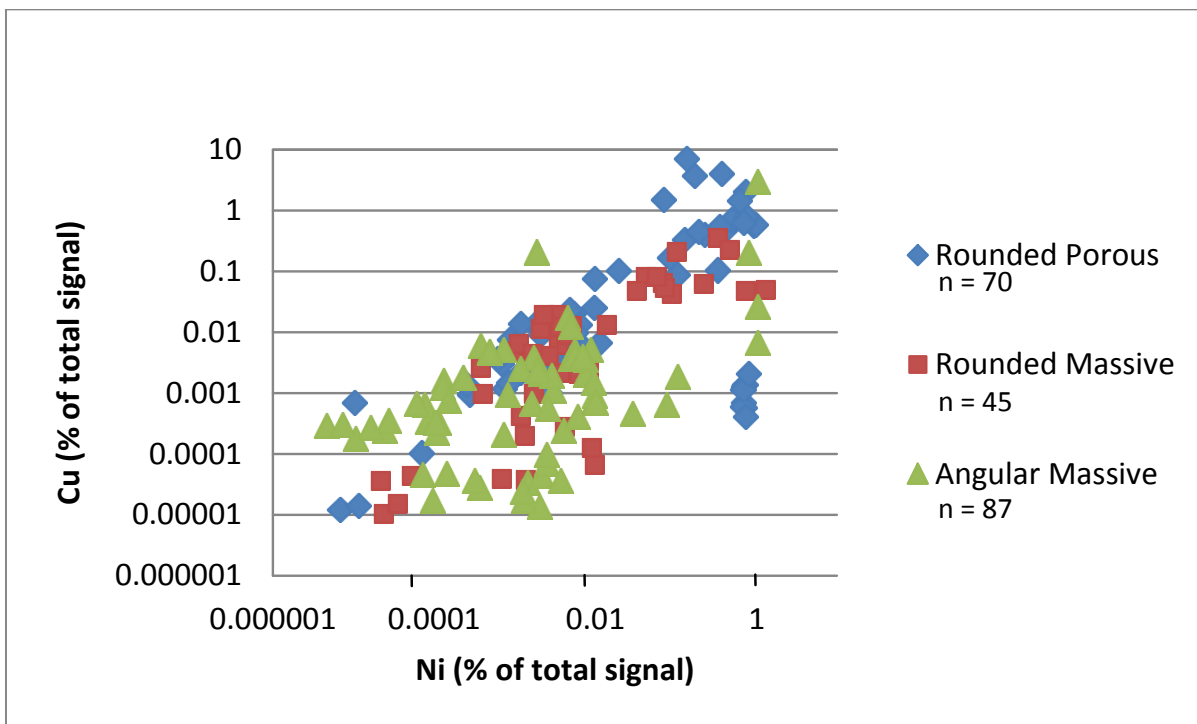
Figure 5.16: *Illustration Ni plotted against Cu for the different types of rounded and angular pyrite grains.*
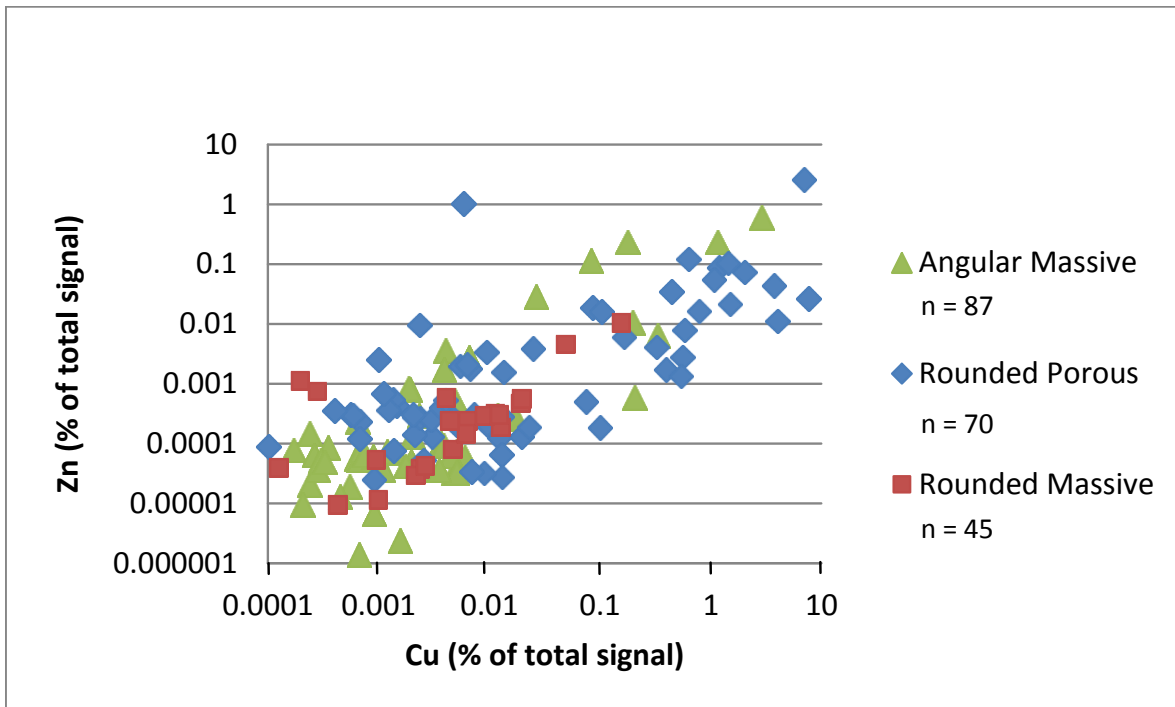
Figure 5.17: *Illustration Cu plotted against Zn for the different types of rounded and angular pyrite grains.*
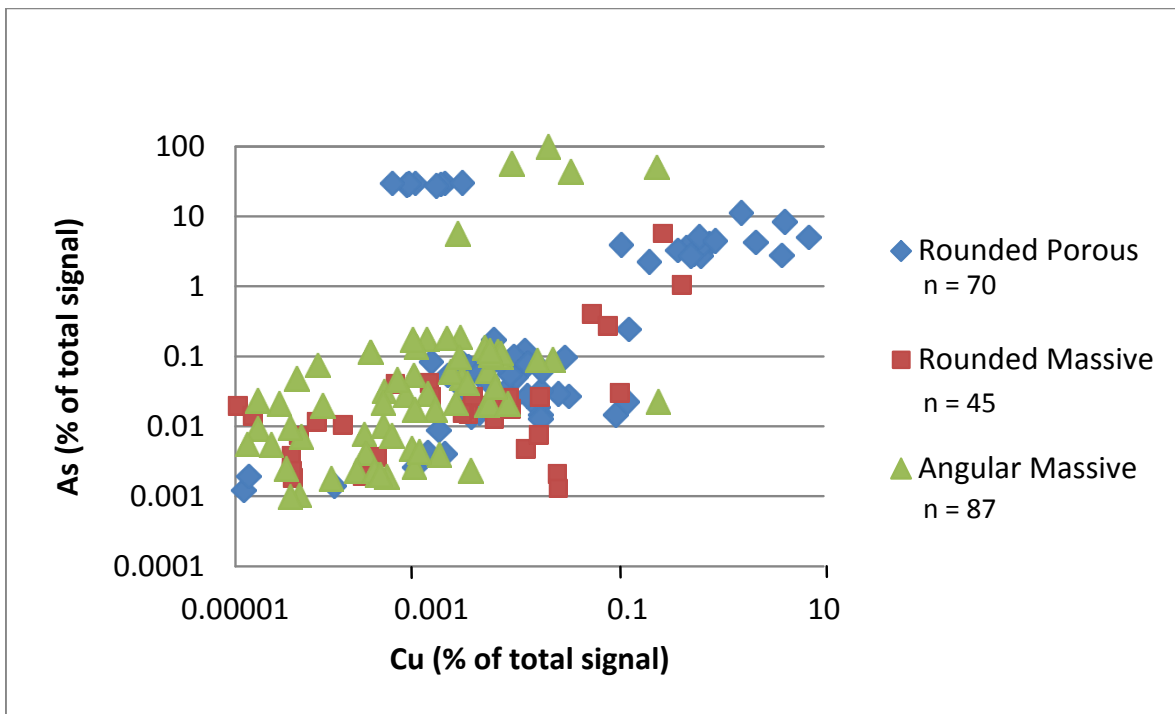
Figure 5.18: *Illustration Cu plotted against As for the different types of rounded and angular pyrite grains.*
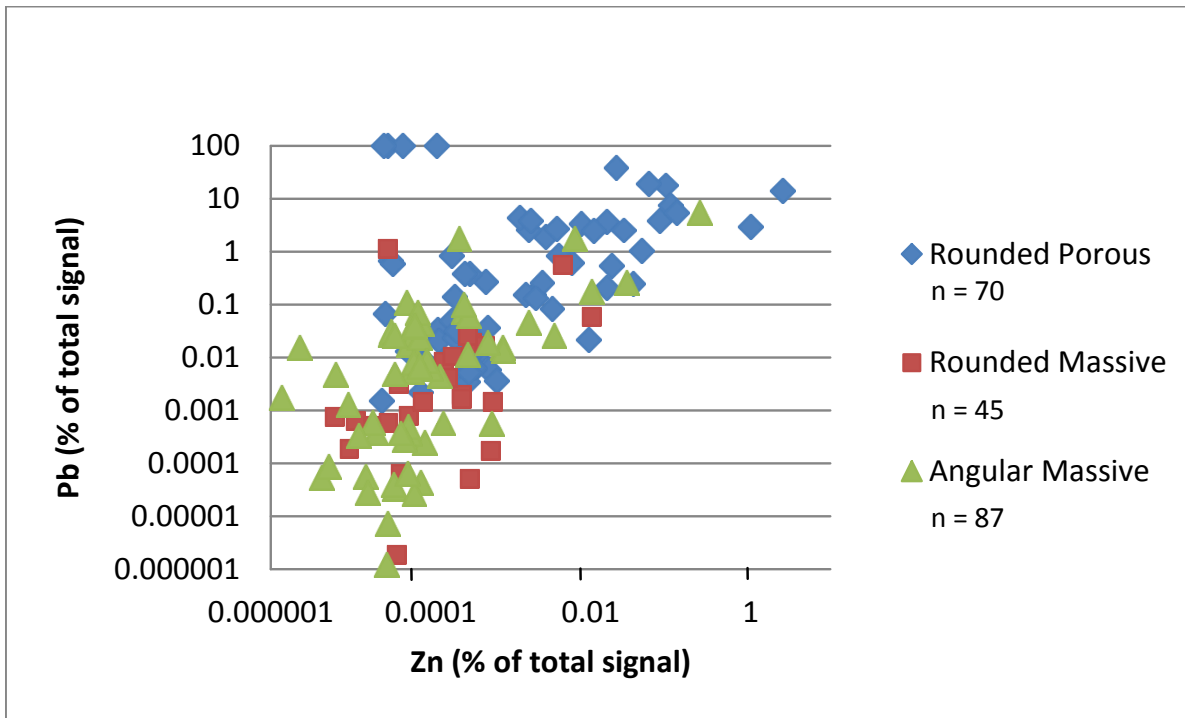
Figure 5.19: *Illustration Zn plotted against Pb for the different types of rounded and angular pyrite grains.*
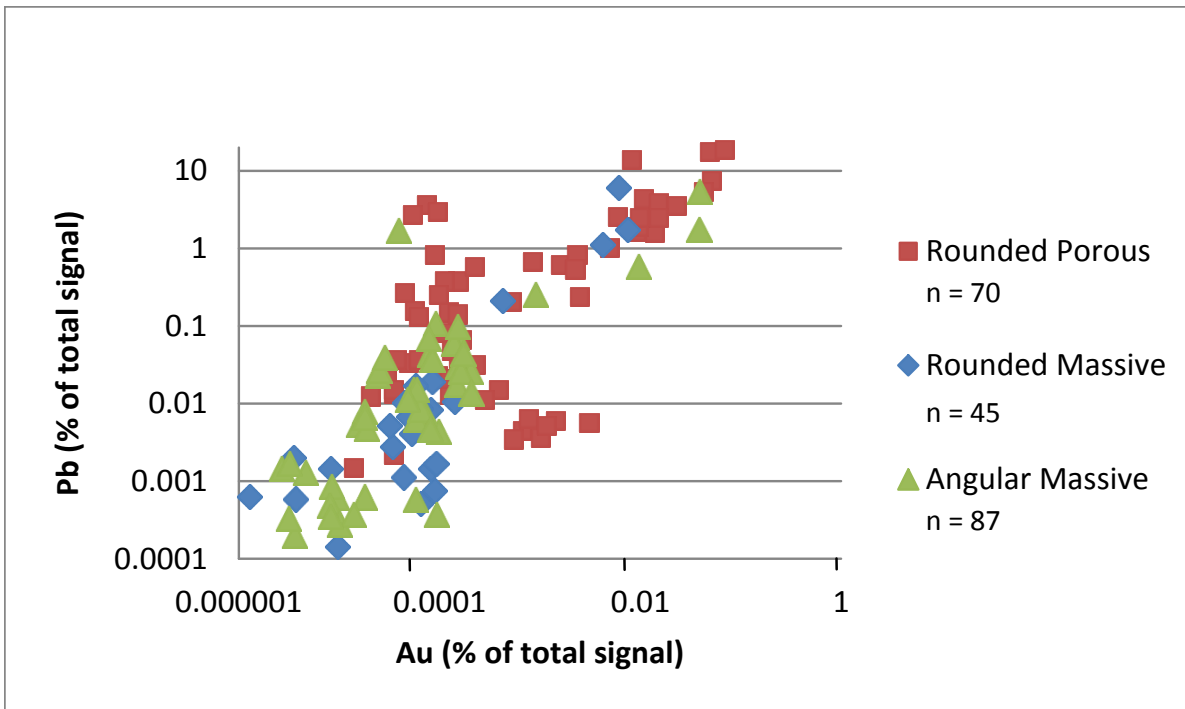
Figure 5.20: *Illustration Au plotted against Pb for the different types of rounded and angular pyrite grains.*
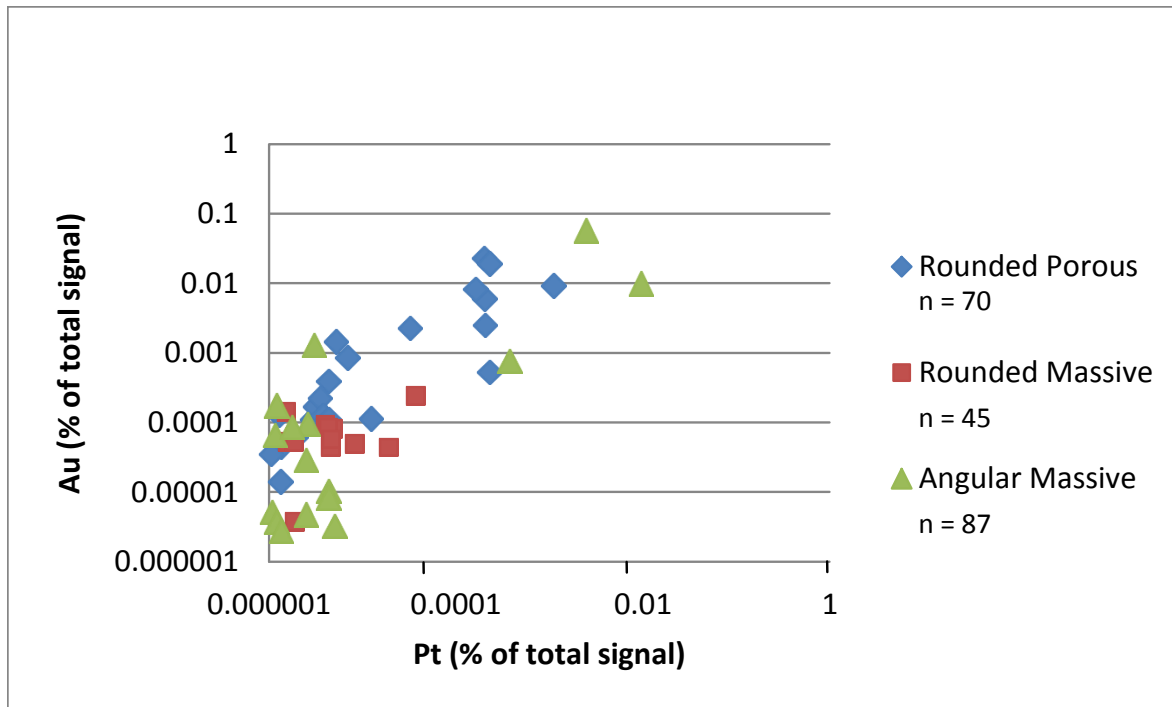
Figure 5.21: *Illustration Au plotted against Pt for the different types of rounded and angular pyrite grains.*
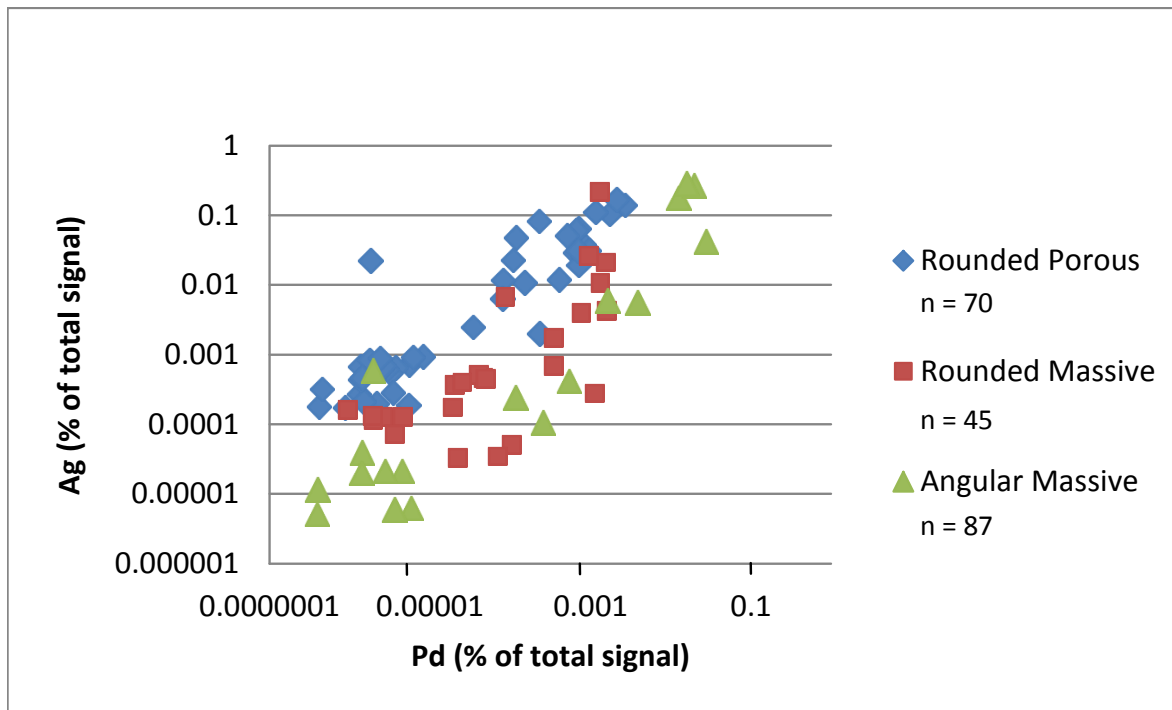

Figure 5.22: *Illustration Pd plotted against Ag for the different types of rounded and angular pyrite grains.*
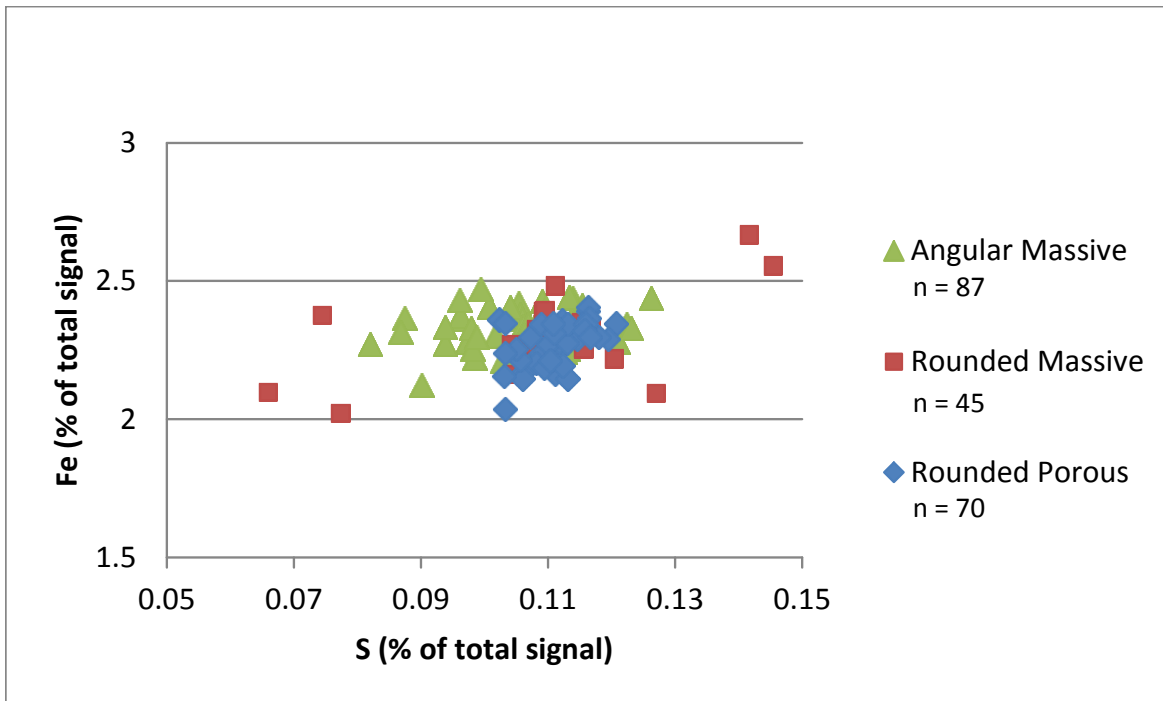
Figure 5.23: *Illustration S plotted against Fe for the different types of rounded and angular pyrite grains.*
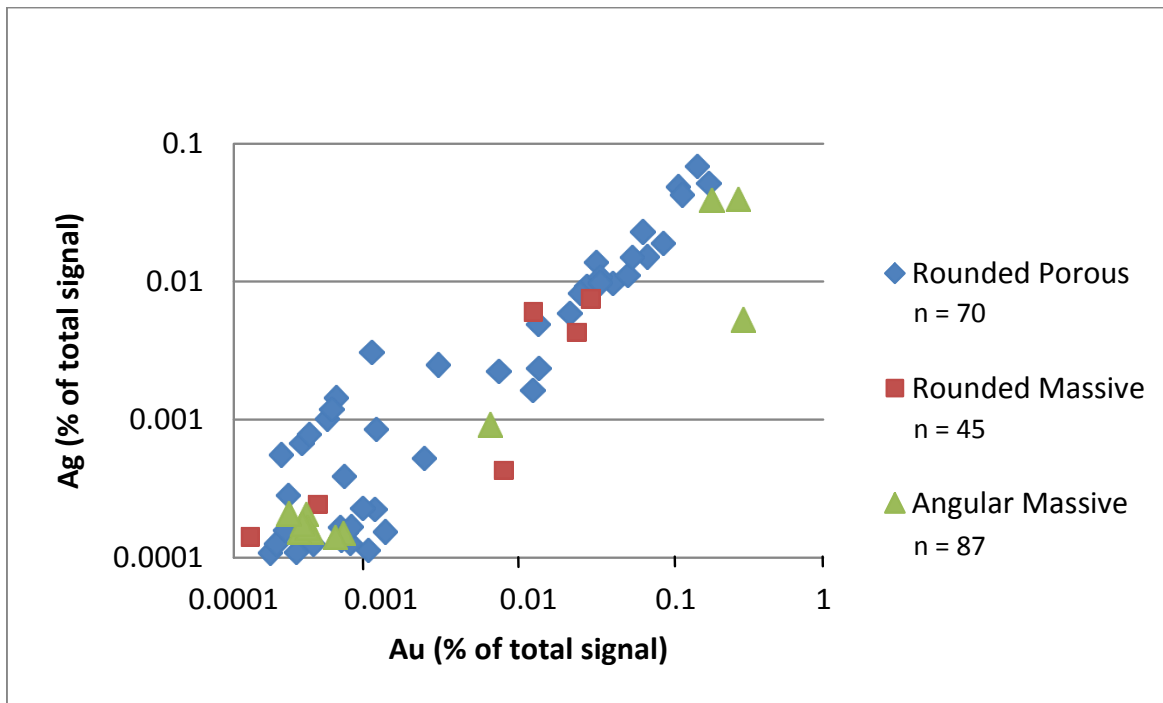
Figure 5.24: *Illustration Au plotted against Ag for the different types of rounded and angular pyrite grains.*
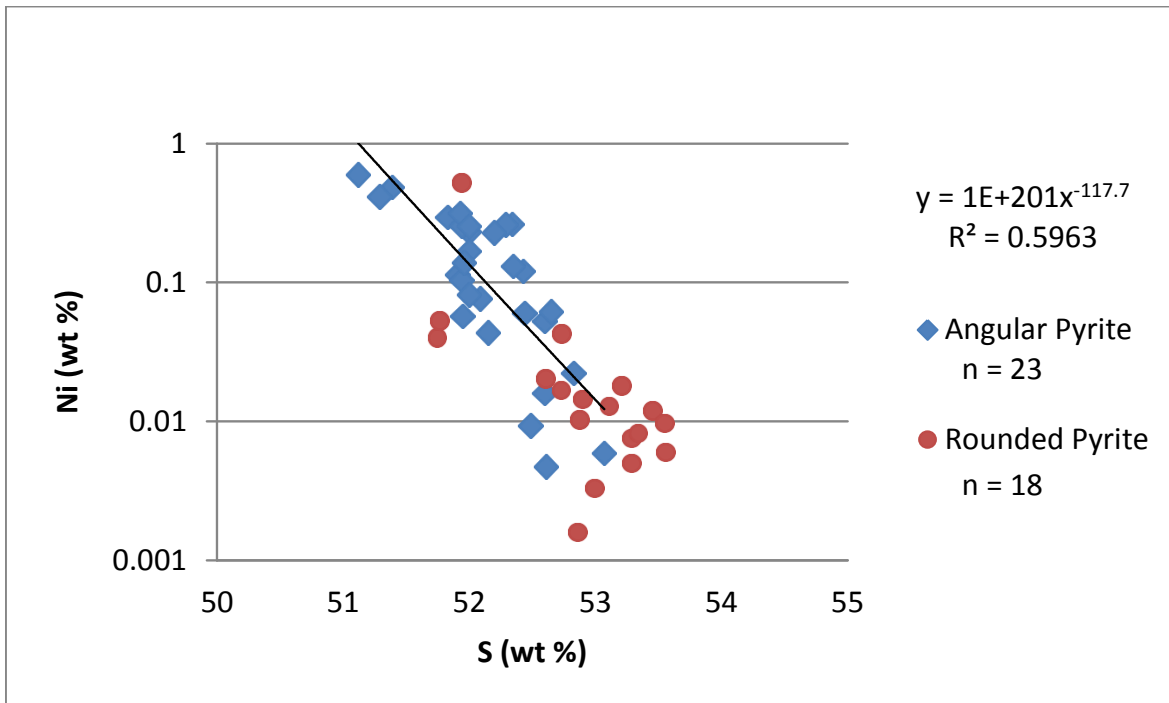
Figure 5.25: *Illustration of Ni plotted against S for the different types of rounded and angular pyrite grains.*